

DESIGN OF NOVEL ALKALI ACTIVATED MATERIALS EXHIBITING
ADSORPTION PERFORMANCE AND PHOTOCATALYTIC ACTIVITY

by

Kardelen Kaya Özkiper

B.S., Chemical Engineering, Istanbul Technical University, 2013

M.S., Chemical Engineering, Boğaziçi University, 2016

Submitted to the Institute for Graduate Studies in
Science and Engineering in partial fulfillment of
the requirements for the degree of
Doctor of Philosophy

Graduate Program in Chemical Engineering

Boğaziçi University

2022

to my family,

ACKNOWLEDGEMENTS

I would like to express my sincere thanks to my thesis supervisor Assoc. Prof. Sezen Soyer Uzun, for her support, encouragement, priceless guidance and help throughout my graduate studies and during the completion of this thesis. I am grateful to her for giving me the opportunity for conducting independent research and providing me a suitable environment where I can focus on what I am really curious about. Her contribution and guidance have helped me to gain new perspectives and she has become one of my role models not just professionally, but also as a human being. I would like to pronounce my gratitude to Assoc. Prof. Alper Uzun. His invaluable mentorship, motivation, and knowledge has been appreciated greatly. He has always been an inspiration for me as an academic and as a scientist. I feel grateful and lucky to have studied and conducted research with them.

I thank to Prof. Ramazan Yıldırım, Assoc. Prof. Uğur Ünal, Prof. Kutlu Ülgen, and Assist Prof. Murat Oluş Özbek for their valuable comments and discussions on my thesis as committee members.

I would like to express my sincere appreciations for Dr. Samira Kurtoğlu Öztulum and all other Uzun Lab members, and also KUTEM members from Koç University for their helps. Sincere thanks to Dr. Barış Yağcı, Dr. Amir Motallebzadeh, and all other KUYTAM members from Koç University for their contributions. Also, special thanks to Prof. Nilüfer Özyurt Zihnioğlu and Onur Pehlivan for their helps.

Feyza Kevser Öner, Işıl Yeşil Gür, Özlem Özbek, Merve Can Bilal, and Özgü Özer deserve special and heartfelt thanks for their support during my PhD studies. Furthermore, I would like to thank to my dear colleagues Ebru Kahraman and Tuğba Hayri Şenel from Istanbul Technical University. Their friendship and support will not be forgotten.

Cordial thanks to Yakup Bal, Dilek Kirkoç and Belgin Balkan for helping me whenever I needed.

Finally, I would like to express my dearest thanks to my beloved family members Nezaket Kaya, Seyit Kaya, Defne Kaya, and Feride Elitok for their support, patience, and encouragement throughout my whole life. Their presence makes my life meaningful and their support motivated me a lot during the hard course of this work. Last but not least, I would like to thank to my dear husband Ömer Özkipper for his support, love, and understanding. He has always balanced me with his kind and encouraging attitude. This thesis is devoted to my family, their endless love and trust in me enabled me to follow my own path and dreams in life.

The financial support provided by Boğaziçi University Research Fund through Project BAP19A05D2 is gratefully acknowledged.

ABSTRACT

DESIGN OF NOVEL ALKALI ACTIVATED MATERIALS EXHIBITING ADSORPTION PERFORMANCE AND PHOTOCATALYTIC ACTIVITY

Alkali activated materials (AAMs) are environmentally friendly alternatives to traditional cement binders with their comparable mechanical properties. Geopolymers are a subcategory of AAMs and synthesized from aluminosilicate sources. The main motivation of this thesis is to understand the methylene blue (MB) adsorption and photocatalytic activity of AAMs and geopolymers by utilizing diffraction and microscopy techniques to establish an structure-performance relationship. Firstly, an industrial waste red mud together with metakaolin were used as raw materials and anatase amount in the geopolymer paste was varied to obtain a photocatalytically active geopolymer (RMGP) to remove MB dye from wastewaters. Findings implied that surface Ti species were responsible for the photocatalytic MB removal and 3.7 wt% addition of anatase was found to result in a tripled rate constant compared to that of pure anatase, due to synergistic effect of adsorption and photocatalysis processes. Secondly, novel and new Sep-based AAMs (Sep-AAM) as adsorbents for MB removal was introduced. Results showed that Sep-AAM has an enhanced MB adsorption capacity of 99.9 mg g⁻¹, adsorption occurs via chemical adsorption, and is slightly endothermic. MB adsorption performance of monolith-formed Sep-AAMs and metakaolin-based counterparts (MKGP) with varying porosities were studied in the third part of this thesis. Outcomes of this part showed that it is possible to tune the MB adsorption performance and compressive strength by adjusting the porosity levels, and both of these monoliths can be regenerated up to four cycles. In the last part, MB adsorption performance of RMGP from part one was significantly enhanced by incorporating urea-based graphitic carbon nitride. The findings of this thesis demonstrate that AAMs and geopolymers with their economical and environmentally-friendly synthesis procedures offer high mechanical strength, enhanced adsorption and photocatalytic performance towards MB, and sustainable alternatives for wastewater treatment applications.

ÖZET

ADSORPSİYON PERFORMANSI VE FOTOKATALİTİK AKTİVİTE GÖSTEREN ALKALİ AKTİF MALZEMELERİN TASARIMI

Alkali aktif malzemeler (AAM) geleneksel çimento bağlayıcılarına çevre-dostu alternatifler olarak bilinen yüksek mekanik performanslı malzemelerdir. AAM'lerin bir alt kategorisi olan jeopolimerler ise aluminosilikat içeriği yüksek malzemelerden sentezlenirler. Bu tezin amacı, AAM ve jeopolimerlerin, metilen mavisi (MB) boyası adsorpsiyonu ve fotokatalitik özelliklerinin anlaşılması; çeşitli karakterizasyon teknikleri kullanılarak yapı-performans ilişkilerinin belirlenmesidir. İlk olarak, endüstriyel bir atık olan kırmızı çamur ve metakaolin kullanılarak sentezlenen jeopolimerlerin kompozisyonlarındaki anataz miktarı değiştirilerek, MB eliminasyonuna yönelik jeopolimerler (RMGP) üretilmiştir. Deneysel sonuçlar, fotokatalitik aktivenin nedeninin yüzey titanyum türleri olduğunu ve ağırlıkça %3.7 anataz içeren RMGP'nin, adsorpsiyon ve fotokataliz mekanizmalarının eş zamanlı etkisinden dolayı saf anataza kıyasla üç kat daha yüksek hız sabitine sahip olduğunu göstermiştir. İkinci olarak, adsorpsiyon literatüründe yeni bir malzeme grubu olarak sepiyolit bazlı bir AAM (Sep-AAM) sentezlenerek bu malzemenin 99.9 mg g^{-1} gibi yüksek bir MB giderim performansı gösterdiği, adsorpsiyonun endotermik olduğu ve adsorpsiyon esnasındaki temel mekanizmanın kimyasal olduğu ortaya koyulmuştur. Üçüncü bölümde, sepiyolit ve metakaolin kullanılarak farklı porozitelere sahip monolit formda AAM ve jeopolimerler sentezlenmiş, MB adsorpsiyonu ve mekanik dayanım özelliklerinin monolitlerin porozitesi ile modifiye edilebileceği ve üretilen malzemelerin rejenere edilebileceği gösterilmiştir. Tezin son kısmında ise, RMGP örneği, üre-bazlı grafitik karbon nitrür ile bir kompozit sentezinde ilk defa kullanılarak grafitik karbon nitrür katkısının MB adsorpsiyon kapasitesini salt grafitik karbon nitrüre göre yaklaşık 3.5 kat artırdığı gösterilmiş, kimyasal mekanizmaların adsorpsiyonda etkin olduğu belirlenmiştir. Bu tezin bulguları, etkin adsorpsiyon ve fotokatalitik aktivite performansları ile AAM ve jeopolimerlerin yenilikçi malzemeler olarak atık su arıtımı gibi uygulamalarda çevre-dostu ve sürdürülebilir alternatifler olabileceğini ortaya koymaktadır.

TABLE OF CONTENTS

ACKNOWLEDGEMENTS	iv
ABSTRACT	vi
ÖZET	vii
LIST OF FIGURES	xii
LIST OF TABLES	xx
LIST OF SYMBOLS	xxvii
LIST OF ACRONYMS/ABBREVIATIONS	xxviii
1. INTRODUCTION	1
1.1. Geopolymerization.....	2
1.2. Raw Materials Used in Geopolymerization	3
1.2.1. Metakaolin	3
1.2.2. Red Mud	5
1.2.3. Fly Ash	7
1.2.4. Sepiolite	9
1.3. Application Areas of Geopolymers	10
1.4. Methodology	12
1.4.1. Evaluation of Adsorption Performance	13
1.4.1.1. Adsorption Isotherms.....	15
1.4.2. Evaluation of Photocatalytic Activity.....	16
1.4.3. Structural Characterization of Materials	17
1.5. Scope and Aim of This Work	18
2. RED MUD- AND METAKAOLIN-BASED GEOPOLYMERS FOR ADSORPTION AND PHOTOCATALYTIC DEGRADATION OF METHYLENE BLUE: TOWARDS SELF-CLEANING CONSTRUCTION MATERIALS	20
2.1. Introduction	20
2.2. Experimental Methods	21
2.2.1. Materials	21
2.2.2. Synthesis of Geopolymers	22

2.2.3. Materials Characterization	23
2.2.4. Evaluation of Photocatalytic Activities	24
2.3. Results and Discussions	25
2.3.1. Bulk Microstructure, Morphological, and Mechanical Properties	25
2.3.2. Surface Characteristics	28
2.3.3. Degradation of MB Dye	30
2.3.3.1. Experiments Under Dark Followed by UV Irradiation	30
2.3.3.2. Experiments Under Direct UV Irradiation.....	35
2.4. Concluding Remarks	39
3. A NOVEL ALKALI ACTIVATED MAGNESIUM SILICATE AS AN EFFECTIVE AND MECHANICALLY STRONG ADSORBENT FOR METHYLENE BLUE REMOVAL	41
3.1. Introduction	41
3.2. Experimental Conditions	44
3.2.1. Materials	44
3.2.2. Preparation of the AAM	44
3.2.3. Materials Characterization.....	44
3.2.4. MB Adsorption Tests.....	45
3.2.4.1. Thermodynamical Properties	46
3.2.4.2. Adsorbent Regeneration Tests	47
3.3. Results and Discussions	47
3.3.1. Morphological, Bulk Microstructure, Thermogravimetric, and Mechanical Properties	47
3.3.2. Surface Characteristics	55
3.3.3. MB Adsorption Tests	57
3.3.3.1. Effect of Contact Time, $C_0 = 20 \text{ mg L}^{-1}$	58
3.3.3.2. Effect of Initial MB Concentration	59
3.3.3.3. Effect of Adsorbent Amount on Adsorption of MB Dye	60
3.3.3.4. Effect of pH on Adsorption of MB Dye	61
3.3.3.5. Effect of Temperature on Adsorption of MB Dye.....	62
3.3.3.6. Adsorption Kinetics Modeling and Mechanism	63
3.3.4. Adsorbent Regeneration	67

3.3.5. Adsorption Isotherm Model Studies and Thermodynamical Properties	69
3.4. Concluding Remarks	73
4. SEPIOLITE AND METAKAOLIN-BASED ALKALI ACTIVATED MONOLITHS FOR METHYLENE BLUE REMOVAL: A COMPARATIVE STUDY.....	75
4.1. Introduction	75
4.2. Experimental Methods	76
4.2.1. Materials	76
4.2.2. Synthesis of AAMs	77
4.2.3. Materials Characterization	78
4.2.4. MB Adsorption Tests	78
4.3. Results and Discussion	79
4.3.1. Morphological, Bulk Microstructure, and Mechanical Properties....	79
4.3.2. MB Adsorption Tests	86
4.3.2.1. Effect of Contact Time, $C_0 = 70 \text{ mg L}^{-1}$	86
4.3.2.2. Effect of Initial MB Concentration	87
4.3.2.3. Adsorption Kinetics Modeling and Mechanism	88
4.3.3. Adsorbent Regeneration	91
4.3.4. Adsorption Isotherm Model Studies	93
4.4. Concluding Remarks	98
5. GRAPHITIC CARBON NITRIDE INCORPORATED RED-MUD- AND METAKAOLIN-BASED GEOPOLYMERS FOR ENHANCED WASTEWATER TREATMENT CAPABILITY	99
5.1. Introduction	99
5.2. Experimental	101
5.2.1. Materials	101
5.2.2. Synthesis of Geopolymers	101
5.2.3. Synthesis of g-C ₃ N ₄ Incorporated RMGP	101
5.2.4. Characterization	101
5.2.5. Adsorption Experiments	102
5.2.5.1. Adsorbent Reusability Experiments	102
5.3. Results and Discussion	103

5.3.1. Morphological Properties	103
5.3.2. Surface Characteristics	107
5.3.3. Adsorption Measurements	109
5.3.3.1. Influence of Contact Time	109
5.3.3.2. Influence of Initial MB Concentration.....	110
5.3.3.3. Influence of Adsorbent Amount	111
5.3.3.4. Influence of pH	112
5.3.3.5. Adsorption Kinetics Modeling and Mechanism	114
5.3.3.6. Adsorbent Regeneration	116
5.3.3.7. Adsorption Isotherm Model Studies	118
5.4. Concluding Remarks.....	120
6. CONCLUSIONS AND RECOMMENDATIONS	122
6.1. Conclusions	122
6.2. Recommendations	125
REFERENCES	126
APPENDIX A: SUPPLEMENTARY INFORMATION 1	162
APPENDIX B: SUPPLEMENTARY INFORMATION 2	178
APPENDIX C: SUPPLEMENTARY INFORMATION 3	196
APPENDIX D: SUPPLEMENTARY INFORMATION 4	216

LIST OF FIGURES

Figure 1.1.	Schematic diagram of geopolymerization reactions.	2
Figure 2.1.	XRD patterns of geopolymers a) 0%A-RMGP, b) 0.4%A-RMGP, c) 1.2%A-RMGP, d) 1.9%A-RMGP, e) 3.7%A-RMGP.	26
Figure 2.2.	FTIR spectra of geopolymers a) 0%A-RMGP, b) 0.4%A-RMGP, c) 1.2%A-RMGP, d) 1.9%A-RMGP, e) 3.7%A-RMGP.	28
Figure 2.3.	XPS patterns of a) survey spectrum, b) O 1s spectrum of 3.7%A-RMGP.	29
Figure 2.4.	Variation of the residual MB dye concentration (C/C_0) with time; values were collected under dark for 12 h followed by UV irradiation for 12 h.	31
Figure 2.5.	Residual MB dye concentration (C/C_0) vs. time values collected under UV light conditions.	35
Figure 2.6.	The change of degraded MB amount under UV in 12 h (black symbols) and change of $k_{app,1}$ with surface Ti amount (at%).	37
Figure 2.7.	Experimental data fit to pseudo-first-order reaction kinetics for anatase-added RMGP samples. Error bars represent the standart error of surface Ti amount (at%).	38
Figure 3.1.	SEM images of materials at a magnification of 20 k \times : a) As-received Sep, b) Calcined Sep, and c) Sep-AAM.	48

Figure 3.2.	XRD patterns of a) as-received Sep, b) Sep calcined at 750 °C, and c) Sep-AAM.	51
Figure 3.3.	FTIR spectra of a) As-received Sep, b) Calcined Sep, and c) Sep-AAM.	52
Figure 3.4.	a) TG and b) DTG curves of as-received Sep, calcined Sep and Sep-AAM.	55
Figure 3.5.	The effect of contact time on a) C_t/C_0 and b) Uptake of calcined Sep and Sep-AAM.	58
Figure 3.6.	Effect of initial MB concentration on uptake (q_e) and removal (%) of MB for a) Calcined Sep, and b) Sep-AAM.	59
Figure 3.7.	The effect of adsorbent amount on MB uptake and MB removal (%) by a) Calcined Sep, and b) Sep-AAM (<i>Contact time</i> = 3.5 h, $C_0 = 20$ mg L ⁻¹).	60
Figure 3.8.	The effect of initial pH on MB uptake by calcined Sep and Sep-AAM (<i>Contact time</i> = 3.5 h, T= 31 °C, $C_0 = 20$ mg L ⁻¹).	61
Figure 3.9.	Effect of temperature on the equilibrium uptakes for MB on a) Calcined Sep, and b) Sep-AAM.	63
Figure 3.10.	Experimental data fit to pseudo-second-order adsorption kinetics for Sep-AAM samples at a) 31 °C, b) 40 °C, and c) 50 °C.	65
Figure 4.1.	XRD patterns of a) Sep-AAMs with different H ₂ O ₂ content, and b) MKGPs with different H ₂ O ₂ content.	82
Figure 4.2.	FTIR spectra of a) Sep-AAMs with different H ₂ O ₂ content, and b) MKGPs with different H ₂ O ₂ content.	83

Figure 4.3.	SEM images of materials at a magnification of 100×: a) Sep-AAM, b) 1% H_2O_2 -Sep-AAM, c) 8% H_2O_2 -Sep-AAM, d) MKGP, e) 0.5% H_2O_2 -MKGP, and f) 1% H_2O_2 -MKGP.	84
Figure 4.4.	Compressive strength of the Sep-AAM and MKGP samples with different H_2O_2 content (Cured for four weeks).	85
Figure 4.5.	The effect of contact time on uptake of a) Sep-AAMs and b) MKGPs with different H_2O_2 content.	87
Figure 4.6.	Effect of initial MB concentration on a) uptake (q_e) and b) removal efficiency (%) of MB for Sep-AAM, 8% H_2O_2 -Sep-AAM, MKGP, and 1% H_2O_2 -MKGP.	88
Figure 4.7.	MB uptake ($mg\ g^{-1}$) removal efficiency (%) values for a) 8% H_2O_2 -Sep-AAM and b) 1% H_2O_2 -MKGP after regeneration cycles.	92
Figure 5.1.	XRD patterns of a) RMGP, b) Calcined RMGP, c) g- C_3N_4 , and d) g- C_3N_4 /RMGP.	105
Figure 5.2.	FTIR spectra of a) RMGP, b) Calcined RMGP, c) g- C_3N_4 , and d) g- C_3N_4 /RMGP.	107
Figure 5.3.	The influence of contact time on a) Uptake and b) C_t/C_0 of g- C_3N_4 /RMGP and g- C_3N_4	110
Figure 5.4.	The influence of initial MB concentration on uptake and removal (%) of MB for a) g- C_3N_4 and b) g- C_3N_4 /RMGP.	111
Figure 5.5.	The influence of adsorbent amount on uptake and removal (%) of MB for a) g- C_3N_4 and b) g- C_3N_4 /RMGP.	112

Figure 5.6.	The influence of pH on MB uptake by g-C ₃ N ₄ and g-C ₃ N ₄ /RMGP (<i>Contact time</i> = 3 h, <i>C</i> ₀ = 20 mg L ⁻¹).	113
Figure A.1.	XRD patterns of the aluminosilicate sources used for geopolymer synthesis: a) MK b) Calcined RM.	164
Figure A.2.	FTIR spectra of raw materials a) MK and b) RM.	164
Figure A.3.	SEM images and corresponding EDS spectrum of a) MK, b) EDS spectrum of MK, c) Calcined RM, d) EDS spectrum of calcined RM.	165
Figure A.4.	Evolution of the ratios of the intensities of the bands corresponding to Si–O–T and Si–O–Si vibrations ($I_{Si-O-T}/I_{Si-O-Si}$ ratio) and compressive strength of geopolymers as a function of anatase content (wt%) in the geopolymer pastes.	166
Figure A.5.	SEM image, corresponding elemental analysis and EDS mapping of 0%A-RMGP: a) SEM image b) Elemental analysis and EDS mapping, including elemental analysis, c) Si, d) Al, e) Na, f) Ti, and g) Fe.	167
Figure A.6.	SEM image, corresponding elemental analysis and EDS mapping of 0.4%A-RMGP: a) SEM image b) Elemental analysis and EDS mapping, including elemental analysis, c) Si, d) Al, e) Na, f) Ti, and g) Fe.	168
Figure A.7.	SEM image, corresponding elemental analysis and EDS mapping of 1.2%A-RMGP: a) SEM image b) Elemental analysis and EDS mapping, including elemental analysis, c) Si, d) Al, e) Na, f) Ti, and g) Fe.	169

Figure A.8.	SEM image, corresponding elemental analysis and EDS mapping of 1.9%A-RMGP: a) SEM image b) Elemental analysis and EDS mapping, including elemental analysis, c) Si, d) Al, e) Na, f) Ti, and g) Fe.	170
Figure A.9.	SEM image, corresponding elemental analysis and EDS mapping of 3.7%A-RMGP: a) SEM image b) Elemental analysis and EDS mapping, including elemental analysis, c) Si, d) Al, e) Na, f) Ti, and g) Fe.	171
Figure A.10.	XPS patterns of a) Fe 2p, b) Ti 2p, and c) O 1s spectrum of 0%A-RMGP, d) Fe 2p, e) Ti 2p and f) O 1s spectrum of 0.4%A-RMGP, g) Fe 2p, h) Ti 2p, and i) O 1s spectrum of 1.2%A-RMGP, j) Fe 2p, k) Ti 2p and l) O 1s spectrum of 1.9%A-RMGP, m) Fe 2p, n) Ti 2p, and o) O 1s spectrum of 3.7%A-RMGP.	173
Figure A.11.	Band gap values of geopolymers calculated by Kubelka Munk function.	175
Figure A.12.	Absorbance vs wavelength values of the geopolymers.	175
Figure A.13.	UV-Vis spectrum of a) 0%A-RMGP and b) 10%A-RMGP.	176
Figure B.1.	SEM images and corresponding EDX spectra of materials: a) As-received Sep (at a magnification of 7956×), b) EDX spectrum of green □ in a), c) Calcined Sep (at a magnification of 17630×), d) EDX spectrum of green □ in c), e) Sep-AAM (at a magnification of 9646×), f) EDX spectrum of green □ in e).	179
Figure B.2.	XPS pattern of survey spectrum for Sep-AAM.	180
Figure B.3.	XPS patterns of a) Si 2p, b) O 1s, c) Mg 2p, and d) Mg 1s spectrum of as-received Sep, e) Si 2p, f) O 1s, g) Mg 2p and h) Mg 1s	

	spectrum of calcined Sep, i) Si 2p, j) O 1s, k) Mg 2p, and l) Mg 1s spectrum of Sep-AAM (Blue lines: fitted individual peaks, green lines: envelope of all fitted peaks).	181
Figure B.4.	The change of zeta potential with pH for calcined Sep and Sep-AAM.	183
Figure B.5.	Pseudo-first and pseudo-second-order kinetic models for the adsorption of MB onto a-b) Sep-AAM, and c-d) Calcined Sep, at different temperatures.	186
Figure B.6.	Experimental data fit to pseudo-second-order adsorption kinetics for calcined Sep at a) 31 °C, b) 40 °C, and c) 50 °C.	187
Figure B.7.	The plot of $\ln(k_{2,ads})$ vs $1/T$ for a) Calcined Sep and b) Sep-AAM. ...	187
Figure B.8.	Intraparticle diffusion model for the adsorption of MB onto Sep-AAM at a) 31 °C, b) 40 °C, and c) at 50 °C.	189
Figure B.9.	MB removal (%) and uptake values for calcined Sep after regeneration cycles.	190
Figure B.10.	MB removal (%) and uptake values for Sep-AAM after regeneration cycles.	190
Figure B.11.	FTIR spectra of MB and Sep-AAM sample before and after adsorption, and after 4 cycles of regeneration (<i>Contact time</i> = 3.5 h).	191
Figure B.12.	The change in the performance (%) of Sep-AAM monoliths during regeneration experiments.	192

Figure B.13.	$\ln(K_{ads})$ vs $1/T$ plot for MB adsorption onto a) Calcined Sep, and b) Sep-AAM.	194
Figure C.1.	XRD patterns of a) Calcined Sep and b) MK.	197
Figure C.2.	FTIR patterns of a) Calcined Sep and b) MK.	197
Figure C.3.	SEM images of materials: a) MK- at a magnification of 50 k \times , b) Calcined Sep- at a magnification of 20 k \times , synthesized materials at a magnification of 100 \times : c) MKGP, d) 0.5% H_2O_2 -MKGP, e) 1% H_2O_2 -MKGP, f) Sep-AAM, g) 0.5% H_2O_2 -Sep-AAM, h) 1% H_2O_2 -Sep-AAM, i) 2% H_2O_2 -Sep-AAM, j) 3% H_2O_2 -Sep-AAM, k) 6% H_2O_2 -Sep-AAM, and l) 8% H_2O_2 -Sep-AAM.	199
Figure C.4.	The change of zeta potential with pH for 1% H_2O_2 -MKGP and 8% H_2O_2 -Sep-AAM.	201
Figure C.5.	Intraparticle diffusion model for the adsorption of MB onto a) 8% H_2O_2 -Sep-AAM and b) 1% H_2O_2 -MKGP (<i>Contact time</i> = 24 h, $C_0 = 70 \text{ mg L}^{-1}$).	208
Figure C.6.	FTIR spectra of MB and a) 8% H_2O_2 -Sep-AAM and b) 1% H_2O_2 -MKGP sample before and after adsorption, and after 4 cycles of regeneration (<i>Contact time</i> = 24 h).	210
Figure C.7.	Stereo microscopy micrographs of the distinct MB diffusion throughout a) Sep-AAM, b) 8% H_2O_2 -Sep-AAM, c) MKGP, and d) 1% H_2O_2 -MKGP, after adsorption (<i>Contact time</i> = 24 h, $C_0 = 110 \text{ mg L}^{-1}$).	214
Figure D.1.	SEM image, corresponding elemental analysis of a) RMGP, b) Calcined RMGP, c) g- C_3N_4 , and d) g- C_3N_4 /RMGP.	217

Figure D.2.	XP survey spectrum of a) RMGP, b) Calcined RMGP, c) g-C ₃ N ₄ , and d) g-C ₃ N ₄ /RMGP.	218
Figure D.3.	XPS patterns of a) C 1s, b) N 1s, c) O 1s of g-C ₃ N ₄ , d) C 1s, e) N 1s, and f) O 1s of g-C ₃ N ₄ /RMGP (Blue lines: fitted individual peaks, green lines: envelope of all fitted peaks).	219
Figure D.4.	The change of zeta potential with pH for g-C ₃ N ₄ and g-C ₃ N ₄ /RMGP.	220
Figure D.5.	The influence of contact time on a) Uptake and b) C_t/C_0 of RMGP and Calcined RMGP.	220
Figure D.6.	Pseudo-first and pseudo-second-order kinetic models for the adsorption of MB onto a) g-C ₃ N ₄ and b) g-C ₃ N ₄ /RMGP.	221
Figure D.7.	Influence of adsorbent amount on the apparent pseudo-second-order adsorption rate constant for a) g-C ₃ N ₄ and b) g-C ₃ N ₄ /RMGP.	222
Figure D.8.	Intraparticle diffusion model for the adsorption of MB onto a) g-C ₃ N ₄ and b) g-C ₃ N ₄ /RMGP.	224
Figure D.9.	MB removal (%) and uptake values for g-C ₃ N ₄ /RMGP after regeneration cycles.	225
Figure D.10.	FTIR spectra of MB and g-C ₃ N ₄ /RMGP sample before and after adsorption, and after 4 cycles of regeneration (<i>Contact time</i> = 3 h).	226

LIST OF TABLES

Table 2.1.	Mix quantities per unit volume (kg m^{-3}) calculated based on densities of the raw materials and assuming that the volumes of the components are additive. Corresponding wt% are given in parenthesis for the RMGP pastes.	23
Table 2.2.	Kinetic parameters for adsorption of MB on anatase added geopolymer samples under dark conditions.	32
Table 2.3.	Pseudo-first- and second-order reaction kinetic parameters obtained for 0.03 g of sample in 5×10^{-5} M 100 ml MB solution under 12 hours of UV-light after 12 hours of dark conditions (data collected under UV light is used for the calculation of the parameters given in this table).	33
Table 2.4.	Pseudo-first and second-order- reaction kinetics parameters and degraded amount (%) values obtained for 0.03 g of sample in 5×10^{-5} M 100 ml MB solution under UV light after 12 hours.	36
Table 3.1.	BET surface area, average pore size, and pore volume of samples.	48
Table 3.2.	Pseudo-first and pseudo-second-order kinetic model parameters and removal efficiency (%) for adsorption of MB onto Sep-AAM at different temperatures (<i>Contact time</i> = 3.5 h, $C_0 = 20 \text{ mg L}^{-1}$ and $m = 10 \text{ mg}$).	64
Table 3.3.	Actual second-order adsorption rate constants ($k_{2,ads}$) of Sep-AAM at different temperatures.	65
Table 3.4.	Langmuir and Freundlich isotherm constants for MB adsorption on Sep-AAM at different temperatures.	70

Table 3.5.	Thermodynamic parameters for adsorption of MB onto Sep-AAM for 31, 40, and 50 °C.	71
Table 3.6.	MB adsorption capacity of various AAMs.	72
Table 4.1.	BET surface area, average pore size, and pore volume of samples.	80
Table 4.2.	Bulk density, total volume, and total porosity of samples.	81
Table 4.3.	Pseudo-first and pseudo-second-order kinetic model parameters and removal efficiency (%) for adsorption of MB onto synthesized AAMs. (<i>Contact time</i> = 24 h, $C_0 = 70 \text{ mg L}^{-1}$).	89
Table 4.4.	Langmuir and Freundlich isotherm constants for MB adsorption on synthesized AAMs.	94
Table 4.5.	MB adsorption capacity of various AAMs.	97
Table 5.1.	BET surface area, average pore size, and pore volume of samples.	103
Table 5.2.	Pseudo-first and pseudo-second-order kinetic model parameters and removal efficiency (%) for adsorption of MB onto g-C ₃ N ₄ and g-C ₃ N ₄ /RMGP (<i>Contact time</i> = 3h, $C_0 = 20 \text{ mg L}^{-1}$ and $m = 10 \text{ mg}$).	115
Table 5.3.	Langmuir and Freundlich isotherm constants for MB adsorption on Sep-AAM at different temperatures.	119
Table 5.4.	MB adsorption capacity of various graphitic carbon nitride-based adsorbents.	120
Table A.1.	Chemical compositions (wt%) of MK, raw RM, and calcined RM used in Chapter 2.	162

Table A.2.	The amounts of raw materials (in g) used in geopolymer synthesis, corresponding molar Si/Al and Al/Na ratios, and synthesis conditions used in RMGP synthesis in Chapter 2.	162
Table A.3.	BET surface area, average pore size, pore volume, and density of RMGP samples.	163
Table A.4.	Atomic % of Si, Al, Na, Fe, and Ti in geopolymers which are calculated by taking the average of values from EDS spectra recorded from three spots.	172
Table A.5.	Binding energy values of geopolymers derived from XPS analysis.	174
Table A.6.	Atomic % of Ti and Fe obtained from fitted peak information of Ti 2p and Fe 2p XP spectra.	174
Table A.7.	Band gap and maximum absorption wavelength values.	174
Table B.1.	Chemical compositions (wt%) of Sep and 1 h 750 °C calcined Sep used in this study, as determined by XRF spectroscopy.	178
Table B.2.	The amounts of raw materials (in g) used in the synthesis of Sep-based AAM, corresponding molar Si/Mg and Na/Mg ratios, and synthesis conditions used in Sep-AAM synthesis in this study.	178
Table B.3.	Mix quantities per unit volume (kg m^{-3}) calculated based on densities of the raw materials and assuming that the volumes of the components are additive. Corresponding wt% are given in parenthesis for the Sep-AAM paste.	178
Table B.4.	Binding energy values of samples derived from XPS analysis for O 1s spectrum.	182

Table B.5.	Binding energy values of samples derived from XPS analysis for Si 2p spectrum.	182
Table B.6.	Binding energy values of samples derived from XPS analysis for Mg 1s and Mg 2p spectrum.	182
Table B.7.	Atomic % of Si, O, Mg, Ca, Al and Na obtained from fitted peak information of these elements' XP spectra.....	183
Table B.8.	The effect of temperature and adsorbent amount on the apparent pseudo-second-order adsorption kinetic rate constant and adsorption parameters for calcined Sep, and Sep-AAM (<i>Contact time</i> = 3.5 h, $C_0 = 20 \text{ mg L}^{-1}$).	184
Table B.9.	Uptake performance and removal efficiency (%) for adsorption of MB onto as-received Sep at different temperatures (<i>Contact time</i> = 3.5 h, $C_0 = 20 \text{ mg L}^{-1}$, and $m = 10 \text{ mg}$).	185
Table B.10.	Pseudo-first and pseudo-second-order kinetic model parameters and removal efficiency (%) for adsorption of MB onto calcined Sep at different temperatures (<i>Contact time</i> = 3.5 h, $C_0 = 20 \text{ mg L}^{-1}$ and $m = 10 \text{ mg}$).	186
Table B.11.	Actual second-order adsorption rate constants ($k_{2,ads}$) of calcined Sep at different temperatures.	187
Table B.12.	Parameters of intraparticle diffusion model for Sep-AAM at different temperatures.	189
Table B.13.	Concentration (ppm) of leached elements from adsorbent to MB solution measured by ICP-MS.	189

Table B.14.	Langmuir and Freundlich isotherm constants for MB adsorption on calcined Sep at different temperatures.	192
Table B.15.	Langmuir separation factor R_L for calcined Sep and Sep-AAM at different temperatures, at all the initial MB concentrations used.	193
Table B.16.	Thermodynamic parameters for adsorption of MB onto calcined Sep for 31, 40, and 50 °C.	194
Table C.1.	Chemical compositions (wt%) of 1 h 750 °C calcined Sep and MK used in this study, as determined by XRF spectroscopy.	196
Table C.2.	The amounts of raw materials (in g) used in the synthesis of Sep-AAMs with distinct H ₂ O ₂ contents, corresponding molar Si/Mg and Na/Mg, and synthesis conditions.	196
Table C.3.	The amounts of raw materials (in g) used in the synthesis of MKGPs with distinct H ₂ O ₂ contents, corresponding molar Si/Al and Na/Al ratios, and synthesis conditions.	197
Table C.4.	BET surface area, average pore size, and pore volume of raw materials.	197
Table C.5.	Compressive strength values of the synthesized samples.	200
Table C.6.	The effect of initial MB concentration on uptake and removal efficiency.	202
Table C.7.	Pseudo-first and pseudo-second-order kinetic model parameters and removal efficiency (%) for adsorption of MB onto synthesized AAMs for different initial MB concentrations (<i>Contact time</i> = 24 h).	205

Table C.8.	Parameters of intraparticle diffusion model for the synthesized AAMs (<i>Contact time</i> = 24h, $C_0 = 70 \text{ mg L}^{-1}$).	209
Table C.9.	Langmuir separation factor R_L for synthesized AAMs at different temperatures, at all the initial MB concentrations used.	211
Table D.1.	Chemical compositions (wt%) of MK, raw RM, and calcined RM used in this study.	216
Table D.2.	The amounts of raw materials (in g) used in geopolymer synthesis, corresponding molar Si/Al and Al/Na ratios, and synthesis conditions used in RMGP synthesis in this study.	216
Table D.3.	BET surface area, average pore size, and pore volume of RMGP and calcined RMGP.	216
Table D.4.	Atomic % of C, N, O, Si, Al, Na, and Fe in samples which are calculated from EDS spectra.	218
Table D.5.	Atomic % of different elements obtained from fitted peak information of C 1s, O 1s, N 1s, Si 2p, Al 2p, Fe 2p, and Na 1s XP spectra.	219
Table D.6.	Pseudo-first and pseudo-second-order kinetic model parameters and removal efficiency (%) for adsorption of MB onto RMGP and calcined RMGP (<i>Contact time</i> = 3 h, $C_0 = 20 \text{ mg L}^{-1}$ and $m = 10 \text{ mg}$).	221
Table D.7.	The influence of adsorbent amount on the apparent pseudo-second-order adsorption kinetic rate constant and adsorption parameters for g-C ₃ N ₄ and g-C ₃ N ₄ /RMGP (<i>Contact time</i> = 3 h, $C_0 = 20 \text{ mg L}^{-1}$).	222
Table D.8.	Parameters of intraparticle diffusion model for g-C ₃ N ₄ and g-C ₃ N ₄ /RMGP.	224

Table D.9.	Langmuir separation factor R_L for g-C ₃ N ₄ and g-C ₃ N ₄ /RMGP for all the initial MB concentrations used.	227
------------	---	-----

LIST OF SYMBOLS

A	Arrhenius pre-exponential factor
at	Atomic
C	Concentration
E_a	Activation energy
h	Hour
K_F	Freundlich constant
K_L	Langmuir constant
$k_{1,ads,app}$	Apparent rate constant of pseudo-first-order kinetics
$k_{2,ads,app}$	Apparent rate constant of pseudo-second-order kinetics
k_{ads}	Actual adsorption rate constant
k_p	Rate constant of intraparticle diffusion model
m	Order of the reaction with respect to adsorbent amount
min	Minute
n	Order of the reaction with respect to dye concentration
q	Uptake
R_L	Langmuir separation factor
T	Temperature
t	Time
V	Volume
wt	Weight

LIST OF ACRONYMS/ABBREVIATIONS

AAM	Alkali activated material
Al	Aluminum
Al ₂ O ₃	Aluminum oxide
ATR	Attenuated total reflectance
BET	Brunauer–Emmett–Teller
BJH	Barrett–Joyner–Halenda
CO ₂	Carbondioxide
FA	Fly ash
FTIR	Fourier transform infrared spectroscopy
GC/MS	Gas chromatography–mass spectrometry
GP	Geopolymer
g-C ₃ N ₄	Graphitic carbon nitride
g-C ₃ N ₄ /RMGP	Graphitic carbon nitride incorporated red mud and metakaolin-based GP
H ₂ O ₂	Hydrogen peroxide
ICP-MS	Inductively coupled plasma mass spectroscopy
LC/MS	Liquid chromatography–mass spectrometry
MB	Methylene blue
MK	Metakaolin
MKGP	Metakaolin-based geopolymer
MIP	Mercury intrusion porosimetry
NaOH	Sodium hydroxide
Na ₂ Si ₃ O ₇	Sodium silicate
EDS	Energy dispersive X-Ray spectroscopy
FE-SEM	Field emission scanning electron microscopy
OPC	Ordinary Portland cement
RM	Red Mud
RMGP	Red Mud and metakaolin-based geopolymer
Sep	Sep
Sep-AAM	Sep-based alkali activated material

Si	Silicon
SiO ₂	Silicon dioxide
TGA	Thermogravimetric analysis
TOC	Total organic compound
TiO ₂	Titanium dioxide
UV-DRS	UV/visible diffuse reflectance spectroscopy
UV	Ultraviolet
UV-Vis	Ultraviolet-Visible spectroscopy
XRD	X-ray powder diffraction
XRF	X-ray fluorescence
XPS	X-ray photoelectron spectroscopy

1. INTRODUCTION

Concrete, being the mostly used construction material in the world, consists of sand, coarse aggregates, and a binding phase which helps holding these ingredients together. In general water and ordinary Portland cement (OPC) in powder form is utilized to bind all of these phases. Even though OPC technology is still one of the biggest industries in the world with a yearly cement production of 4,600 million tons, environmental options of this technology is a developing research area. Greenhouse gas emissions resulting from Portland cement production can be decreased by using environmental alternatives of these materials [1].

Alkali activated materials (AAMs) are sustainable versions of current cement binders. Even though there have been many controversial statements about their definition, these materials, which are also known as ‘geopolymers’ or ‘inorganic polymers’, can be produced as a result of a reaction between aluminosilicate sources and an alkaline solution. In fact AAM is the most general classification that covers all of the binding systems that are obtained as a result of a reaction between an alkaline salt and solid silicate powder [2]. The solid silicate powder can both be a calcium silicate source or a aluminosilicate source. Alkaline salts used for the synthesis can be solid or dissolved, and most commonly preferred alkaline salts can be listed as alkali hydroxides, carbonates, silicates or oxides. These salts should increase the pH of the reaction medium and dissolve the solid raw material. Inorganic polymers, on the other hand are a subcategory of AAMs and primary binding phase in inorganic polymers is a disordered silicate network. From this respect, comparably higher amounts of total SiO_2 and Al_2O_3 are needed than it is needed for ordinary portland cements. Geopolymers are a subcategory of inorganic polymers and the binding phase for geopolymers composes almost entirely of aluminosilicates. Calcium content in the raw material should therefore be low for the formation of a pseudo-zeolitic structure rather than unique chains of calcium silicate hydrates [2]. Raw materials preferred for the synthesis, which are also known as ‘aluminosilicate precursors’ may be chosen by taking different aspects into consideration such as availability, cost, and reactivity [3].

1.1. Geopolymerization

Geopolymerization reaction consists of several steps. Firstly, solid aluminosilicate sources are dissolved in an alkaline medium to produce aluminate and silicate species. Secondly, an equilibrium between different species of silicate, aluminate, and aluminosilicates is established. Then, as a result of the presence of a basic medium, a saturated aluminosilicate solution occurs and this supersaturated aluminosilicate solution causes a gel formation due to the condensation of oligomers in the medium. Lastly, as a result of a continuous rearrangements and reorganizations and with the formation of a gel network, a three dimensional aluminosilicate network, so called ‘geopolymers’ occur [4]. In summary, dissolution of aluminosilicates, polycondensation, and structural reorganization can be considered as main steps of geopolymerization and the schematic diagram is provided in Figure 1.1 [5, 6].

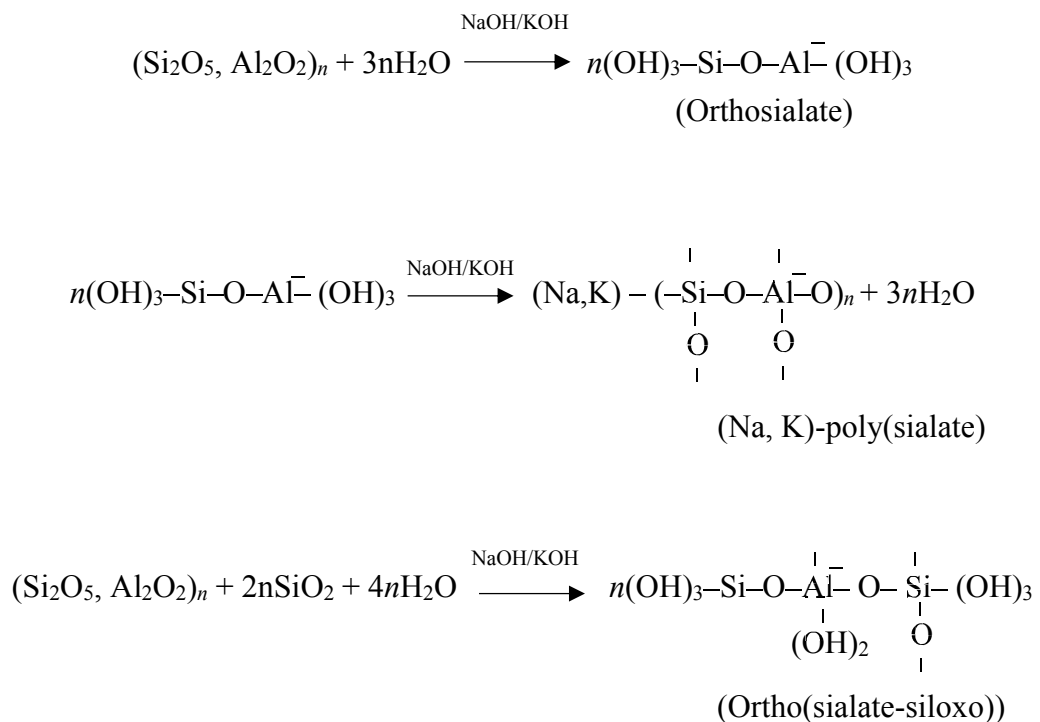


Figure 1.1. Schematic diagram of geopolymerization reactions [5, 6].

1.2. Raw Materials Used in Geopolymerization

1.2.1. Metakaolin

Kaolin is a white colored, soft clay and includes mainly kaolinite ($\text{Al}_2\text{Si}_2\text{O}_5(\text{OH})_4$) mineral as a crystalline structure. Kaolinite is a 2D mineral and has a 1:1 type of layered structure consisting of an octahedral AlO_6 layer and tetrahedral SiO_2 layer [7]. It is abundant in nature and used as a raw material in industry, especially in paper, ceramics, plastics, pharmaceutical and catalyst industries [8, 9]. Its low cost, abundance, high adsorption performance, and high ion exchange capacity makes it a good candidate specifically for adsorption research field [9]. Chemical and physical properties of this mineral can be modified by different surface modification techniques including mechanochemical activation, thermal treatment, or acid activation [9].

Acid activation is known to be an effective procedure and studies in the literature showed that methylene blue (MB) dye adsorption capability of kaolinite can be increased by acid treatment [8, 10, 11]. For instance, acid activation via concentrated sulphuric acid of kaolinite together with thermal treatment was found to be an effective method to increase the surface area of kaolinite. This method led to an enhancement in the MB uptake capacity of kaolinite due to an increase in the porosity and surface area values. Approximately 20-fold increase in surface area and 6-fold increase in pore volume was detected, which as a result caused 1.3-fold increase in the uptake capacity of this material towards MB adsorption [8].

Calcined-hydrothermal approach was used to modify kaolinite mineral and obtain kaolin nanospheres [12]. Resulting material in this study displayed superior surface area to that of raw kaolin (157 mg g^{-1} to 29.3 mg g^{-1}) and uptake capacity had increased from 49.8 to 184.9 mg g^{-1} [12].

Aside from acid activation and thermal treatment procedures, one of the techniques widely used for increasing the adsorption capacity of kaolinite is to modificate the surface of this mineral with metal oxide nanoparticles [13, 14]. A research study of Meigoli et al. had shown that a nanocomposite of kaolin/ CuFe_2O_4 exhibits remarkable adsorption capacity

for MB and methyl violet dyes, which was mainly related with the high surface area of the kaolin/CuFe₂O₄ nanocomposite produced by a chemical co-precipitation method [14]. Graphene oxide was also utilized for improving the adsorption performance of kaolin [15]. Study of He et al. had investigated the effect of graphene oxide content on the adsorption performance of graphene oxide modified kaolin composites. Outcomes of this study had demonstrated that composites including 10 wt% graphene oxide shows superior adsorption capacity towards MB dye due to its higher surface area [15].

One of the application areas of kaolin mineral is in geopolymerization. Thermal treatment of raw materials before geopolymerization process is a common and effective process which helps increasing the solubility of these materials in an alkaline medium. A series of phase transformations take place when kaolinite group clay is thermally treated under an atmospheric pressure. Dehydration of kaolinite group starts to occur at about 550-600 °C and this endothermic dehydroxylation gives rise to the formation of disordered metakaolin (MK) (Al₂Si₂O₇) [16]. MK-based geopolymer spheres by using three different techniques were produced by Medri et al, and these sphere's mechanical performance and MB adsorption capacity was investigated. Injection and solidification in polyethylene glycol, liquid nitrogen, and ionotropic gelation were applied to synthesize these materials and results pointed out that different methods resulted geopolymer spheres with different porosity levels; liquid nitrogen technique displaying the sample with the highest porosity (64%). Compressive strength measurements showed that mechanical performance and porosity of MK-based geopolymer spheres produced by different techniques were inversely proportional and porosity level had a positive effect on the adsorption capacity of a geopolymer [17]. The sample with the highest porosity level of 64% displayed a 2.1 MPa compressive strength and 5.4 mg g⁻¹ of MB uptake capacity [17]. Studies in the literature demonstrate that when MK-based geopolymers are used for MB dye adsorption [17, 18], experimental data better suit to pseudo-second-order adsorption kinetics, showing that the adsorption involves anion exchange process [17].

To be able to benefit from adsorptive properties of geopolymers, it would be better to use these materials in solid form rather than in powder form. Even though geopolymers can be casted into different shaped moulds and show promising mechanical performance, their adsorption properties when they are in solid form is limited. To increase their porosity and

therefore to cause an enhancement in their adsorption performance, several pore forming agents were considered in the existing literature. Most commonly used pore forming agents can be summarized as hydrogen peroxide (H₂O₂) [19, 20], expanded glass aggregates [21], sodium dodecyl sulphate [22], and aluminum oxide [23]. Rozek et al. had shown that 1 wt% expanded glass addition to MK-based geopolymer samples increases the MB uptake capacity of the sample from 3.5 to 4.9 mg g⁻¹ with a concomitant decrease in mechanical performance from 20.4 MPa to 1.6 MPa [21].

1.2.2. Red Mud

Red mud (RM) is a waste product of alumina production. The type of bauxite ore that is used to extract alumina has an effect on the RM properties. This material has a red colour owing to its high iron oxide content. It has been reported that about 1-1.8 tons of RM are discharged for every ton of alumina produced [24]. RM production data of some countries reported by Wang et al. show that China, Australia, Brazil, and India are the leading countries in RM production. It was shown that 105,169 million tons of RM is produced only in China in 2018 [24].

Even though chemical components present in different RM sources are the same, their content may vary. The constituents of RM are iron oxide, aluminum oxide, silicon oxide, calcium oxide and sodium oxide [25]. Some most common mineral phases existing in RM are hematite, calcite, and sodium aluminate. The morphological analysis of this material had shown that it has a porous structure and pore characteristics may differ [24].

Because of its highly alkaline nature, its storage is of great concern and two storage methods; wet storage and dry storage, are widely used for storing RM. Wet storage method consists of discharging RM into a pool and the water in RM is removed during the course of this method. One possible concern regarding this method is related with RM being highly basic and the effluents from RM may penetrate to the groundwater and may pose a serious risk to the environment. Dry storage method is currently the widely used method for storing RM. Water present in RM waste is removed by mechanical pressure filtration method and the rest of the RM is dried under air. One problem accompanied by using this method is the mixing of fine RM particles into the air as a result of wind blowing. Both of these storage

methods have negative effects on the environment and also require huge land areas for the storage [26]. Even though it is estimated that more than 130 million tonnes of alumina were produced annually by 2018 [27], total utilization rate of RM is only about 4-5 wt% [24], [28]. This huge gap between production and evaluation rate implies the importance and necessity of utilizing RM in different fields.

One of the mostly studied application areas of RM is in adsorption research field. Several distinct studies had shown that RM and RM-based materials can be evaluated in wastewater remediation applications. Wang et al. showed that heat treatment and HNO_3 treatment applied on RM decreases the adsorption capacity of RM upon MB dye and the adsorption process between RM and MB dye is an endothermic process [29]. Another study conducted by Zhang et al. revealed that HCl-treated sintering process RM displays superior adsorption properties than sintering process RM itself, that was correlated with the increased surface area of acid activated sample [30]. A similar finding was reported by Çoruh et al. where HCl-activated RM was found to display higher adsorption capacity upon MB dye than as received RM and heat treated RM. Enhanced adsorption properties of acid activated RM in this study was associated with the dissolution of sodalite phase present in RM, as a result of acid activation. As sodalite dissolves, there occurs an increase in the number of pores and specific surface area of the material increases [31]. Two different studies had shown that RM activated by a hydrochloric acid digestion that is followed by an ammonium hydroxide precipitation method increases surface area results an increase in MB uptake performance [32, 33]. Calcination of RM was shown to cause a decrease in adsorption capacity of MB dye due to the decrease in total surface area of RM because of reduction in particle size and decomposition of goethite and gibbsite phases [34]. These different studies using RM and modified RM samples as adsorbents for MB dye adsorption had proven that the adsorption of MB onto RM samples are due to chemisorption and experimental data follow pseudo-second-order adsorption kinetics and Langmuir model better described the data [30, 32, 34].

Another application area of RM is in photocatalysis. Melamine-based graphitic carbon nitride integrated RM composite that was synthesized by one-step thermal polymerization method was found to show an ability to remove organic pollutants and antibiotics from wastewater through synergistic effect of adsorption and photocatalysis under visible-light conditions [35]. Cobalt-doped neutralized RM samples were prepared via impregnation

method and their visible light photocatalytic activity upon MB dye was investigated under natural solar light. Results showed that cobalt doping enhances the photocatalytic activity of RM due to accelerated photo induced electron-hole transfer and separation, and decreased recombination rate [36].

Aside from adsorption and photocatalysis, another option for evaluating this waste material is in construction industry. RM together with fly ash were used in geopolymerization for the development of paving blocks. It was revealed that RM addition causes an enhancement in the the degree of geopolymerization reaction and structural reorganization. Material composed of 10-20 wt% RM were found to be environmentally reliable with the leaching amount of toxic metals being within the permissible limit [37]. RM and MK-based geopolymers's structural characteristics and mechanical performance was examined by systematically increasing the RM content in the solid raw materials basis. Results pointed out that RM addition limits the dissolution of raw materials and decrease the mechanical performance of the geopolymers [38]. As mentioned previously, surface characteristics of RM can be tuned by applying different modification techniques. From this point forth, RM was structurally modified by applying an acid digestion procedure that is followed by calcination, and the effect of acid molarity and digestion temperature on geopolymerization degree and thermal stability was investigated [39]. Results of this study proved that acid modification significantly changes the surface characteristics of RM and improves the thermal stability of geopolymers synthesized form acid activated RMs, and calcination plays an important role in geopolymerization rate [39].

1.2.3. Fly Ash

Fly ash (FA) is an industrial waste that is released from the flue gas of coal fire power plants [40] and is mainly a by-product of thermal power plants. Unavoidable increase in the production of this waste material makes its evaluation crucial. It was reported that the total accumulation of FA in China had reached to 6.86×10^{11} kg [40], and for Brazil total annual production amount of FA is estimated to be about 4 million tonnes; with only 30% of this waste being recycled for construction-related applications [41]. Studies from Turkey had shown that approximately 150 million tonnes of FA were produced in Turkey between 1970 and 2013 [42], and only 1% of this produced FA was evaluated in cement and brick industry

[43]. It is generally stored in landfills, however its disposal still is of great concern due to economical and environmental aspects [44, 45]. The recycling of this waste material should be put in the process carefully as it involves high amount of trace elements and radionuclides that may cause serious effects on human health and also to the environment [44].

This waste product, FA, is used as a supplementary material of cement in concrete production, road construction and asphalt [44, 46]. One of the application areas of this waste material is also in adsorption [47]. FA-based materials can be utilized for adsorbing different organic and non-organic chemicals [48]. Current literature on MB adsorption capacity of FA is very rich and FA and its modified forms were found to display a MB uptake capacity of 0.3 and 96 mg g⁻¹. Adsorption performance of these materials depend on different factors such as modification, initial adsorbate concentration, pH of the solution, and adsorbent amount [29, 40, 41, 45, 47, 49-53, 54-61]. Tuning adsorption capacity by changing some parameters or applying modifications on FA material are good advantages and provides flexibility, however FA also has some drawbacks such as limited adsorption capacity towards some dyes and using high amounts of FA for dye adsorption may also result a sludge disposal problem [48]. From this point forth utilizing this waste material in geopolymerization is a good alternative that may increase the adsorption capacity and regeneration ability of this material.

Studies in the literature showed that FA together with different clay minerals such as granulated blast furnace slag, bottom ash [62] and MK [22] can also be used as a raw material for geopolymer synthesis [6, 63-65]. In these studies, produced geopolymers were evaluated as MB adsorbents. In a study of Padmapriya et al. for instance, coal FA, bottom ash and granulated blast furnace slag were used as geopolymer raw materials. Results of this study had shown that adsorption capacity of the geopolymer synthesized here shows an adsorption capacity of 59.52 mg g⁻¹ at an optimum dosage of 0.08 g L⁻¹. It was asserted in this study that, proposed geopolymer formulation causes an enhancement in the pore properties and surface area of the final geopolymer compared to the existing geopolymer literature, and superior adsorption properties were mainly correlated with this enhancement [62].

1.2.4. Sepiolite

Sepiolite (Sep) is a fibrous clay mineral that is composed of magnesium hydrosilicates and has a formula of $\text{Si}_{12}\text{Mg}_8\text{O}_{30}(\text{OH})_4(\text{H}_2\text{O})_4 \cdot 8\text{H}_2\text{O}$ [16]. It has negatively charged 2:1 layers consisting of blocks and channels, and each block involves tetrahedral silica sheets and magnesium octahedral sheets [66]. High surface area and unique fibrous structure of Sep with interior channels provide a suitable environment for the penetration of inorganic and organic ions into its structure [67]. The adsorption capacity of Sep and its modified forms was studied by many researchers [68-70].

Largo et al. for instance demonstrated that Sep clay can effectively adsorb MB dye molecules and the adsorption performance increases at basic conditions showing that electrostatic interactions take place during the adsorption process. Experiments showed that nearly 99% of the MB dye is removed from the solution when pH of the solution medium is 12, whereas only 60% of MB dye is removed when pH of the solution is 4, under identical experimental conditions. It was also shown that several factors including pH of the medium, temperature, adsorbent amount, and initial dye amount have an influence on the adsorption performance of Sep [68].

To improve the adsorption performance of Sep, many strategies were offered including sonication [67], thermal treatment [71], incorporation of an organic material [72-75], acid treatment [66, 71, 76], and alkaline treatment [76]. These modifications generate alterations at the surface of the Sep; generally cause an increase in the surface area [67, 75], and therefore increase the adsorption capacity of these materials.

Treating these materials with alkaline solutions can be taken one step further by using Sep as the main raw material for AAM synthesis. It has been reported previously that magnesium analogues of geopolymers can be synthesized by using Sep as a raw material [77]. In this respect, alkali activating of Sep offers a good potential to increase adsorption capacity of as-received Sep and newly synthesized material can also be evaluated as a construction material with a good mechanical strength. This potential of Sep mineral is discussed in detail in Chapter 3 of this thesis.

1.3. Application Areas of Geopolymers

Geopolymers (GP) have different application areas in construction industry [78] such as in paving blocks [37] and concrete products [79], or in waste management applications for immobilizing hazardous or radioactive wastes [42, 79]. One of the emerging application areas of geopolymers are also in adsorption and photocatalysis.

Adsorption studies in the literature have shown that geopolymers from different raw materials can successfully be utilized for the adsorption of dyes [6, 21, 80]. Geopolymers produced from different raw materials are highly alkaline in nature and increase the pH of the solution when they are immersed into aqueous solutions. As a result of mechanism of geopolymer formation (Figure 1.1.), these materials include negatively charged surface hydroxyl groups and this situation makes them good candidates as adsorbents especially for cationic dyes [6].

In a study of Novais et al. for instance, FA and MK-based GP spheres were synthesized and their adsorption performance upon MB dye were investigated. Several parameters including adsorption time, MB initial concentration, and the amount of the adsorbent effects on adsorption performance were studied in detail. Findings had shown that initial dye concentration have a huge effect on the adsorption capacity of geopolymers and uptake value was increased from 1.1 to 30.1 mg g⁻¹ when initial MB concentration was increased from 10 to 250 ppm [22].

Another parameter that has an important effect on the adsorption capacity of geopolymers is the pH of the solution medium. As stated previously, negatively charged surface of geopolymers provides a suitable medium for the adsorption of cationic molecules. In this respect, the adsorption performance of geopolymers can be enhanced by adjusting the pH of the solution medium. The effect of solution pH on the MB dye adsorption performance was investigated for volcanic ash-based geopolymers by Tome et al [81]. Experiments in this study showed that adsorption of MB is improved at higher pH values and low pH of the solution negatively effects the adsorption performance due to competition between the cationic MB molecules and hydrogen ions for the same binding sites [81]. The MB uptake

capacity of volcanic ash-based geopolymer in this study increased from 6 to 22.5 mg g⁻¹ when the pH value of the solution was increased from 2 to 12 [81].

In addition to applications related to construction industry and adsorption, another emerging application area of geopolymers is utilizing them for photocatalytic applications. Self-cleaning ability of a geopolymer may become important when it is used for construction purposes and geopolymers can be designed to display photocatalytic properties. This ability is introduced by including a photocatalyst within the geopolymer structure. The photocatalytic effect of geopolymers can be used to remove these organic pollutants from the geopolymer surface. FA-based geopolymers were used as a photocatalyst in the literature for the removal of MB dye from a wastewater under UV light [82]. Steel slag based Ni,Ca-geopolymer had also been used for photodegradation of MB from wastewater [83].

Titanium dioxide (TiO₂) is one of the semiconductors which has been studied due to its superior properties such as high physical and chemical stability, low cost, easy availability, low toxicity, great photoactivity [84] and superhydrophilicity [85]. One of the ways to incorporate TiO₂ into the geopolymer is an ion exchange procedure in which geopolymers are immersed into an aqueous solution to form a geopolymer with a reactive surface that has TiO₂ in its structure. This procedure was carried out by Gasca-Tirado et al. and a degradation of a volatile organic compound 2-Butanone was recorded by using a gas chromatography [86]. In a different study, Mn⁺² doped, CuO loaded graphene bottom ash based geopolymeric composite was produced by a four step method involving an ion exchange procedure. Zhang et al. cured graphene bottom ash-based geopolymeric composite by aqueous solution of ammonium acetate to substitute NH₄⁺ ions for Na⁺ ions and then impregnated the GP sample in an aqueous solution of Cu(NO₃)₂.H₂O and manganese nitrate. Coupling graphene with semiconductor is known to be an effective method that enhances the separation efficiency of photogenerated electron-hole pairs that causes an increase in photocatalytic activity [87]. In the study of Zhang et al., Mn²⁺ doping amount was kept nearly constant for all of the samples, however CuO loading was increased up to a value of 20 wt%. Photocatalytic reduction to produce hydrogen under visible light by solar water splitting increased with the increasing amounts of Mn⁺² doping and CuO loading. The degradation efficiency of composites with different contents was measured under UV light by following the direct sky blue 5B dye absorption values with UV-Vis spectrophotometer at 365 nm. It was observed that sample with 15 wt% CuO loading displayed the highest

degradation efficiency of 100% and the degradation reaction fitted the first order kinetics [88].

Geopolymers can also be coated with thin films of photocatalytic materials. Coating TiO₂ films onto different supports by sol-gel method is known to be an efficient process to enhance photocatalytic activity and wear resistance of the TiO₂ film [89, 90]. In a study of Chen et al., geopolymer supported photocatalytic TiO₂ films were produced via sol-gel dip coating process. MK and FA-based geopolymers were produced and sliced geopolymer samples were dip-coated with a solution of butyl titanate, diethanolamine and ethyl alcohol. Dip-coated slices were then annealed at different temperatures to induce the crystallization of TiO₂. TiO₂ film which was thermally treated at 600 °C was found to consist mainly of anatase phase and revealed the highest degradation efficiency (~80%) of MB under UV light [89].

Within the scope of this thesis, geopolymers were synthesized from different raw materials including MK, RM, and Sep; the adsorption and photocatalytic performance of these materials in terms of MB removal were explored in detail. By extracting knowledge from various characterization tools, a relationship between structure and adsorption and/or photocatalytic performance was established.

1.4. Methodology

For measuring the MB removal performance of synthesized materials, firstly a MB solution with a known concentration was prepared. Then, a measured amount of adsorbent was immersed into this solution. Agitation speed was kept constant during the experiments and reported. These experiments were conducted under atmospheric pressure, whereas pH and temperature of the solution medium were also reported if they were varied within experiments. Samples were syringed from solutions at regular time intervals and their concentration was measured by using a UV-Vis spectrometer.

To extract information about synthesized material's adsorption and photocatalytic performance, data collected during experiments were studied by considering adsorption and reaction kinetics.

1.4.1. Evaluation of Adsorption Performance

The removal efficiency (%) can be calculated as

$$\text{Removal efficiency (\%)} = \left(\frac{C_o - C_t}{C_o} \right) \times 100 = \left(\frac{A_o - A_t}{A_o} \right) \times 100 \quad (1.1)$$

where C_o and C_t are the concentration of MB solution at initial time $t = 0$ and at time t , respectively. A_o and A_t denotes to absorbance values at initial time $t = 0$ and at time t , respectively [91].

The amount of MB adsorbed on adsorbents can be determined as,

$$q_e = \left(\frac{C_o - C_e}{m} \right) \times V \quad (1.2)$$

where q_e is the amount of MB dye uptake by the adsorbent (mg MB dye/g adsorbent), m is the mass of the adsorbent (g) and V is the volume of the MB solution (L).

Pseudo-first-order and pseudo-second-order adsorption kinetic models can be used to reveal the MB adsorption mechanism of materials as

$$\ln(q_e - q_t) = \ln q_e - k_{1,ads,app} \times t, \quad (1.3)$$

$$\frac{t}{q_t} = \frac{1}{k_{2,ads,app} \times q_e^2} + \frac{t}{q_e} \quad (1.4)$$

where q_e (mg g⁻¹) and q_t (mg g⁻¹) represent the amounts of dye adsorbed on adsorbents at equilibrium and time t , respectively; $k_{1,ads,app}$ (min⁻¹) and $k_{2,ads,app}$ (g mg⁻¹ min⁻¹) are the apparent rate constants of pseudo-first- and pseudo-second-order adsorption kinetics, respectively.

The dependence of adsorption rate on both the adsorbent amount and adsorbed amount of MB dye can be determined as

$$\frac{dq_t}{dt} = k_{ads} \times (\text{adsorbent amount})^m \times (q_e - q_t)^n \quad (1.5)$$

where m is the order of the reaction with respect to adsorbent amount, n is the order of the reaction with respect to dye concentration, k_{ads} is the actual adsorption rate constant. If adsorbent amount is assumed to be constant, the adsorption rate can be expressed in terms of apparent adsorption rate constant, $k_{ads,app}$ as

$$\frac{dq_t}{dt} = k_{ads,app} \times (q_e - q_t)^n, \quad (1.6)$$

$$k_{ads,app} = k_{ads} \times (\text{adsorbent amount})^m. \quad (1.7)$$

Equation (1.7) can also be utilized to determine the order of the adsorption rate with respect to adsorbent amount by taking the natural logarithm of both sides as

$$\ln k_{ads,app} = \ln k_{ads} + m \times \ln(\text{adsorbent amount}). \quad (1.8)$$

The Arrhenius equation was used to determine the activation energy of adsorption which shows the minimum required energy for adsorption to take place. It is shown as

$$\ln k_{ads} = \ln A - \frac{E_a}{R} \times \frac{1}{T} \quad (1.9)$$

where, k_{ads} is the actual adsorption rate constant, E_a is the activation energy (J/mol), R is the gas constant and is equal to 8.314 J/(mol.K) and A is the Arrhenius pre-exponential factor.

Intraparticle diffusion model can also be applied to experimental data in order to identify the diffusion mechanism as

$$q_t = k_p \times t^{\frac{1}{2}} + C \quad (1.10)$$

where q_t (mg g^{-1}) represents the amount of dye adsorbed on adsorbents at time t , k_p ($\text{mg g}^{-1} \text{min}^{-0.5}$) is the rate constant of intraparticle diffusion model and C (mg g^{-1}) is the intercept that gives information about the boundary layer thickness.

1.4.1.1. Adsorption Isotherms

Two most common isotherm models, Langmuir and Freundlich models, were used to fit the equilibrium data of the samples. The Langmuir model assumes that the interaction between sorbed molecules are negligible and that the surface has homogeneous binding sites and equal sorption energies [19] and suitable for describing the chemisorption process [92]. The linearized form of Langmuir model is given as

$$\frac{C_e}{q_e} = \frac{1}{K_L \times q_{max}} + \frac{C_e}{q_{max}} \quad (1.11)$$

where K_L (L mg^{-1}) indicates the Langmuir constant that shows the affinity of the sorbate for binding sites, q_{max} (mg g^{-1}) is the maximum adsorption capacity [19] and q_e (mg g^{-1}) is the equilibrium monolayer adsorption capacity. K_L can be used to calculate a separation factor R_L and Langmuir isotherm can then be expressed by this factor as

$$R_L = \frac{1}{1 + K_L \times C_0} \quad (1.12)$$

If $0 \leq R_L \leq 1$ there is favorable adsorption [19, 93]. The Freundlich model assumes a multilayer adsorption on a heterogeneous surface that has sites which show different affinity. The binding strength exponentially decays and stronger binding sites are occupied first [19, 92]. The linearized form of Freundlich model, on the other hand, can be described as

$$\ln q_e = \ln K_F + \frac{1}{n} \times \ln C_e \quad (1.13)$$

where K_F (mg g^{-1}) is the Freundlich constant and is associated with adsorption capacity, n (g L^{-1}) being a parameter describing adsorption intensity and shows the absence of linearity of the adsorbed quantity in function C_e . When $1 \leq n \leq 10$, there is a favorable adsorption. When the value of n is greater than 10, there is a stronger interaction between surface of the adsorbent and adsorbate. When n equals to 1, a linear adsorption takes place [19, 80] which shows the identical adsorption energies for all sites [94].

1.4.2. Evaluation of Photocatalytic Activity

To understand the kinetics of MB dye degradation reaction under UV light, Equations (1.14)-(1.19) were used [95]. MB degradation rate as a function of catalyst and dye concentration can be used to detect the kinetic rate as

$$-r_{dye} = k \times C_{cat}^a \times C_{dye}^b \quad (1.14)$$

where, k is the degradation rate constant, C_{cat} is the catalyst concentration, a is the order of the reaction with respect to catalyst concentration, C_{dye} is the MB dye concentration and b is the order of the reaction with respect to MB dye concentration. If catalyst concentration is assumed to be constant, the rate of degradation reaction can be expressed in terms of apparent rate constant, k_{app} as

$$-r_{dye} = \frac{dC_{dye}}{dt} = k_{app} \times C_{dye}^b, \quad (1.15)$$

$$k_{app} = k \times C_{cat}^a. \quad (1.16)$$

Pseudo-first-order and pseudo-second-order kinetic models had previously been used to represent the degradation kinetics of organic dyes [88, 96]. Therefore, in the case where the degradation reaction is assumed to be first order with respect to MB dye concentration ($b = 1$), Equation (1.15) can be expressed as

$$\frac{\ln C_{dye_0}}{C_{dye}} = k_{app} \times t. \quad (1.17)$$

Similarly, for the case where degradation reaction is considered as second-order with respect to MB dye concentration ($b = 2$), Equation (1.15) becomes

$$\frac{1}{C_{dye}} = k_{app} \times t. \quad (1.18)$$

Furthermore, Equation (1.16) can also be used to find the order of the reaction with respect to catalyst amount by taking the natural logarithm of both sides to obtain

$$\ln k_{app} = \ln k + a \times \ln C_{cat}. \quad (1.19)$$

1.4.3. Structural Characterization of Materials

The structure of materials used in this thesis including raw materials, geopolymeric adsorbents and photocatalysts were characterized in detail by a variety of methods including X-ray fluorescence (XRF) spectroscopy, X-ray diffraction (XRD) spectroscopy, Fourier transform infrared (FTIR) spectroscopy, X-ray photoelectron spectroscopy (XPS), Scanning electron microscopy coupled with energy dispersive X-ray spectroscopy (SEM-EDS), Brunauer–Emmett–Teller (BET surface) area analysis, UV/visible diffuse reflectance spectroscopy (UV-DRS), and thermogravimetric analysis (TGA). XRF analysis was performed to determine the chemical composition of the raw materials. XRD was employed to determine the crystal constituents and amorphous character in the samples. FTIR spectroscopy was utilized to detect the vibrational spectra of the samples. XPS analysis was performed to understand the surface chemistry, composition, and binding state of the atoms. SEM-EDS measurements were conducted to have an understanding on the surface structure and morphology of the samples. BET analysis was employed to determine the surface area of the samples. UV-DRS was performed to investigate the band-gap values and maximum absorption wavelengths. TGA was conducted to determine the thermal stability of the materials. Zeta potential of the materials was also measured to determine the surface charge stability. Additionally, to determine the mechanical performance, compressive strength of the materials were evaluated by using servo-hydraulic test. The parameters and conditions regarding these characterization techniques slightly vary for each dataset in this thesis; therefore these are thoroughly presented in the relevant parts.

1.5. Scope and Aim of This Work

Geopolymers have a huge potential to be used in different research areas including construction, catalysis, photocatalysis, and adsorption. Wide range of raw material options and easy tunability of the processing conditions make them convenient materials for their evaluation in different fields of research. Intrinsic nature of these materials provides environmentally friendly options and increase their contribution as sustainable materials.

The objective of this thesis is to determine the MB adsorption and photocatalytic performance of geopolymeric materials synthesized by using different raw materials and techniques, and to establish an understanding of the structure and performance relationship. Within this framework, the results of this thesis point out that, these materials which were produced in a sustainable and environmentally friendly way, are promising and can successfully be used for environmentally friendly wastewater treatment applications

In Chapter 2 of this thesis, RM and MK-based geopolymers with varying anatase content were produced and their ability adsorption and photocatalytic degradation of MB. The effect of anatase content in the geopolymeric structure was studied in detail by considering both reaction and adsorption kinetics. Chapter 2 has been published in *Journal of Cleaner Production* in 2021 (K Kaya-Özkiper, A Uzun, S Soyer-Uzun, *Journal of Cleaner Production* (2021) 288, 125120) [25].

Findings of Chapter 2 demonstrated that geopolymers have a potential to be used in adsorption research area. Therefore, in Chapter 3, Sep mineral, which is a commonly mined clay mineral in Turkey, was evaluated as a new raw material for the synthesis of magnesium analogues of aluminosilicate geopolymers. The adsorption performance of these materials towards MB dye was studied in detail, kinetic and thermodynamic analysis were established. The findings presented in Chapter 3 has been published in *Journal of Hazardous Materials* in 2022 (K Kaya-Özkiper, A Uzun, S Soyer-Uzun, *Journal of Hazardous Materials* (2022) 424, 127256) [97].

In Chapter 4, monolith forms of the magnesium analogues of geopolymers introduced in Chapter 3 were enhanced to display varying porosities. These solid-formed monoliths

produced from Sep were used as an adsorbent for MB removal and the influence of porosity on the adsorption performance was studied in detail. MK-based counterparts of Sep-based monoliths were also studied and differences in adsorption performance was discussed by characterizing each sample with distinct characterization tools. The manuscript derived from Chapter 4 is being prepared for publication.

A new composite consisting of RM and MK-based geopolymer and graphitic carbon nitride was introduced in Chapter 5 to develop a composite with improved adsorption performance towards MB dye. The MB adsorption performance of this newly introduced composite was compared to that of pure graphitic carbon nitride. Main adsorption performance determining parameters were explored and discussed. The manuscript form of Chapter 5 is being prepared for publication.

2. RED MUD- AND METAKAOLIN-BASED GEOPOLYMERS FOR ADSORPTION AND PHOTOCATALYTIC DEGRADATION OF METHYLENE BLUE: TOWARDS SELF-CLEANING CONSTRUCTION MATERIALS

2.1. Introduction

A continuous increase in the demand for aluminum leads to the accumulation of tremendous amounts of red mud (RM) and the elimination of this hazardous industrial waste gains significant importance. Concerns about the storage problem of RM motivate researchers to evaluate its utilization in different fields; i.e., as concrete [98], geopolymers [38, 39], and catalysts [99, 100]. Utilization of RM in the cement-related applications is one of the paths in its remediation [101]. However, Pontikes et al. reported that only less than 5 wt% of RM has been evaluated in the cement related-applications [102]. In this direction, several studies demonstrated that RM used together with ordinary Portland cement (OPC) shows good mechanical strength; and thus, it can be used in applications regarding cement-based construction materials [26, 98, 103]. However, the generation of OPC is known to be responsible for 7-17% of the total anthropogenic CO₂ release in the world [104, 105]. Even though the study by Xi et al. demonstrated that a cumulative amount of 4.5 GtC has been sequestered in carbonating cement materials from 1930 to 2013, offsetting 43% of the CO₂ emissions from production of cement over the same period [106], the production of OPC can still be considered as one of the major sources of CO₂ emissions.

Possible evaluation of industrial wastes or ashes produced in huge amounts in geopolymerization is one of the several advantages of geopolymer production. One of the emerging application areas regarding geopolymers is utilizing them as “self-cleaning” construction materials. Studies in the literature showed that geopolymers synthesized from different raw materials can be evaluated as adsorbents and/or photocatalysts [80, 83, 107].

Most of these studies focus mainly on the photodegradation of representative dyes under UV-light. However, geopolymers are also known to offer high adsorption capabilities

thanks to their porous characteristics. Even though there are some studies evaluating them as adsorbents for the removal of organic dyes [22] and heavy metals [108], there are a very limited number of studies demonstrating both adsorption and photo-degradation performance of these materials on the removal of a representative dye from wastewater [82], [109]. Besides, it is envisioned that utilization of RM, an environmental hazardous material, in the synthesis of geopolymers with self-cleaning ability not only offers opportunities for “cleaner production” but also presents a broad potential for sustainability.

In this part of this thesis, it is focused on investigating these opportunities and RM and MK were used as raw materials for the synthesis of geopolymers (RMGPs). RM is utilized for photocatalytic purposes because of its very high amount of Fe_2O_3 (~37 wt%) and TiO_2 (~6 wt%) content, which are known as photocatalytically active. The effect of both adsorption and photodegradation of MB were investigated by conducting experiments both under dark conditions that is subsequently followed by a UV-light exposure, and solely directly under UV-light exposure. Additionally, incorporation of photocatalytically active anatase, into the RMGP system demonstrated that the self-cleaning performance of RMGPs can be improved to an exceptionally high level. This chapter was published as a paper [25] and the original manuscript has been rearranged to conform to the format requirements of the dissertation.

2.2. Experimental Methods

2.2.1. Materials

Raw materials used as the aluminosilicate sources were MK (2.50 g/cm^3) and RM (2.70 g/cm^3). MK was obtained by the calcination of kaolinite mineral at $700 \text{ }^\circ\text{C}$ for 1 h [110]. RM was kindly supplied by Eti Seydişehir Aluminum Factory, Konya-Turkey. Before utilizing RM in geopolymer synthesis, RM was first kept at $100 \text{ }^\circ\text{C}$ in air to remove water molecules and then calcined at $800 \text{ }^\circ\text{C}$ for three hours in air. Chemical compositions of raw materials are provided in Table A.1. Sodium silicate ($\text{Na}_2\text{Si}_3\text{O}_7$) solution (9 wt% of Na_2O , 28 wt% of SiO_2 , 63 wt% of H_2O , Merck, 1.35 g/cm^3) was used together with sodium hydroxide pellets (NaOH , Merck, 2.13 g/cm^3) as an alkali activator to synthesize RMGPs. Anatase (powder, 325 mesh, 3.90 g/cm^3) was purchased from Sigma Aldrich.

2.2.2. Synthesis of Geopolymers

The amounts of raw materials used in the synthesis of RMGPs, synthesis conditions used in this study together with the corresponding molar Si/Al and Na/Al ratios are shown in Table A.2. Mix proportions (in terms of mass per unitary volume) calculated based on densities of the raw materials and assuming that the volumes of the components are additive are provided in Table 2.1. It should be noted that, right after mixing, total volumes for all samples are measured to be approximately 17% less than the hypothetical total volumes calculated from raw material densities which is associated with the presence of nonidealities in the system and geopolymerization reactions. RM and MK are the aluminosilicate sources, while anatase was the main photocatalytic component in the system. Earlier results demonstrated that a mixture with 20 wt% RM and 80 wt% MK in raw material basis leads to good mechanical properties in the final geopolymer [38]. Therefore, in the present study this ratio was employed for all samples. Anatase amounts added into the solid raw material mixtures were arranged to be 0, 1, 3, 5, and 10 wt% of the RM and MK mixture prior to the addition of alkali activating solution. Based on the values given in Table 2.1 and Table A.2, anatase content in the geopolymer pastes studied here are 0, 0.4, 1.2, 1.9, and 3.74 wt%. Therefore, the samples were named as $x\%A$ -RMGP, where x corresponds to anatase loading in the geopolymer pastes. It should be noted here that these initial concentration values actually change with time as geopolymerization is a time-dependent process where water gradually leaves the system and concentrations change with solidification. Mixtures of NaOH and $\text{Na}_2\text{Si}_3\text{O}_7$ solution were used as alkali activators. Physical properties of geopolymers predominantly depend on molar Si/Al and Al/Na ratios as previously reported [4, 111]. Therefore, in the experimental design of this part, molar Si/Al and Na/Al ratios were set to be constant as 2 and 0.83, respectively (Table A.2). During the synthesis of geopolymers, powdered and sieved (#70 mesh sieve, 200 μm) raw materials; RM, MK, and anatase were mixed thoroughly with alkali activators. These samples were kept at room temperature for a few hours and then thermally treated at 60 °C for one day followed by further aging at 25 °C for a week before being used as catalysts for MB degradation.

Table 2.1. Mix quantities per unit volume (kg m^{-3}) calculated based on densities of the raw materials and assuming that the volumes of the components are additive. Corresponding wt. % are given in parenthesis for the RMGP pastes.

Sample	Anatase	RM	MK	$\text{Na}_2\text{Si}_3\text{O}_7$ solution	NaOH	Total
0%A-RMGP	0 (0)	132.3 (7.8)	529.4 (31.1)	927.1 (54.5)	111.8 (6.6)	1700.6 (100)
0.4%A-RMGP	6.6 (0.4)	132.1 (7.7)	528.5 (31.0)	925.5 (54.3)	111.6 (6.5)	1704.3 (100)
1.2%A-RMGP	19.7 (1.2)	131.7 (7.7)	526.7 (30.8)	922.4 (53.9)	111.3 (6.5)	1711.8 (100)
1.9%A-RMGP	32.8 (1.9)	131.2 (7.6)	524.9 (30.5)	919.3 (53.5)	110.9 (6.5)	1719.1 (100)
3.7%A-RMGP	65.1 (3.7)	130.1 (7.5)	520.5 (30.0)	911.6 (52.5)	109.9 (6.3)	1737.2 (100)

2.2.3. Materials Characterization

Elemental analysis of raw materials was carried out by a Bruker S8 Tiger XRF spectrometer that was used in standartless mode under He atmosphere with an 18 mm mask. XRD patterns were collected from 10 to 90° 2 θ with a 0.01263° step size by using a Bruker D8 Discover Diffraction system with a Cu $K\alpha_1$ radiation source employing a wavelength of 1.5418 Å. The power rating of X-ray generator was set to 40 kV, and 40 mA and a Vantec-1 detector with a slit of 1 mm was used. Phase identification was achieved by using ICDD PDF-4 2016 database. FTIR spectroscopy was carried out on a Bruker Vertex 80v spectrometer using an attenuated total reflectance (ATR) cell at a resolution of 2 cm^{-1} in a spectral range of 400-2000 cm^{-1} .

To understand the morphology and microstructure of raw materials and geopolymers, Zeiss Ultra Plus Field Emission SEM coupled with an EDS was used. For EDS measurements Bruker XFlash 5010 EDS detector with 123 eV resolution was used. To measure the density of synthesized geopolymers powder samples were pelleted in a lab press

under 225 psi. Then, the Archimedes method was applied by using an OHAUS PA224C Pioneer analytical balance equipped with an OHAUS density kit. As the liquid, absolute ethanol was used with a density of 0.785 g/cm^3 . At first, each sample's weight was determined. Then the samples were placed into the measurement place inside of ethanol solution and waited for a reasonable time. The samples were weighed inside of the ethanol solution again. The measurements were repeated three-times on each sample to determine the corresponding error ranges.

Surface areas of the samples were determined by the BET analysis conducted on a Micromeritics ASAP 2020-Physisorption Analyzer. Approximately 400 mg sample was used for each measurement and each sample were degassed at $120 \text{ }^\circ\text{C}$ under vacuum for 8 hours before the measurement. Free space measurement was conducted in He gas and the volumetric N_2 adsorption/desorption isotherm was measured between $P/P_0 = 0.01\text{-}0.96$ at cryogenic temperature. BET surface area was calculated between $P/P_0 = 0.05\text{-}0.3$ using liquid nitrogen (10 data points). Pore size distribution was obtained by the Barrett-Joyner-Halenda (BJH) model by using an adsorption isotherm. For XPS analysis a Thermo Scientific K-Alpha X-ray Photoelectron Spectrometer was utilized and Avantage 5.9 software was used to establish XPS data fitting. UV-DRS has been performed to investigate the band-gap values and maximum absorption wavelengths of each geopolymer on a Shimadzu UV-3600 UV-VIS-NIR Spectrophotometer.

A MTS model servo-hydraulic test machine with the capacity of 100 kN with a loading rate of 0.01 mm per second is used to obtain the compressive strength values of geopolymers. To prepare specimens for mechanical performance tests, geopolymers were transferred into $10 \text{ mm} \times 10 \text{ mm} \times 10 \text{ mm}$ silicon molds after mixing. The specimens were thermally treated at $60 \text{ }^\circ\text{C}$ for 24 h followed by a resting period of 30 days at ambient temperature before the mechanical strength measurements. The compressive strength tests were conducted in triplicates and average values were reported.

2.2.4. Evaluation of Photocatalytic Activities

Powdered and sieved solid RMGP samples (0.03 g) were mixed with an aqueous MB dye ($5 \times 10^{-5} \text{ M}$). Then, MB solution was irradiated by a UV-C lamp (OSRAM Puritec HNS

S, dominant wavelength: 253 nm, 4×9 W) under magnetic stirring at room temperature. Syringed MB solutions were centrifugated and analyzed by using a Flame-S-UV-Vis-ES spectrometer, Ocean Optics, USA. Each sample was studied under two different conditions: i) a treatment under dark conditions for 12 hours subsequently followed by a treatment under UV-light exposure for 12 hours; and ii) a treatment under direct UV-light only. The absorbance values were collected by the spectrometer at the characteristic maximum absorption wavelength of 664 nm. Degraded amount (%) was calculated according to Equation (1.1). Data collected under dark conditions were fitted to pseudo-first and second-order adsorption kinetics equations given in Equation (1.3) and Equation (1.4). To understand the kinetics of MB dye degradation reaction under UV light, Equations (1.14) – (1.19) were used.

2.3. Results and Discussion

2.3.1. Bulk Microstructure, Morphological, and Mechanical Properties

BET surface areas, average pore sizes, pore volumes, and the corresponding density values of geopolymers are given in Table A.3. Density values obtained by Archimedes method showed that the density of all geopolymers are very similar and values fluctuate between 2.10 and 2.13 g/cm³. The surface area of the calcined RM and MK were 11.3 and 14.4 m²/g, respectively. Their XRD and FTIR characterization results are provided in Figures A.1 and A.2 and A.3, respectively.

BET analysis results shown in Table A.3 imply that the pore size distribution was mainly in the mesoporous range and no significant change occurred in both surface area and pore size values upon the addition of anatase into the structure.

The XRD patterns of the synthesized geopolymers are given in Figure 2.1. The results indicate that geopolymers display an amorphous structure evident from a broad halo positioned at approximately 28°. The special feature observed at approximately 28° is an indication of the amorphous geopolymer formation [38]. It should be noted that one of the main raw materials, RM, is an industrial waste with amorphous, heterogenous and complex structure. Therefore, it is challenging to follow the changes in the crystalline components.

Based on Figure 2.1, quartz (SiO_2) together with hematite phase (Fe_2O_3) seemed to be the dominant crystalline components within the disordered framework. Sodalite phase detected for 0%A-RMGP was not observed in the rest of the geopolymers. For the 0.4%A-RMGP sample sodium iron oxide ($\text{Na}_3\text{Fe}_5\text{O}_9$) phase was also identified together with quartz and hematite phases. Even though the characteristic peak of anatase observed at 25° has not been detected for 0%A-RMGP and 0.4%A-RMGP, upon a further increase in anatase loading, it becomes visible (Figure 2.1). Albite phase ($\text{Na}(\text{Si}_3\text{Al})\text{O}_8$) seems to be present in 3.7%A-RMGP sample.

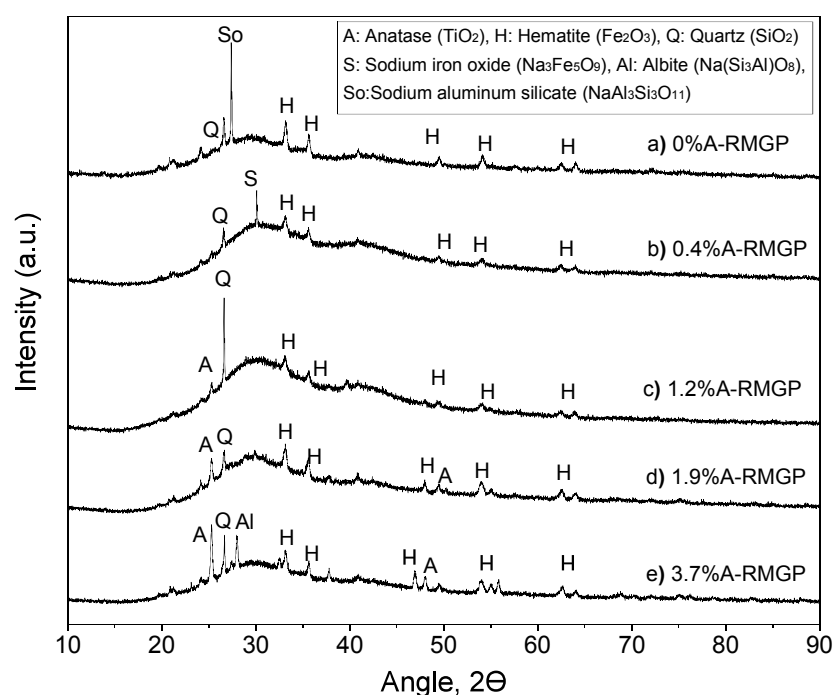


Figure 2.1. XRD patterns of geopolymers a) 0%A-RMGP, b) 0.4%A-RMGP, c) 1.2%A-RMGP, d) 1.9%A-RMGP, e) 3.7%A-RMGP.

FTIR spectra of all geopolymers, shown in Figure 2.2, display broad features in $900\text{--}1200\text{ cm}^{-1}$ region confirming the presence of geopolymerization [4, 38, 39]. The band at approximately 870 cm^{-1} indicates the presence of Si–OH bending vibrations [112]. The most dominant band observed at 970 cm^{-1} indicates the asymmetric stretching vibrations of Si–O–T (T: Al or Si) bonds [113], which indicate the formation of the geopolymeric framework upon alkali activation. This broad feature called the ‘main band’ observed in the region of

900-1200 cm^{-1} is a common indication of the geopolymer formation [38, 110]. The band at 1065 cm^{-1} is assigned to the asymmetric stretching band of Si–O–Si bonds [114] in MK. Peaks at 670 cm^{-1} verifies the presence of Ti–O–Ti bonds resulting from the presence of anatase phase in the geopolymeric matrix [115]. The bands in the region of 900-1200 cm^{-1} were deconvoluted into corresponding contributions, Si–OH, Si–O–T, and Si–O–Si bonds, respectively. The ratio of the intensity of the Si–O–T feature, indicating a newly formed geopolymer framework to that of the intensity of the peak associated with the Si–O–Si feature, related to unreacted MK, ($I_{\text{Si-O-T}}/I_{\text{Si-O-Si}}$) is evaluated to have an understanding on the change in the extent of geopolymerization with the addition of anatase. Figure A.4 displays the evolution of the $I_{\text{Si-O-T}}/I_{\text{Si-O-Si}}$ ratio and the compressive strength of the specimens as a function of anatase content in the geopolymer pastes. Microstructural characteristics seem to be correlated with the changes in compressive strength. The compressive strength values of the specimens vary between 37.7 and 43.2 MPa, indicating that these materials are promising for construction applications. Addition of 1.2 wt% anatase into the RMGP paste (1.2%A-RMGP), seemed to increase the compressive strength by approximately 15% from 37.7 to 43.2 MPa. This increased trend observed in the compressive strength seems to be mainly associated with the evolution of $I_{\text{Si-O-T}}/I_{\text{Si-O-Si}}$ ratio with the increasing anatase content (Figure A.4); this result indicates the presence of anatase, up to a certain limit, could have a positive effect in the geopolymerization process. This enhancement could also be correlated with the fact that the anatase acts as a filler in the geopolymer system resulting in a denser structure consistent with the previous reports [116], [117]. SEM images and corresponding EDS spectrum of geopolymers together with intensity maps of elements Si, Al, Na, Ti, and Fe are provided in Figures A5-A9. Atomic % of these elements in geopolymers which are calculated by additional EDS spectra recorded from 3 spots are given in Table A.4. As it is seen in Figure A.3, MK displays a layered structure composing mainly of Si, Al, and O elements. Calcined RM exhibits granulated surface and consists of various irregularly shaped aggregates due to including different metal oxides and several elements as detected by XRF and EDS analyses. SEM images of geopolymers and the intensity mapping of different elements (Figures A.5-A.9) show that geopolymer surface microstructures are rather homogenous and consist mainly of Si, Al, Na, and O atoms which form the geopolymeric framework together with minor amounts of iron and titanium atoms. The intensity of titanium atoms increased with the addition of anatase. Iron content was

found to be very similar for all of the geopolymers (Table A.4) which is found to be consistent with XPS results.

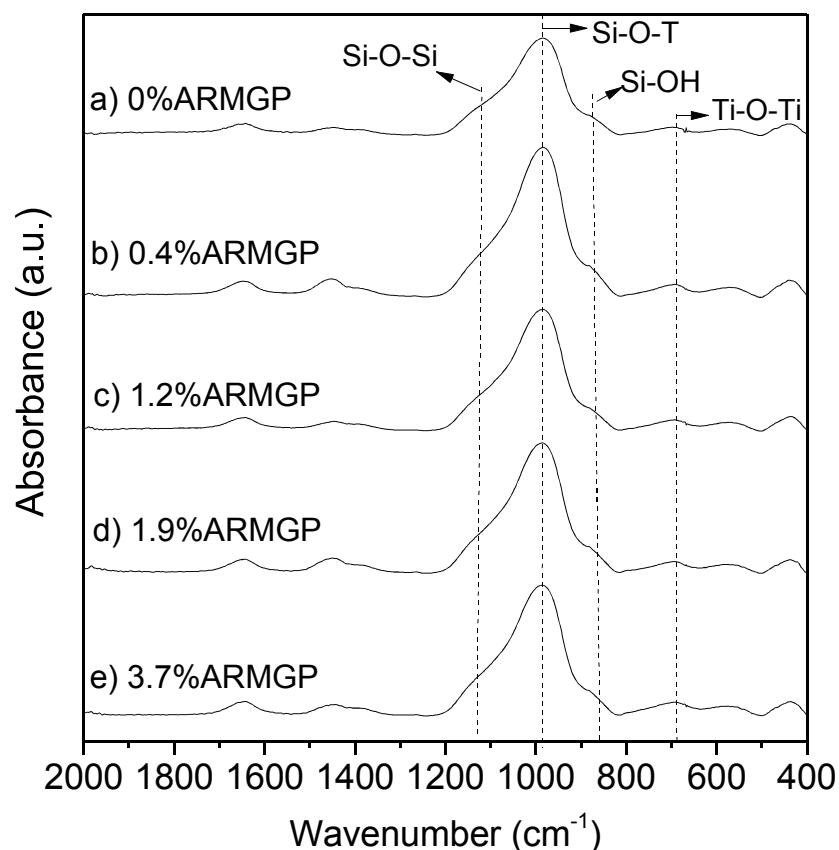


Figure 2.2. FTIR spectra of geopolymers a) 0%A-RMGP, b) 0.4%A-RMGP, c) 1.2%A-RMGP, d) 1.9%A-RMGP, e) 3.7%A-RMGP.

2.3.2. Surface Characteristics

XP survey spectrum of the sample with the highest anatase content of 3.7 wt% (3.7%A-RMGP) together with its O 1s spectrum are given in Figure 2.3. O 1s spectrum is deconvoluted into two main peaks that are centered at 531.6 and 532.5 eV. These features correspond to the surface hydroxyl groups [118] and the presence of metal-oxygen bonds associated with the presence of TiO₂ [36], respectively. Deconvoluted Ti 2p, Fe 2p, and O 1s XP spectra of all RMGPs and their corresponding peak positions are given in Figure A.10 and Table A.5, respectively. The XPS of anatase is characterized with bands at approximately 458.6 (Ti 2p_{3/2}) and 464.3 eV (Ti 2p_{1/2}) [119], consistent with Ti 2p XPS of

geopolymers investigated in this study as shown in Figure A.10 and Table A.5. However, our data presented in Figure A.10 also indicated the presence of new Ti-related features at 454 and 460 eV as well. These new features might be indicating that anatase could be partly present within the geopolymeric framework.

Besides, two main contributions detected at approximately 711 (Fe 2p_{3/2}) and 723 eV (Fe 2p_{1/2}) are characteristic features of hematite phase [120] originated from RM (Figure A.10a,d,g,j,m). Even though the surface atomic % obtained from the XPS results regarding the Fe element was relatively low for all of the samples (Table A.6), its presence was also verified by the XRD measurements (Figure 2.1).

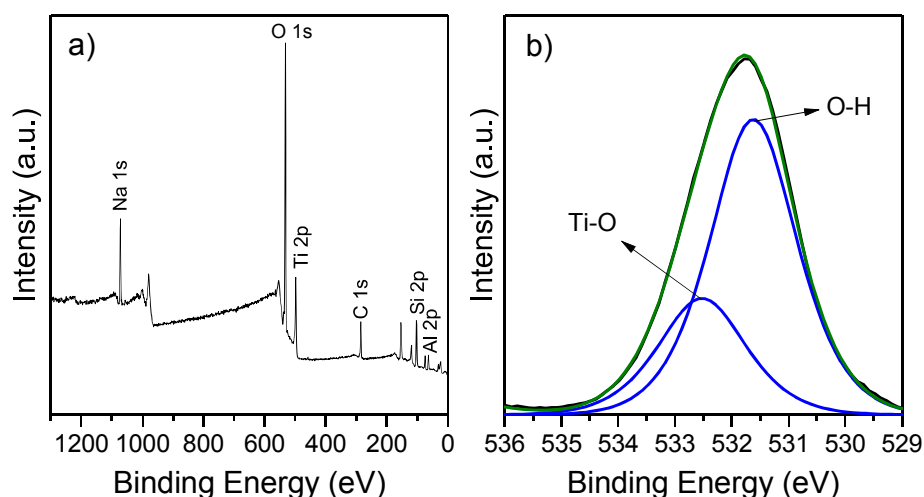


Figure 2.3. XPS patterns of a) survey spectrum, b) O 1s spectrum of 3.7%A-RMGP.

The availability of surface Ti atoms on the surface increases with anatase addition (Table A.6). However, the corresponding amounts for Fe atoms seem not to be affected by anatase addition.

Maximum absorption wavelength and band gap values of the raw materials as well as the geopolymer samples are provided in Table A.7, while Figure A.11 is listing the band gap values of the geopolymers. Maximum absorption wavelengths (λ_{\max}) of MK and RM were 381 nm and 588 nm, respectively. With geopolymerization, the spectral response was extended to a longer wavelength, which might be an indication of photocatalytic activity under visible light for the synthesized geopolymers. Furthermore, the absorption threshold of anatase-

added samples, especially for 1.9%A-RMGP and 3.7%A-RMGP, had shifted to a slightly higher wavelength (Figure A.12 and Table A.7). It is seen from Table A.7 that upon anatase addition, the band gap values of geopolymers approach to that of anatase; 3.2 eV. Concomitantly, a shoulder was detected at approximately 380 nm for the anatase-added samples (Figure A.12), referring the absorption at wavelengths shorter than 400 nm. This situation, observed only for the anatase-added samples, is an indication of the absorption across the band gap of TiO₂ for the excitation of valence band electrons [121], [122].

2.3.3. Degradation of MB Dye

To evaluate the photocatalytic activity and distinguish it from the adsorption, the measurements were conducted at two different conditions: First, the measurements were conducted under dark conditions for 12 hours followed by exposure to UV irradiation for an additional 12 hours. The dark portion of this treatment provides information on the adsorption capability of the samples. Second, the experiments were performed directly under UV irradiation for 12 hours to explore the photodegradation of MB.

2.3.3.1. Experiments Under Dark Followed by UV Irradiation

It was reported that negatively charged [AlO₄]⁵⁻ tetrahedrons in the geopolymeric porous structure could provide a suitable medium for the adsorption of MB cations [82] and they can adsorb cationic dyes because of the surface hydroxyl groups present on their surfaces [6, 109]. In this regard, the initial experiments were carried out under dark conditions for 12 h and then data were collected under UV light for 12 h to understand photodegradation capability of geopolymers. Residual MB concentrations, denoted as C/C_0 , are shown in Figure 2.4. Even though the adsorption takes place for all of the samples, anatase content was found to be the main factor determining the removed amount of MB dye at the end of 24 h.

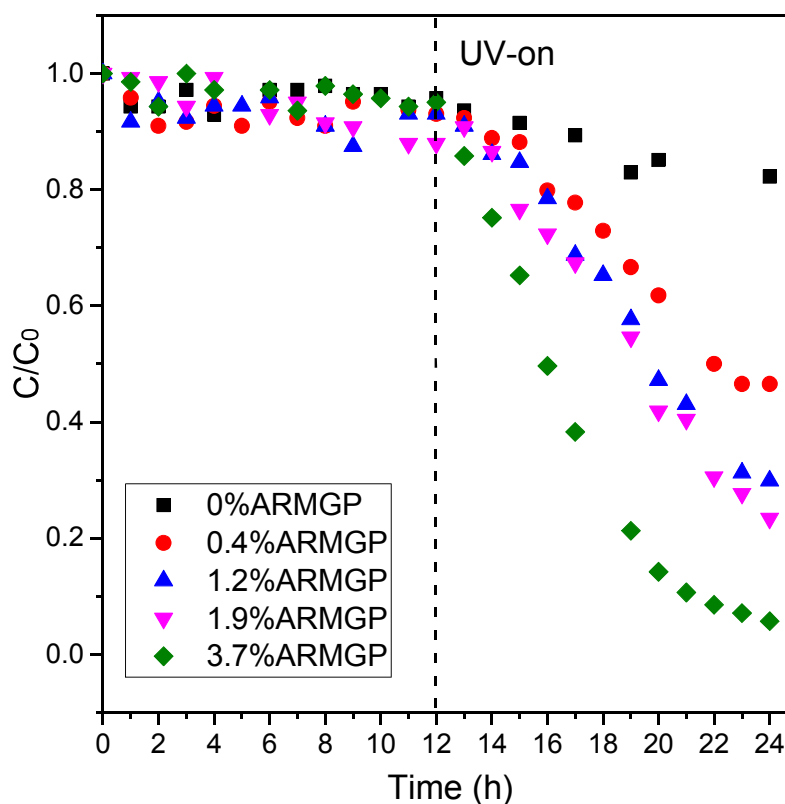


Figure 2.4. Variation of the residual MB dye concentration (C/C_0) with time; values were collected under dark for 12 h followed by UV irradiation for 12 h.

The results collected during the dark-run were fitted to pseudo-first- and second-order adsorption kinetics. Extracted kinetics data are shown in Table 2.2 together with the corresponding degraded amounts (%) of MB dye under dark (initial 12 h under dark), and the total degraded amounts (%) of MB dye under dark followed by UV irradiation (12 h under dark + 12 h under UV irradiation).

Data imply that the adsorption behaviour of geopolymers under dark conditions are well-described by pseudo-second-order adsorption kinetics and both experimental and calculated values of q_e ($q_{e,exp}$ and $q_{e2,calc}$, respectively) are close to each other. This result is consistent with the literature, where second-order adsorption was used for defining the adsorption behaviour of geopolymers under dark conditions [82, 109], for which the process is most possibly controlled by the chemisorption process [123] implying an electron

exchange and share between MB dye (adsorbate) and functional groups of geopolymer samples (adsorbent) on the surface [18, 124].

Table 2.2. Kinetic parameters for adsorption of MB on anatase added geopolymer samples under dark conditions.

Sample	$k_{1,ads}$ (min^{-1})	R^2	$k_{2,ads}$ (g mg^{-1} min^{-1})	R^2	$q_{e,exp}$ (mg g^{-1})	Degraded amount (%) (12 h dark)	Degraded amount (%) (12 h dark + 12 h UV)	$\Delta(\text{UV-}$ Dark) [*]
0%A-RMGP	0.0028	0.77	0.025	0.94	2.27	4.2	17.7	13.4
0.4%A-RMGP	0.1476	0.15	0.050	0.86	3.33	6.2	53.4	47.2
1.2%A-RMGP	0.0008	0.14	0.007	0.90	3.70	6.9	70.1	63.2
1.9%A-RMGP	0.0009	0.99	0.003	0.90	6.43	12.0	76.6	64.5
3.7%A-RMGP	0.0008	0.62	0.005	0.90	2.65	4.9	94.3	89.3

* $\Delta(\text{UV-Dark})$ identifies the difference between degraded amounts (%) obtained at the end of the 12 h dark+12 h UV period and 12 h dark period.

Since there is a lack of any significant difference between the surface characteristics, such as surface area and pore size values (Table A.3), Figure 2.4 shows that the behavior under dark conditions for all of the samples are not equal but similar.

It is known from the literature that pore volume and density of the geopolymers are related [125] and high density value of an adsorbent used for wastewater treatment may cause high uptake capability [126]. Density measurements presented in Table A.3 also show that anatase addition does not cause a significant difference in density values. However, when UV-light is switched on after a waiting period under dark conditions, further removal of MB dye takes place (Figure 2.4). Corresponding kinetic parameters which are obtained by fitting the experimental data collected under UV-light to pseudo-first- and pseudo-second-order reaction kinetics are displayed in Table 2.3.

Values given in Table 2.3 show that even though adsorption mechanism under dark conditions is defined better by pseudo-second-order kinetics (Table 2.2), with the introduction of UV-light to this system, the reaction mechanism suits better to pseudo-first-order reaction kinetics. It was previously mentioned that for the samples kept under dark

conditions for 12 hours, adsorption was most possibly controlled by the chemisorption process. However, in the presence of UV-light, the switch of mechanism from pseudo-second-order adsorption kinetics to pseudo-first-order reaction kinetics shows that photocatalytic rate limiting step in the presence of UV-light is physisorption [127]. Consequently, to achieve photocatalytic removal of MB dye, firstly MB molecules should be adsorbed on surface of the adsorbent [128].

Table 2.3. Pseudo-first- and second-order reaction kinetic parameters obtained for 0.03 g of sample in 5×10^{-5} M 100 ml MB solution under 12 hours of UV-light after 12 hours of dark conditions (data collected under UV light is used for the calculation of the parameters given in this table).

Sample	Pseudo-first-order		Pseudo-second-order	
	$k_{app,1}$ (1/h)	R^2	$k_{app,2}$ (L/g.h)	R^2
0%A-RMGP	0.01	0.97	0.96	0.97
0.4%A-RMGP	0.05	0.94	5.57	0.88
1.2%A-RMGP	0.10	0.95	2.79	0.89
1.9%A-RMGP	0.11	0.96	17.22	0.90
3.7%A-RMGP	0.25	0.99	91.08	0.90

In the proposed mechanism describing the removal of MB dye with subsequent adsorption and photodegradation, first step is the ionization of MB dye into cationic form in aqueous solution. Cationized MB can either be adsorbed on the surface hydroxyl groups of the geopolymer surface. When the energy of the excitation source exceeds the band-gap energy value of the semiconductors, which are TiO_2 and Fe_2O_3 for this system, that are present in the geopolymeric framework, the separation of an electron (e^-) from the valence band to the conduction band of the semiconductor creates a positive electron hole (h^+) in the valence band. These electron and hole pairs on the surface react with oxygen and may reduce oxygen to superoxide radicals ($\cdot\text{O}_2^-$), or oxidize the water adsorbed on the surface, respectively [84]. These reactive oxygen species released can oxidize the adsorbed MB cation to the degradation products [82]. It was previously shown that MB can be degraded

by TiO₂-based photocatalysts [129-131] and degradation products and the degradation mechanism were also investigated in detail [129].

Houas et al, used total organic carbon (TOC) analysis together with GC/MS and LC/MS to understand the mineralization of organic carbon, and to determine the intermediate compounds, respectively [129]. Results of this study showed that, as a consequence of photodegradation of MB, gaseous CO₂, and nitrogen and sulfur containing inorganic ions occur. Even though the degradation mechanism of MB under UV conditions involves several steps, this detailed process can be summarized in three main steps. Firstly, sulfate ions are produced as a result of an interaction between negatively charged TiOH and TiO⁻ forms of TiO₂; that occurs especially at high pH values, and C-S⁺=C functional group of MB. It is proposed that OH^o radical, which had occurred as a result of oxidation of water, attacks C-S⁺=C group that is in coulombic interaction with the photocatalyst's surface. Secondly, nitrogen containing groups in MB molecules mineralize to form ammonia (NH₃) and ammonium (NH⁴⁺). Lastly, organic carbon is oxidized to form CO₂, which is due to oxidative mineralization as a result of the opening of aromatic rings with the carboxylic acid formation [129].

Table 2.2 also demonstrates the variation of $\Delta(\text{UV-Dark})$, defined as the difference between the degraded amounts (%) obtained at the end of the treatments for 12 hours in dark followed by 12 hours under UV-light and at the end of the 12 hours under dark treatment, with changes in the amount of TiO₂ added. Results imply that anatase addition is the main factor controlling the $\Delta(\text{UV-Dark})$, it gradually increased from 13.4 to 89.3%, when the amount of TiO₂ added into the system increased from 0 to 3.7 wt%. Even though there is a lack of any significant variation between pore characteristics between the samples, the adsorption parameters given in Table 2.2 indicate that there are still small variations in samples' adsorption properties.

These small differences may also have an effect on the corresponding photodegradation behavior of samples. For instance, as the adsorption capabilities of each sample is different, the initial MB concentrations at the beginning of the photodegradation process (at $t = 12$ hours) would be different (even though the starting amounts are identical); and this difference influences the photodegradation rate as it also depends on the MB

concentration. However, apparently, this possible difference was compensated with the addition of anatase, as the results indicated a positive correlation between anatase content (wt%) and degraded amount (%) at the end of 24 hours.

2.3.3.2. Experiments Under Direct UV Irradiation

During the experiments starting directly with the UV light conditions (skipping the treatment under dark period) it is challenging to distinguish the individual strengths of simultaneously occurring adsorption and photodegradation mechanisms. However, Figure 2.5 demonstrates that at the beginning of the experiments (0-3 hours) the main mechanism responsible for a slight decrease in MB concentration was nearly the same for all geopolymer samples and therefore it was mostly independent of the corresponding anatase content of the samples. Because there is a lack of any significant difference between the surface areas of the geopolymer samples (Table A.3), such similar behaviour at the beginning of the UV treatment can be mostly attributed to the adsorption mechanism. However, during a long exposure of up to 12 hours, the effect of anatase content becomes dominant and the samples present various extents of MB degradation performance, demonstrating an increased degradation performance well-correlated with their corresponding anatase amounts (Figure 2.5).

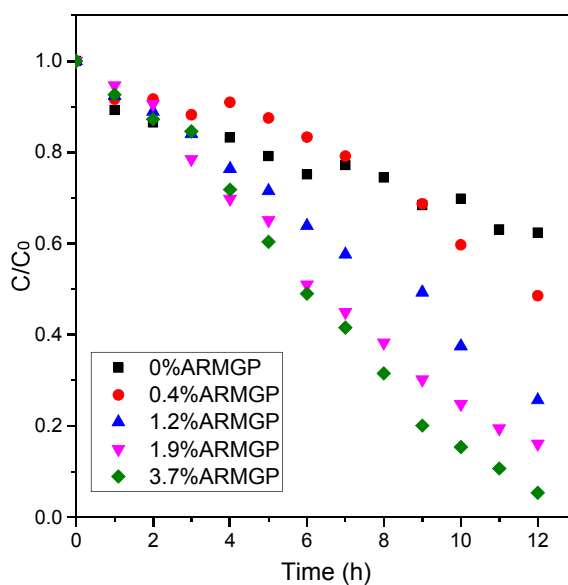


Figure 2.5. Residual MB dye concentration (C/C_0) vs. time values collected under UV light conditions.

Reaction data of MB photodegradation by using anatase-added geopolymers were fitted to pseudo-first-order and pseudo-second-order reaction kinetics. Table 2.4 summarizes the corresponding degraded MB amounts (%) along with the corresponding pseudo-first- and pseudo-second-order reaction kinetics parameters after 12 hours of UV light irradiation together with their corresponding R^2 values. For each sample, degraded MB amounts (%) of the samples, which were irradiated directly by UV-light for 12 hours (Table 2.4) were found to be higher than those of the samples that were kept under dark conditions followed by a UV-light (12 hours dark + 12 hours UV) given in Table 2.2. It is speculated that keeping the samples under dark conditions at the beginning possibly led to a blockage of the photocatalytically active sites because of the adsorption of MB particles during the dark run.

Table 2.4. Pseudo-first and second-order- reaction kinetics parameters and degraded amount (%) values obtained for 0.03 g of sample in 5×10^{-5} M 100 ml MB solution under UV light after 12 hours.

Sample	Pseudo-first-order		Pseudo-second-order		Degraded MB amount (%) in 12 h under UV
	$k_{app,1}$ (1/h)	R^2	$k_{app,2}$ (L/g.h)	R^2	
0%A-RMGP	0.03	0.99	2.97	0.98	37.6
0.4%A-RMGP	0.08	0.96	7.27	0.93	51.4
1.2%A-RMGP	0.13	0.98	18.08	0.92	74.3
1.9%A-RMGP	0.17	0.99	30.11	0.89	83.9
3.7%A-RMGP	0.28	0.99	95.36	0.83	94.6
Anatase	0.09	0.96	9.24	0.97	87.7

Table 2.4 shows that the degraded MB % under UV irradiation for 12 h increases with an increase in the anatase content of the corresponding geopolymer. UV spectrum of samples 0%A-RMGP and 3.7%A-RMGP are provided in Figure A.13, which was found to be in accordance with the data obtained in Table 2.4. Absorption intensity gradually decreases for 3.7%A-RMGP, whereas the decrease in intensity is comparatively very lower for 0%A-RMGP. Figure 2.6 indicates that this variation presents a correlation between these degraded

amounts with the corresponding atomic surface concentrations of Ti, determined by XPS measurements, on each geopolymer. The degraded MB amount with 3.7%A-RMGP was 94.6%. Compared to the corresponding degraded MB amount with pure anatase (87.7%), the performance of the 3.7%A-RMGP was superior. This result indicates that the anatase-added geopolymers successfully remove MB, besides they have good mechanical properties and offers an environmentally friendly and efficient way of utilizing a hazardous industrial waste, RM.

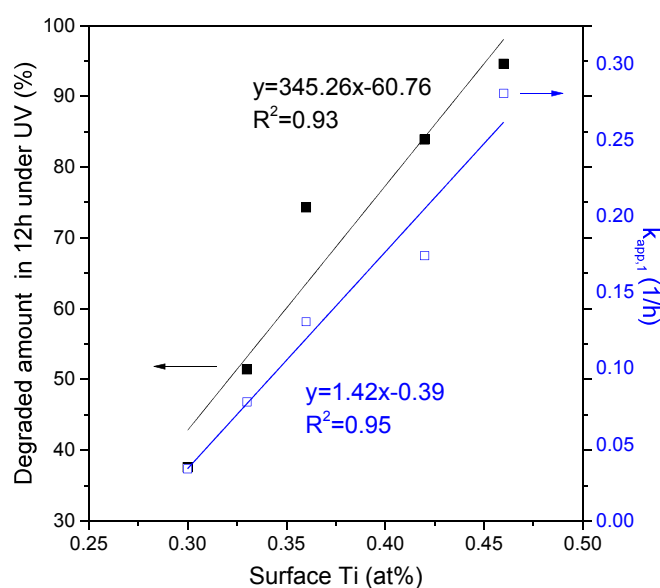


Figure 2.6. The change of degraded MB amount under UV in 12h (black symbols) and change of $k_{app,1}$ with surface Ti amount (at%) (blue symbols).

Comparison of the R^2 values obtained by fitting the data presented in Figure 2.5 to reaction rate expressions indicated that the pseudo-first-order reaction rate kinetics provide a better model for the experimental data as shown in Table 2.4, consistent with the previous inference where the data collected under UV-light after dark conditions displayed a better fit to pseudo-first-order reaction kinetics (Table 2.3). These values compare well with the corresponding values for pure anatase, where the degraded MB amount and $k_{app,1}$ value was 87.7% and 0.09 (1/h), respectively, at a corresponding theoretical surface Ti amount of 33 atomic % for pure anatase. Values of $k_{app,1}$ clearly show a systematic positive trend upon anatase addition. The $k_{app,1}$ value starts to exceed that of pure anatase, when the anatase loading in the geopolymer was 1.2 wt% or higher.

This phenomenon might be originated from the aggregation behavior of pure anatase particles [132], such that the light emitted from the UV source cannot diffuse into the aggregated forms of TiO_2 as good as the geopolymers having a more efficient TiO_2 dispersion. The second cause of this situation is possibly originated from the reaction mechanism of the photocatalytic degradation reaction; as it is mentioned above, the reaction follows a pseudo-first-order kinetics in the presence of UV-light and the photocatalytic rate limiting step is physisorption. To accomplish the photocatalytic degradation, the first step is the adsorption of dye molecules on the adsorbent. Owing to the surface characteristics of the geopolymer structure, compared to pure anatase, geopolymer surface, possessing negatively charged surface species, offering a more suitable adsorption site for the adsorption of a cationic dye compared to the surface of pure anatase.

To determine the dependency of the photocatalytic degradation rate on the surface Ti atomic percent (at%), the variation of k_{app} with the surface Ti amount determined by XPS measurements is investigated, as shown in Figure 2.7. The data present a strong correlation with an R^2 of 0.95.

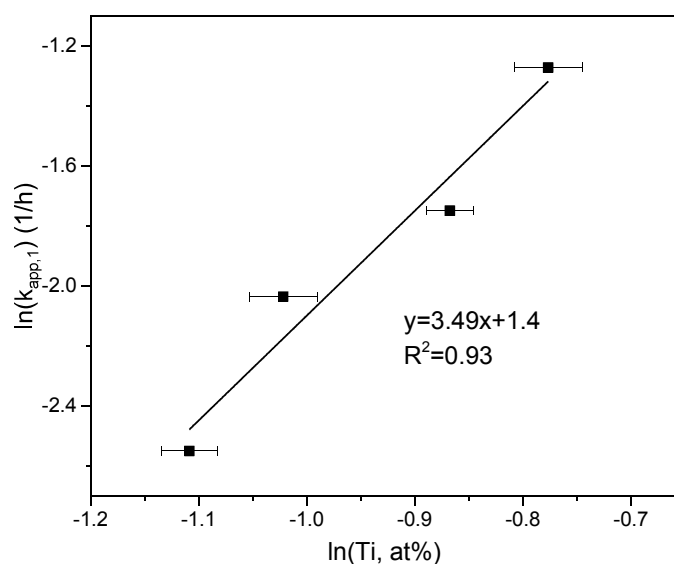


Figure 2.7. Experimental data fit to pseudo-first-order reaction kinetics for anatase-added RMGP samples. Error bars represent the standard error of surface Ti amount (at%).

Besides surface Ti species, it is also well known that hematite originated from RM have photocatalytic activity and Fe sites might also be playing a role in MB degradation. However, the Fe atomic % is rather low at the geopolymer surface as revealed by XPS (Table A.6). To investigate any effects of surface iron species on the photocatalytic activity, variation of k_{app} with the surface Fe amount was investigated. However, the corresponding plot employing surface Fe atomic% did not present any correlation ($R^2 = 0.3$), ruling out any strong photocatalytic contribution of surface Fe species in RMGP system investigated here. Thus, we infer that the surface Ti species are the dominant species responsible for the photocatalytic activity in RMGP system.

Strini et al. demonstrated that segregated TiO_2 molecules that are present in the layers of anatase-added geopolymer samples show photocatalytic activity depending on the amount of surface TiO_2 molecules [133]. Accordingly, the first-order degradation rate constant (k) was evaluated (this rate constant is different than the apparent rate constant, please see Section 1.4.2 for detailed discussion) and the reaction rate order with respect to surface Ti amount (a) using Equation (1.19) on the anatase-added samples (0.4%A-RMGP, 1.2%A-RMGP, 1.9%A-RMGP, and 3.7%A-RMGP). For this analysis, it is assumed that all surface Ti atoms behave nearly the same for MB photodegradation in each A-RMGP samples on the basis of an R^2 value of 0.93 in Figure 2.6 and the identification of surface Ti atoms as the dominant active species responsible for photocatalytic activity. The line presented in Figure 2.7 had a slope of 3.49, setting the reaction order with respect to the surface atomic% Ti for the A-RMGP samples based on Equation (1.19). Based on this slope and the intercept values of the line presented in Figure 2.7, the MB degradation rate constant, k , is determined as 4.04 (surface atomic% Ti) $^{-3.49} \times h^{-1}$.

2.4. Concluding Remarks

The effects of systematic anatase addition into RM- and MK-based geopolymer systems on the corresponding mechanical strength and MB removal performance were investigated in this part. Adsorption behavior of geopolymers under dark conditions is described by pseudo-second-order adsorption kinetics, possibly controlled by the chemisorption processes. When UV-light was turned on following a treatment under dark conditions, the photocatalytic degradation of MB took place at significantly enhanced rates

as a function of anatase content in the system. Data indicated that the dominant responsible sites for the photocatalytic activity in the geopolymers were identified as the surface Ti species. MB degradation under direct UV light conditions was described by pseudo-first-order kinetics. Data revealed that addition of anatase up to 3.7 wt% in the geopolymeric paste (3.7%A-RMGP) resulted in a tripled $k_{app,1}$ value compared to that of pure anatase. These results demonstrate that a hazardous industrial waste, RM, has a huge potential as a cost-free raw material for obtaining self-cleaning geopolymers. The resulting geopolymers offer a sustainable-route towards self-cleaning construction materials with competitive mechanical properties.

3. A NOVEL ALKALI ACTIVATED MAGNESIUM SILICATE AS AN EFFECTIVE AND MECHANICALLY STRONG ADSORBENT FOR METHYLENE BLUE REMOVAL

3.1. Introduction

Dyes are synthetic organic compounds that have extensive applications in textile, printing, leather, cosmetics, and other industries [134, 135]. Each year more than 100,000 types of different dyes are produced with an annual production rate of 7×10^5 tonnes [136], and after use, they are mostly discharged to the hydrosphere with effluent waters and cause a huge environmental problem. Considering the inevitable possibility of half of the population living in water-stressed areas in 2025 [137], it becomes crucial to find solutions for the removal of dyes in wastewaters. If purification of wastewaters that are contaminated with harmful organic dyes cannot be managed adequately, not only the water ecosystem but also humans will be affected drastically from this situation. Several distinct methods were suggested for this purpose, including ozonation [138], photocatalytic degradation [91], membrane separation [135], and adsorption [136]. Among these techniques, adsorption is regarded as a widely accepted and preferred method for the removal of dyes owing to the presence of various distinct adsorbent materials, cost effectiveness; which can be arranged by the appropriate selection of the adsorbent material, fast reaction rate, and ease of operation [134, 139, 140].

Various different adsorbent materials were developed by many researchers for the removal of dyes from aqueous solutions involving activated carbons [134, 141, 142], biochars [140, 143], clays [67, 144], metallic organic frameworks [93, 145], membranes [135, 146], and geopolymers, which are also known as AAMs [22,147, 148]. Even though adsorbent design may differ with the type of the dye, there are some accepted properties which are common for a desired adsorbent. These features include low cost and availability, ease of synthesis, high adsorption capacity, fast kinetics, good chemical stability, and regeneration and reusability capability [139]. Moreover, it is also desired to have high mechanical strengths so that these materials can be practically utilized in various

applications, such as water storage and water purification [147]. However, this latter criterion has been overlooked for many of the studies in the literature. Besides, it is very challenging to synthesize an adsorbent which can offer properties satisfying all of these desired properties. The synthesis of most of the adsorbents stated above requires tedious energy intensive procedures with very limited yields and/or complex processing of raw materials that also causes inevitable side products. Most of the time, these specially made materials offer good adsorption capabilities but they generally lack in mechanical performance and also economical sustainability. In this regard, AAMs come forward, as these materials have a great potential to be tuned to ensure all of the above listed preferred properties of a desired adsorbent with high yield and less environmental footprint during the synthesis procedure.

When the AAMs are synthesized, use of cheap and abundant minerals as raw materials can offer significant cost benefits. In this regard, sepiolite (Sep) offers a broad potential because of several reasons. For instance, it is a naturally existing phyllosilicate clay with a general formula of $\text{Mg}_8\text{Si}_{12}\text{O}_{30}(\text{OH})_4(\text{OH}_2)_4 \cdot n\text{H}_2\text{O}$; $n \leq 8$, offering a significantly high silica content [149]. The unique structure of Sep is composed of blocks and channels. Each structural block of Sep mineral consists of continuous tetrahedral silica sheets with discontinuous magnesium octahedral sheets [67, 77, 150]. Mining of Sep mainly takes place in Spain, USA, France, China, and Turkey [149, 151] totalling approximately 850,000 tons globally [152]. Besides, it has distinct properties, such as a high specific surface area that may reach up to $320 \text{ m}^2 \text{ g}^{-1}$ [153], fibrous morphology, and characteristic microporosity, offering broad opportunities in various applications, such as in catalysis, where it is used as a support to disperse metal nanoparticles [154], in construction, where it is used as an additive to improve the mechanical properties of construction materials [155, 156], and in separation, where it is used as an adsorbent [157, 158]. In this regard, previous studies showed that Sep can effectively adsorb water or organic molecules due to its specific structure involving zeolite-like channels with an approximate width of $5.6 \text{ \AA} \times 11.0 \text{ \AA}$ [159]. The adsorption properties of both as-received Sep and its modified form obtained by different treatments were investigated by many researchers [67, 68]. Some of these studies illustrated an enhanced adsorption capability of Sep towards cationic dyes, MB and methyl violet removal [69]. In addition to these cationic dyes, this mineral was also tested for the removal of anionic dyes, reactive blue 221 and acid blue 62 [68, 157], as well.

Even though these studies demonstrated a broad potential of Sep in wastewater treatment, the literature broadly lacks its use as a raw material in the synthesis of AAMs with high performance for dye removal from water. Treatment of Sep with alkaline NaOH solution was established in an attempt to investigate the CO₂ sorption capacity by Walczyk et. al, and it was shown that Sep may transform into loughlinite mineral upon suggested NaOH treatment procedure [160]. Sodalite synthesis from Sep mineral was also conducted by an energy intensive alkali fusion and hydrothermal treatment procedure to investigate heavy metal removal from aqueous solutions [161]. Even though these studies offer alternatives for evaluating Sep mineral for different purposes, utilizing Sep for the synthesis of AAMs with high mechanical performance values, which are also green construction materials with low energy requirement, has not been studied in the existing literature for MB dye removal. Besides, the adsorbent materials used in reactors or columns should meet the necessary mechanical properties to prevent possible problems that may cause malfunctioning of industrial units [162].

Sep itself or its modified forms do not offer any mechanical performance, which prevents their broad utilization for different purposes that may need a certain level of integrity and mechanical endurance. In this regard, having high mechanical strength in these materials is crucial for practical applications, however, most of the time, this property is overlooked. Here, we are geared up to fill this gap in the literature and introduce a Sep-based AAM (Sep-AAM) as an effective adsorbent for the removal of dyes from water. The adsorbent was synthesized by the alkali activation of Sep, characterized in deep detail revealing its structural and mechanical characteristics, and tested for MB removal from water. Kinetic and thermodynamical parameters of adsorption of MB onto calcined Sep and Sep-AAM were determined. Mechanical performance together with surface characteristics-performance relationship for Sep-AAM have also been established and discussed in detail. This chapter was published as a paper [97] and the original manuscript has been rearranged to conform to the format requirements of the dissertation.

3.2. Experimental Conditions

3.2.1. Materials

Sep mineral was kindly supplied by Dolsan Mining, Eskişehir-Turkey. Calcined Sep was obtained by the calcination of Sep mineral at 750 °C for 1 h (2.8 g/cm³) [77]. MB hydrate (Sigma-Aldrich, purity >97%, molecular weight 319.85 g/mol) was used as a model adsorbate. Sodium silicate (Na₂Si₃O₇) solution (9 wt% of Na₂O, 28 wt% of SiO₂, 63 wt% of H₂O, Merck, 1.35 g/cm³) was used as an alkali activator for the synthesis of Sep-AAM. Chemical compositions of the as-received Sep and its calcined form are provided in Table B.1 (in the Appendix B).

3.2.2. Preparation of the AAM

Preliminary experimental results revealed that highest mechanical performance (compressive strength) is obtained when Si/Mg and Na/Mg ratios are 3 and 1, respectively. Therefore, initial gel chemical composition of Sep-AAMs in this study was set to have the molar Si/Mg and Na/Mg ratios of 3 and 1, respectively, as given in Table B.2. To ensure these ratios in the synthesized material, the XRF results presented in Table B.1 were used and the added necessary amount of Na₂Si₃O₇ solution is arranged simply by calculating the amount needed to obtain desired Si/Mg and Na/Mg ratios. Mix proportions in terms of mass per unitary volume are presented in Table B.3. Na₂Si₃O₇ solution was used as an alkali activator. Powdered and sieved (#70 mesh sieve, 200 µm) calcined Sep was mixed thoroughly with Na₂Si₃O₇ solution and then thermally treated at 40 °C for 24 hours that is followed further by aging at room conditions for a week before being utilized as an adsorbent for MB adsorption.

3.2.3. Materials Characterization

Bruker S8 Tiger XRF spectrometer was utilized to determine the elemental composition of raw materials. XRD measurement of the samples were performed on a Bruker D8 Discover Diffraction system with a Cu K α ₁ radiation source employing a wavelength of 1.5418 Å. For FTIR spectroscopy, a Bruker Alpha II with an ATR cell, in

absorption mode was used. A Zeiss Ultra Plus FE-SEM coupled with an EDS was used to designate the microstructure and morphology of raw materials and the synthesized geopolymer. BET surface area, pore size, and pore volume values of samples were performed on a Micromeritics ASAP 2020 –Physisorption Analyzer. To find pore size distribution of the BJH model is utilized by using desorption adsorption isotherm. XPS analysis was conducted on a Thermo Scientific K-Alpha X-ray Photoelectron Spectrometer and Avantage 5.9 software was utilized for XPS data fitting. TGA was conducted on a TA Instruments TGA Q500 instrument. The temperature of each sample (25 mg) placed in a platinum pan was increased to 800 °C at a ramp rate of 3 °C/min in flowing N₂ (60 mL/min N₂). Compressive strength measurements were conducted on a MTS model servo-hydraulic test machine with capacity of 500 kN with a loading rate of 0.01 mm per second. Prior to mechanical performance tests, alkali activated materials which were mixed thoroughly were moved into 10 mm × 10 mm × 10 mm silicon molds and kept at 40 °C for 24 h followed by a resting period of 28 days at ambient temperature. The compressive strength tests were conducted in quadruplicates and average value was reported together with standard deviation value. pH of the solutions was measured by using a lab pH meter (VTW, model 7110). A Malvern Zetasizer Nano ZS was utilized to determine the zeta potential of the samples. Zeta potential measurements were conducted at ambient temperature (25 °C) and 0.1 M HCl and NaOH solutions were used to adjust the pH. The chemical composition of the MB solution after adsorption were determined by using inductively coupled plasma mass spectrometry (ICP-MS, Agilent 7700x, Agilent Technologies Inc., Tokyo, Japan) and measurements were replicated five times.

3.2.4. MB Adsorption Tests

Adsorption behaviors of materials was studied by immersing 10 mg of powdered and sieved (#70 mesh sieve, 200 μm) forms of the adsorbents into 50 ml of MB solution with various predetermined MB concentrations (5-40 mg L⁻¹). The mixtures were magnetically stirred at 700 rpm until equilibrium was reached. Aliquots collected from MB solutions at regular time intervals were centrifugated and then analyzed by using a Flame-S-UV-Vis-ES spectrometer (Ocean Optics, USA) by measuring the absorbance value at $\lambda = 664$ nm. Removal efficiency (%) was measured as given in Equation (1.1). The amount of MB adsorbed on adsorbents were determined by Equation (1.2). Pseudo-first- and pseudo-

second-order adsorption kinetic models were used to reveal the MB adsorption mechanism of materials. The dependence of adsorption rate on both the adsorbent amount and adsorbed amount of MB dye was evaluated by using Equation (1.8). The Arrhenius equation given in Equation (1.9) was used to determine the activation energy of adsorption. Intraparticle diffusion model given in Equation (1.10) was also applied to experimental data in order to identify the diffusion mechanism. Langmuir and Freundlich models shown in Equation (1.11) and Equation (1.13) were used to fit the equilibrium data of the samples.

3.2.4.1. Thermodynamical Properties

The thermodynamic parameters of adsorption, such as Gibbs Free Energy (ΔG°), enthalpy (ΔH°) and entropy (ΔS°) changes were calculated [163] as

$$\Delta G^\circ = \Delta H^\circ - T \times \Delta S^\circ. \quad (3.1)$$

To obtain the value of ΔH° and ΔS° , Van't Hoff equation is used in the following form

$$\ln K_{ads} = -\frac{\Delta H^\circ}{R \times T} + \frac{\Delta S^\circ}{R} \quad (3.2)$$

where R is the universal gas constant (8.314 J/(mol.K)), T is the temperature (K), K_{ads} is the adsorption equilibrium constant. When there is a non-ionic solute or ionic solute in a dilute solution (which is the case in this study) equilibrium constant term (K_{ads}) in Equation (3.2) can be written as [163]

$$K_{ads} = K_L \times M_A \quad (3.3)$$

where M_A is the molecular weight of the adsorbate (mg/mol). Equation (3.3) becomes

$$\ln(K_L \times M_A) = -\frac{\Delta H^\circ}{R \times T} + \frac{\Delta S^\circ}{R}. \quad (3.4)$$

3.2.4.2. Adsorbent Regeneration Test

Calcined Sep in powder form and powdered form (#70 mesh sieve, 200 μm) of the Sep-AAM was used for four consecutive adsorption experiments of 3.5 h. Thermal treatment procedure is known to be an effective method for removing surface adsorbed MB molecules [19], [80]. After each use, calcined Sep and Sep-AAM was regenerated by calcination at 400 $^{\circ}\text{C}$ in static air for 2 hours. The initial MB concentration was 40 mg L^{-1} (500 ml) and the amount of adsorbent used for the first adsorption experiment was 100 mg. MB concentration was adjusted between each regeneration experiment to compensate the mass loss of the adsorbent by keeping the MB amount per adsorbent amount constant.

Regeneration performance of the Sep-AAM was also investigated in the monolith form to be able to estimate the regeneration performance by minimizing the mass loss. Desorption tests were conducted prior to regeneration experiments for calcined Sep and Sep-AAM with the highest MB initial concentration in this study. For this purpose, adsorbents that were magnetically stirred in 50 ml of 40 mg L^{-1} MB solution for 3.5 h at room temperature were separated by centrifugation which were later immersed into 50 ml of distilled water for 24 h at room temperature. The quantity of MB dye that was leached to distilled water at the end of this period were measured by using a UV-Vis spectrometer.

3.3. Results and Discussions

3.3.1. Morphological, Bulk Microstructure, Thermogravimetric, and Mechanical Properties

BET surface areas, pore volumes, and average pore sizes of Sep, calcined Sep, and Sep-AAM are summarized in Table 3.1. Data showed that there is a significant decrease in the surface area of Sep upon calcination at 750 $^{\circ}\text{C}$. This decrease is associated with the loss of the water molecules with an increase in the temperature, consistent with the previous reports [157]. It is known from the literature that the amounts of soluble silica and alumina content increase upon the calcination of the raw mineral, and this increase is accompanied with an increase in the amorphous content of the clay minerals [164]. These changes in the amorphous contents favor the alkali activation. Our characterization results are consistent

with these earlier findings. Table B.1 shows that the available silica, alumina, and magnesium content, which are obtained from XRF spectroscopy, increases with calcination (as expected by the removal of the water molecules trapped in the structure). Further drop in the surface area upon alkali activation is sourced from the formation of a denser structure with alkali activation.

Table 3.1. BET surface area, average pore size, and pore volume of samples.

Sample	Surface area (m ² /g)	Pore volume (cm ³ /g)	Pore size (Å)
As-received Sep	251.8	0.4	165.4
Calcined Sep	101.8	0.5	273.8
Sep-AAM	8.6	0.007	770.5

Morphological characteristics of the materials are shown in Figure 3.1. The as-received Sep consists mainly of crystal bundles together with particles that are aggregated by fibrous clusters as also stated previously in the literature [165, 166]. Calcination seems not to affect the morphology as the fibrous structure of Sep was not altered. With the effect of alkali activation, however, there is a substantial transformation. SEM image given in Figure 3.1c illustrates more homogeneous and continuous morphology upon alkali activation. The decrease in specific surface area detected by BET measurements (Table 3.1) are in line with this newly formed denser and less porous morphology. The EDX results indicate that the surface of Sep-AAM consists mainly of Si, Mg, Na, Ca, Al, and O atoms constituting the main framework (Figure B.1).

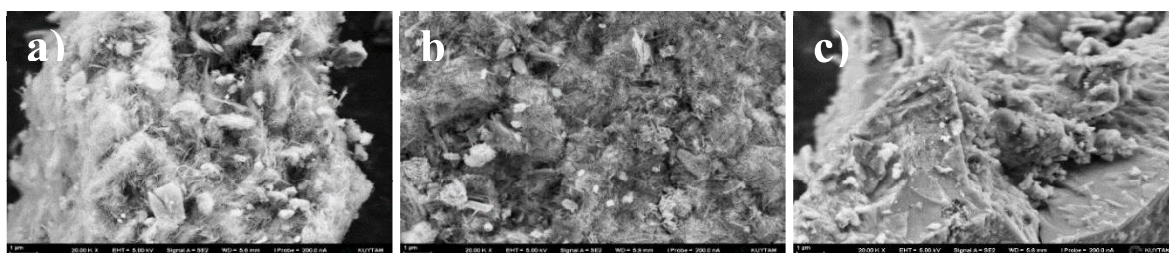


Figure 3.1. SEM images of materials at a magnification of 20 k \times : a) As-received Sep, b) Calcined Sep, and c) Sep-AAM.

Compositional factors, including the molarity and type of the alkali activator used, water amount, and additives have a determining effect on the surface properties of the geopolymers [167, 168]. From this respect, each AAM has its unique surface properties that not only depends on the origin raw material composition, but also on the alkali activator preference and the molarity of the alkali activator. As it is reported in the literature previously for FA-based geopolymers, obtaining geopolymers with small pore volumes and low surface area corresponds to a dense geopolymer matrix with low permeability, high durability and is an indication of a compact and denser structure [169].

During the alkali activation of a precursor several reactions occur. However, as well documented by Glukhovskiy et. al, this process can be summarized in three main stages involving, destruction-coagulation, coagulation-condensation, and condensation crystallization [4, 170]. The presence of higher degree of polycondensation during these series of reactions results a lower surface area of the final AAM [168]. With the hardening of the gel phase and as a result of a structural reorganization and densification during time, it is common for an AAM to form into a denser structure, as it is also the case for synthesized Sep-AAM in this chapter (Figure 3.1).

The decrease in surface area upon alkali activation observed in this part (Table 3.1) is in accordance with the previous findings of the study of Walczyk et. al [160], where Sep is treated with NaOH solution to form loughlinite and a major reduction in the surface area of Sep is detected upon alkali treatment. The decrease in the surface area observed in this part accompanied by a concomitant decrease in pore volume and a parallel increase in pore size values upon alkali activation have occurred. During the alkali activation, because of presence of high amounts of OH^- ions in the alkali activator, hydroxides might have precipitated to form the magnesium silicate framework with surface structural hydroxyl groups that are linked to Mg sites.

Figure 3.2 compares the XRD patterns of Sep, calcined Sep (750 °C, 1 h), and Sep-AAM over a 2θ range between 10 to 90°. Main crystalline phase detected for as-received Sep is found to be Sep and dolomite phases together with minor amount of quartz and main peaks of these crystalline phases were detected at 35, 31, and 27°, respectively. Calcination of the raw materials before alkali activation is a common procedure since thermal treatment

has a positive effect on the solubility of the aluminosilicate materials and [112] and magnesium silicate materials [77]. Data indicated that calcination of Sep caused some structural changes associated with the dehydroxylation and dehydration of the starting material. The peaks owing to dolomite and Sep, located at 31 and 35°, respectively, disappeared upon calcination and formed calcium aluminum silicate, calcium magnesium silicate, and periciase phases indicated by the formation of features at 28, 33, and 43°, respectively. The formation of periciase phase that is accompanied by the disappearance of dolomite phase is most possibly related with the release of CO₂ in the dolomite upon calcination [166].

As pointed out in the previous studies, AAMs display a featureless hump located in between 18° and 38° and centered at approximately 28°, which is an indication of the amorphous geopolymer formation [4, 38, 110]. During the alkali activation, complex multiphase series of reactions occur including dissolution, reorientation and solidification [171].

Obtaining less crystalline structure that is accompanied by the the formation of an amorphous phase upon alkali activation has previously been observed for high calcium FA-based, RM and MK-based geopolymers [25, 172]. As it is deduced from Figure 3.2, the XRD pattern of Sep-AAM has the characteristic feature of amorphous structure displayed by the hump located at 28° together with minor amounts of undissolved MgO phase. Upon alkali activation there is a profound decline in the amount of crystalline phases. Therefore, from a mechanistic perspective, a slight dissolution of calcium magnesium silicate existing in calcined Sep is an indication that this crystalline material partly takes place in alkali activation process. The decrease in the amount of crystal components (calcium magnesium silicate and periciase) in Sep-AAM sample demonstrates the dissolution of magnesium and silicate related phases within geopolymeric framework.

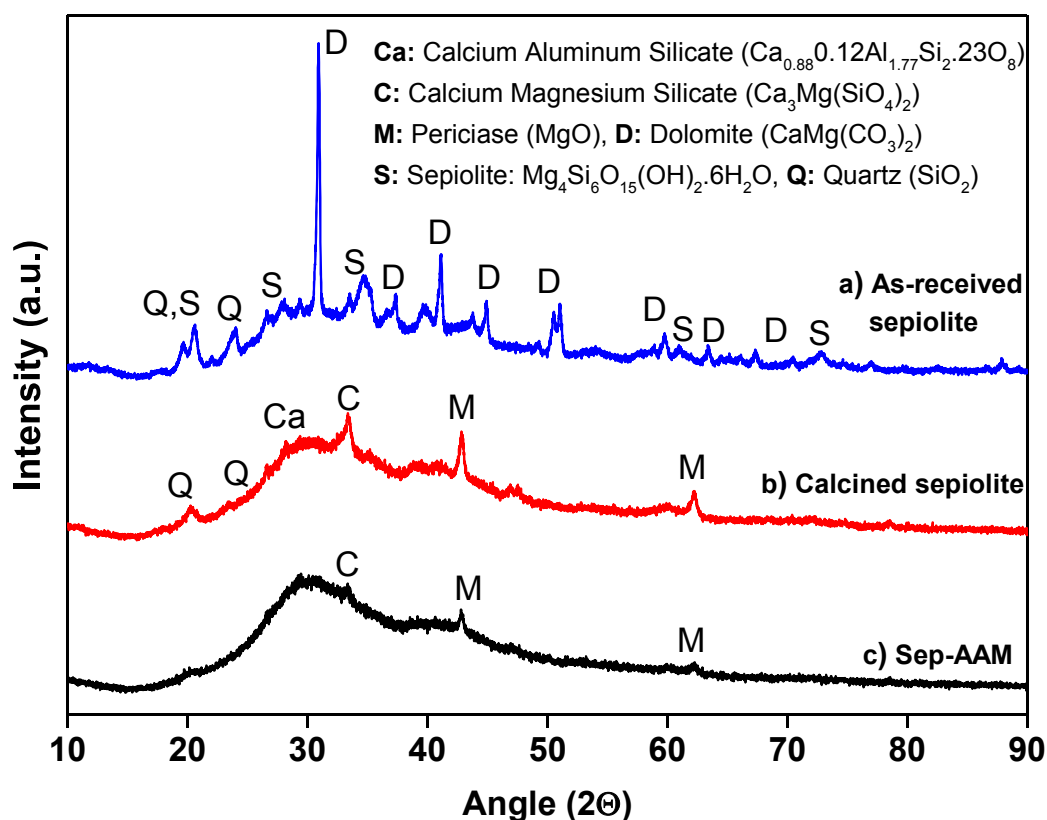


Figure 3.2. XRD patterns of a) as-received Sep, b) Sep calcined at 750 °C, and c) Sep-AAM.

Figure 3.3 demonstrates the FTIR spectra of Sep, calcined Sep, and Sep-AAM. FTIR spectrum of Sep displays features at 3632, 3557, 3380, and 3236 cm^{-1} , indicating the presence of water molecules. The band at $\sim 3632 \text{ cm}^{-1}$ is associated with the stretching vibrations of hydroxyl groups that are linked to octahedral Mg ions inside the Sep mineral. The feature observed at 3557 cm^{-1} is related to magnesium coordinated water, and the peaks at 3380, 3236 and 1656 cm^{-1} are attributed to vibrations of $-\text{OH}$ stretching and bending of water molecules in the channels [173, 174]. Two minor contributions positioned at 786 and 661 cm^{-1} are assigned to octahedrally coordinated $\text{Mg}-\text{OH}$ bending vibrations [173]. The feature located at 1458 cm^{-1} is associated with the stretching vibration of $\text{C}-\text{O}$ indicating the presence of carbonate groups [37] that are related to dolomite ($\text{CaMg}(\text{CO}_3)_2$) impurities. Furthermore, peak positioned at 879 cm^{-1} is also related to the deformation mode of carbonate impurities [160, 175]. Two major contributions located at 1021 and 974 cm^{-1} are assigned to out-of-plane stretching vibrations of $\text{Si}-\text{O}$ [160, 176]. The peak observed at ~ 443

cm^{-1} is due to the presence of Si–O–Mg bonds that are between the tetrahedral and the octahedral sheets of Sep mineral [173, 177].

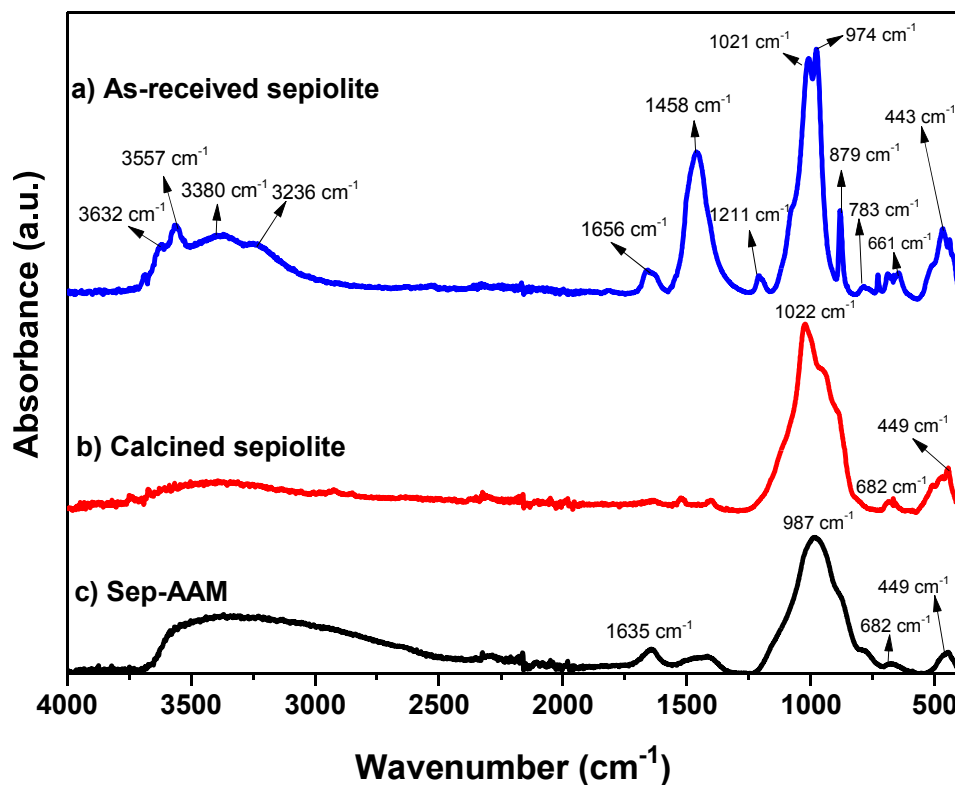


Figure 3.3. FTIR spectra of a) As-received Sep, b) Calcined Sep, and c) Sep-AAM.

Several changes were observed in these features upon calcination of Sep at 750 °C for 1 h. Data presented in Figure 3.3 indicated the disappearance of IR features associated with water molecules upon calcination. As stated previously, calcination temperature was chosen in this part as 750 °C, since it is known from the literature that coordinated and structural water loss from Sep mineral takes place at elevated temperatures [77, 150]. FTIR analysis results presented in Figure 3.3. are also in line with this information, as the disappearance of contributions regarding the magnesium coordinated water (3557 cm^{-1}), and –OH stretching and bending of water molecules in the channels (3380, 3236, and 1656 cm^{-1}) of Sep material, is observed upon calcination. The remaining major contributions located at 1022 and 449 cm^{-1} are related to the presence of Si–O–Si vibrations and Si–O–Mg bonds, respectively [173]. The shoulders observed at 950 and 876 cm^{-1} are contributed to asymmetric stretching vibrations of Si–O–Si and Si–OH bending vibrations, respectively [112]. Minor feature at

682 cm^{-1} is assigned to asymmetric stretching vibrations of Si–O–Si bonds [112]. After calcination, the peak at 1460 cm^{-1} , ascribed to carbonite impurities (dolomite), disappeared, consistent with XRD results (Figure 3.2) showing the dissolution of dolomite phase upon calcination.

The broad characteristic feature positioned between 900-1200 cm^{-1} indicates the presence of geopolymerization [38, 178] and is also found to be the main feature observed for alkali activated Sep in Figure 3.3c. This main feature points out the structural transformation showing the dissolution of calcined Sep as a consequence of alkali activation. The position of the main contribution of calcined Sep (1022 cm^{-1}) shifted to a lower wavenumber (987 cm^{-1}) upon alkali activation and is attributed to the formation of a tridimensional geopolymeric framework with silicon and magnesium tetrahedra. This feature corresponds to asymmetric stretching vibrations of Si–O–Si bonds [178]. The shoulder detected at 876 cm^{-1} contributed to Si–OH bending vibrations in calcined Sep is still present for Sep-AAM sample. The relatively weak band at 1635 cm^{-1} is related with the stretching (–OH) and bending (H–O–H) vibrations of bound water molecules [114, 160]. The intensity of the feature at 443 cm^{-1} observed in the spectra of both as-received Sep and its calcined counterpart decreases upon alkali activation. As stated earlier, this contribution is related to the Si–O–Mg bonds between the tetrahedral and the octahedral sheets and weakening in the intensity of this feature possibly indicates that more Mg ions become located in tetrahedral sites upon the alkali activation, as expected for a conventional geopolymer.

Formation of a denser structure upon alkali activation (Figure 3.1) resulted in satisfactory compressive strength values, showing the possible applicability of these materials also for construction purposes, where the adsorption capability brings in significant benefits. Four repetitive compressive strength measurements were conducted on the Sep-AAM specimens and the average value was determined as 39.8 ± 4.9 MPa. Here we note that the literature lacks any study reporting the compressive strength of an analogous Sep-based AAMs. The literature mostly focuses on the strength development of AAMs, which were produced from conventional raw materials, such as MK, FA, and granulated blast furnace slag [4, 38, 110, 179] and these studies indicate a typical compressive strength of 20-70 MPa for these AAMs. For instance, on a volcanic ash-based geopolymer, compressive

strength was reported to be almost 20 MPa [180]. The strength enhancement in these materials was found to be strongly correlated with the amount of aluminosilicate gel formation, which is also controlled by the molar Si/Al ratios [181]. During the synthesis of AAMs, the presence of impurities, such as calcium, iron, and titanium, in the raw material affects the formation of final product and its mechanical properties by adding reaction pathways to gel formation [4]. The use of non-conventional raw materials for the synthesis of AAMs, such as RM, which has a very high Fe_2O_3 content, and C-type FA, which has a very high CaO content, were found to result in compressive strength values of 1 MPa [80] and 23-32 MPa [182], respectively. Thus, it is inferred that a compressive strength in the order of 40 MPa of the Sep-AAM introduced here is very promising in terms of offering opportunities for practical usage of these materials as adsorbents.

Thermal stability is also crucial for determining the practical usability of these materials. Figure 3.4 compares the TG and DTG curves of Sep, calcined Sep, and Sep-AAM. Mass losses occurred during a temperature ramp from room temperature to 800 °C in flowing N_2 (60 ml/min) were determined as 28.1, 8.5, and 17.8 wt% for Sep, calcined Sep, and Sep-AAM, respectively. The as-received Sep exhibits five stages of thermal decomposition corresponding to mass losses of 9.16 wt% (between room temperature to 84 °C), 2.1 wt% (84-283 °C), 4.6 wt% (283-623 °C), 11.5 wt% (623-721 °C) and 0.7 wt% (721-800 °C). These losses were attributed to release of adsorbed water, release of structural water related to dehydration, dehydration of hydroxyls along the octahedral edge, release of water by dehydroxylation, such as dehydroxylation of Mg–OH groups, calcination of dolomite [150, 151, 159], respectively. The highest amount of mass loss detected in the region between 623 and 721 °C is thought to be related with the loss of water due to dehydroxylation of Sep phase. Water loss observed from 721 to 800 °C is ascribed to calcination of dolomite phase [151]. On the other hand, Sarı Yılmaz et. al reported that for Sep mineral, mass loss observed in the temperatures between 564-822 °C denotes both calcination of dolomite, and dehydroxylation of Sep [183]. For this reason, mass losses observed in temperatures between 623-800 °C in this chapter are thought to be sourced both from dehydroxylation of Sep phase and calcination of the dolomite phase.

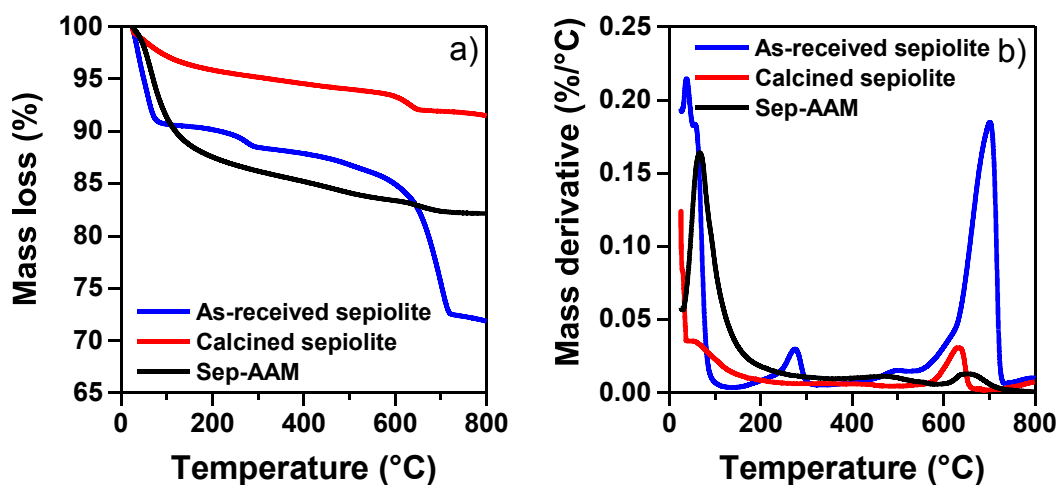


Figure 3.4. a) TG and b) DTG curves of as-received Sep, calcined Sep and Sep-AAM.

Dehydroxylation of Sep and calcination of dolomite phases conform with the findings from XRD analysis, where these two phases were found to be no longer exist in calcined Sep (Figure 3.2b). Calcined Sep was found to be more thermally stable as expected and only 8.5 wt% of mass loss was observed. Vast majority of the mass loss in calcined Sep (6.3 wt%) was observed from room temperature to 560 °C, attributed to loss of water due to dehydration of hydroxyls. Mass loss detected for Sep-AAM mostly occurs up to 150 °C, approximately 11.2 wt%, in this region occurs as a result of release of adsorbed water. Further mass loss detected in the region between 150 and 600 °C is associated with the release of chemically bounded water from Si–OH and/or Al–OH groups [184].

3.3.2. Surface Characteristics

Aiming at understanding the changes in the surface composition of elements in Sep, calcined Sep, and Sep-AAM, we performed XPS analysis. XP spectrum of Sep-AAM, given in Figure B.2, shows that the surface composes mainly of O, Si, Mg, Al, Ca, and Na elements. Results indicated the changes in surface composition upon the alkali activation of calcined Sep. Deconvoluted O 1s, Mg 2p, and Mg 1s together with Si 2p spectra of the samples and related peak positions are provided in Figure B3 and Tables B.4-B.6.

Deconvolution of O 1s spectra showed that intensity of the contribution detected at ~532 eV, which is related with the surface hydroxyl groups [160, 185], decreased upon

calcination (Figure B.3b&f) for Sep. This situation is associated with the release of surface hydroxyl groups in Sep with calcination [173]. Concomitantly, a slight decrease in intensity was also observed on the feature located at 534 eV upon the calcination of Sep. This decrease is related with the evaporation of water molecules [186]. Strong peak detected at approximately 531 eV for all of the samples is correlated with the O 1s in Si–O–Si environment [187]. Upon alkali activation the amount of contribution detected at 531–532 eV increased. This increase is associated with the expected formation of surface hydroxyl groups on the surface of the AAM which is due to the presence of structural hydroxyl groups that are linked to Mg sites [187] and OH⁻ groups on the surface [185]. Band observed at approximately 530 eV in the calcined Sep and Sep-AAM is related with the presence of Si–O oxygens [160]. Peak at 536 eV detected for Sep-AAM sample indicates the presence of water in vapor phase [188]. Corresponding peak positions of O 1s spectra are provided in Table B.4.

Si 2p spectra of Sep and calcined Sep display two main characteristics located at approximately 102.1 and 102.8 eV for Sep, and 102.4 and 103 eV for calcined Sep (Table B.5, Figure B.3a&e) corresponding to Si bonding in Si–O–Mg and Si–O–Si environments [187]. Upon alkali activation there is a slight shift to lower binding energies. Two contributions located at 101.8 and 102.8 eV for Sep-AAM also correspond to tetrahedral Si bonding in Si–O–Al [160, 189] and amorphous SiO_x derivatives, respectively [190], showing the possible existence of Si atoms in different environments.

Two main contributions positioned at 1303 and 1304 eV in the Mg 1s spectra for Sep and calcined Sep are related with the Mg–O and Mg–O–Si bonds of Sep clay, respectively [120]. Mg 2p spectra of samples given in Figure B.3c, Figure B.3g and Table B.6 display two main features that are located at 50 and 45 eV. Contribution at 50 eV corresponds to the presence of Mg–Al bonds [160].

As it can also be seen from Table B.6, there is a slight red shift in the order of almost 1 eV in binding energies of Mg 1s and Mg 2p spectra in Sep-AAM sample, this lowering in binding energy is most possibly related with the transition of octahedral Mg atoms into tetrahedral coordination upon alkali activation since low number of oxygen atoms are needed in tetrahedral Mg than it is for octahedrally coordinated Mg [191]. Furthermore, the

transformation of coordinated Mg atoms present in calcined Sep from octahedral to tetrahedral coordination occurs upon alkali activation and was previously verified by ^{25}Mg MAS NMR spectroscopy [77]. Zhuang et al. reported that the contribution observed at 532.1 eV in O 1s spectrum is also related with the presence of $[\text{SiO}_4]$ tetrahedra and $[\text{Mg}(\text{Al})\text{O}_6]$ octahedra [186]. In this perspective, the reduction in contribution at 532 eV upon alkali activation (Figure B.3j) indicates that the amount of octahedrally coordinated Mg sourced from calcined Sep decreases with alkali activation. Atomic % of Si, O, Mg, Ca, Al, and Na elements obtained from XPS fitting are shown in Table B.7.

3.3.3. MB Adsorption Tests

The pH of the medium, and thus, the zeta potential of the adsorbents, plays an important role in adsorption kinetics. Thus, the pH of the MB solutions at initial and equilibrium conditions was recorded. The pH of the 40 mg L^{-1} MB solution at the beginning of the adsorption test was recorded as 6.2. After 210 minutes of MB adsorption, pH values detected for calcined Sep and Sep-AAM were found to be 10.6 and 10 for calcined Sep and Sep-AAM, respectively. The change of zeta potential with pH are presented in Figure B.4. Results illustrate that both for calcined Sep and Sep-AAM zeta potential is negative for a wide range of pH values. The zeta potential evolution of calcined Sep with pH is found to be more stable for calcined Sep with a profound lowest zeta potential of -30.6 detected at a pH of 12. The zeta potential evolution of Sep-AAM decreased with an increase in pH and reached its lowest value of -39.6 when pH is equal to 12. Still, for all of the pH values measured, the zeta potential of Sep-AAM was found to be lower than calcined Sep. These results point out that the surface of Sep-AAM is more negatively charged than calcined Sep for the studied equilibrium pH values (10-10.6), suggesting superior adsorptive properties of Sep-AAM towards the adsorption of cationic MB molecules. Higher electrostatic attraction between cationic MB dye and negatively charged surface of Sep-AAM enhances the adsorption capability. It is known from the literature that the surface of AAMs is normally negatively charged due to the dissociation of various oxygen containing hydroxyl groups makes it an effective adsorbent for removing organic pollutants from wastewater [6, 192, 193]. Furthermore, silanol groups existing on the surface of AAMs induce a negative charge at basic medium enhancing the adsorption of cationic species [194]. Therefore, superior adsorption properties for Sep-AAM can be expected and are most possibly

associated with the existence of surface hydroxyl groups on Sep-AAM surface which is confirmed by a lower zeta potential value of Sep-AAM sample in Figure B.4. The effect of initial pH on adsorption performance of both calcined Sep, and Sep-AAM is investigated in detail in Section 3.3.3.4.

3.3.3.1. Effect of Contact Time, $C_0 = 20 \text{ mg L}^{-1}$

The effect of contact time needed to reach the adsorption-desorption equilibrium was determined for calcined Sep and Sep-AAM by setting the initial MB concentration to 20 mg L^{-1} and adsorbent amount to 10 mg . Typical patterns of the changes in C_t/C_0 ratio and uptake values with time are presented in Figure 3.5. For calcined Sep, after 60 minutes of adsorption experiment, C_t/C_0 and uptake values stabilized at 0.57 and 46 mg g^{-1} , respectively, and remained nearly constant until the end of the adsorption experiment. Even though the equilibrium time needed for calcined Sep (60 min) is less than it is for Sep-AAM, experimental results revealed that optimum time needed for both calcined Sep and Sep-AAM can be taken as 3.5 h (210 min) since further contact time does not cause any significant change in the adsorbed amount of MB dye for Sep-AAM. For Sep-AAM, C_t/C_0 and uptake values changed systematically with time and stabilized at 0.26 and 74.64 mg g^{-1} , respectively, after 210 minutes.

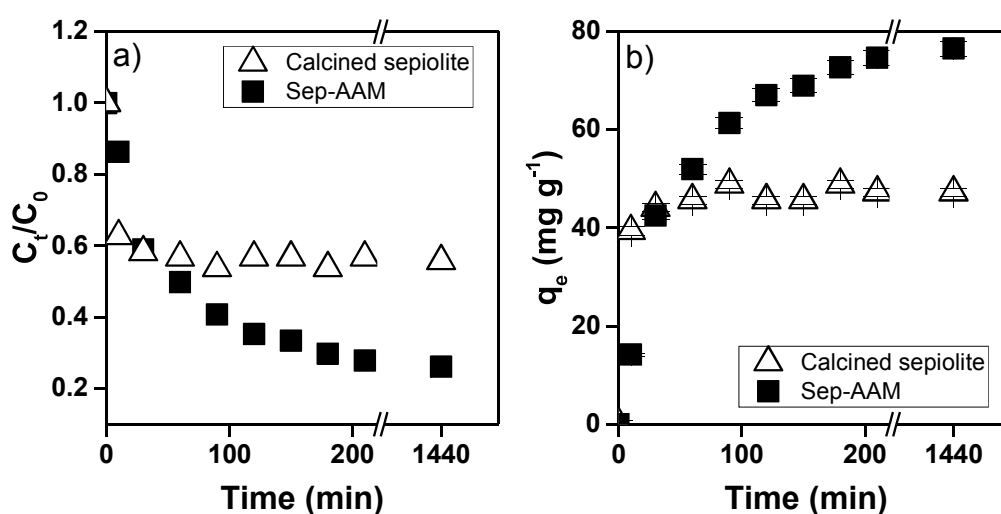


Figure 3.5. The effect of contact time on a) C_t/C_0 and b) Uptake of calcined Sep and Sep-AAM.

3.3.3.2. Effect of Initial MB Concentration

Figure 3.6 shows the uptake and removal capability of calcined Sep and Sep-AAM for different initial MB concentrations using 10 mg sample for each run. As it is seen from this figure, both for calcined Sep and Sep-AAM, uptake capacity increases with the increase in MB concentration. Within the studied highest concentration of 40 mg L^{-1} MB concentration, uptake values were 55.9 and 80.3 mg g^{-1} for calcined Sep and Sep-AAM, respectively. The effect of the increase in MB initial concentration is more evident for Sep-AAM than it is for calcined Sep. For instance, 8-fold increase in initial MB concentration caused a 3.5-fold enhancement in the uptake value for Sep-AAM, whereas this enhancement was found to be 2.5 for calcined Sep. Concomitantly, a decreasing trend was observed in the MB removal efficiency (%) upon increasing MB concentration. Since there are a higher number of active sites that are available for dye adsorption at lower concentrations, the interaction between adsorbate and adsorbent is promoted at low concentrations. With the increase in MB concentration, the active sites become more occupied with MB dye molecules blocking the further adsorption of MB, consistent with the existing literature for FA-based geopolymers and MK-based geopolymers [19].

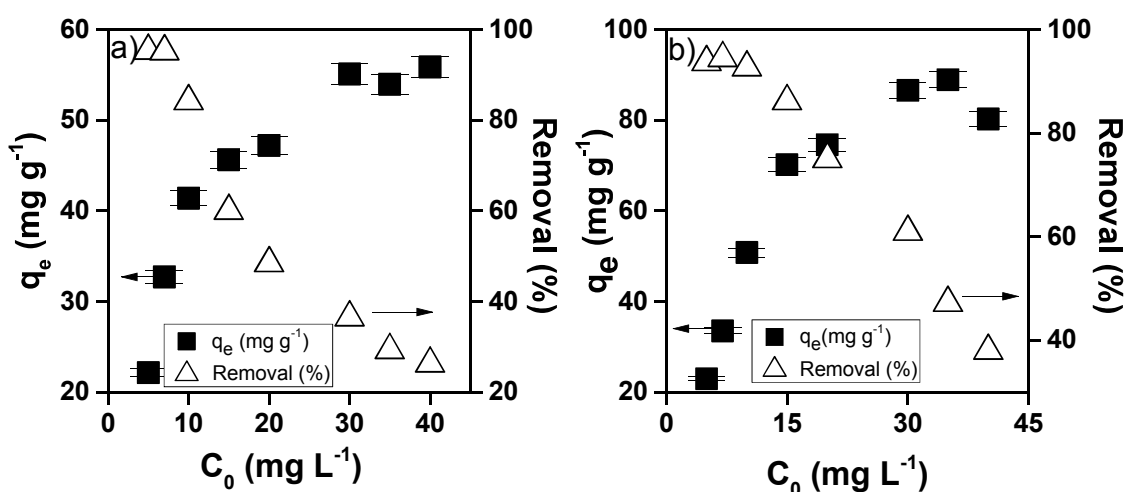


Figure 3.6. Effect of initial MB concentration on uptake (q_e) and removal (%) of MB for a) Calcined Sep, and b) Sep-AAM.

3.3.3.3. Effect of Adsorbent Amount on Adsorption of MB Dye

The effect of adsorbent amount on the adsorption properties was further investigated and results are given in Figure 3.7 together with the results showing the effect of both the adsorbent amount and temperature on Table B.8.

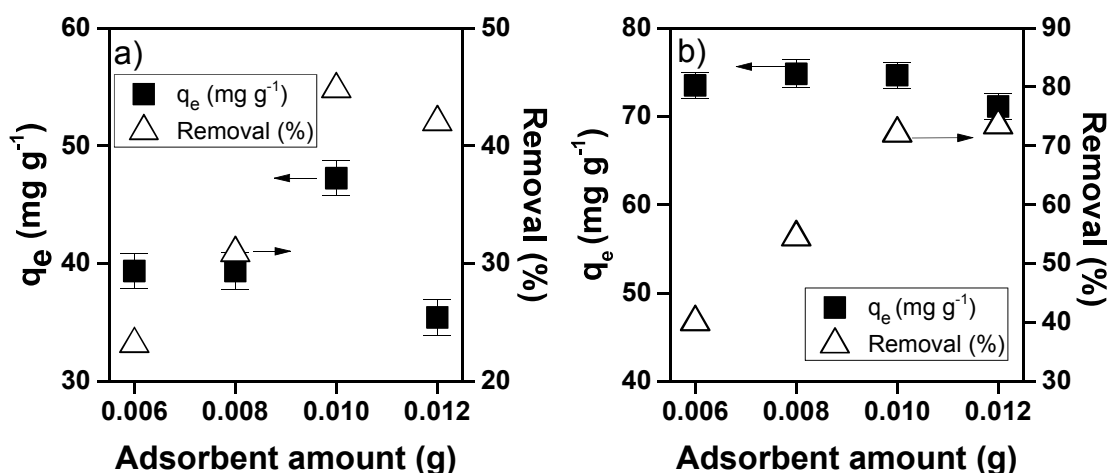


Figure 3.7. The effect of adsorbent amount on MB uptake and MB removal (%) by a) Calcined Sep, and b) Sep-AAM (*Contact time* = 3.5 h, $C_0 = 20 \text{ mg L}^{-1}$).

As it is seen from Figure 3.7, both for calcined Sep and Sep-AAM, uptake values and removal efficiency are influenced differently from the increase in adsorbent amount. This increase is more profound for the removal efficiency, whereas there is a non-monotonous trend in the uptake capacity. Both the uptake capacity and removal amount obtained by using Sep-AAM as an adsorbent are more profound than that are for calcined Sep, which is in line with the observations from previous section where the effect of the increase in MB initial concentration was found to be superior for Sep-AAM than it is for calcined Sep.

With the increase in adsorbent amount, the number of available adsorption sites also increases explaining the increase in removal efficiency. However, the uptake capacity of Sep-AAM seems to be directed towards to slightly lower values with an increase in adsorbent dosage (Figure 3.7b) which is possibly associated with the presence of unsaturated adsorption sites [195]. The very minor decrease in the uptake capacity with an increase in adsorbent amount was also previously reported for FA-based geopolymers [22, 196]. For

calcined Sep (Figure 3.7a), similar to Sep-AAM, removal efficiency increases with the adsorbent amount. Trend observed in the uptake capacity with adsorbent amount increase is non-monotonous and adsorption performance of calcined Sep for all of the adsorbent amounts was found to be lower than that of Sep-AAM.

3.3.3.4. Effect of pH on Adsorption of MB Dye

Another important parameter that has an effect on the adsorption efficiency is the pH of the effluent. To determine the influence of pH on the MB adsorption performance of both calcined Sep and Sep-AAM, adsorbents with definite amounts (10 mg) were mixed with 50 ml of MB dye solution (20 mg L^{-1}) at initial pH values of 2, 3, 4, 7, 8, and 9. The pH of the 20 mg L^{-1} MB solution at the beginning of the adsorption test was recorded as 7.0 without any interference, whereas to obtain different pH values, initial pH of the solutions was adjusted by using 0.1 M hydrochloric acid and sodium hydroxide solutions. pH values of these solutions were recorded by using a lab pH meter. Effect of initial pH on the adsorption performance was investigated at $31 \text{ }^\circ\text{C}$ and presented in Figure 3.8.

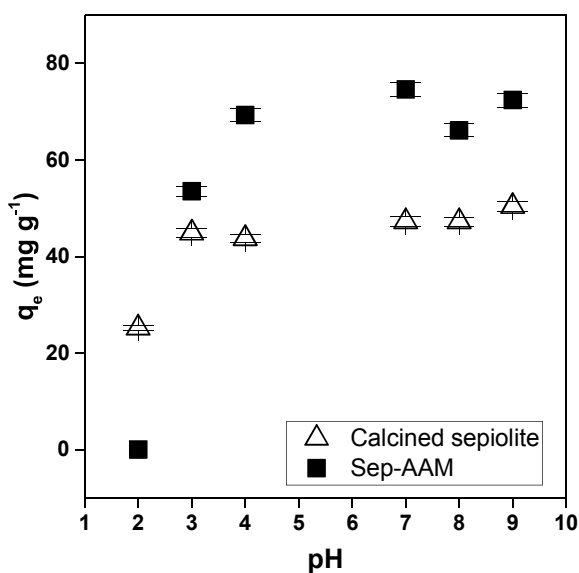


Figure 3.8. The effect of initial pH on MB uptake by calcined Sep and Sep-AAM (*Contact time* = 3.5 h, $T = 31 \text{ }^\circ\text{C}$, $C_0 = 20 \text{ mg L}^{-1}$).

The results presented in Figure 3.8. show that both for calcined Sep and Sep-AAM, increase in the initial pH values causes an increase in the MB adsorption capacity of the adsorbents. Even though calcined Sep and Sep-AAM display differences regarding adsorption capacities, they still show similar trends upon an increase of pH values. For both of these adsorbents, uptake values increase and becomes stable after an initial pH of 7. As investigated also in the previous sections, uptake capacity of Sep-AAM is superior to calcined Sep for a wide range of initial pH values (initial pH = 3-9), indicating that alkali activation enhances the MB adsorption performance, especially at alkaline conditions.

This enhancement in adsorption performance is related with the increased amount of negatively charged surface hydroxyls upon alkali activation, that can be arranged during the synthesis of an AAM by simply changing the alkali activator content. When pH of the solution medium is highly acidic (pH = 2), on the other hand, Sep-AAM does not show any adsorption performance and calcined Sep displays an adsorption capacity of 25.2 mg g⁻¹, most possibly related with the comparably high surface area of calcined Sep with respect to Sep-AAM. However, as evident from this figure, the effect of presence of high amounts of surface hydroxyls on Sep-AAM becomes dominant at higher initial pHs, which is correlated with the zeta potential profile of these adsorbents (Figure B.4). The highest uptake capacity is obtained at normal pH for Sep-AAM (74.64 mg g⁻¹). A higher adsorption at higher initial pH values is related with the presence of OH⁻ ions and these ions attract positively charged MB molecules, increasing the adsorption performance. At acidic conditions, on the other hand, the existence of protons hinders the attraction between the adsorbate and the adsorbent and therefore caused a decrease in the adsorption performance. This profile is in accordance with the current literature, showing that adsorption performance of cationic MB dye is favoured at basic pH values, and acidic pH of the solution medium has a negative effect on the adsorption performance [23, 197].

3.3.3.5. Effect of Temperature on Adsorption of MB Dye

To understand the effect of temperature on the adsorption behavior of MB dye onto calcined Sep, and Sep-AAM, experiments were conducted at 31, 40, and 50 °C for different initial MB concentrations. The data presented in Figure 3.9 verify that the adsorption capability of both of these adsorbents enhances with increasing temperature from 47.25 to

49.28 and to 62.99 mg g^{-1} for calcined Sep and from 74.64 to 79.07, and to 99.92 mg g^{-1} for Sep-AAM as the temperature increases from 31 to 40 $^{\circ}\text{C}$, and to 50 $^{\circ}\text{C}$, respectively, for an initial MB concentration of 20 mg L^{-1} . Adsorption capacity of calcined Sep for all of the studied temperature values were found be less than those obtained on Sep-AAM. The enhancement in adsorption capacity with temperature points out the endothermic nature of the adsorption process at these experimental conditions, as investigated further below. Increase in the chemical potential of MB dye molecules with temperature to permeate to the adsorbent surface [67, 144] is one of the possible reasons of the improvement obtained for both calcined Sep, and Sep-AAM adsorption capacity. According to the observations presented in Figure 3.7, the optimum adsorbent amount for this experimental set up is 10 mg. Therefore, similar adsorption tests for as-received Sep were also conducted at three different temperatures for as-received Sep and uptake performance of as-received Sep was detected as 31.5, 26.8, and 26.8 mg g^{-1} for temperatures 31, 40, and 50 $^{\circ}\text{C}$, respectively and details of these experiments are provided in Table B.9.

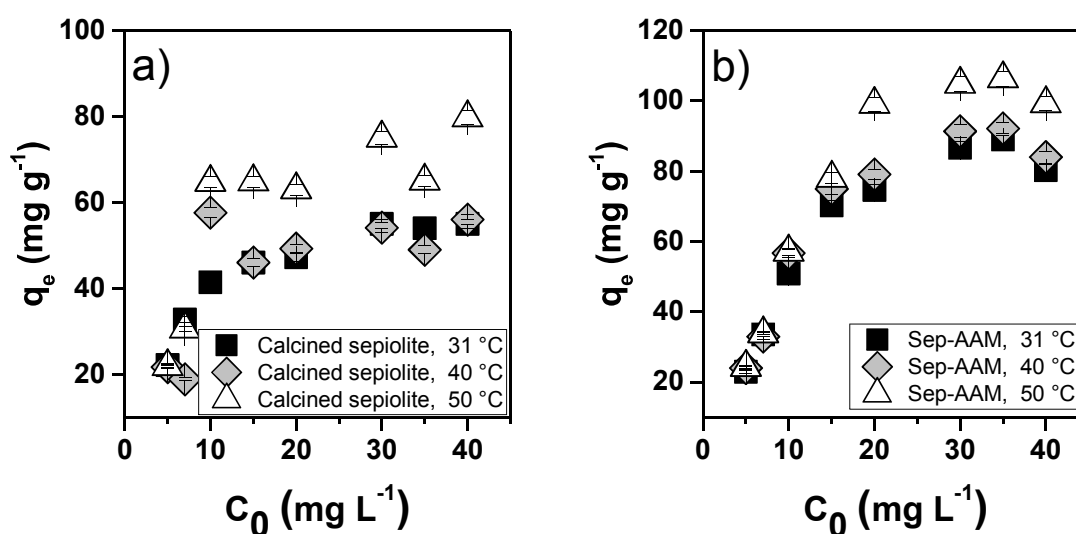


Figure 3.9. Effect of temperature on the equilibrium uptakes for MB on a) Calcined Sep, and b) Sep-AAM.

3.3.3.6. Adsorption Kinetics Modeling and Mechanism

Adsorption data were assessed by considering pseudo-first and pseudo-second-order kinetic models, as shown in Figure B.5, in Table 3.2 for Sep-AAM, and in Table B.10 for

comparison of the corresponding data of calcined Sep. As it is given in Figure B.5, Table 3.2, and Table B.10, the pseudo-second-order plot of the samples at different temperatures reflects linearity with high correlation coefficient values ($R^2 > 0.98$). High consistency between calculated and experimental values of q_e given in these tables also infers that adsorption mechanism for these samples are better described by the pseudo-second-order kinetics than the pseudo-first-order kinetics. Thus, we infer that the adsorption of MB dye on calcined Sep and Sep-AAM at different temperatures are in accordance with pseudo-second-order adsorption model and that the adsorption process is possibly dominated by chemical adsorption process, suggesting the presence of electron exchange and/or sharing between the adsorbate and the adsorbent [198, 199], especially for Sep-AAM. Table 3.2 shows that both the value of apparent pseudo-second-order rate constant and removal efficiency (%) of MB increases with temperature for Sep-AAM.

Table 3.2. Pseudo-first and pseudo-second-order kinetic model parameters and removal efficiency (%) for adsorption of MB onto Sep-AAM at different temperatures (*Contact time* = 3.5 h, $C_0 = 20 \text{ mg L}^{-1}$ and $m = 10 \text{ mg}$).

Adsorbent	$q_{e,exp}$ (mg g^{-1})	Pseudo-first-order adsorption kinetics ($C_0 = 20 \text{ mg L}^{-1}$)			Pseudo-second-order adsorption kinetics ($C_0 = 20 \text{ mg L}^{-1}$)			Removal (%)
		$k_{1,ads,app}$ (min^{-1})	$q_{e,cal}$ (mg g^{-1})	R^2	$k_{2,ads,app}$ ($\text{g mg}^{-1} \text{ min}^{-1}$)	$q_{e,cal}$ (mg g^{-1})	R^2	
Sep-AAM, 31 °C	74.64	1.87×10^{-2}	67.49	0.98	6.65×10^{-4}	78.74	0.98	72.11
Sep-AAM, 40 °C	79.07	1.61×10^{-2}	55.45	0.87	9.45×10^{-4}	80.01	0.98	75.20
Sep-AAM, 50 °C	99.92	1.30×10^{-2}	67.82	0.95	9.80×10^{-4}	96.15	0.99	81.25

As it is stated earlier, to evaluate the actual pseudo-second-order adsorption constant ($k_{2,ads}$), the dependence of the adsorption rate on the adsorbent amount should also be evaluated. Therefore, the adsorbent amount was varied and results are presented in Table B.8.

As it is also evident from Table B.8, for both Sep-AAM and calcined Sep, the increase in adsorbent amount causes a systematic increase in the apparent pseudo-second-order adsorption rate constant ($k_{2,ads,app}$). For this reason, by using the values from Table B.8, for Sep-AAM, the variation of $k_{2,ads,app}$ ($\text{g mg}^{-1} \text{ min}^{-1}$) with the adsorbent amount (g) is

investigated, as given in Figure 3.10. The data demonstrate a strong correlation with R^2 values greater than 0.95 for all three temperatures considered.

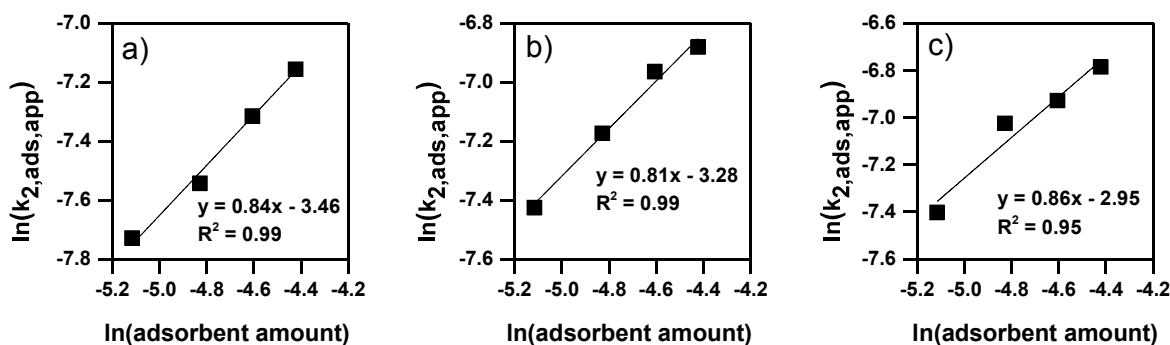


Figure 3.10. Experimental data fit to pseudo-second-order adsorption kinetics for Sep-AAM samples at a) 31 °C, b) 40 °C, and c) 50 °C.

Concordantly, the actual second-order adsorption rate constant ($k_{2,ads}$) (Please see Equation (1.8) for more information on its difference from its apparent counterpart, $k_{2,ads,app}$), and the adsorption rate order with respect to adsorbent amount for Sep-AAM was calculated. The slopes of the lines given in Figure 3.10 are the same at 0.84 ± 0.03 for all temperatures considered. Therefore, based on the slope and intercept values presented in Figure 3.10, the actual second-order adsorption rate constants ($k_{2,ads}$) for Sep-AAM were calculated and reported in Table 3.3 as follows:

Table 3.3. Actual second-order adsorption rate constants ($k_{2,ads}$) of Sep-AAM at different temperatures.

Temperature (°C)	$k_{2,ads} ((\text{g adsorbent})^{0.16} (\text{mg MB})^{-1} \text{min}^{-1})$
31	0.031
40	0.037
50	0.052

For comparison the corresponding data for calcined Sep are also provided in Figure B.6 and Table B.11. The slopes of the lines shown in Figure B.6 are 4.2 ± 0.75 for all temperatures considered and based on these values presented in Figure B.6, the actual

second-order adsorption rate constants ($k_{2,ads}$) for calcined Sep were evaluated and shown in Table B.11.

By using Arrhenius Equation (Equation (1.9)) and plotting $\ln(k_{2,ads})$ values that were collected from Table 3.3 and Table B.11, vs $1/T$ graph, the activation energy of the adsorption process of MB onto Sep-AAM and calcined Sep was calculated as 21.9 kJ/mol and 260.20 kJ/mol, respectively, and shown in Figure B.7.

As it was stated previously, to make a correct estimation about the rate limiting step and the time dependent diffusion mechanism, kinetic results extracted from the experimental data were further investigated by using intraparticle diffusion model. Intraparticle diffusion model for the adsorption of MB onto Sep-AAM at different temperatures together with parameters of intraparticle diffusion model are provided in Figure B.8 and Table B.12, respectively. Considering relatively lower correlation coefficients obtained for pseudo-first-order adsorption model and intraparticle diffusion model (Table 3.2 and Table B.12), the adsorption mechanism between Sep-AAM and MB dye was better defined by pseudo-second-order adsorption kinetics, where adsorption process is dominated by chemisorption [200]. The adsorption mechanism between calcined Sep and MB dye molecules was also better defined by pseudo-second-order adsorption kinetics (Table B.10). Chemisorption process involves a chemical reaction between the adsorbate and the adsorbent during the adsorption and involves the presence of interactions between the adsorbate and the adsorbent [201]. Our adsorbate, MB, is a cationic dye that is ionized in water to form a cationic portion and a chlorine portion [202]. Surface chemistry plays a major role for the determination of the specific adsorbent towards a pollutant removal [203]. Thus, it is claimed that the chemical attraction between the anionic surface hydroxyl groups present on Sep-AAM, which were also verified by XPS analysis and zeta potential measurements, and the cationic portion of MB molecule is mainly responsible for the high MB adsorption capacity. As stated earlier, XPS analysis indicated that Mg ions are located in tetrahedral sites upon the alkali activation. For the magnesium analogues of conventional AAMs, the negative charge on the tetrahedral magnesium is charge balanced by Na^+ cations. The presence of negative charge in geopolymeric network also creates an electrostatic interaction between the negatively charged AAM network and positively charged MB molecules, therefore also accounts for the enhanced adsorption capacity.

Even though Sep-AAM shows low surface area and low porosity, the existence of a denser structure and the presence of surface hydroxyl groups (evident from XPS and zeta potential analyses) makes this material a very suitable adsorbent for MB dye and this material also displays high mechanical strength, making it a possible candidate for practical applications. XPS results showed that contribution observed at 531-532 eV in O1s spectra increases (Figure B.3) that is related with the formation of negatively charged surface hydroxyl groups that are linked to Mg sites [187] and OH⁻ groups on the surface [185]. These negatively charged hydroxyl groups present on the surface are responsible to make an ion exchange when there are cations present in the medium [204]. Therefore, negatively charged surface of these materials offer a suitable medium for electron exchange or sharing between the cationic adsorbate MB.

3.3.4. Adsorbent Regeneration

Regeneration of the spent adsorbents is important both for the economics and the sustainability of the adsorption process. Before conducting regeneration experiments, dye fixation capability of both calcined Sep and Sep-AAM were determined by immersing them into distilled water. MB desorption from calcined Sep and Sep-AAM were found to be 4.02 % and 6.72 %, respectively, offering a rather strong fixation capability of these adsorbents upon cationic MB dye prohibiting the leaching in water. From this point of view, desorption can possibly be conducted more effectively by using several other solutions that have a higher capacity of solving MB dye, such as 2-propanol, ethanol, and acetone [202], or by using acidic solutions [192]. The possibility of leaching was also checked by analyzing the used solution by ICP-MS. The data presented in Table B.13 indicate that the leaching is almost negligible, with the amounts of leached elements associated with the adsorbent, remaining in trace amounts (<4 ppm). Among different regeneration techniques, thermal regeneration is a cost-effective method that is extensively used and in wastewater treatment plants [205] and widely preferred for the regeneration of AAMs in the literature [22], [80]. Thus, we performed the regeneration by calcination at 400 °C in static air for 2 h in between the consecutive adsorption runs. Consecutive thermal regeneration experiment results for calcined Sep are shown in Figure B.9. Results demonstrated that regeneration via thermal treatment increased the adsorption capacity of calcined Sep and regeneration can be conducted for four consecutive runs. The increase in uptake capacity after a calcination

process had previously been reported also for different clay minerals based adsorbents [206], [207], and the increase in adsorption performance after calcination was ascribed to the removal of non-claymatter and the formation of anionic sites for binding MB cations [207]. MB removal efficiency (%) and uptake values for powderized Sep-AAM sample detected during the regeneration experiments are presented in Figure B.10. As it is seen from Figure B.10, there is a decrease in the MB uptake and removal efficiency values up to four cycles. The drop in performance within regeneration experiments can be related with the loss of adsorbent which is known to be one of the drawbacks of using powder formed adsorbents. The decrease in the amount of the adsorbent during regeneration causes an alteration in the adsorption kinetics and possibly responsible for the reduction in adsorption performance. Furthermore, as it was deduced from TGA results (Figure 3.4), Sep-AAM sample loses about 15 % of its own mass when temperature rises to 400 °C that is associated with the release of adsorbed and structural water. Another possible reason for the decrease in adsorption performance within regeneration experiments is related with the pH of the medium. The pH value of the MB solution at the end of the first adsorption experiment was recorded as 10 after 3.5 h of adsorption. This value dropped to 6.5 at the end of the last regeneration run, which is related with the decrease of the amount of alkalis in the solution medium. This situation causes a reduction in the attraction between cationic MB dye and negatively charged surface of Sep-AAM sample.

Figure B.11 shows the FTIR patterns of MB, powderized Sep-AAM before and after MB adsorption and thermally regenerated form of Sep-AAM. The FTIR spectrum of MB consists of distinct peaks located at 3342, 1592, 1464, 1379, 1322, 1145, and 876 cm^{-1} which correspond to bonded -OH groups, stretching vibrations of C=N and C=C groups, CH₂ deformation vibration, C-N bonds, C-S bonds, and wagging vibration of C-H in aromatic ring, respectively [208]. Peaks located at 1635 and 987 cm^{-1} for Sep-AAM before adsorption shifted to 1600 and 1005 cm^{-1} , respectively (Figure B.11), upon MB adsorption indicating that C=O and C-O groups and nitrogen containing groups participate in the adsorption process [143], [208]. Newly occurred peaks at 1400 cm^{-1} for MB adsorbed Sep-AAM indicate that -CH₃ and nitro groups of MB causes an interaction between MB and surface of the adsorbent [143]. It is known that the pH of the medium has an effect on the dissociation of functional groups and the surface charge of the adsorbent and the adsorbate [209]. For the system in this chapter, high pH values sourcing from the alkaline nature of the AAMs

increases the electrostatic interactions between functional groups of MB dye and Sep-AAM. Therefore, dissociation of functional groups on the surface at studied high pH values (pH = ~10) designated the interactions between the surface of the adsorbent and the adsorbate [210] causing a dissociative chemisorption mechanism as also supported by pseudo-second-order adsorption kinetics (Table 3.2).

However, considering the inevitable loss of the adsorbent during the regeneration which possibly altered the adsorption mechanism, regeneration experiments were further conducted by utilizing monolith form of the same Sep-AAM specimen. To establish a similar environment enabling a fair comparison between the powdered and monolith form of Sep-AAM, same MB amount per amount of adsorbent is used as a starting point of the regeneration test for monolith versions of Sep-AAM. The variation in the uptake performance within regeneration experiments reported in terms of percentage are presented in Figure B.12 for monolith Sep-AAM samples. Data showed that the performance was the same within 5%, for four cycles of regeneration tests. Obtaining a higher uptake stability during regeneration with monolith samples is thought to be mainly associated with the conservation of the adsorbent mass. Another parameter contributing to stability is about the surface area. Monolith samples have a lower surface area that is in interaction with MB solution than it is for powderized samples, therefore the pH of the solution is less affected by AAMs presence. After four cycles of regeneration, the pH value of the MB solution was recorded as 7.05, which is a slightly higher pH value than that is obtained for powder counterpart of the same sample obtained (6.55) at the end of fourth regeneration.

3.3.5. Adsorption Isotherm Model Studies and Thermodynamical Properties

For the sample with the highest adsorption capability, Sep-AAM, and for calcined Sep, data obtained at three different temperatures were fitted using Freundlich and Langmuir models. Freundlich and Langmuir parameters for adsorption of MB dye onto Sep-AAM and calcined Sep are shown in Table 3.4 and Table B.14, respectively. The R^2 values presented in these tables were found to be greater than 0.98 for all of the samples for Langmuir isotherm, whereas R^2 values were between 0.68 and 0.89 for Freundlich isotherm model. Langmuir model demonstrating a better fit for these two adsorbents with higher correlation coefficients offers a monolayer adsorption and the homogeneity of the surface in terms of

functional groups. Comparatively very high q_{max} values detected for Sep-AAM indicates that alkali activation of calcined Sep is an effective method that enhances the adsorption performance and surface of this novel material is homogeneous in terms of functional groups. This situation points out that, in theory, Sep-AAM has a finite adsorption capability upon MB dye and when a MB molecule occupies a site on the surface of Sep-AAM, this site becomes unavailable for adsorption [67]. The results obtained here for the Sep-AAM are in line with the previous findings, where MK-based counterparts of Sep-AAMs were found to display a better fit to Langmuir isotherm and pseudo-second-order adsorption kinetics for MB adsorption [23]. Similar results were also obtained for FA-based geopolymers upon MB adsorption [6]. The value of the Langmuir separation factor (Table B.15) R_L , calculated by using Equation (1.12), is found to be between 0 and 1 implying favourable adsorption within the studied experimental conditions.

Table 3.4. Langmuir and Freundlich isotherm constants for MB adsorption on Sep-AAM at different temperatures.

Adsorbents	Langmuir Model			Freundlich Model		
	K_L (L mg ⁻¹)	q_{max} (mg g ⁻¹)	R^2	K_F (mg g ⁻¹)	n (g L ⁻¹)	R^2
Sep-AAM, 31 °C	1.90	86.21	0.99	43.59	3.95	0.83
Sep-AAM, 40 °C	2.33	89.29	0.99	47.99	4.25	0.72
Sep-AAM, 50 °C	3.07	103.31	0.99	55.56	3.93	0.72

Next, a thermodynamics study by replacing the adsorption equilibrium constant (K_{ads}) in Equation (3.2) with the multiplication of Langmuir equilibrium constant (K_L) and molecular weight of the adsorbate (Equation (3.3)) was conducted. Van't Hoff plot of $\ln(K_{ads})$ vs $1/T$ was found to be linear (Figure B.13) and the increase in K_{ads} value with temperature increase was observed (Table 3.5 for Sep-AAM and Table B.16 for calcined Sep) as expected from an endothermic process. The endothermic behaviour of the adsorption process can also be seen from Figure 3.9. ΔH° value was found to be 8.68 and 20.6 kJ/mol, for calcined Sep and Sep-AAM, respectively and other thermodynamic parameters calculated from Van't Hoff plot are presented in Table 3.5 and Table B.16.

Negative ΔG° values indicate that adsorption onto calcined Sep and Sep-AAM is spontaneous. The results obtained in this part, shown in Table 3.5 indicate that ΔG° increases slightly with temperature and become more negative than -20 kJ/mol (-33.6 kJ/mol for 31 °C, -35.2 for 40 °C and -37.0 for 50 °C for Sep-AAM), implying that the interaction between Sep-AAM surface and MB possibly involves weak chemical bonding, consistent with our interpretation presented above [67].

For Sep-AAM, ΔS° was calculated as 178.44 J/mol.K from the Van't Hoff plot (Figure B.13b and Table 3.5). The positive value of ΔS° indicates the affinity between MB dye molecules and Sep-AAM demonstrating the randomness at solid-liquid interface, stability and irreversibility during adsorption [67, 211]. ΔS° being greater than zero shows that number of degrees of freedom of adsorbed species is higher than it is for before adsorption. This situation shows that chemical adsorption takes place for MB molecule and Sep-AAM system causing a positive entropy change and endothermicity throughout adsorption [212]. The electron share and/or loss between the cationic portion of MB and negatively charged surface hydroxyl groups on the surface of Sep-AAM during adsorption is found to be main reasons for chemisorption together with dissociative adsorption in this system, as confirmed by FTIR analysis (Figure B.11). Calculated ΔH° value for calcined Sep is lower than it is for Sep-AAM. Even though adsorption kinetic results for calcined Sep better suited to pseudo-second-order adsorption model (Table B.10), which possibly indicates chemisorption mechanism takes place, this comparatively small enthalpy value for calcined Sep implies that physisorption mechanism dominates with minor contribution of chemisorption mechanism.

Table 3.5. Thermodynamic parameters for adsorption of MB onto Sep-AAM for 31, 40, and 50 °C.

Sample	T (°C)	Thermodynamic parameters				
		K_L (L/mg)	K_{ads} (L/mol) x 10 ⁴	ΔG° (kJ/mol)	ΔH° (kJ/mol)	ΔS° (J/mol.K)
Sep-AAM	31	1.90	60.80	-33.63	20.61	178.44
	40	2.33	74.53	-35.24		
	50	3.07	98.19	-37.02		

The comparison of maximum adsorption capacity of various AAMs towards MB dye removal is given in Table 3.6.

Table 3.6. MB adsorption capacity of various AAMs.

Adsorbent	Form of the adsorbent	T (°C)	q_e (mg g ⁻¹)	Compressive strength (MPa)	Ref.
Biomass FA-geopolymer	Cylindrical monolith	RT	15.4	8	[19]
Modified bauxite residue-based porous inorganic polymer	Cylindrical monolith	25	17	1	[80]
MK-based geopolymer	Powder	40	39.2	-	[18]
Foamed coal FA geopolymer	Cubic monolith	25	50.7	0.55	[196]
MK-based geopolymer with Cu ₂ O/TiO ₂ content	Powder	RT	19.7	-	[109]
Graphene oxide added kaolin based geopolymer	Powder	RT	4.7	-	[213]
Potassium activated FA based geopolymer	Cubic monolith	RT	84	1.7	[63]
Phosphoric acid activated MK-based geopolymer	Powder	28	3.35	-	[23]
MK-based geopolymer with expanded glass aggregates	Monolith	RT	4.9	1.6	[21]
MK-based geopolymer spheres	Sphere	RT	0.9	3.3	[17]
MK -based ice-templated geopolymer beads	Bead	RT	5	5.9	[214]
Geopolymer prepared from Jordanian kaolin and zeolitic tuff filler	Powder	RT	22.4	21	[147]
Sep-AAM	Powder	31	74.64	40 (measured in monolith form)	<i>This thesis</i>
Sep-AAM	Powder	40	79.07	-	<i>This thesis</i>
Sep-AAM	Powder	50	99.92	-	<i>This thesis</i>

*RT: Room temperature.

This comparison indicates that the equilibrium experimental uptake values reported in this part for three different temperatures are higher than that of most of the AAMs in the

literature used for the purpose of MB adsorption. Table 3.6 further shows that even though AAMs used for adsorptive purposes synthesized from different raw materials were widely studied with focus mainly on their performance upon dye removal, their mechanical performance still needs improvement. Sep-AAM synthesized in this part provides a satisfactory option in terms of both adsorptive and mechanical performance. Superior adsorption properties of Sep-AAM is sourced from the presence of high amount of surface hydroxyl groups on the surface of this novel material as confirmed by zeta potential measurements.

Mechanical strength measurements suggested that these materials also offer a high compressive strength values making these materials a perfect promising candidate for further practical water remediation applications. Newly introduced adsorbent Sep-AAM in this part sets a benchmark value in terms of both adsorptive and mechanical properties and assures the successful utilization of alkali activated materials for adsorption related applications.

3.4. Concluding Remarks

In this part of this thesis, calcined Sep without any additives has been used as a raw material for the first time for the synthesis of Sep-AAM to be employed for MB adsorption. It is evaluated as an adsorbent for MB removal and its adsorption properties were compared with calcined Sep. The influence of alkali activation in terms of MB adsorption and also on the corresponding microstructural properties and mechanical performance were investigated. Adsorption results revealed that Sep-AAM exhibits significantly higher adsorption capacity upon MB dye than calcined Sep itself, which was mainly related with the more negatively charged surface of Sep-AAM as confirmed by zeta potential measurements. The adsorption process was found to follow pseudo-second-order adsorption kinetics and Langmuir isotherm model demonstrated a better fit altogether revealing the dominant effect of chemisorption during the adsorption process. Calculation of thermodynamical parameters showed that the adsorption of MB onto Sep-AAM is a slightly endothermic process and the interaction between Sep-AAM surface and MB is due to weak chemical bonding. Adsorptive properties of Sep-AAM was found to enhance with temperature increase. Pseudo-second-order adsorption rate constant with respect to adsorbent dosage and activation energy of the adsorption of MB onto Sep-AAM were also

calculated. Regeneration results revealed that Sep-AAM can be regenerated up to four cycles for both in powder and monolith forms with monolith forms showing higher regeneration capability. Data revealed that Sep-AAM are sustainable and innovative options as adsorbents for MB removal with an MB uptake value of 74.64 mg g^{-1} in 3.5 hours that is further enhanced to 99.92 mg g^{-1} with an increase in temperature to $50 \text{ }^{\circ}\text{C}$ due to endothermic nature of the adsorption process. The remarkable compressive strength value of 40 MPa shows that these materials may have a wide application area in the construction industry.

4. SEPIOLITE- AND METAKAOLIN-BASED ALKALI ACTIVATED MONOLITHS FOR METHYLENE BLUE REMOVAL: A COMPARATIVE STUDY

4.1. Introduction

Existing literature on alkali activated materials (AAMs) for adsorptive purposes utilize powder formed AAMs. However, for many practical applications monolith formed adsorbents with sufficient mechanical strength can offer opportunities such as ease of regeneration, suitability for applications in water storage and water purification, and in packed bed reactors. Monolithic AAMs have been utilized for MB dye removal [19, 21], cesium removal from a nuclear waste [215], as a thermal insulator [216], and also in heat exchangers [217]. Some recent studies focused on monolith formed AAMs [63, 215] showed that adsorption performance of these materials can be enhanced by inducing porosity via several pore foaming agents including hydrogen peroxide (H_2O_2) [19, 63, 215, 216, 218], aluminum powder [80], sodium dodecyl [22], and glass aggregates [21]. One of the best well-known and studied blowing agents is H_2O_2 . Hydrogen peroxide is thermodynamically unstable in alkaline environment and can easily decompose into water and oxygen. As a result of this reaction and due to oxygen formation, there occurs an increase in the volume of the materials causing an increase in the macropores [218]. However, most of these foamy and monolith formed AAMs display lower levels of mechanical strength compared to their counterparts with no pore foaming agent content. Even though adding a foaming material increases the adsorption ability of these materials, they have lower mechanical performance, limiting their utilization in practical applications.

A recent study showed that, magnesium silicate rich sepiolite (Sep) mineral; an uncommon raw material for AAM synthesis, can successively be used as a powder formed adsorbent for MB dye adsorption with high adsorption performance and Sep-based AAMs (Sep-AAM) in monolith form display high mechanical performance [97]. The adsorption performance of Sep-AAM's in monolith form, on the other hand, has not been investigated yet. Furthermore, it has been shown that inclusion of foaming agents in classical geopolymer

systems could modify porosity and adsorption characteristics of solid adsorbents [19, 219]. From this point forth, this part of this thesis aims to investigate the adsorption performance of cubic monolith formed Sep-AAMs with different porosity levels obtained by varying H₂O₂ content between 0 and 8 wt%. Metakaolin (MK) counterparts of Sep-AAMs, MK-based geopolymers (MKGP), were also produced to represent traditional aluminosilicate geopolymer systems for comparing adsorption characteristics. Mechanical performance of these materials are investigated and structure-performance relationships are presented. The effect of raw material selection and porosity of AAMs on MB adsorption performance are investigated. Hydrogen peroxide was used as a foaming agent. Adsorption kinetics of monolith formed adsorbents synthesized based on Sep and MK is also investigated to establish an understanding on the adsorption mechanism. The manuscript form of this chapter is being prepared to be submitted for publication.

4.2. Experimental Methods

4.2.1. Materials

Raw materials that are used for AAM synthesis in this study are Sep and MK. Sep is utilized as a magnesium silicate source, whereas MK is evaluated as an aluminosilicate source. Sep mineral was kindly supplied by Dolsan Mining, Eskişehir-Turkey. Calcination procedure was conducted before the alkali activation process since calcination is known to have a positive effect on solubility of aluminosilicate raw materials [112] and magnesium silicate raw materials [77]. Calcined Sep was obtained by calcining Sep mineral at 750 °C for one hour before utilizing in alkali activation (2.8 g/cm³). MK, on the other hand, was obtained by the calcination of kaolinite mineral at 700 °C for 1 h (2.5 g/cm³). Sodium silicate (Na₂Si₃O₇) solution (28 wt% of SiO₂, 9 wt% of Na₂O, 63 wt% of H₂O, Merck, 1.35 g/cm³) and sodium hydroxide pellets (NaOH, Merck, 2.13 g/cm³) was used together as an alkali activator. H₂O₂ solution (30%, Merck, 1.11 g/cm³) was used as a blowing agent. MB hydrate (Sigma-Aldrich, purity > 97%, molecular weight 319.85 g/mol) was used as a model adsorbate. Chemical compositions of calcined Sep and MK are provided in Table C.1 (in the Appendix C).

4.2.2. Synthesis of AAMs

Tables C.2 and C.3 show the amounts of raw materials (in g) utilized during the synthesis of Sep-AAMs and MKGPs, respectively, together with molar Si/Mg, Na/Mg ratios of Sep-AAMs and molar Si/Al and Na/Al ratios of MKGPs with different H₂O₂ contents. These molar ratios belong to initial gel compositions of the synthesized material. Na/Mg ratio of Sep-AAMs and Na/Al ratio of MKGPs were kept constant at 1.2. Molar Si/Mg ratio of Sep-AAMs and molar Si/Al ratios of MKGPs, on the other hand, were kept constant at values of 3 and 2, respectively, as previous mechanical performance results revealed that highest compressive strength values are obtained within these ratios [38, 97]. To arrange these molar ratios in initial gel compositions, chemical compositions of raw materials shown in Table C.1 was employed and required amount of NaOH and Na₂Si₃O₇ solution was adjusted simply by calculating the amount needed to provide desired ratios. As stated previously, Sep was used as a magnesium silicate source and MK was used as an aluminosilicate source in this study. Na₂Si₃O₇ solution and sodium hydroxide pellets were used as alkali activators. For the synthesis of Sep-AAMs, powdered and sieved (#70 mesh sieve, 200 μm) calcined Sep was mixed thoroughly with alkali activators. Previously determined amounts of H₂O₂ solution were added to the alkali activator solution prior to mixing to ensure different levels of porosity. After mixing solid raw materials with H₂O₂ added alkali activator solutions, samples were transferred into 10 mm × 10 mm × 10 mm silicon molds and kept at 40 °C for 24 h followed by aging at room temperature for a week before being used as adsorbents for MB adsorption. Identical procedure was followed for the synthesis of MKGPs, however, unlike Sep-AAMs, thermal treatment was conducted at 60 °C, that is chosen based on our preliminary experimental results, for 24 h which is followed by aging at room temperature for a week. Details of the mixture composition of Sep-AAMs and MKGPs are displayed in Table C.2 and C.3, respectively. Based on the H₂O₂ amounts and weight % given in these tables, H₂O₂ content in synthesized samples are 0, 0.5, 1, 2, 3, 6, and 8 wt% for Sep-AAMs and 0, 0.5, and 1 wt% for MKGPs. These H₂O₂ amounts in AAMs are adjusted to ensure the integrity of the synthesized material at the end of thermal treatment procedure. Displaying a certain level of integrity and therefore having a comparable mechanical performance are important parameters that directly affect the practical usability of these materials. Further addition of H₂O₂ caused a loss of the integrity of the samples so that mechanical performance tests could not be applied.

4.2.3. Materials Characterization

Elemental composition of raw materials and AAMs were carried out XRF spectrometer. XRD patterns of all the samples were conducted by a Bruker D8 Discover Diffraction system with a Cu $K\alpha_1$ radiation source employing a wavelength of 1.5418 Å. FTIR spectroscopy was conducted by a Bruker Alpha II with ATR cell, in absorption mode and at a resolution of 2 cm^{-1} in a spectral region of 400-2000 cm^{-1} .

To determine BET surface area, pore size, and pore volume values of the samples a Micromeritics ASAP 2020–Physisorption Analyzer was utilized. Approximately Pore size distribution of the samples was determined by BJH model, by using adsorption isotherm. Total porosity and bulk density of the materials were measured by using mercury intrusion porosimetry, MIP (Micromeritics Autopore IV Mercury Porosimeter). Morphology and microstructure of the materials were analyzed by using a Zeiss Ultra Plus FE-SEM with a secondary electron detector. To perform compressive strength measurements, a MTS model servo-hydraulic test machine with 500 kN capacity and a 0.01 mm per second loading rate was used. Mechanical performance of the specimens (10 mm \times 10 mm \times 10 mm in size) were implemented after a resting period of 4 weeks at ambient temperature. Malvern Zetasizer Nano ZS was used for recording the zeta potential of the samples and pH of the solutions were measured by utilizing a lab pH meter (VTW, 7110).

4.2.4. MB Adsorption Tests

To understand the adsorption performance of monoliths (cubic bodies with a size of 1 cm^3), each sample was immersed into 100 ml of MB solutions with different previously determined concentrations (30-110 mg L^{-1}). These solutions were magnetically stirred at 300 rpm to reach an equilibrium and aliquots from these solutions are syringed at definite time intervals. Syringed samples absorbance values at $\lambda = 664 \text{ nm}$ were measured and analyzed by using a Flame-S-UV-Vis-ES spectrometer (Ocean Optics, USA).

Removal efficiency (%) was calculated according to Equation (1.1). The amount of MB adsorbed on synthesized adsorbents were calculated by using Equation (1.2). Data collected under dark conditions were fitted by using pseudo-first- (Equation (1.3)) and

pseudo-second-order (Equation (1.4)) adsorption kinetic models. Langmuir and Freundlich adsorption isotherm models were used to fit the equilibrium data of the specimens.

4.3. Results and Discussion

4.3.1. Morphological, Bulk Microstructure, and Mechanical Properties

BET surface area, average pore size, and pore volume of raw materials and synthesized samples are shown in Table C.4 and Table 4.1, respectively. As it is evident from these tables, both for Sep and MK -based AAMs, alkali activation caused a significant decrease in surface area values followed by a parallel decrease in pore volume values. This reduction is related with the formation of a denser structure with alkali activation and is in accordance with the previous findings [39, 97].

Raw material selection, processing conditions, and compositional factors such as type of the alkali activator and concentration of the alkali activator have a huge effect on surface properties and mechanical performance of AAMs [4, 168]. In this respect, both the processing conditions (such as curing time and curing temperature selection) and initial molar Si/Mg, Na/Mg ratios for Sep-AAMs, and Si/Al and Na/Al ratios for MKGPs were arranged to obtain an AAM with optimum properties. Alkali activation is a time-dependent process and therefore involves structural reorganization and densification with time [97]. As a result of higher degree of polycondensation occurring during series of reactions, it is common for AAMs to display a lower surface area compared to their origin raw materials [168].

Similar results of obtaining a lower surface area and pore volume upon alkali activation, were also reported for FA and Sep-based AAMs [97, 169]. As stated previously, adding H_2O_2 to an alkaline environment causes formation of oxygen and water, which also changes the porosity of the material. In this respect, as a result of this reaction by adding H_2O_2 into the paste, the water content of the initial gel composition is also affected which is known to be an important parameter influencing the final properties of the AAMs [4]. Comparatively lower surface area determined for H_2O_2 added samples (Table 4.1) therefore might be associated with the shrinkage that have occurred by the evaporation of increased

amount of water molecules introduced by H₂O₂ addition during the curing procedure (40 °C for 24 h for Sep-AAMs, and 60 °C for 24 h for MKGPs).

Table 4.1. BET surface area, average pore size, and pore volume of samples.

Sample	Surface area (m²/g)	Pore volume (cm³/g)	Pore size (Å)
Sep-AAM	1.5	0.006	519.3
0.5%H ₂ O ₂ -Sep-AAM	2.4	0.002	636.4
1%H ₂ O ₂ -Sep-AAM	0.6	0.004	1176.8
2%H ₂ O ₂ -Sep-AAM	2.43	0.004	672.3
3%H ₂ O ₂ -Sep-AAM	1.6	0.003	619.9
6%H ₂ O ₂ -Sep-AAM	0.9	0.003	558.2
8%H ₂ O ₂ -Sep-AAM	4.6	0.005	156.2
MKGP	29.7	0.170	269.8
0.5%H ₂ O ₂ -MKGP	2.6	0.028	563.2
1%H ₂ O ₂ -MKGP	3.4	0.034	689.6

However, mercury intrusion porosimetry results presented in Table 4.2 designate that increase in H₂O₂ content cause a significant increase in total porosity (%) and total intrusion volume values with a concomitant decrease in bulk density of each sample. The increase in total porosity (%) with H₂O₂ addition is more profound for MK-based samples, than they are for Sep-based samples, showing that binder nature has a significant effect on the behaviour of material's porosity upon H₂O₂ addition.

Table 4.2. Bulk density, total volume, and total porosity of samples.

Sample	Bulk density (g/cm ³)	Total volume (cm ³ /g)	Total porosity (%)
Sep-AAM	1.92	0.068	13.12
0.5%H ₂ O ₂ -Sep-AAM	1.65	0.147	24.36
1%H ₂ O ₂ -Sep-AAM	1.59	0.174	27.67
2%H ₂ O ₂ -Sep-AAM	1.39	0.252	35.02
3%H ₂ O ₂ -Sep-AAM	1.37	0.266	36.35
6%H ₂ O ₂ -Sep-AAM	1.32	0.296	39.03
8%H ₂ O ₂ -Sep-AAM	1.26	0.320	40.48
MKGP	1.42	0.224	31.88
0.5%H ₂ O ₂ -MKGP	0.82	0.606	49.58
1%H ₂ O ₂ -MKGP	0.69	0.921	63.54

Figure C.1 shows the XRD patterns of calcined Sep (750 °C, 1 h) and MK over a 2θ range between 10 to 90°, which are main raw materials that are alkali activated to obtain monolith samples with different porosity levels. As it is evident from Figure C.1a, for calcined Sep, main crystalline phases are calcium magnesium silicate and periclaise which were detected at 34°, 43° and 62°, respectively. For MK (Figure C.1b), feature positioned at 27° is assigned to quartz phase. XRD patterns of Sep-AAMs and MKGPs with different H₂O₂ contents are shown in Figure 4.1. Data presented in Figure 4.1 and Figure C.1 imply that XRD patterns of calcined Sep and MK were transformed into an amorphous form displaying a special broad feature positioned at 28° with different crystalline components. This special broad feature observed for both Sep-AAMs and MKGPs indicates the formation of an AAM with an amorphous structure [25, 38]. Similar patterns were reported for geopolymers synthesized from different sources including volcanic ash, RM and MK [97, 180]. Decrease observed in the amount of crystalline phases upon alkali activation for both Sep-AAM and MKGP demonstrates the ability of dissolution of raw materials in an alkaline environment. According to Figure 4.1a, crystalline phases observed for Sep-AAMs are

muscovite (M, $(\text{Na}_2\text{K}_2(\text{Al}_{12}\text{Si}_{12}\text{O}_{40}(\text{OH})_8)$, quartz (Q, SiO_2), anorthite (A, $\text{CaAl}_2\text{Si}_2\text{O}_6$), merwinite (Mer, $\text{Ca}_3\text{Mg}(\text{SiO}_4)$, and pericicase (P, MgO), and very similar patterns were detected for Sep-AAMs with different H_2O_2 contents. Based on Figure 4.1b, on the other hand, for MKGPs main crystalline component is quartz, which is in accordance with the current literature [38, 220]. As deduced from this figure, the addition of H_2O_2 into Sep-AAM and MKGP does not cause an alteration in the crystalline structure of the end product. Modification of geopolymers by addition of H_2O_2 reported in the existing literature did not also induced a change in the mineralogical composition of FA and MK-based geopolymers [19, 219, 221].

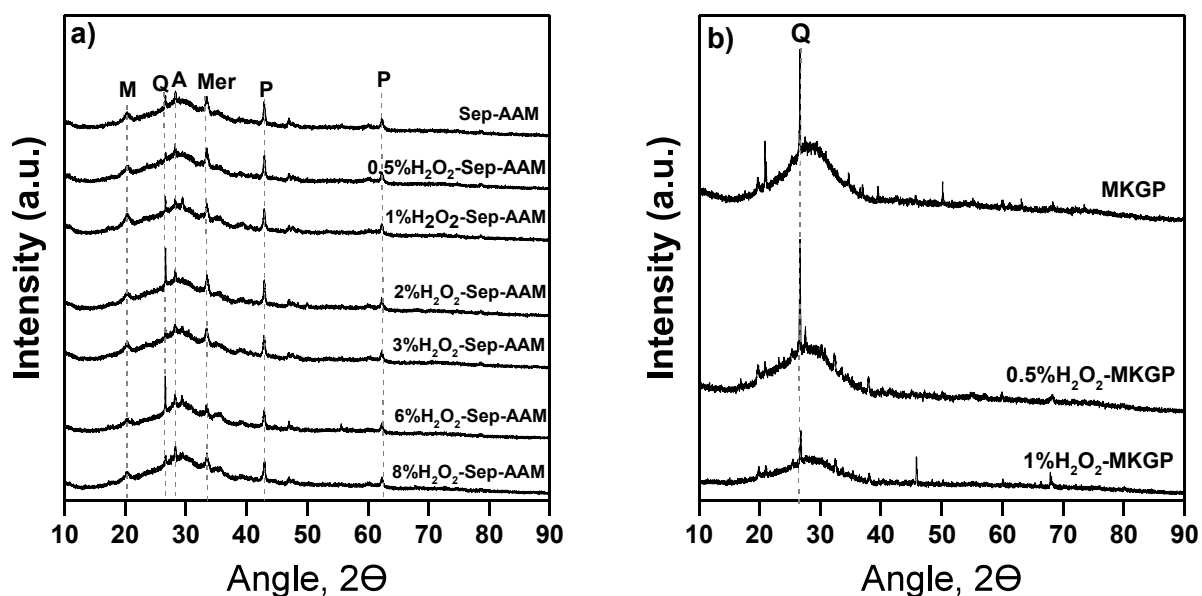


Figure 4.1. XRD patterns of a) Sep-AAMs with different H_2O_2 content, and b) MKGPs with different H_2O_2 content.

FTIR spectra of raw materials calcined Sep and MK are provided in Figure C.2. For calcined Sep, two major contributions located at 1022 and 449 cm^{-1} are assigned to Si–O–Si vibrations and Si–O–Mg bonds, respectively [173, 177]. Two shoulders observed at 950 and 876 cm^{-1} are due to stretching vibrations of Si–O bonds [177] and Si–OH bending vibrations [112], respectively. Very minor contribution detected at 682 cm^{-1} is related with the presence of asymmetric stretching vibrations of Si–O–Si bonds [112]. For MK (Figure C.2b), the most intense feature located at 1063 cm^{-1} is assigned to stretching vibrations of Si–O bonds of the amorphous MK structure, whereas the contribution detected at 797 cm^{-1} is related with the vibrations of AlO_4 tetrahedra in MK [38, 110]. Feature observed at the low frequency region

at 442 cm^{-1} is most possibly sourced from bending vibration of Si–O/Al–O bonds [113]. Figure 4.2 shows the FTIR spectra of Sep-AAM and MK-based geopolymers (MKGP) having different H_2O_2 content. For both Sep-AAMs and MKGPs, broad characteristic feature located between $900\text{--}1200\text{ cm}^{-1}$ indicates the formation of a geopolymeric network [25]. This major contribution refers to the structural transformation as a result of dissolution of raw materials in an alkali activator. Main feature located at 1022 and 1063 cm^{-1} for calcined Sep and MK, respectively, had shifted to 986 cm^{-1} for Sep-AAMs and 975 cm^{-1} for MKGPs as a result of alkali activation. This shift to lower wavenumbers as a consequence of alkali activation detected for Sep-AAM and MKGP, refer to the formation of a tridimensional geopolymeric framework with silicon and magnesium tetrahedra for Sep-AAMs, and formation of a framework with silicon and aluminum tetrahedra for MKGPs [97, 180]. Features positioned at 1639 and 1648 cm^{-1} for Sep-AAMs and MKGPs, respectively, denote to bending vibrations (H–O–H) and stretching (–OH) vibrations of water molecules [114, 160]. Minor shoulder located at about $873\text{--}876\text{ cm}^{-1}$ contributes to the Si–OH bending vibrations [112].

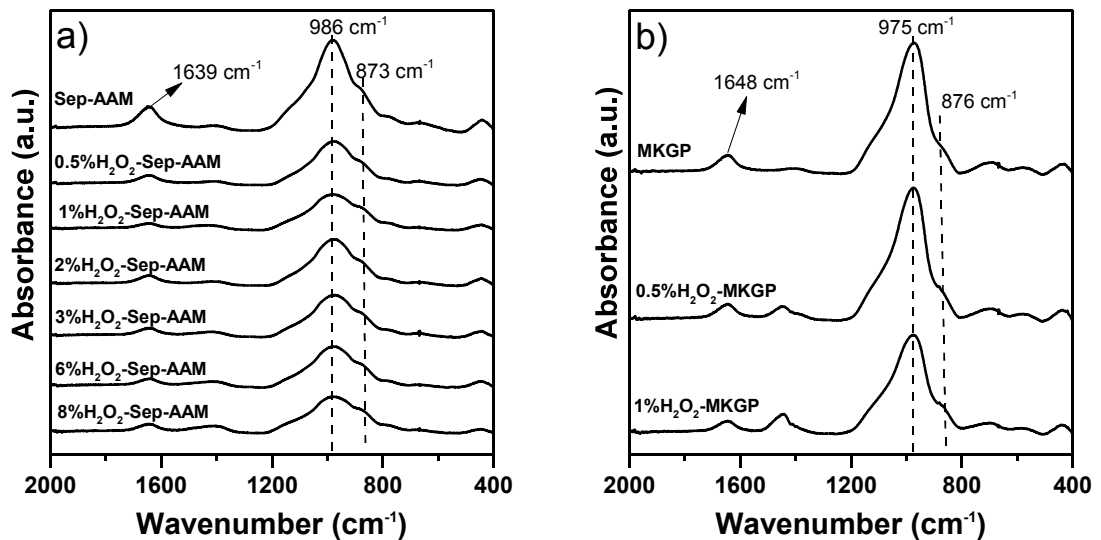


Figure 4.2. FTIR spectra of a) Sep-AAMs with different H_2O_2 content, and b) MKGPs with different H_2O_2 content.

Figure C.3 shows SEM images of calcined Sep, MK, and synthesized AAMs. Sep and MK-based AAMs with no H_2O_2 content and their highest H_2O_2 contented counterparts

synthesized in this study together with 1 wt% H_2O_2 content for comparison are provided in Figure 4.3.

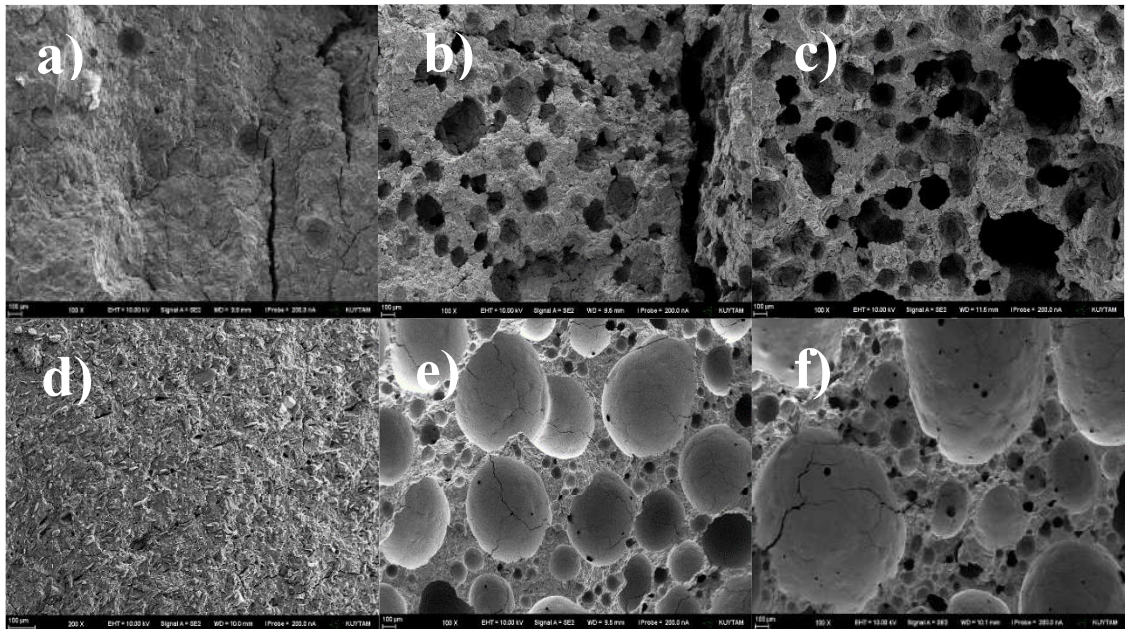


Figure 4.3. SEM images of materials at a magnification of 100 \times : a) Sep-AAM, b) 1% H_2O_2 -Sep-AAM, c) 8% H_2O_2 -Sep-AAM, d) MKGP, e) 0.5% H_2O_2 -MKGP, and f) 1% H_2O_2 -MKGP.

As it is seen from both of these figures, there is a formation of a denser structure with alkali activation and this situation causes satisfactory mechanical performance results both for MK and Sep based AAMs as presented in Figure 4.4. This figure shows the results of three repetitive compressive strength measurements employed on synthesized materials in this study. As seen from Figure 4.4, both for Sep-AAMs and MKGPs with distinct H_2O_2 content, compressive strength values show a decreasing trend upon H_2O_2 addition and results are presented in Table C.5. Increase in porosity levels introduced by H_2O_2 addition resulted a consistent decrease in mechanical performance values as expected. This decrease is more profound for MKGP samples, since even 1 wt% H_2O_2 addition caused 13.3-fold decrease in compressive strength values from 28 to 2.1 MPa. For Sep-AAMs on the other hand, 8 wt% H_2O_2 addition caused 5.7-fold decrease in compressive strength value, corresponding to a reduction from 37 to 6.5 MPa. These reduction levels in mechanical performance of these materials are correlated with the changes in the porosity levels that are observed for Sep-AAMs and MKGPs with distinct H_2O_2 contents. As stated previously, MKGP is more

sensitive to H_2O_2 addition and introduction of H_2O_2 into MKGP system causes a comparatively higher porosity levels compared to Sep-AAMs that are accompanied with a decrease in bulk densities of these samples (Table 4.2).

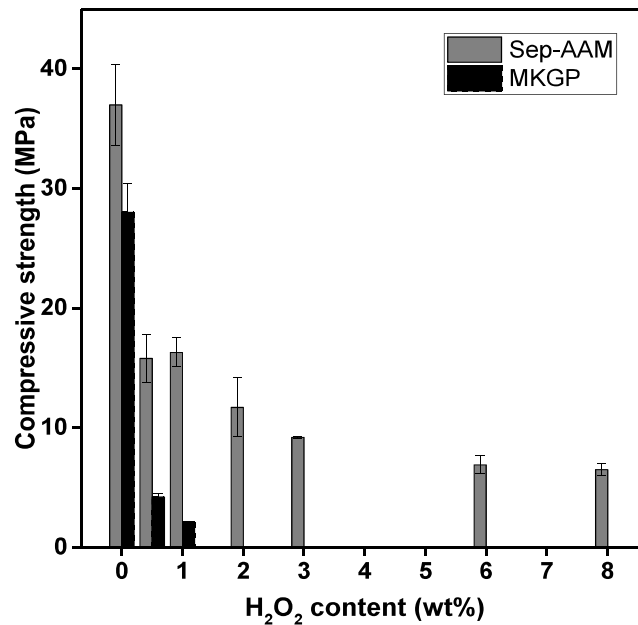


Figure 4.4. Compressive strength of the Sep-AAM and MKGP samples with different H_2O_2 content (Cured for four weeks).

As mentioned earlier, several factors including raw material selection, gel formation, molar Si/Al ratios, and processing conditions have a huge effect on the mechanical performance of the final product [4, 222]. Existing literature on the mechanical performance of AAMs with different foaming agent content revealed that all different types of foaming agents, such as glass aggregates, H_2O_2 , aluminum powder, cause a reduction in mechanical performance [19, 21, 80]. For instance, it was reported by Novais et al. that for FA-based geopolymers, H_2O_2 content increase from 0.11 to 0.57 wt% resulted a decrease in compressive strength from 7.9 MPa to 180 kPa [19]. From this respect, compressive strength value in the order of 6.5 MPa for 8% H_2O_2 -Sep-AAM sample and 2.1 MPa for 1% H_2O_2 -MKGP sample are very promising and show that these materials can be utilized for different practical applications and may offer a high regeneration capability.

4.3.2. MB Adsorption Tests

As stated earlier, negatively charged surface hydroxyl groups provide a suitable environment for the attraction of cationic MB molecules. The presence of these functional groups was verified by FTIR analysis both for MK- and Sep-based samples (Figure 4.2). To be able to understand the change in the nature of surface charge on adsorption capacity for the samples with highest porosity levels (8% H_2O_2 -Sep-AAM and 1% H_2O_2 -MKGP), pH of the MB solution was measured at initial ($t=0$) and equilibrium conditions ($t=24$ h). The initial pH of the 30 mg L^{-1} MB solution was recorded as 7. At the end of 24 hours of adsorption experiment, pH of the MB solution was measured as 10.6 and 10.1 for 8% H_2O_2 -Sep-AAM and 1% H_2O_2 -MKGP, respectively. Zeta potential evolution for these two samples as a function of pH was recorded and presented in Figure C.4. Results suggest that zeta potentials of 8% H_2O_2 -Sep-AAM and 1% H_2O_2 -MKGP are negative for all of the studied pH values (pH = 2-12). Zeta potential being negative for the equilibrium pH values (pH = 10.1-10.6) implies that the adsorption occurs as a result of electrostatic interaction [97, 192] between the adsorbate and the adsorbent.

4.3.2.1. Effect of Contact Time, $C_0 = 70$ mg L^{-1}

The effect of contact time that is required to obtain adsorption-desorption equilibrium was determined for all of the synthesized porous AAMs by setting the initial concentration of MB solution to 70 mg L^{-1} .

Changes observed in the uptake values with time are shown in Figure 4.5 both for Sep-AAMs and MKGPs having different porosity levels. Patterns presented in this figure demonstrate that a similar exponential increase in MB uptake values over time is detected for all samples and an adsorption-desorption equilibrium is reached within 24 h. Same experiments were also conducted for different initial MB concentrations ($C_0 = 30$ -110 mg L^{-1}) and results showed that equilibrium time of 24 h is sufficient enough both for the highest and the lowest initial MB concentration values.

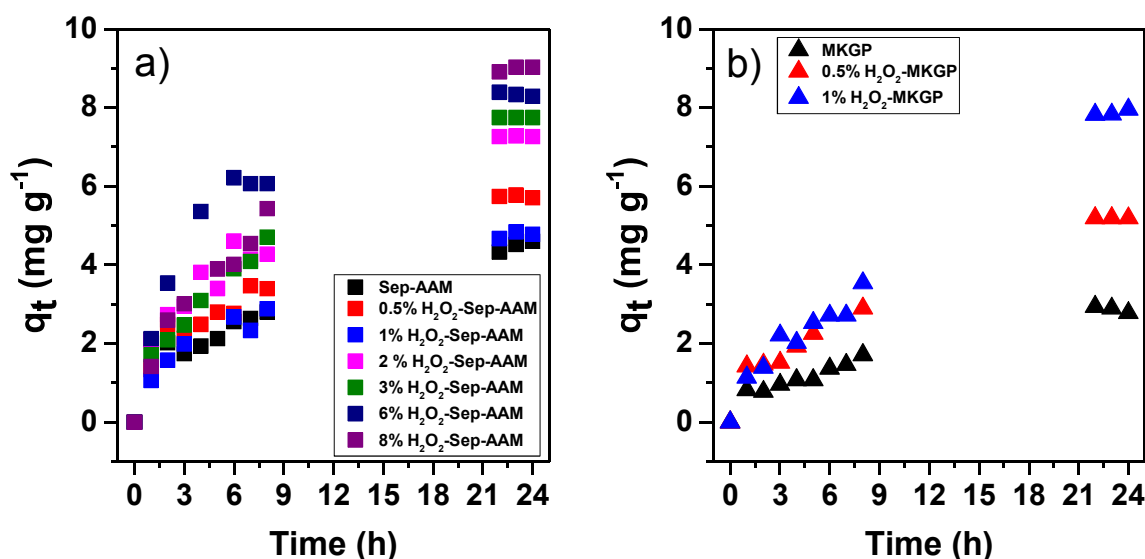


Figure 4.5. The effect of contact time on uptake of a) Sep-AAMs and b) MKGPs with different H_2O_2 content.

4.3.2.2. Effect of Initial MB Concentration

Figure 4.6 displays the change of uptake capacity with initial MB concentration for Sep-AAM, 8% H_2O_2 -Sep-AAM, MKGP, and 1% H_2O_2 -MKGP. For the sake of brevity, only the samples with no H_2O_2 content (Sep-AAM and MKGP), and highest H_2O_2 content (8% H_2O_2 -Sep-AAM and 1% H_2O_2 -MKGP) are included in this figure. As it is evident from this figure, both for Sep-AAM and MKGP samples, uptake capacity enhances with an increase in initial MB concentration and adding H_2O_2 have a positive effect on the adsorption performance. Within the studied highest initial MB concentration of 110 mg L^{-1} , uptake values at the end of 24 hours for Sep-AAM and 8% H_2O_2 -Sep-AAM are 6.6 and 10.3 mg g^{-1} , respectively. For MK-based counterparts on the other hand, uptake values reach to 4.3 and 7.8 mg g^{-1} for MKGP and 1% H_2O_2 -MKGP, respectively with an initial MB concentration of 110 mg L^{-1} . When the initial MB concentration was 110 mg L^{-1} , the pH of the solution at the end of 24 hours of adsorption experiments had reached to 8.3 and 7.9 for 8% H_2O_2 -Sep-AAM and 1% H_2O_2 -MKGP, respectively. In a similar manner, when the initial MB concentration was 30 mg L^{-1} , the pH of the solution had reached to 10.6 and 10.1 for 8% H_2O_2 -Sep-AAM and 1% H_2O_2 -MKGP, respectively.

The effect of initial MB concentration on uptake performance and removal efficiency for all of the synthesized materials are provided in Table C.6. For the sample with the highest H_2O_2 content of Sep-AAM samples, namely 8% H_2O_2 -Sep-AAM, 3.67-fold increase in initial MB concentration caused 2.34-fold enhancement in the uptake value. In a similar manner, for 1% H_2O_2 -MKGP, same amount of increase in initial MB concentration resulted a 1.56-fold increase in uptake capacity. A concomitant decrease in removal efficiency (%) is detected for all of the samples (Figure 4.6 and Table C.6) upon an increase in MB concentration. This situation points out that at lower initial MB concentrations, the number of active sites available per adsorbent is higher, explaining the favored interaction between adsorbents and MB dye at low concentrations. However, with the increase in MB concentration, available active sites are occupied with MB molecules and hinders the further adsorption of MB. This situation is in accordance with the results reported for FA-based geopolymers, MK-based geopolymers [19], and powder-formed Sep-based geopolymers with no H_2O_2 content [97].

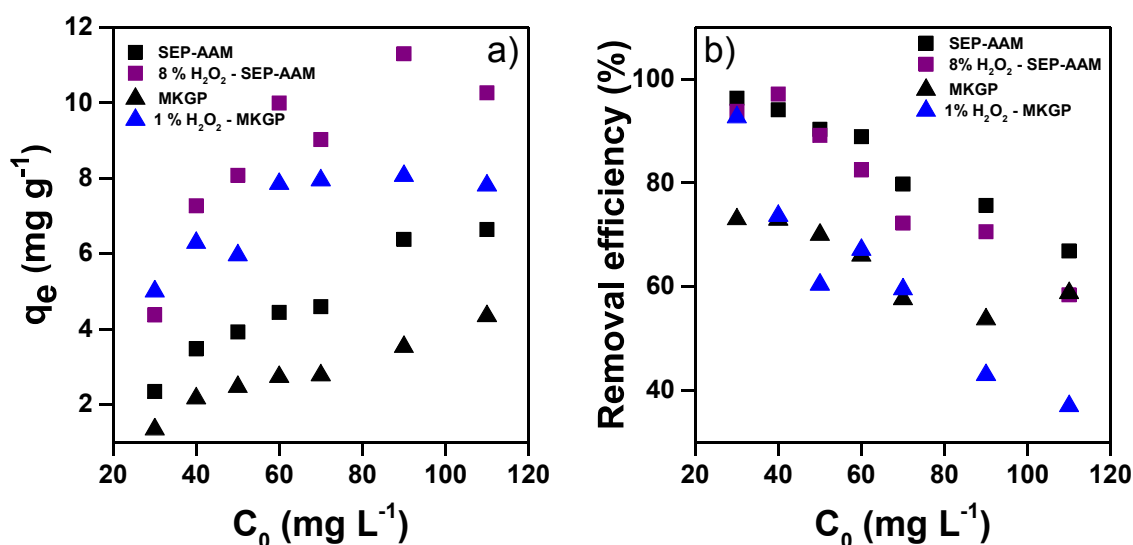


Figure 4.6. Effect of initial MB concentration on a) uptake (q_e) and b) removal efficiency (%) of MB for Sep-AAM, 8% H_2O_2 -Sep-AAM, MKGP, and 1% H_2O_2 -MKGP.

4.3.2.3. Adsorption Kinetics Modeling and Mechanism

Adsorption data were further studied by fitting experimental data to pseudo-first- and pseudo-second-order kinetic models, as presented in Table 4.3 for an initial MB concentration of 70 mg L^{-1} , and in Table C.7 for all of the studied initial MB concentrations.

Obtaining higher compatibility for pseudo-second-order kinetic model is mostly attributed to rate limiting step being the chemisorption process [21, 25], whereas presence of a higher correlation for pseudo-first-order kinetic model refers to existence of physisorption process [25, 223].

Table 4.3. Pseudo-first and pseudo-second-order kinetic model parameters and removal efficiency (%) for adsorption of MB onto synthesized AAMs. (*Contact time* = 24 h, $C_0 = 70 \text{ mg L}^{-1}$).

Adsorbent	$q_{e,exp}$ (mg g^{-1})	Pseudo-first-order adsorption kinetics ($C_0 = 70 \text{ mg L}^{-1}$)			Pseudo-second-order adsorption kinetics ($C_0 = 70 \text{ mg L}^{-1}$)			Removal (%)
		$k_{1,ads,app}$ (min^{-1})	$q_{e,cal}$ (mg g^{-1})	R^2	$k_{2,ads,app}$ ($\text{g mg}^{-1} \text{ min}^{-1}$)	$q_{e,cal}$ (mg g^{-1})	R^2	
Sep-AAM	4.59	2.5×10^{-3}	4.44	0.93	6.8×10^{-4}	5.22	0.93	79.8
0.5% H_2O_2 -Sep-AAM	5.70	1.7×10^{-3}	4.86	0.87	4.3×10^{-4}	6.90	0.93	76.98
1% H_2O_2 -Sep-AAM	4.77	2.8×10^{-3}	5.24	0.96	5.6×10^{-4}	5.67	0.93	65.74
2% H_2O_2 -Sep-AAM	7.26	1.7×10^{-3}	5.98	0.87	4.2×10^{-4}	8.31	0.93	82.75
3% H_2O_2 -Sep-AAM	7.41	1.9×10^{-3}	8.85	0.98	2.7×10^{-4}	9.49	0.92	73.67
6% H_2O_2 -Sep-AAM	8.28	2.3×10^{-3}	6.24	0.96	7×10^{-4}	9.06	0.99	77.45
8% H_2O_2 -Sep-AAM	9.02	3.3×10^{-3}	11.94	0.95	2.2×10^{-4}	11.17	0.88	72.26
MKGP	2.78	1.6×10^{-3}	2.49	0.91	6.2×10^{-4}	3.64	0.88	57.62
0.5% H_2O_2 -MKGP	5.69	1.8×10^{-3}	5.56	0.99	3.4×10^{-4}	6.82	0.89	58.56
1% H_2O_2 -MKGP	7.95	3×10^{-3}	11.52	0.92	1×10^{-4}	11.52	0.63	59.51

As it is seen from these tables, both of these kinetic models demonstrate a good fit for the studied concentrations and none of these models have a superiority on providing a better fit to experimental data; showing that both of these adsorption processes occur simultaneously. Furthermore, according to Table C.7, both $k_{1,ads,app}$ and $k_{2,ads,app}$ values show a non-monotonous decreasing trend upon an increase in initial MB concentration, implying that both physical and chemical adsorption processes govern the adsorption process [224] and further analysis is needed to determine the dominating adsorption mechanism.

To evaluate the diffusion mechanism and have an understanding on the rate limiting step, experimental results were further studied by considering intraparticle diffusion model.

Intraparticle diffusion model for the adsorption of MB onto synthesized AAMs are presented for Sep and MK-based samples with highest H₂O₂ contents as an example in Figure C.5. Obtained parameters for all of the synthesized AAMs are also provided in detail in Table C.8. As it is seen from Figure C.5 and Table C.8, the fit of experimental data to intraparticle diffusion does not show a single linear trend over the time, indicating multiple processes taking place during the adsorption [225].

It is challenging to identify the exact rate controlling mechanisms during adsorption. However, two different patterns obtained in Figure C.5 implies that the main rate controlling mechanism in first eight hours includes combined effects of boundary layer diffusion and gradual adsorption stage due to intraparticle diffusion [199]. As also shown in Table C.8, the numerical values of intercepts in the first linear region (*C*) are very low and obtained linear fit almost passes through the origin, showing that the effect of initial boundary layer resistance is low. This situation might be related with the sufficient agitation of the solution medium, minimizing the external diffusion resistance [226]. The slope of the first region increases upon H₂O₂ addition both for Sep-AAM and MKGP samples, showing the increased rate of adsorption upon boosted porosity levels introduced by H₂O₂ addition within first eight hours. On the other hand, as presented in Table C.8, the numerical values of the intercepts (*C*) shows a non-monotonous and still increasing trend upon H₂O₂ content increase both for Sep and MK-based AAMs, showing the higher uptake values detected for more porous samples, which is consistent with the values of experimental uptake values given in Table 4.3. This situation is related with the presence of viscous drag between the adsorbent surface and MB solution diffusing through the boundary layer thickness [199] and similar findings were reported also for powder formed Sep-based AAMs [97]. The second portion of the data presented in Figure C.5 provides information on the equilibrium stage of the intraparticle diffusion where adsorption starts to slow down due to presence of fewer available adsorption sites and low adsorbate concentration [199, 226]. Second portion of these patterns not passing through the origin also supports that intraparticle diffusion is not the only rate controlling step for this system and the adsorption of MB onto monolith formed Sep and MK-based AAMs is a complex process.

4.3.3. Adsorbent Regeneration

A feasibility study was conducted to explore the regeneration ability of the spent adsorbents that will bring economical profit and gives an idea on the sustainability of the adsorbents by minimizing the need for landfilling procedure and reducing carbon emissions. Among various types of regeneration methods, thermal regeneration is a widely applied and regarded as the most cost-effective procedure in wastewater treatment facilities [205, 207]. This procedure is extensively studied for the regeneration of AAMs in the literature [19, 63, 97]. From this respect, regeneration by calcination at 400 °C in static air for 2 hours in between each consecutive adsorption cycle is performed for Sep and MK-based samples with highest H₂O₂ content, 8%H₂O₂-Sep-AAM and 1%H₂O₂-MKGP, respectively. Reusability of these samples was evaluated at an initial MB concentration of 110 mg L⁻¹, which is the highest concentration value investigated in this study. Figure 4.7 summarizes the findings obtained at the end of four regeneration cycles for both 8%H₂O₂-Sep-AAM and 1%H₂O₂-MKGP. As it is seen from Figure 4.7a, for 8%H₂O₂-Sep-AAM, removal efficiency (%) shows a non-monotonous decreasing trend upon regeneration cycles. The uptake capacity, on the other hand, displays a non-monotonous but increasing trend upon regeneration cycles. After the first adsorption test (before conducting regeneration experiments) the mass of 8%H₂O₂-Sep-AAM monolith was decreased by ~40%. The main reason for this situation is related with geopolymers involving free alkalis in their structure that are available for leaching. In fact this observation was also verified by pH measurements. Recorded pH value at the beginning of the first regeneration cycle was 10.4, and dropped to 8.55 at the end of the fourth cycle. Similar mass reduction was also reported for FA-based geopolymer spheres [22]. Between first and fourth regeneration cycles on the other hand, 8%H₂O₂-Sep-AAM sample had lost further 6% of its mass. Previous interferences on the thermogravimetric analysis applied on Sep-AAM samples showed that this mass reduction is related with the removal of physically adsorbed and structural water [25]. Even though the mass of the adsorbent decreased upon adsorption and thermal regeneration, recorded uptake values show that this reduction in mass for 8%H₂O₂-Sep-AAM sample is thought to be compensated by the increase in porosity as a result of thermal treatment [19]. The initial concentration of MB solution was kept constant at 110 mg L⁻¹ during the regeneration experiments and results imply that after the fourth cycle, the uptake

value for the sample 8% H_2O_2 -Sep-AAM is 16.4 mg g^{-1} , showing the high regeneration ability of this sample without any compromise in adsorption performance.

As shown in Figure 4.7b, for 1% H_2O_2 -MKGP, both the uptake capacity and removal efficiency display a decreasing pattern upon regeneration cycles. After the first adsorption test, the mass of 1% H_2O_2 -MKGP monolith was decreased by $\sim 21\%$ which is associated with leaching of alkalis present in the geopolymer structure. pH of the MB solution at the beginning of the first regeneration cycle was recorded as 10.1, which dropped to 8.1 at the end of the fourth cycle. For this sample, further mass loss of 1.2% was recorded in between first and fourth regeneration cycle, related with the removal of water molecules. The uptake capacity of 1% H_2O_2 -MKGP had decreased from 7.8 to 6.2 mg g^{-1} during the regeneration experiments, however, as evident from Figure 4.7-b, after the first regeneration cycle, there is a stabilization in the adsorption performance and only very minor changes are detected both in removal efficiency and uptake values, revealing that porous MKGP samples can be evaluated as adsorbents for consecutive adsorption cycles without a significant loss in adsorption performance.

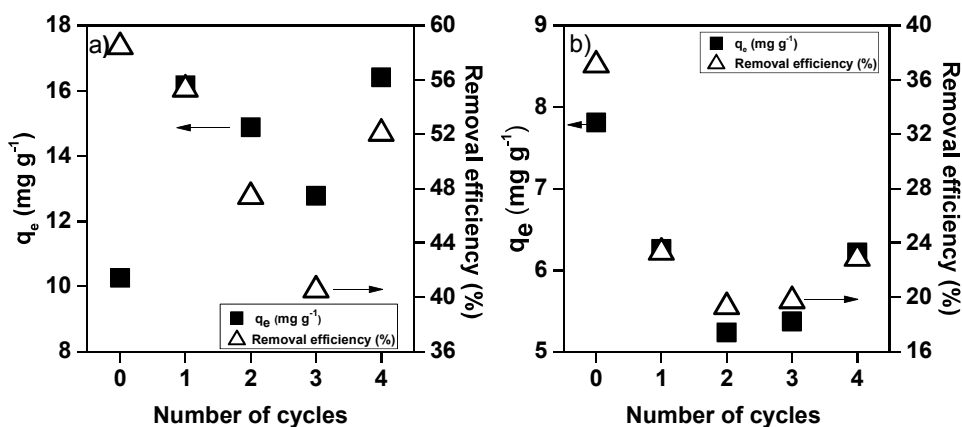


Figure 4.7. MB uptake (mg g^{-1}) removal efficiency (%) values for a) 8% H_2O_2 -Sep-AAM and b) 1% H_2O_2 -MKGP after regeneration cycles.

FTIR spectra of MB, 8% H_2O_2 -Sep-AAM, and 1% H_2O_2 -MKGP before and after adsorption, and after thermal regeneration are provided in Figure C.6. As it is seen from this figure, FTIR spectrum of MB displays contributions that are positioned at 3342 , 1592 , 1464 , 1379 , 1322 , 1145 , and 876 cm^{-1} , corresponding to bonded $-\text{OH}$ groups, stretching vibrations

of C=N and C=C groups, CH₂ deformation vibration, C–N bonds, C–S bonds, and wagging vibration of C–H in aromatic ring, respectively [97], [208].

FTIR spectrum of 8%H₂O₂-Sep-AAM shown in Figure C.6a shows that peaks located at 1649 and 983 cm⁻¹ had shifted to 1615 and 1003 cm⁻¹, upon MB adsorption, corresponding to the possible participation of C=O and C–O groups [208] and also nitrogen containing functional groups and Si–O–Si groups [143] in the adsorption of MB onto 8%H₂O₂-Sep-AAM. New peaks that have appeared around 1464 cm⁻¹ denote to the existence of MB on the surface of 8%H₂O₂-Sep-AAM, indicating –CH₃ and aromatic nitro groups of MB caused an interaction between MB dye and adsorbent [143].

According to Figure C.6b, the peak positioned at 1646 cm⁻¹ of 1%H₂O₂-MKGP had shifted to 1653 cm⁻¹ upon MB adsorption. On the other hand, the contribution centered at 983 cm⁻¹, which corresponds to the main band of a geopolymeric network denoted to the asymmetric stretching vibrations of Si–O–T (T: Si or Al) [38], remained constant and no position change was detected for this contribution.

The effect of pH of the solution medium on surface charge and the functional group dissociation had previously been reported [97, 209, 210]. In this respect, as both Sep and MK-based AAMs synthesized in this study are alkaline in nature causing high basicity in the solution medium, high pH values cause an enhancement in the electrostatic interactions between functional groups of MB dye and adsorbents of this study. FTIR analyses conducted before and after adsorption process are also in line with this observation as observed shifts confirm the presence of electrostatic interactions between adsorbents and MB dye [228] and shows that chemisorption dominates the adsorption process.

4.3.4. Adsorption Isotherm Model Studies

For all of the synthesized samples, adsorption data were fitted using Langmuir and Freundlich models. Table 4.4 shows the Langmuir and Freundlich parameters for adsorption of MB dye onto synthesized AAMs. Comparatively higher R^2 values are obtained for Langmuir isotherm than they are for Freundlich isotherm for all of the AAMs.

Table 4.4. Langmuir and Freundlich isotherm constants for MB adsorption on synthesized AAMs.

Adsorbents	Langmuir Model			Freundlich Model		
	K_L (L mg ⁻¹)	q_{max} (mg g ⁻¹)	R^2	K_F (mg g ⁻¹)	n (g L ⁻¹)	R^2
Sep-AAM	0.94	4.97	1	2.55	3.82	0.91
0.5% H_2O_2 -Sep-AAM	0.34	7.09	0.99	3.19	4.81	0.88
1% H_2O_2 -Sep-AAM	0.15	7.67	0.94	3.37	3.37	0.66
2% H_2O_2 -Sep-AAM	0.24	10.86	0.98	3.57	3.42	0.99
3% H_2O_2 -Sep-AAM	0.17	10.54	0.99	2.98	3.10	0.96
6% H_2O_2 -Sep-AAM	0.31	10.53	1	4.17	4.40	0.96
8% H_2O_2 -Sep-AAM	0.68	10.80	0.99	5.63	5.40	0.64
MKGP	0.04	5.70	0.90	0.54	1.90	0.90
0.5% H_2O_2 -MKGP	0.06	8.85	0.93	1.34	2.43	0.71
1% H_2O_2 -MKGP	0.37	8.24	0.99	4.58	7.16	0.76

The Langmuir isotherm model showing a better fit for these materials imply that the surface of the adsorbents are homogeneous in terms of functional groups and these active sites have identical binding ability to the adsorbate [67, 97, 142]. Furthermore, Langmuir model assumes that there is no interaction between adsorbate molecules on adjacent sites and each active site can hold only one molecule of the adsorbate when an adsorbate molecule occupies a site on the surface of the adsorbent, this site becomes unavailable for adsorption; suggesting a formation of a monolayer structure [25, 142]. It is reported in the literature that Langmuir isotherm model is convenient for defining chemisorption process, where there is a chemical interaction between molecules or ions of the adsorbate and surface of the adsorbent [201, 229]. Therefore, from a theoretical point of view, it can be said that AAMs synthesized in this study have finite adsorption capabilities.

These observations are in line with the existing literature on MB adsorption of geopolymers as C-type FA-based cubic-shaped geopolymer samples also showed a better fit to Langmuir isotherm and adsorption was described by a chemisorption process [63]. In a

similar manner, MK-based geopolymers also demonstrated a better fit to Langmuir isotherm model for MB adsorption and chemisorption was also found to be the main mechanism for the adsorption process [18]. Table C.9 shows the values of the Langmuir separation factor, R_L , calculated for all MB concentrations. As it is evident from Table C.9, R_L values are in between 0 and 1, showing that adsorption within the considered experimental conditions is favorable.

Considering high and similar correlation coefficients obtained from fitting the experimental data to pseudo-first, pseudo-second-order and intraparticle diffusion models (Table C.7 and Table C.8), the adsorption mechanism between MB dye and monolith formed AAMs is found to be affected synergistically from physisorption, chemisorption and diffusion. However, isotherm model studies and regeneration experiments pointed out that chemisorption has a dominant effect on the adsorption mechanism.

Our previous findings on powder formed Sep-based AAMs showed that natural presence of surface hydroxyl groups on AAMs presents a good environment for chemical adsorption as there occurs a chemical attraction between the anionic surface hydroxyl groups and cationic portion of MB dye [97]. This electrostatic interaction between cationic MB dye and the adsorbent is also accounted for MK-based counterparts of Sep-AAMs. In fact, the finding of this study is in accordance with the existing literature, where FA [63], RM and MK-based [25] AAMs displayed chemical adsorption to MB dye, revealing that adsorption process between AAMs are mostly controlled by chemisorption.

Even though H_2O_2 addition does not provide an increased surface area (Table 4.1), it leads to an increase in the availability of MB molecules due to increased level of total porosity values (Table 4.2). The enhanced porosity due to H_2O_2 addition helps MB molecules to reach to inside of the each monolith, and therefore increase the accessible surface area for MB molecules to be adsorbed. This situation is also verified by the micrographs obtained from stereo microscope (Figure C.7). As Figure C.7 shows, both for MKGP and Sep-AAM, H_2O_2 addition induces an increase in the length of MB molecules that have entered into the monolith structure. According to digital stereo microscope results, the highest path length of MB molecules that have entered into the monolith are 287.2,

1343.9, 2105.5, and 3587.8 μm for Sep-AAM, 8% H_2O_2 -Sep-AAM, MKGP, and 1% H_2O_2 -MKGP, respectively (Figure C.7).

Larger pore size formation with H_2O_2 addition has previously been reported for coal FA-based geopolymers and it was concluded that increased pore size values resulted a faster diffusion rate and MB molecules have more access into the pore and therefore be adsorbed on the adsorbents surface [63]. Similar case is also observed in our system. The length of MB molecule is reported to be in the range between 13.82-14.47 \AA , depending on the location of the chloride ion [230]. Regarding the length of MB molecule and pore size values of synthesized AAMs (Table 4.1), it may be suggested that MB molecules can enter into the pores of AAMs synthesized in this study.

Maximum adsorption capacities of AAMs synthesized from various raw materials together with their corresponding mechanical performance are shown in Table 4.5. This table shows that MK-based and Sep-based AAMs with the highest H_2O_2 content (1% H_2O_2 -MKGP and 8% H_2O_2 -Sep-AAM, respectively) in this study show comparable uptake values to that of other counterparts in this table. Adsorption performance of these samples in powder form is also provided as an example in this table. Relatively higher uptake capacities obtained in powder forms is an expected situation as the amount of accessible adsorption sites are higher for powder formed samples. Compressive strength values of these monoliths, especially 8% H_2O_2 -Sep-AAM, also show superior mechanical performance and therefore offers a huge potential for future practical water remediation applications.

Making an optimization by taking two different parameters; uptake and compressive strength, showed that adsorption performance of both MK and Sep-based AAM's uptake capacity can be enhanced by increasing the porosity levels. However, the trade-off between these two parameters should be well adjusted in order to obtain an adsorbent with good mechanical performance. As mentioned earlier, increased porosity levels cause a decrease in mechanical performance values.

Table 4.5. MB adsorption capacity of various AAMs.

Adsorbent	Form of the adsorbent	q_e (mg g ⁻¹)	Compressive strength (MPa)	Reference
Biomass FA-geopolymer	Cylindrical monolith	15.4	8	[19]
Modified bauxite residue-based porous inorganic polymer	Cylindrical monolith	17	1	[80]
FA-based geopolymer	Sphere	30.1	-	[22]
Potassium activated FA based geopolymer	Cubic monolith	84	1.7	[63]
MK-based geopolymer with expanded glass aggregates	Monolith	4.9	1.6	[21]
MK-based geopolymer spheres	Sphere	0.9	3.3	[17]
MK-based ice-templated geopolymer beads	Bead	5	5.9	[214]
Sep-AAM	Cubic monolith	6.6	37	<i>This thesis</i>
0.5% H_2O_2 -Sep-AAM	Cubic monolith	6.5	15.8	<i>This thesis</i>
1% H_2O_2 -Sep-AAM	Cubic monolith	7.1	16.3	<i>This thesis</i>
2% H_2O_2 -Sep-AAM	Cubic monolith	10.1	11.7	<i>This thesis</i>
3% H_2O_2 -Sep-AAM	Cubic monolith	9.4	9.2	<i>This thesis</i>
6% H_2O_2 -Sep-AAM	Cubic monolith	9.8	6.9	<i>This thesis</i>
8% H_2O_2 -Sep-AAM	Cubic monolith	10.3	6.5	<i>This thesis</i>
8% H_2O_2 -Sep-AAM	Powder	62.5	-	<i>This thesis</i>
MKGP	Cubic monolith	4.3	28	<i>This thesis</i>
0.5% H_2O_2 -MKGP	Cubic monolith	7.2	4.2	<i>This thesis</i>
1% H_2O_2 -MKGP	Cubic monolith	7.8	2.1	<i>This thesis</i>
1% H_2O_2 -MKGP	Powder	19.5	-	<i>This thesis</i>

4.4. Concluding Remarks

Monolith formed Sep-based AAMs with distinct porosity levels are synthesized in this study. The MB adsorption capacity of these materials is compared to MK-based geopolymers with different porosity levels. The effect of binder nature and porosity in terms of microstructural properties, mechanical performance, and also adsorption performance were explored. Results showed that Sep-based AAMs are less sensitive to foaming agent addition when compared to MK-based counterparts and they can carry higher H₂O₂ amounts with good mechanical performance values. Zeta potential measurements demonstrated that surface of both Sep and MK-based AAMs with the highest H₂O₂ content surface is negatively charged within the studied pH region. Both pseudo-first-order and pseudo-second-order adsorption kinetics showed a good fit to experimental data, showing that both physical and chemical adsorption processes govern the adsorption process. However, adsorption isotherm model studies revealed that Langmuir isotherm model shows a better fit and therefore chemisorption process has a dominating effect on the adsorption mechanism and supported by FTIR analyses. Regeneration experiments conducted on samples with the highest porosity levels show that both MK and Sep-based AAMs can be regenerated up to four cycles without any loss in their integrity. Current part of this thesis shows that H₂O₂ addition induces different porosity levels in Sep and MK-based AAMs and binder nature has an effect on the porosity levels of the end material. Still, these AAMs synthesized from different sources are sustainable options with a promising potential and their adsorption capacity can be tuned by arranging the porosity levels. In comparison to previous study where Sep-AAMs in powder forms were used effectively as MB adsorbents [97], results of this chapter is an important step forward since monolith formed AAMs can easily be regenerated without compromising from the adsorption performance.

5. GRAPHITIC CARBON NITRIDE INCORPORATED RED-MUD- AND METAKAOLIN-BASED GEOPOLYMERS FOR ENHANCED WASTEWATER TREATMENT CAPABILITY

5.1. Introduction

Graphitic carbon nitride ($g\text{-C}_3\text{N}_4$) is one of the prospective adsorbent candidates that has a potential to be used for wastewater remediation systems. It is a 2D material consisting of s-triazine or s-heptazine units that are bonded by tertiary or secondary amino groups [231, 232]. It is known from the literature that $g\text{-C}_3\text{N}_4$ preserves its stability up to 600 °C and shows resistance to weak acids and bases, dissoluble in water, acetone, ethanol, and diethyl ether [231, 233]. It can be synthesized via a thermal procedure by using different nitrogen-rich organic precursors including melamine [35, 234], urea [235], cyanamide [236], dicyandiamide [237, 238], and thiourea [238]. Due to its unique structure and the presence of conjugated π regions, $g\text{-C}_3\text{N}_4$ has the ability to adsorb organic pollutants [232] and used for the removal of organic pollutants in the literature [35, 239]. This material has different morphological forms that can be produced by different methods depending on its final application area. Different morphological forms of $g\text{-C}_3\text{N}_4$ include bulky $g\text{-C}_3\text{N}_4$, 3D porous $g\text{-C}_3\text{N}_4$, 2D nanosheets of $g\text{-C}_3\text{N}_4$, 1D nanorods of $g\text{-C}_3\text{N}_4$, and 0D quantum dots of $g\text{-C}_3\text{N}_4$ [240]. One of the mostly studied morphological form of $g\text{-C}_3\text{N}_4$ is its bulky form; this form of $g\text{-C}_3\text{N}_4$ can easily be produced by thermally condensating the nitrogen-rich precursors [240, 241].

Owing to its band gap, oxidation and reduction potential, and flexibility of modification with metals and non-metals [232, 233], $g\text{-C}_3\text{N}_4$ is also a widely studied visible-light active photocatalyst, especially for water splitting and oxidation of hydrocarbons [242]. As stated previously, $g\text{-C}_3\text{N}_4$ -based materials are prospective candidates as adsorbents for wastewater treatment applications. In this regard, Shi et al. had studied RM and $g\text{-C}_3\text{N}_4$ -based composites for their synergistic adsorption and photocatalysis performance for wastewater treatment [35]. Results of this study had shown that both adsorption and photocatalytic performance of the synthesized composite is increased compared to pure $g\text{-C}_3\text{N}_4$.

C_3N_4 , which was related with the increased surface area, increased visible-light absorption capability, and enhanced separation of photogenerated electron-hole pairs [35].

Adsorbents that are based on g- C_3N_4 require specific attention as the adsorption capacity of these materials can be improved by increasing the porosity via soft and hard templates, chemical functionalization, or synthesis of functional composites [231]. Bulk g- C_3N_4 does not show high adsorption performance due to its low surface area, however functionalizing the surface of this material with different techniques offers good opportunities for evaluating these materials in adsorption [243] and also in photocatalysis research area [35].

The adsorption performance of geopolymers towards organic pollutants depends on electrostatic or ionic interactions and also on oxygen containing groups. Electrostatic or ionic interactions between the geopolymer and target pollutant imply a process where negatively charged geopolymer sourcing from the Al atom in tetrahedral position attracts the positively charged portion of the cationic dye in the aqueous medium.

For MB, which is one of the most commonly known cationic dye for instance, cationic portion of MB exchange sites with Na^+ charge balancing cations of the geopolymer structure [21]. Additionally, oxygen containing groups such as surface hydroxyls, also produce affinity for MB adsorption [21, 97] and therefore responsible for the adsorption performance of geopolymers in general.

For g- C_3N_4 , alkaline $-NH-$ and $-NH_2-$ functional groups present at the edges induce electrostatic interactions and contributes to the adsorption of pollutants [243]. In this regard, in this chapter a new composite consisting of red mud (RM) and metakaolin (MK)-based geopolymer and g- C_3N_4 is introduced for the first time. To the best of our knowledge, this is the first attempt of investigating the adsorption capacity of geopolymer and g- C_3N_4 -based composites for the removal of MB dye from wastewaters. The manuscript form of Chapter 5 is to be submitted as a publication.

5.2. Experimental

5.2.1. Materials

MK and RM are the aluminosilicate sources utilized for the geopolymers. Chemical compositions of MK, RM, and calcined RM are given in Table D.1 (in the Appendix D). To synthesize MK and RM-based geopolymers, sodium silicate ($\text{Na}_2\text{Si}_3\text{O}_7$) solution and sodium hydroxide pellets was used. Urea (Merck, 1.34 g/cm^3) was used as a $\text{g-C}_3\text{N}_4$ precursor.

5.2.2. Synthesis of Geopolymers

The ratio of MK to RM was optimised based on our previous studies [25, 38]. 20 wt% RM and 80 wt% MK were used in solid raw material basis [38] and synthesis conditions together with molar Si/Al and Na/Al ratios are given in Table D.2. Powdered and sieved (#70 mesh sieve, $200 \mu\text{m}$) RM and MK were mixed with alkali activators and then thermally treated at $60 \text{ }^\circ\text{C}$ for 24 hours.

5.2.3. Synthesis of $\text{g-C}_3\text{N}_4$ Incorporated RMGP

$\text{g-C}_3\text{N}_4$ incorporated RMGP composites ($\text{g-C}_3\text{N}_4/\text{RMGP}$) were produced by a calcination method. 30 g urea and 0.5 g of RMGP were mixed thoroughly and the mixture was grinded for 30 mins. Grinded mixture was then transferred into a crucible with a cap. The solid powder-formed mixture was heated from room temperature to $550 \text{ }^\circ\text{C}$ with a heating rate of $3 \text{ }^\circ\text{C/min}$, and then kept at $550 \text{ }^\circ\text{C}$ for further two hours. At the end of this thermal procedure, a two phased material is obtained. The upper part of the material was red in color and consists of RMGP and $\text{g-C}_3\text{N}_4$, whereas the lower part was pure $\text{g-C}_3\text{N}_4$ with a yellow color. These two phases were easily separated from each other and evaluated for adsorption experiments separately.

5.2.4. Characterization

Chemical compositions of raw materials were analyzed by XRF spectrometer that is used in in standartless mode under He atmosphere. XRD patterns of the materials were

determined by utilizing a Bruker D8 Discover Diffraction system with a Cu $K\alpha_1$ radiation source with a wavelength of 1.5418 Å. FTIR spectroscopy was performed on a Bruker Alpha II with an ATR cell, in absorption mode. A Zeiss Ultra Plus FE-SEM coupled with an EDS was performed to determine the microstructure and morphology of materials. Micromeritics ASAP 2020 –Physisorption Analyzer was used to determine the BET surface area, pore size, and pore volume values of materials. Pore size distribution of the materials were identified by using BJH model utilizing desorption adsorption isotherms. XPS analyses were performed on a Thermo Scientific K-Alpha X-ray Photoelectron Spectrometer and XPS data fitting were established by employing Avantage 5.9 software. A lab pH meter was used to measure the pH of the MB solutions. Zeta potential measurements were performed on a Malvern Zetasizer Nano ZS.

5.2.5. Adsorption Experiments

To understand the adsorption behaviour of the materials, sieved (200 μm , #70 mesh sieve) and powdered adsorbents were immersed into 50 ml of MB solution with different specified MB concentrations (10-70 mg L^{-1}), and magnetically stirred at 700 rpm until an equilibrium was obtained. Samples were syringed at definite time intervals, centrifugated, and their concentration was evaluated with a Flame-S-UV-Vis-ES spectrometer (Ocean Optics, USA) by collecting the absorbance values at $\lambda = 664 \text{ nm}$. The amount of MB adsorbed by the adsorbents were calculated by Equation (1.1). The removal efficiency (%) was calculated using Equation (1.2). Linearized forms of pseudo-first- (Equation (1.3)) and pseudo-second-order (Equation (1.4)) adsorption kinetic models were employed to interpret the kinetics data. To determine the individual effects of adsorbed amount and adsorbent amount on the adsorption rate, Equation (1.8) was used. Intraparticle diffusion model (Equation (1.10)) was also used to determine the diffusion mechanism: Langmuir and Freundlich adsorption isotherm models were applied to equilibrium adsorption data of the adsorbents.

5.2.5.1. Adsorbent Reusability Experiments

Reusability of newly introduced composite ($\text{g-C}_3\text{N}_4/\text{RMGP}$) was investigated for four successive adsorption experiments of three hours. As thermal treatment was known to be an

efficient technique that is applicable both to geopolymers and g-C₃N₄ itself [80, 244], after each adsorption experiment g-C₃N₄/RMGP was kept at 400 °C in static air for two hours to remove adsorbed MB molecules [97]. At the beginning of these experiments adsorbent amount was 100 mg and the initial MB concentration was 70 mg L⁻¹ (500 ml). MB concentration was arranged between each cycle to compensate the reduction in powder-formed adsorbent amount. Therefore, MB amount per g-C₃N₄/RMGP amount was kept constant within each cycle.

5.3. Results and Discussion

5.3.1. Morphological Properties

BET surface areas, pore volumes, and average pore sizes of RMGP and calcined RMGP are given in Table D.3. As it is seen from Table D.3, there is a slight decrease in surface area of RMGP as a result of calcination due to removal of water molecules. Table 5.1 presents the BET surface area, average pore size, and pore volume of g-C₃N₄ and g-C₃N₄/RMGP. Data implies that g-C₃N₄/RMGP has a comparatively lower surface area and pore volume to that of g-C₃N₄. Incorporation of RMGP causing a reduction in surface area is related with the formation of a denser structure with the introduction of a geopolymer into graphitic carbon nitride.

Table 5.1. BET surface area, average pore size, and pore volume of samples.

Sample	Surface area (m ² /g)	Pore volume (cm ³ /g)	Pore size (Å)
g-C ₃ N ₄	62.02	0.261	254.25
g-C ₃ N ₄ /RMGP	13.92	0.081	410.15

SEM images together with corresponding EDS spectra of RMGP, calcined RMGP, g-C₃N₄, and g-C₃N₄/RMGP are presented in Figure D.1. Atomic % of different surface elements in these materials are calculated and provided in Table D.4. SEM images and EDS spectra of RMGP and calcined RMGP (FigureD.1a&b) imply that both of these materials display a homogeneous surface microstructure and consist of different elements including

O, Si, Na, and Al atoms, constituting the main geopolymeric network. Due to removal of surface adsorbed water upon calcination of RMGP, the amount of surface oxygen atoms had decreased from 62.3 to 59.8 % (Table D.4).

SEM image of g-C₃N₄ shown in Figure D.1c demonstrates that the surface of g-C₃N₄ is porous and composes of flake-like and fluffy structures, consistent with the existing literature on the morphology of urea-derived g-C₃N₄s [245-247]. As it is evident from Table D.4, the surface of g-C₃N₄ consists mainly of C and N atoms. With the incorporation of RMGP, the morphology changed significantly and the newly synthesized g-C₃N₄/RMGP composite shows a more homogeneous morphology that holds morphological fingerprints of both g-C₃N₄ and RMGP. Surface atomic % of C and N decreased for the newly synthesized composite whereas surface O, Si, Al, and Na amounts resulting from RMGP increased (Table D.4). The alteration observed in the morphology for g-C₃N₄/RMGP and the formation of a more homogeneous system is consistent with the decrease in surface area and pore volume values from BET analyses (Table 5.1).

XRD patterns of RMGP, calcined RMGP, g-C₃N₄, and g-C₃N₄/RMGP are provided in Figure 5.1. To obtain calcined RMGP, the same thermal procedure to produce g-C₃N₄/RMGP was followed; powdered form of RMGP was heated from room temperature to 550 °C with a heating rate of 3 °C/min, and then kept at 550 °C for additional two hours.

XRD pattern shown in Figure 5.1c denotes to the XRD pattern of yellow part that is obtained from the lower part of the crucible as a result of thermal treatment procedure and is mainly pure g-C₃N₄. The pattern at the bottom in Figure 5.1d shows the XRD spectrum of the red part that was collected from the upper part of the crucible and includes footprints sourcing from RMGP and g-C₃N₄.

As it is evident from Figure 5.1, RMGP and calcined RMGP display an amorphous structure and there is a main feature located at 28°, demonstrating the formation of an amorphous geopolymer [39]. Crystalline phases for RMGP was quartz (SiO₂) and hematite (Fe₂O₃) phases and crystalline structure did not change by calcination, as calcined RMGP (Figure 5.1c) also showed similar XRD pattern to that of RMGP. RM is an aluminosilicate

source with high iron oxide content and the XRD pattern of as-received RM consists mainly of hematite phase [25].

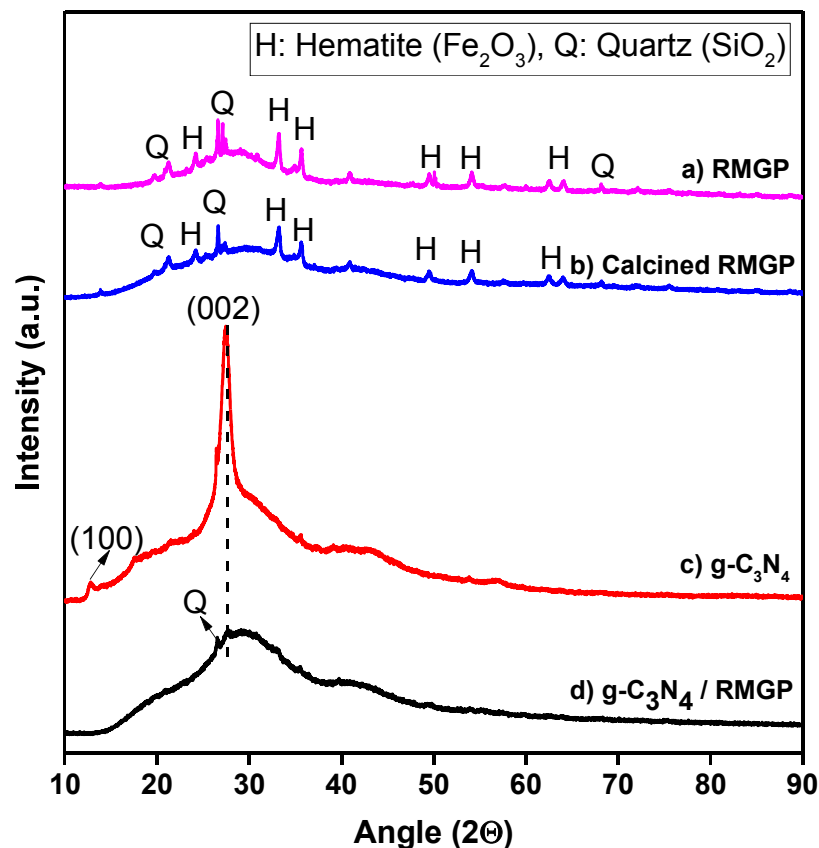


Figure 5.1. XRD patterns of a) RMGP, b) Calcined RMGP, c) g-C₃N₄, and d) g-C₃N₄/RMGP.

MK on the other hand is also an aluminosilicate source, and dominating crystalline phase in its XRD spectrum is quartz phase [25]. In this respect, hematite and quartz phases present in RMGP are sourced from RM and MK, respectively. The crystallographic structure of the synthesized g-C₃N₄ demonstrates two characteristic peaks of pure g-C₃N₄ located at 12.7° and 27.4° that correspond to (100) and (002) diffraction planes of the g-C₃N₄ [248], [249]. The main diffraction peak positioned at 27.4° is associated with the interplanar structural packing of aromatic units of g-C₃N₄ [246], [249]. The presence of the low angle diffraction peak located at 12.7° denotes to the crystal plane of repeating tri-s-triazine units of g-C₃N₄ [246, 249, 250]. Crystallographic structure of g-C₃N₄/RMGP is similar to RMGP, and the intensity of the diffraction peak related with the (002) diffraction plane of pure g-C₃N₄, is only partly detectable.

FTIR spectra of RMGP, calcined RMGP, g-C₃N₄, and g-C₃N₄/RMGP are shown in Figure 5.2. FTIR spectrum of RMGP displays typical characteristic feature in the region positioned between 900-1200 cm⁻¹, denoting to the formation of geopolymer structure [38, 251] and the main feature located at 980 cm⁻¹ is ascribed to the asymmetric stretching vibrations of T–O–Si bonds (T: Al or Si) that are formed during geopolymer production as a consequence of TO₄ reorganization [38, 110]. This main contribution verifies the presence of geopolymeric network with tetrahedral SiO₄⁴⁻ and AlO₄⁵⁻ monomers together with exchangeable charge balancing cations (Na⁺ or K⁺) [220].

For RMGP, shoulders located at 1139 cm⁻¹ and 885 cm⁻¹ correspond to asymmetric stretching vibrations of Si–O–Si bonds sourcing from MK [25] and Si–OH bending vibrations [112], respectively. Weak contributions at 1653 cm⁻¹ and 1415 cm⁻¹ can be attributed to the H–O–H bending vibrations of adsorbed H₂O molecule [113] and stretching vibrations of C–O groups sourcing from the carbonate impurities [37], respectively. The features related with the presence of water molecules disappeared upon calcination of RMGP (Figure 5.2b). Weak contribution at 1415 cm⁻¹ had also disappeared upon calcination and indicates the dissolution of carbonate impurities as a result of thermal treatment procedure.

FTIR spectrum of g-C₃N₄ consists of several different peaks. The feature located in between 3000-3500 cm⁻¹ is resulted from N–H stretching vibrations of uncondensed amino functional groups primary amine (–NH₂) and absorbed hydroxyl groups [241, 246]. Intense contributions in the region between 1200 and 1650 cm⁻¹ are sourced from stretching vibrations of C–N and C=N units in aromatic ring of g-C₃N₄ [35, 241, 243]. More specifically, intense features at 1400 and 1600 cm⁻¹ can be assigned to stretching vibrations of heptazine derived units, whereas contributions at lower wavenumber 1200 and 1400 cm⁻¹ are sourced from out of plane bending vibrations of heptazine rings [235, 246]. Peaks positioned at 1446 and 1313 cm⁻¹, also correspond to the presence of C=O and C–OH surface functional groups, respectively [252]. Feature detected at 807 cm⁻¹ is assigned to breathing mode of tri-s-triazine units of g-C₃N₄ [35, 246, 253].

The characteristic bands of g-C₃N₄/RMGP are similar to those of RMGP and g-C₃N₄. The main band of RMGP positioned at 980 cm⁻¹ is still visible for g-C₃N₄/RMGP. Additionally, contributions in the region between 1200 and 1600 cm⁻¹, and 807 cm⁻¹ still

exist in the newly formed $g\text{-C}_3\text{N}_4/\text{RMGP}$ composite. In this regard, synthesized composite holds fingerprints of both RMGP and $g\text{-C}_3\text{N}_4$.

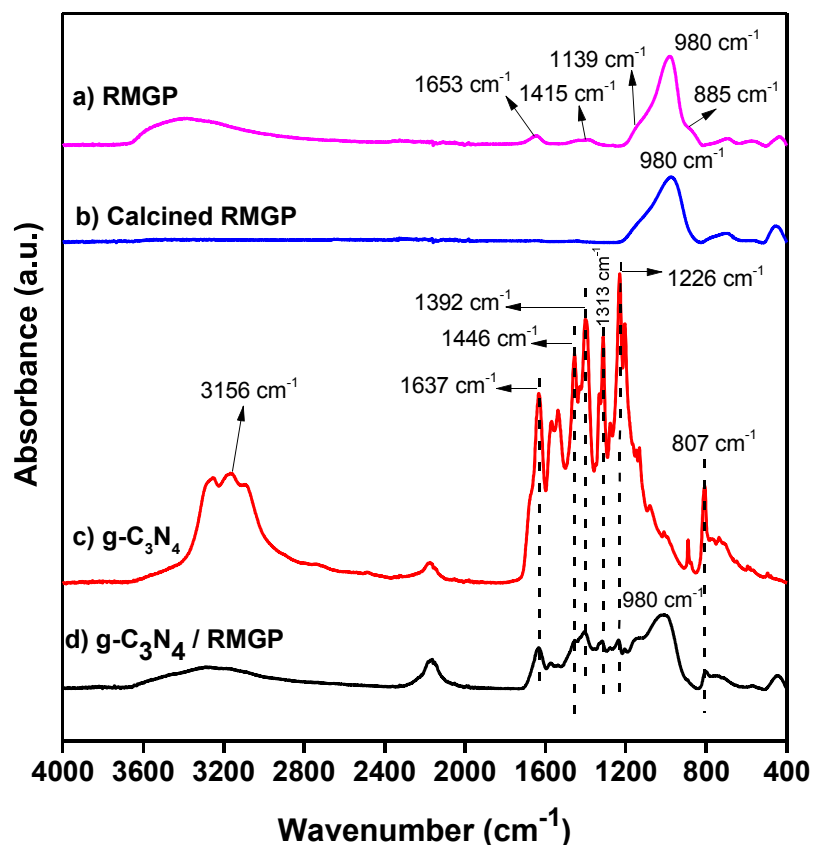


Figure 5.2. FTIR spectra of a) RMGP, b) Calcined RMGP, c) $g\text{-C}_3\text{N}_4$, and d) $g\text{-C}_3\text{N}_4/\text{RMGP}$.

5.3.2. Surface Characteristics

To determine the alterations in surface elemental compositions for $g\text{-C}_3\text{N}_4$ and $g\text{-C}_3\text{N}_4/\text{RMGP}$, XPS analysis was conducted. XP survey spectra of RMGP, calcined RMGP, $g\text{-C}_3\text{N}_4$, and $g\text{-C}_3\text{N}_4/\text{RMGP}$ are provided in Figure D.2. As is evident from these graphs, the surface of RMGP and calcined RMGP consists of same elements. $g\text{-C}_3\text{N}_4/\text{RMGP}$, on the other hand displays fingerprints of both RMGP and $g\text{-C}_3\text{N}_4$.

Deconvoluted C 1s, O 1s, and N 1s XP spectra of $g\text{-C}_3\text{N}_4$ and $g\text{-C}_3\text{N}_4/\text{RMGP}$ and surface atomic % obtained from XPS results regarding all surface elements for RMGP, calcined RMGP, $g\text{-C}_3\text{N}_4$, and $g\text{-C}_3\text{N}_4/\text{RMGP}$ were given in Figure D.3 and Table D.5,

respectively. C 1s spectrum of g-C₃N₄ consists primarily of three peaks located at 284.5, 286.2, and 287.9 eV. Major contribution positioned at higher binding energy corresponds to sp² hybridized carbon (N–C=N) of g-C₃N₄ [253]. Weaker contributions at 284.5 eV and 286.2 eV are assigned to graphitic C=C bonds and C–NH₂ species [254]. O 1s spectrum of g-C₃N₄ displays two peaks at 531.9 eV and 535.03 eV. These peaks are related with the OH⁻ groups on the surface due to absorbed water [245] and oxygen in molecular water [160], respectively. N 1s spectrum of g-C₃N₄ was deconvoluted into three peaks at the binding energies of 398.4, 399.8, and 400.9 eV. The main contribution at 398.4 eV is associated with sp² hybridized nitrogen groups [245, 254, 255]. Peaks at 399.8 and 400.9 eV are related with the presence of tertiary nitrogen atoms (N–(C)₃) [246, 255] and hydrogen bonded nitrogen groups (C–N–H) [253, 255].

Even though C 1s and N 1s spectra of g-C₃N₄/RMGP show similar characteristics and peaks to that of g-C₃N₄, it can be seen that the effect of surface oxygen atoms is more obvious for g-C₃N₄/RMGP. O 1s spectrum of g-C₃N₄/RMGP demonstrate that main peak is observed at a binding energy value of 531.5 eV and this significant contribution is related with the presence of surface hydroxyls for this material [25, 118]. As stated previously, g-C₃N₄/RMGP composite is a combination of g-C₃N₄ and RMGP, therefore shows characteristics of both of these materials. The increased contribution of surface hydroxyl groups for g-C₃N₄/RMGP is also evident from Table D.5, where surface atomic % of oxygen element was detected as 3.4 and 38.6% for g-C₃N₄ and g-C₃N₄/RMGP, respectively.

5.3.3. Adsorption Measurements

The change of zeta potential with pH is shown in Figure D.4 for both g-C₃N₄ and g-C₃N₄/RMGP. For both of these materials, zeta potential values were found to be negative within the studied pH region (2-12). This situation implies that surface of these adsorbents are negatively charged in these pH interval. For g-C₃N₄, with the increase of pH from 2 to 4, there is a significant decrease in zeta potential value from -12.1 to -36.3 eV. Further increase in pH did not cause major alterations, however, minor but systematic decrease in zeta potential values were observed. The trend for g-C₃N₄/RMGP is similar with a steeper decline from -5.7 to -38.8 eV when pH is increased from 2 to 4. When pH was equal to 12, zeta potential values of g-C₃N₄ and g-C₃N₄/RMGP were -49.6 and 50 eV, respectively.

Initial pH of the solutions during adsorption experiments were arranged to be neutral and results point out that zeta potential of g-C₃N₄/RMGP composite is systematically lower than it is for g-C₃N₄ for a wide range of pH values. Existence of higher electrostatic interactions between negatively charged surface of g-C₃N₄/RMGP composite and positively charged MB molecules increases the adsorption performance.

Surface of the geopolymers synthesized from different raw materials is known to have a negative charge that is associated with the presence of different oxygen-rich hydroxyl groups [192, 256, 257]. Additionally, the surface of geopolymers contains silanol groups and therefore have a negative charge in an alkaline environment [194, 258]. On these grounds, existence of surface hydroxyl groups and silanol groups, make geopolymers suitable candidates especially for the removal of cationic molecules from wastewater. Surface functional groups evaluated by FTIR and XPS analyses also shows that C and O involving surface functional groups results in a negatively charged surface leading to an enhanced interaction for cationic adsorbates [259].

5.3.3.1. Influence of Contact Time

The influence of contact time on the adsorption performance of g-C₃N₄/RMGP and g-C₃N₄ were determined by setting the adsorbent amount to 10 mg and initial MB concentration to 20 mg L⁻¹. Uptake capacities (q_t (mg g⁻¹)) and C_t/C_0 ratio were followed by measuring the concentration of MB by taking samples at regular time intervals and presented in Figure 5.3. As it is evident from Figure 5.3, for both of these adsorbents, adsorption-desorption equilibrium was reached within the first one hour. Since only very minor changes in adsorption performance were observed after one hours, optimum contact time for these adsorbents were taken as 180 minutes (3 h). At the end of three hours, uptake and C_t/C_0 ratio for g-C₃N₄/RMGP were 92.9 mg g⁻¹ and 0.13, respectively. The adsorption performance of g-C₃N₄ was found to be lower than that of g-C₃N₄/RMGP and uptake and C_t/C_0 were determined as 34.6 mg g⁻¹ and 0.67, respectively. As mentioned previously, presence of surface functional groups were verified by XPS and FTIR analyses. In this regard, g-C₃N₄/RMGP composite demonstrating higher performance upon MB removal is in accordance with these information, and shows that surface functional groups are of great importance.

The same measurements were conducted also for RMGP and calcined RMGP for comparison and results are provided in Figure D.5. Uptake values for RMGP and calcined RMGP were measured as 18.9 and 9.5 mg g⁻¹. The decrease from 18.9 mg g⁻¹ to 9.5 mg g⁻¹ is most possibly related with the loss of surface Si–OH hydroxyl groups upon calcination, which was also verified by FTIR measurements (Figure 5.2) Adsorption measurements for these materials implied that both g-C₃N₄/RMGP and g-C₃N₄ exhibit superior performance than RMGP and calcined RMGP.

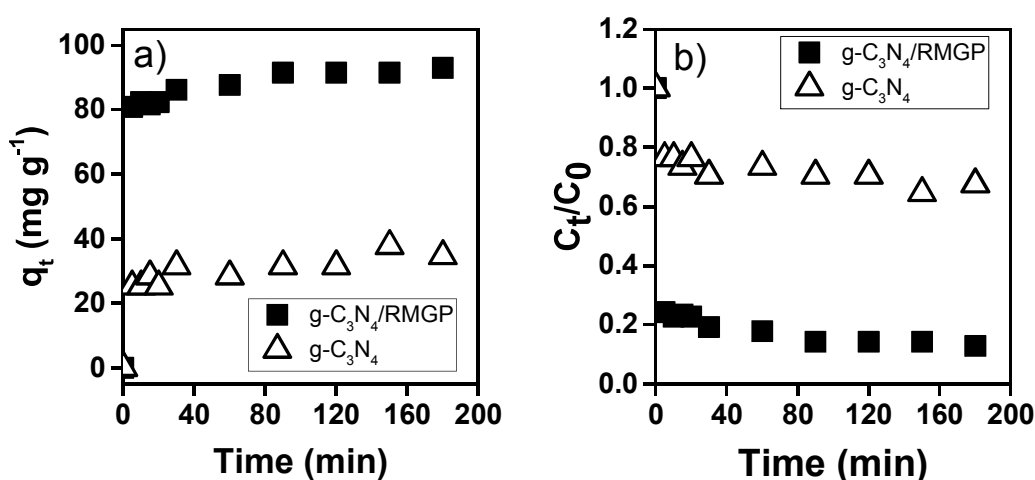


Figure 5.3. The influence of contact time on a) Uptake and b) C_t/C_0 of g-C₃N₄/RMGP and g-C₃N₄.

5.3.3.2. Influence of Initial MB Concentration

The effect of initial MB concentration on uptake and removal efficiency of g-C₃N₄/RMGP and g-C₃N₄ are presented in Figure 5.4 by setting sample amount to 10 mg for each run. Patterns presented in this figure imply that for both of these samples, removal efficiency decreases with an increase in the initial MB concentration. The quantity of available active sites for adsorption per adsorbate is lower at high MB concentrations to that of at low initial MB concentrations. As the available active sites for adsorption are not sufficient, removal efficiency decreases at higher concentrations both for g-C₃N₄/RMGP and g-C₃N₄. Similar observations had also been made for FA and MK-based geopolymers [19] and activated carbon [260]. As mentioned previously, g-C₃N₄/RMGP exhibits superior adsorption performance and Figure 5.4 shows that uptake capacity of g-C₃N₄/RMGP increases upon an increase in initial MB concentration and nearly reaches a plateau for MB

concentrations equal and higher than 40 mg L^{-1} . Initial MB concentration increase from 10 to 70 mg L^{-1} resulted a 3.8-fold enhancement in the uptake value of g-C₃N₄/RMGP from 44.6 mg g^{-1} to 170.9 mg g^{-1} .

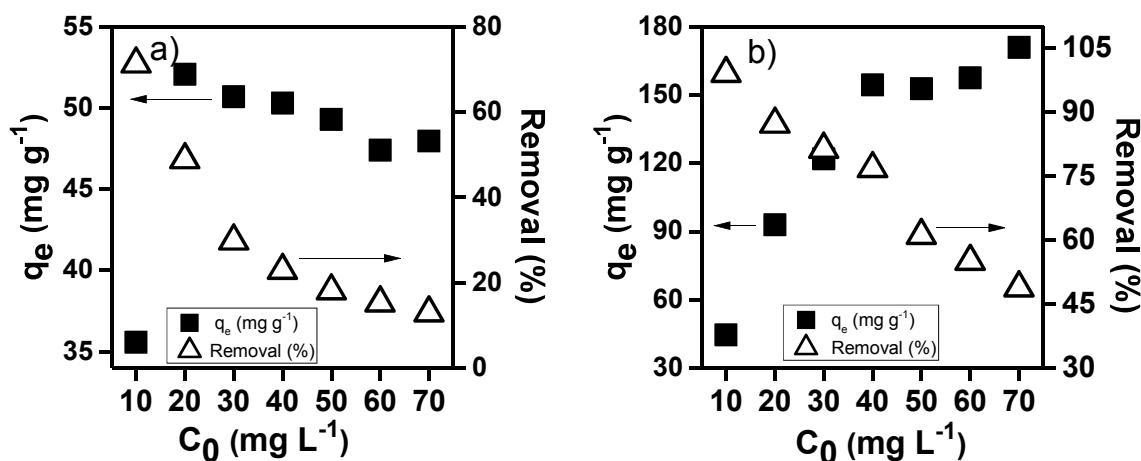


Figure 5.4. The influence of initial MB concentration on uptake and removal (%) of MB for a) g-C₃N₄ and b) g-C₃N₄/RMGP.

Surface functional groups of this adsorbent compensate the increase in adsorbate amount up to a certain level, and then uptake capacity reaches a saturation point where further adsorbate molecules cannot be adsorbed as all of the active sites had already been occupied by MB molecules. The effect of initial MB concentration was less profound for g-C₃N₄; 7-fold increase in initial MB concentration was found to cause an increase in the uptake value from 35 to 47.9 mg L^{-1} .

5.3.3.3. Influence of Adsorbent Amount

The influence of adsorbent amount on uptake capacity and removal efficiency results are shown in Figure 5.5 for both g-C₃N₄ and g-C₃N₄/RMGP. Figure 5.5. implies that for both of these adsorbents, MB uptake capacity decreases with an increase in the adsorbent amount. This decrease in uptake capacity upon change in adsorbent amount is more obvious for g-C₃N₄/RMGP sample. When the amount of adsorbent is increased from 0.006 g to 0.012 g, the uptake capacity (mg g^{-1}) had decreased from 143.5 to 72.7 mg g^{-1} .

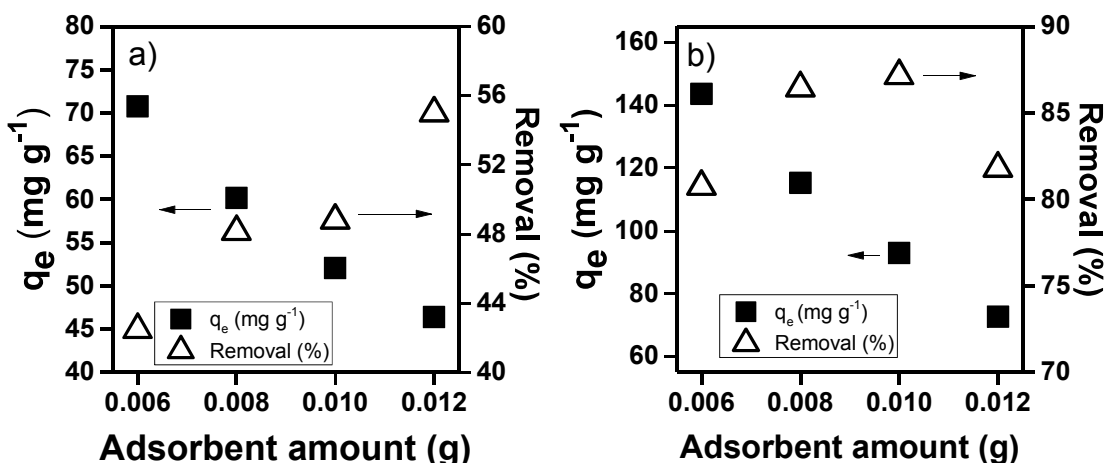


Figure 5.5. The influence of adsorbent amount on uptake and removal (%) of MB for a) g-C₃N₄ and b) g-C₃N₄/RMGP.

Similar patterns were observed for geopolymer materials and activated carbon used for dye adsorption [22, 196,261]. This pattern was explained by the increased presence of unsaturated adsorption sites with an increase in adsorbent amount [261]. Removal efficiency displays a different trend than uptake capacity; with the increase in adsorbent amount removal efficiency enhances for both g-C₃N₄ and g-C₃N₄/RMGP. This enhancement in removal efficiency is more profound for g-C₃N₄ and this trend is related with the increased quantity of available adsorption sites with an increase in adsorbent amount [22, 262].

5.3.3.4. Influence of pH

pH of the solution medium also has an influence on the adsorption occurring at the water-adsorbent interfaces [263]. To identify the effect of changes in pH values on adsorption efficiency, pH of the effluent was adjusted by using 0.1 M HCl and NaOH solutions. Adsorption experiments at distinct initial pH values of 2, 3, 4, 7, 8, and 9 were conducted both for g-C₃N₄ and g-C₃N₄/RMGP by using 10 mg adsorbent and 50 ml of MB solutions with definite concentrations (20 mg L⁻¹). pH measurements of these effluents were performed on a lab pH-meter. The pH of MB solution with 20 mg L⁻¹ initial concentration was measured as 7.0 without any adjustment. Figure 5.6 shows the adsorption performance of g-C₃N₄ and g-C₃N₄/RMGP at different initial pH values.

Experimental results pointed out that increase in the initial pH value results similar trends for both of these adsorbents. Adsorption performance of g-C₃N₄/RMGP is superior to that of g-C₃N₄ within all studied pH values (pH = 2-9), however these two adsorbents behave in a similar manner under different pH conditions. Uptake capacity increases with an increase in the initial pH and stabilizes when pH exceeds 7. The reason of this enhancement in adsorption performance for g-C₃N₄/RMGP is sourced from the synergistic effect of surface functional groups from g-C₃N₄ itself and negatively charged geopolymeric framework of RMGP, which is equipped with exchangeable charge balancing cations (Na⁺).

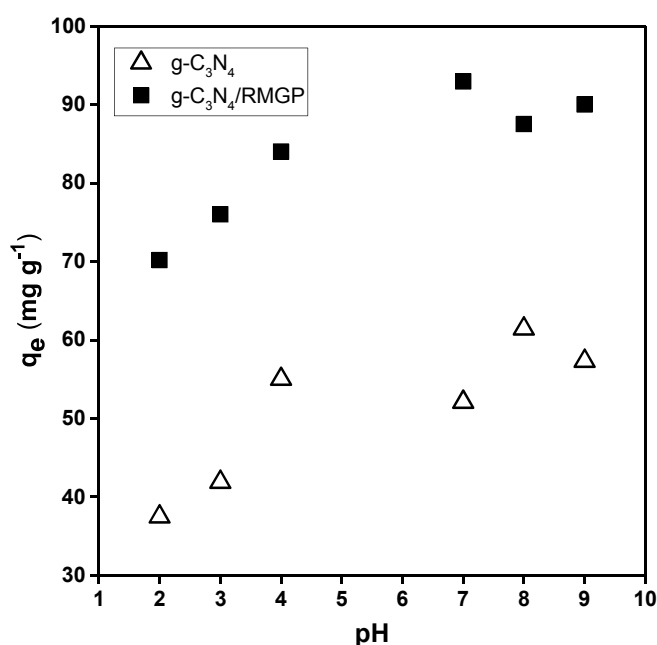


Figure 5.6. The influence of pH on MB uptake by g-C₃N₄ and g-C₃N₄/RMGP (Contact time = 3h, C₀ = 20 mg L⁻¹).

It was reported that both surface area and surface functional groups have an effect on the adsorption properties of the materials [252]. In this respect, the enhanced adsorption capacity of g-C₃N₄/RMGP composite is sourced from its unique surface structure. Increased amount of surface functional groups, and the existence of a geopolymeric framework, which were previously identified by both FTIR and XPS analyses, are the main performance determining parameters for this system. As there are more OH⁻ ions in the medium at higher pH values, these negatively charged anions attract cationic MB dye molecules more than they attract in lower pH values. Alkalinity of the effluent provides a suitable environment and causes an increase in the electrostatic attraction between these positively and negatively

charged ions. Therefore, adsorption performance is higher at alkaline conditions. This finding conforms with the existing literature where MB adsorption density is favored at higher pH values when geopolymers [23] and g-C₃N₄ [264] were used as an adsorbent.

5.3.3.5. Adsorption Kinetics Modeling and Mechanism

Results of adsorption experiments were further analyzed by using pseudo-first- and pseudo-second-order kinetic models and provided in Table 5.2 and Figure D.6 for g-C₃N₄ and g-C₃N₄/RMGP samples. For both of these adsorbents, pseudo-second-order adsorption kinetic model demonstrated a better fit and Figure D.6 shows that experimental data display linearity with very high correlation coefficients ($R^2=1$). Additionally, as it is seen from Table 5.2, there is a high consistency between experimental and calculated values of uptake values, implying that adsorption mechanism for both of these adsorbents are better defined by pseudo-second-order kinetics, and pseudo-first-order kinetics model did not show a good fit to experimental data.

In this regard, it is deduced that MB adsorption onto g-C₃N₄ and g-C₃N₄/RMGP samples conform with pseudo-second-order adsorption model and adsorption is mostly due to chemisorption. This situation signifies that there is an electron sharing or exchange between MB dye molecules and the adsorbent [198]. Similar findings was also observed for RMGP and calcined RMGP (Table D.6), however as it can also be seen from this table, uptake performance of these two materials are limited and are not further considered.

The adsorption mechanism between geopolymer samples and cationic MB dye was previously studied for MK-based geopolymers [214] and experimental data suited well to pseudo-second-order adsorption kinetics, showing that chemical adsorption takes place [214]. Surface functional groups were reported as being the main parameter determining the adsorption capacity of geopolymers [6]. In a similar manner, adsorption of cationic molecules onto urea-based g-C₃N₄ was studied, and it was asserted that adsorption is dominated by chemisorption as adsorption process involves electron exchange and transfer [265, 266].

Table 5.2. Pseudo-first and pseudo-second-order kinetic model parameters and removal efficiency (%) for adsorption of MB onto g-C₃N₄ and g-C₃N₄/RMGP (*Contact time* = 3 h, $C_0 = 20 \text{ mg L}^{-1}$ and $m = 10 \text{ mg}$).

Adsorbent	$q_{e,exp}$ (mg g^{-1})	Pseudo-first-order adsorption kinetics			Pseudo-second-order adsorption kinetics			Removal (%)
		$k_{1,ads,app}$ (min^{-1})	$q_{e,cal}$ (mg g^{-1})	R^2	$k_{2,ads,app}$ ($\text{g mg}^{-1} \text{ min}^{-1}$)	$q_{e,cal}$ (mg g^{-1})	R^2	
g-C ₃ N ₄	52.07	1.25×10^{-2}	12.43	0.56	1.1×10^{-2}	50.0	0.99	48.82
g-C ₃ N ₄ /RMGP	92.96	1.84×10^{-2}	17.61	0.77	5.06×10^{-3}	93.45	1	87.15

To determine the real pseudo-second-order adsorption rate constant ($k_{2,ads}$) for both g-C₃N₄ and g-C₃N₄/RMGP, the dependency of adsorption rate on the adsorbent amount should be taken into consideration. For this reason, for both of these adsorbents, the adsorbent amount was varied and corresponding apparent pseudo-second-order adsorption rate constant values were recorded and presented in Table D.7. This table shows that for both of these samples apparent pseudo-second-order rate constant ($k_{2,ads,app}$) increases as adsorbent amount is increased from 0.006 g to 0.012 g. Corresponding changes in $k_{2,ads,app}$ ($\text{g mg}^{-1} \text{ min}^{-1}$) values as a result of variation in adsorbent amount (g) are shown in Figure D.7. As it is seen from this figure, data for g-C₃N₄/RMGP displays comparatively higher correlation coefficient with an R^2 value of 0.95. Still, the systematic enhancement as a result of an increase in adsorbent amount was detected for both g-C₃N₄ and g-C₃N₄/RMGP. The actual pseudo-second-order adsorption rate constant ($k_{2,ads}$) and the order of adsorption rate in regard to adsorbent amount were calculated by using Equation (1.8). The slope and intercept values of Figure D.7 were used and the actual second-order adsorption rate constants ($k_{2,ads}$) for g-C₃N₄ and g-C₃N₄/RMGP were calculated based on these values. These calculations showed that $k_{2,ads}$ for g-C₃N₄ is $639.06 ((\text{g adsorbent})^{-1.31} (\text{mg MB})^{-1} \text{ min}^{-1})$, whereas $k_{2,ads}$ for g-C₃N₄/RMGP was found as $64.71 ((\text{g adsorbent})^{-1.08} (\text{mg MB})^{-1} \text{ min}^{-1})$.

To help understanding the rate limiting step of the adsorption and to designate the diffusion mechanism, adsorption data were further studied by applying intraparticle diffusion model in addition to pseudo-first-order and pseudo-second-order adsorption kinetic models. Experimental data showing the intraparticle diffusion model for MB adsorption on g-C₃N₄ and g-C₃N₄/RMGP, together with the corresponding intraparticle

diffusion model parameters are given in Figure D.8 and Table D.8, respectively. As it is seen from Table 5.2 and Table D.8, comparably very higher correlation coefficients were observed for the pseudo-second-order adsorption model, designating that responsible adsorption mechanism between g-C₃N₄ and g-C₃N₄/RMGP and MB dye is chemisorption [200, 267]. During chemisorption there occurs a bond interaction between anionic ends of adsorbents and the cationic adsorbate molecules [201, 231]. As stated by many researchers in the literature, surface of g-C₃N₄ and also surface of geopolymers are negatively charged due to the presence of negatively charged nitrogen atoms for g-C₃N₄ [231, 263, 268] and surface hydroxyl groups for geopolymers [25, 109]. This fact was also verified in this study, as both FTIR and XPS analyses implies the presence of different types of surface functional groups of these adsorbents. The content of active sites, and therefore surface chemistry is a very important parameter that has a huge effect on the correct decision of adsorbent towards a specific adsorbate [231]. In our case, the adsorbate MB molecule is a cationic dye that is dissolved into a cationic portion and a chlorine ion in aqueous solutions [202]. In this respect, it is assumed that the advanced adsorption capacity of g-C₃N₄/RMGP, to that of g-C₃N₄, is sourced from the increased amount of surface functional groups for this adsorbent. These negatively charged surface active sites cause an increased level of electrostatic interaction between MB dye molecules and enhances the adsorption capacity.

5.3.3.6. Adsorbent Regeneration

To be able to perform an adsorption that is both sustainable and durable, reusability of the adsorbents should also be taken into consideration. The g-C₃N₄/RMGP composite with very high adsorption capacity towards MB dye molecules introduced in this study holds imprints of geopolymers and graphitic carbon nitride. Therefore, a regeneration procedure that is effective for both of these materials should be conducted. Our previous observations showed that thermal treatment applied on spent geopolymer materials is an effective procedure [97] and this had previously been verified by researchers of this area [205], [269]. It was shown that a temperature of 400 °C applied for geopolymer samples is sufficient enough to remove the adsorbed MB molecules [19, 80] and geopolymers regenerated within this procedure can successfully be re-used. Additionally, regeneration ability of graphitic carbon nitride-based adsorbents' used for methyl blue adsorption was also investigated by carrying out a thermal treatment during regeneration [244, 270]. In the light of these

information, reusability of g-C₃N₄/RMGP in this study was investigated by calcination at 400 °C in static air with an isothermal step of 2 h to remove an thermally degenerate MB molecules adsorbed on the surface of g-C₃N₄/RMGP. This procedure was applied in between each consecutive adsorption experiments and experimental results are provided in Figure D.9. Data presented in Figure D.9 demonstrates that regeneration with thermal treatment reduces the adsorption performance of g-C₃N₄/RMGP. Uptake capacity of g-C₃N₄/RMGP decreased from 170.9 to 20.8 mg g⁻¹, at the end of the first experiment and fourth regeneration, respectively. One of the reasons of this reduction in adsorption performance is related with the loss of adsorbents during the regeneration experiments and this is accepted as one of the disadvantages of using powder-formed adsorbents. Nevertheless, after fourth regeneration, g-C₃N₄/RMGP still displays a better adsorption performance compared to calcined RMGP (please see Table D.6) and cumulative uptake value had reached 461.9 mg g⁻¹ during these four regeneration cycles.

FTIR spectra of MB, g-C₃N₄/RMGP, g-C₃N₄/RMGP after first and fourth regeneration and g-C₃N₄/RMGP after adsorption of MB are shown in Figure D.10. FTIR pattern of MB displays different peaks positioned mainly at 1591, 1322, 1145 and 876 cm⁻¹ [97]. The presence of these peaks were related with the existence of different functional groups such as stretching vibrations of C=N and C=C (1591 cm⁻¹), N-CH₃ bond (1322 cm⁻¹), C-S bonds (1142 cm⁻¹), and wagging vibration of C-H in aromatic ring (876 cm⁻¹) [208].

As it is seen from Figure D.10, the peak positioned at 1154 cm⁻¹ had shifted to 1145 cm⁻¹ upon MB adsorption, showing that C=O groups participate in the MB adsorption process. In a similar manner, peak located at 1637 cm⁻¹ had shifted to 1591 cm⁻¹, and peak at 1406 cm⁻¹ had shifted to 1389 cm⁻¹ with adsorption, implying the participation of C-O groups and nitrogen containing functional groups [143, 208], and also participation of multiple peaks of carbon nitride heterocycles stretching modes [263] during MB adsorption. This finding was verified from FTIR and XPS analyses which show the presence of surface functional groups that have a positive effect on the adsorption capacity of an adsorbent. On the contrary, the peak located at 876 cm⁻¹ for MB adsorbed g-C₃N₄/RMGP was not available for g-C₃N₄/RMGP prior to adsorption and this shows that aromatic C-H groups of MB result in an increased interaction between the surface of for g-C₃N₄/RMGP and MB.

Additionally, Figure D.10 shows that FTIR spectrum at the end of first regeneration displays more contribution from g-C₃N₄ (bands in the region between 1700-1250 cm⁻¹), whereas at the end of the fourth regeneration very little contribution from g-C₃N₄ was detected and adsorbent's FTIR spectrum at the end of fourth regeneration is very similar to that of calcined RMGP (Figure 5.2). g-C₃N₄/RMGP at the end of fourth regeneration still have a peak at 807 cm⁻¹, sourcing from the breathing mode of tri-s-triazine units of g-C₃N₄, however it is clear that the reduction of g-C₃N₄-related surface functional groups during thermal regeneration causes a reduction in the uptake values.

5.3.3.7. Adsorption Isotherm Model Studies

Experimental data collected at ambient temperatures were fitted by utilizing Langmuir and Freundlich adsorption isotherm models for both g-C₃N₄/RMGP and g-C₃N₄. Parameters obtained for the adsorption of MB dye molecules onto these two adsorbents are displayed in Table 5.3. According to this table, for both g-C₃N₄/RMGP and g-C₃N₄, Langmuir isotherm exhibits a better fit with very high correlation coefficients. R^2 values for Langmuir isotherm model is 1 for both of these adsorbents, however for Freundlich isotherm R^2 values were found to be 0.49 and 0.85 for g-C₃N₄ and g-C₃N₄/RMGP, respectively. Higher compatibility to Langmuir model suggests that surface functional groups of these adsorbents are homogeneously dispersed and therefore these adsorbents display monolayer adsorption with no sites being available for further adsorption when an active site is occupied by a MB molecule, and there are no interactions between MB molecules [232], [266]. Previously presented adsorption experiments revealed that g-C₃N₄/RMGP exhibits comparatively higher adsorption performance than g-C₃N₄. Concordantly, q_{max} values presented in Table 5.3 supports this finding and higher q_{max} values are determined for g-C₃N₄/RMGP, indicating the higher availability of surface functional groups in this material compared to g-C₃N₄. The value of Langmuir separation factor (R_L) was also calculated at all the studied initial MB concentrations and provided in Table D.9.

Adsorption kinetic and isotherm model results determined for g-C₃N₄/RMGP are in accordance with the existing literature where carbon-doped graphitic carbon nitride adsorbents were found to exhibit higher compatibility to pseudo-second-order adsorption kinetics and Langmuir model for MB adsorption which was correlated with the electrostatic

interactions between the adsorbent and MB molecules [232]. Concordantly, urea-based graphitic carbon nitride was used as an adsorbent for Pb(II) and aniline removal and experimental data suited better to pseudo-second-order kinetics and Langmuir isotherm model which was attributed to the electrostatic interaction between g-C₃N₄ and cationic adsorbates [266].

All of the R_L values presented in Table D.9 being in between 0 and 1 shows that adsorption is favorable within the given experimental conditions.

Table 5.3. Langmuir and Freundlich isotherm constants for MB adsorption on Sep-AAM at different temperatures.

Adsorbents	Langmuir Model			Freundlich Model		
	K_L (L mg ⁻¹)	q_{max} (mg g ⁻¹)	R^2	K_F (mg g ⁻¹)	n (g L ⁻¹)	R^2
g-C ₃ N ₄	2.19	48.07	1	36.56	12.47	0.49
g-C ₃ N ₄ /RMGP	0.36	181.82	1	56.81	2.89	0.85

Table 5.4 summarizes the reported maximum adsorption capacities of different graphitic carbon nitride-based adsorbents towards MB dye together with corresponding experimental conditions of the studies that uptake values were recorded.

According to this table, equilibrium experimental MB uptake value offered by g-C₃N₄/RMGP is very promising among various graphitic carbon nitride-based adsorbents. Remarkable uptake performance towards MB dye for g-C₃N₄/RMGP is due to presence of surface functional groups that are sourced from both RMGP and g-C₃N₄. This newly introduced composite offers a sustainable and easy-to-synthesize route for remediation of wastewaters with high adsorption performance. Simultaneous effects of surface functional groups from geopolymers and graphitic carbon nitride has been introduced for the first time, which proved that this combination may further be developed and brings in advantages including high adsorption performance, evaluation of industrial wastes, and providing an easy route for synthesis of effective adsorbents for MB removal.

Table 5.4. MB adsorption capacity of various graphitic carbon nitride-based adsorbents.

Adsorbent	q_e (mg g ⁻¹)	Experimental conditions	Reference
Carbon-doped graphitic carbon nitride	57.87	$C_0= 15$ mg L ⁻¹ , pH- not given, m_{ads} =not given	[232]
Biochar carbonitride carbon	302.25	$C_0= 50$ mg L ⁻¹ , pH=11, m_{ads} =0.16 g L ⁻¹	[265]
Tetragonal C ₃ N ₄ hollow tubes	7.0	$C_0= 15$ mg L ⁻¹ , pH- not given, m_{ads} =1 g L ⁻¹ , RT	[271]
Carbon nitride hydrogel	402	$C_0= 1000$ mg L ⁻¹ m_{ads} = not given, pH- not given, RT	[272]
Phosphorus-doped graphitic carbon nitride	100	$C_0= 18$ mg L ⁻¹ , pH=8, m_{ads} = not given, T=18 °C	[273]
g-C ₃ N ₄	47.9	$C_0= 70$ mg L ⁻¹ , pH=7, m_{ads} =0.2 g L ⁻¹ , RT	<i>This thesis</i>
g-C ₃ N ₄ /RMGP	170.9	$C_0= 70$ mg L ⁻¹ , pH=7, m_{ads} =0.2 g L ⁻¹ , RT	<i>This thesis</i>

* m_{ads} is the adsorbent dosage (g adsorbent/L MB solution), RT: room temperature.

5.4. Concluding Remarks

In this chapter, a RM and MK-based geopolymer and urea-based graphitic carbon nitride were combined to obtain g-C₃N₄/RMGP composite for MB adsorption for the first time. This composite was utilized as an adsorbent for MB removal and its adsorption performance was compared with urea-based g-C₃N₄. The effect of surface functional groups on MB adsorption was investigated with the main focus being also on microstructural properties. Experimental results pointed out that g-C₃N₄/RMGP composite exhibits superior MB adsorption capacity than urea-based g-C₃N₄ due to presence of higher amount of surface functional groups as also verified by XPS and FTIR analyses. Results showed that the adsorption of MB molecules onto g-C₃N₄/RMGP follows pseudo-second-order adsorption kinetics and according to adsorption isotherm model studies Langmuir model provides a better fit. Therefore, chemisorption was found to be the main controlling process during adsorption and electrostatic interaction between cationic MB molecules and negatively

charged surface of g-C₃N₄/RMGP created a suitable environment for chemical adsorption. Pseudo-second-order adsorption rate constant that is dependent on adsorbent amount was calculated and reusability of g-C₃N₄/RMGP was also investigated. Structure and adsorption performance relationship was established and it was observed that combining geopolymers and graphitic carbon nitride is an effective strategy towards MB removal for wastewater remediation applications.

6. CONCLUSIONS AND RECOMMENDATIONS

6.1. Conclusions

The motivation of this thesis is to investigate the potential evaluation of geopolymers in adsorption and photocatalysis research area. Different raw materials used for geopolymer synthesis were introduced and their characteristics are discussed. Among various raw materials, particular emphasis was placed on MK, RM, and Sep. Geopolymers synthesized from these materials were used for MB removal from wastewaters. Ability of these materials' for MB removal and their structure-removal performance relations were investigated by using different characterization tools and techniques. Kinetic analyses were performed to be able to comment on the photocatalytic mechanism and/or adsorption mechanism.

In Chapter 2, performance of RM and MK-based geopolymers was investigated for the adsorption and photocatalytic degradation of MB to demonstrate their potential as self-cleaning, environmentally friendly construction materials. Compressive strength measurements showed that the mechanical performances of the synthesized RM- and MK-based geopolymers vary between 37.7 and 43.2 MPa, indicating that these materials are promising for construction applications. Next, the materials were tested for MB removal both under dark and UV-light conditions. Data showed that the RM- and MK-based geopolymer, without any anatase addition, worked both as an adsorbent and a photocatalyst for the removal of MB from wastewater. Systematic increase of anatase concentration resulted in an increase in the photocatalytic activity. For instance, the geopolymer with an anatase loading of 3.7 wt% provided more than three-times higher apparent photodegradation rate constant compared to that of pure anatase under identical conditions.

Chapter 3 focused on the introduction of a novel, cheap, and easy-to-synthesize Sep-AAM, that was synthesized by the reaction of a magnesium silicate source, sepiolite, with $\text{Na}_2\text{Si}_3\text{O}_7$ solution, demonstrating high mechanical strength and MB removal performance. Kinetics data in this section indicated that MB adsorption occurs through pseudo-second-

order adsorption kinetics model, while the Langmuir isotherm model provided a better fit to adsorption isotherms. The Sep-AAM provided a removal capacity of 99.92 mg g⁻¹ at 50 °C, setting a new benchmark value among the materials used for this purpose. Thermodynamical parameters indicated that the adsorption of MB onto Sep-AAM was endothermic and the interaction between Sep-AAM and MB included weak chemical bonding. Regenerability of the Sep-AAM in powder and monolith forms was confirmed up to four-cycles. Structural parameters determined by several characterization tools demonstrated that the surface hydroxyl groups are responsible for the superior MB adsorption performance. The mechanical strength measurements showed that Sep-AAM in monolith form displayed a remarkable compressive strength value of 40 MPa.

In Chapter 4, Sep-AAM with varying porosities were introduced and their MB adsorption characteristics were comparatively evaluated for the first time. MK-based counterparts of these adsorbents were also produced to compare their structure and adsorption performance properties. H₂O₂ was used as a foaming agent in these monoliths and varied in the range of 0-8 wt.% and 0-1 wt.% for Sep-AAMs and MKGPs, respectively. Experimental results pointed out that both MK and Sep-based AAMs display adsorption performance towards MB dye with comparatively higher adsorption capacity for Sep-based samples. As porosity of Sep-AAMs increased from about 13% to 40%, the uptake capacity rose from 6.6 to 10.3 mg g⁻¹. It is noteworthy that the compressive strength of the Sep based monolith with high uptake was 6 MPa which was much higher than most of the solid formed lightweight specimens reported. On the other hand, as the porosity of MKGP monoliths vary from 31.9% to 63.5%, corresponding uptake capacity increases from 4.3 to 7.8 mg g⁻¹. Zeta potential measurements indicated that the surface of the synthesized samples were negatively charged. Both pseudo-first-order and pseudo-second-order adsorption kinetics showed good fit to experimental data, signaling that both physical and chemical adsorption processes govern the adsorption process. Adsorption isotherm model studies show that Langmuir isotherm model showed a better fit indicating chemisorption process controls the adsorption mechanism, which was also verified FTIR analysis and zeta potential measurements. Regeneration experiments conducted on samples with the highest porosity levels showed that both MK and Sep-based AAMs could be regenerated up to four cycles without any loss in their integrity. Mechanical performance of these monoliths was strongly affected by increased porosity levels and compressive strength values were found to decrease with

increased porosity. For Sep-AAM and 8% H_2O_2 -Sep-AAM, compressive strength values were reported as 37 and 6.5 MPa, respectively. For MK-based samples, compressive strength values for MKGP and 1% H_2O_2 -MKGP were measured as 28 and 2.1 MPa, respectively. Results pointed out that it is possible to tune the adsorption performance of AAM monoliths by changing the porosity levels and these monoliths may display a certain level of mechanical performance, making these materials good candidates for wastewater remediation applications.

In Chapter 5, a novel composite consisting of an industrial waste RM and MK-based geopolymer ($\text{g-C}_3\text{N}_4/\text{RMGP}$) and urea-derived $\text{g-C}_3\text{N}_4$ was introduced and evaluated as an adsorbent for MB dye for the first time. The adsorption capacity of $\text{g-C}_3\text{N}_4/\text{RMGP}$ was compared with urea-derived $\text{g-C}_3\text{N}_4$. Experimental data revealed that adsorption of MB onto $\text{g-C}_3\text{N}_4/\text{RMGP}$ follows pseudo-second-order kinetics and chemisorption had an important effect on adsorption, which was verified also by FTIR analysis. Adsorption isotherm model studies demonstrated that Langmuir model offered a better fit. It was shown that, under same experimental conditions $\text{g-C}_3\text{N}_4/\text{RMGP}$ showed an uptake capacity of 170.9 mg g^{-1} , whereas uptake capacity of $\text{g-C}_3\text{N}_4$ was recorded as 47.9 mg g^{-1} . Regenerability of $\text{g-C}_3\text{N}_4/\text{RMGP}$ was studied up to four consecutive cycles. Differences between the adsorption capacities of $\text{g-C}_3\text{N}_4$ and $\text{g-C}_3\text{N}_4/\text{RMGP}$ were investigated in detail by using different characterization tools. Results extracted from these analyses pointed out that surface functional groups sourcing from $\text{g-C}_3\text{N}_4$ and surface hydroxyl groups and silanol groups of RMGP provided a unique structure for $\text{g-C}_3\text{N}_4/\text{RMGP}$, making it a strong candidate for MB adsorption.

These results demonstrate that a hazardous industrial waste, RM, globally produced in huge amounts, can be effectively utilized in the production of environmentally friendly construction materials with self-cleaning ability without sacrificing from mechanical performance. As presented in the final part, the adsorption performance of the geopolymer synthesized from RM and MK can be improved by incorporating graphitic carbon nitride. Furthermore, to establish a new approach forward on the development of AAMs for wastewater treatment, this thesis shows that Sep can effectively be utilized and Sep-AAM provides a sustainable solution for dye removal both in powder and monolith forms, with advanced mechanical properties.

6.2. Recommendations

AAMs are studied in detail in this thesis to understand their potential applicability in adsorption and photocatalysis research area. Aiming to overcome the limitations and challenges encountered during the experiments of this study, the following points can be further considered as recommendations for future studies. As observed by the results of Chapter 2, it is possible to produce mechanically strong and photocatalytically active geopolymers by using industrial waste RM, MK, and anatase as a photocatalyst. To expand these geopolymers usability for practical applications by ensuring visible-light photocatalytic activity, doping of anatase with metals and/or non-metals can be conducted.

Chapter 3 had shown that Sep mineral offers a huge potential as an adsorbent towards MB dye. In this regard, considering the findings from Chapters 2 and 3, to increase the MB removal efficiency, Sep-based AAMs with different anatase content can be further studied to benefit from combined effects of adsorption and photocatalysis for dye removal.

From the standpoint of mechanical performance and adsorption performance results that were found to be arranged by changing the porosity levels in Chapter 4, a coating procedure can be applied to these monolith-formed AAMs to make these materials beneficial for the utilization in construction, adsorption, and photocatalysis research area.

As mentioned in Chapter 5, graphitic carbon nitride has different morphological forms and bulky-graphitic carbon nitride were studied in this chapter. To ensure enhanced visible-light photocatalytic activity, various graphitic carbon nitride precursors and synthesis procedures may be further studied and resulting material can be tested for adsorption and visible-light activity.

In Chapters 2 and 5 of this thesis, an industrial waste, RM, was utilized for geopolymer synthesis. To make a contribution to circular economy, another widely produced industrial wastes such as FA and slags could also be used for geopolymer synthesis. Mechanical performance of these geopolymers can also be measured and their adsorption and photocatalysis potential can be evaluated to have a broader perspective on the importance of raw material type on different aspects of materials engineering.

REFERENCES

1. Ramos, G. A., P. R. De Matos, F. Pelisser, and P. J. P. Gleize, “Effect of Porcelain Tile Polishing Residue on Eco-Efficient Geopolymer: Rheological Performance of Pastes and Mortars”, *Journal of Building Engineering*, Vol. 32, No. 101699, 2020.
2. Van, Deventer J. S. J., J. L. Provis, P. Duxson, and D. G. Brice, “Chemical Research and Climate Change as Drivers in the Commercial Adoption of Alkali Activated Materials”, *Waste and Biomass Valorization*, Vol. 1, No. 1, pp. 145–155, 2010.
3. Provis, J. L., “Alkali-Activated Materials”, *Cement and Concrete Research*, Vol. 114, pp. 40–48, 2018.
4. Duxson, P., A. Fernández-Jiménez, J. L. Provis, G. C. Lukey, A. Palomo, and J. S. J. Van Deventer, “Geopolymer Technology: The Current State of the Art”, *Journal of Materials Science*, Vol. 42, No. 9, pp. 2917–2933, 2007.
5. Davidovits, J. and S. Quentin, “Geopolymers: Inorganic Polymeric New Materials”, *Journal of Thermal Analysis*, Vol. 37, pp. 1633–1656, 1991.
6. Li, L., S. Wang, and Z. Zhu, “Geopolymeric Adsorbents from Fly Ash for Dye Removal From Aqueous Solution”, *Journal of Colloid and Interface Science*, Vol. 300, pp. 52–59, 2006.
7. Fei, F., Z. Gao, H. Wu, W. Wurendaodi, S. Zhao, and S. Asuha, “Facile Solid-State Synthesis of Fe₃O₄/Kaolinite Nanocomposites for Enhanced Dye Adsorption”, *Journal of Solid State Chemistry*, Vol. 291, p. 121655, 2020.
8. Gao, W., S. Zhao, H. Wu, W. Deligeer, and S. Asuha, “Direct Acid Activation of Kaolinite and Its Effects on the Adsorption of Methylene Blue”, *Applied Clay Science*, Vol. 126, pp. 98–106, 2016.

9. Yavuz, Ö. and C. Saka, "Surface Modification with Cold Plasma Application on Kaolin and Its Effects On The Adsorption Of Methylene Blue", *Applied Clay Science*, Vol. 85, pp. 96–102, 2013.
10. Boukhemkhem, A. and K. Rida, "Improvement Adsorption Capacity of Methylene Blue onto Modified Tamazert Kaolin", *Adsorption Science & Technology*, Vol. 35, No. 9–10, pp. 753–773, 2017.
11. Sarma, G. K., S. SenGupta, and K. G. Bhattacharyya, "Methylene Blue Adsorption on Natural and Modified Clays", *Separation Science and Technology*, Vol. 46, No. 10, pp. 1602–1614, 2011.
12. Zhang, Q., Y. Zhang, J. Chen, and Q. Liu, "Hierarchical Structure Kaolinite Nanospheres with Remarkably Enhanced Adsorption Properties for Methylene Blue", *Nanoscale Research Letters*, pp. 29–31, 2019.
13. Asuha, S., F. Fei, W. Wurendaodi, S. Zhao, H. Wu, and X. Zhuang, "Activation of Kaolinite by a Low-Temperature Chemical Method and Its Effect on Methylene Blue Adsorption", *Powder Technology*, Vol. 361, pp. 624–632, 2020.
14. Meigoli, M. H. Esmaili, and R. Foroutan, "Ultrasonic Assisted Synthesis of Kaolin /CuFe₂O₄ Nanocomposite for Removing Cationic Dyes from Aqueous Media", *Journal of Environmental Chemical Engineering*, Vol. 8, No. 4, p. 103869, 2020.
15. He, K., G. Chen, G. Zeng, A. Chen, Z. Huang, J. Shi, M. Peng, T. Huang, and L. Hu, "Enhanced Removal Performance for Methylene Blue by Kaolin with Graphene Oxide Modification", *Journal of the Taiwan Institute of Chemical Engineers*, Vol. 89, pp. 77–85, 2018.
16. Ajibola, A., A. Idowu, O. Adeoye, and O. Solomon, "Adsorption of Dyes Using Different Types of Clay: A Review", *Applied Water Science*, Vol. 7, No. 2, pp. 543–568, 2017.

17. Medri, V., E. Papa, M. Mor, A. Vaccari, A. N. Murri, L. Piotte, C. Melandri, and E. Landi, “Mechanical Strength and Cationic Dye Adsorption Ability of Metakaolin-Based Geopolymer Spheres”, *Applied Clay Science*, Vol. 193, p. 105678, 2020.
18. El Alouani, M., S. Alehyen, M. El Achouri, and M. Taibi, “Preparation, Characterization, and Application of Metakaolin-Based Geopolymer for Removal of Methylene Blue From Aqueous Solution”, *Journal of Chemistry*, 2019.
19. Novais, R. M., G. Ascensão, D. M. Tobaldi, M. P. Seabra, and J. A. Labrincha, “Biomass Fly Ash Geopolymer Monoliths for Effective Methylene Blue Removal From Wastewaters”, *Journal of Cleaner Production*, Vol. 171, pp. 783–794, 2018.
20. Bouna, L., A. A. El Fakir, A. Benlhachemi, K. Draoui, M. Ezahri, B. Bakiz, S. Villain, F. Guinneton, and N. Elalem, “Synthesis and Characterization of Mesoporous Geopolymer Based on Moroccan Kaolinite Rich Clay”, *Applied Clay Science*, Vol. 196, No. 105764, 2020.
21. Rozek, P., M. Król, and W. Mozgawa, “Lightweight Geopolymer-Expanded Glass Composites for Removal of Methylene Blue from Aqueous Solutions”, *Ceramics International*, Vol. 46, pp. 19785–19791, 2020.
22. Novais, R. M., J. Carvalheiras, D. M. Tobaldi, M. P. Seabra, R. C. Pullar, and J. A. Labrincha, “Synthesis of Porous Biomass Fly Ash-Based Geopolymer Spheres for Efficient Removal of Methylene Blue from Wastewaters”, *Journal of Cleaner Production*, Vol. 207, pp. 350–362, 2019.
23. Khan, M. I., T. K. Min, K. Azizli, S. Sufian, H. Ullah, and Z. Man, “Effective Removal of Methylene Blue from Water Using Phosphoric Acid Based Geopolymers: Synthesis, Characterizations and Adsorption Studies”, *RSC Advances*, Vol. 5, No. 75, pp. 61410–61420, 2015.
24. Wang, M. and X. Liu, “Applications of Red Mud as an Environmental Remediation Material: A Review”, *Journal of Hazardous Materials*, Vol. 408, No. 124420, 2021.

25. Kaya-Özkiper, K., A. Uzun, and S. Soyer-Uzun, “Red Mud- and Metakaolin-Based Geopolymers for Adsorption and Photocatalytic Degradation of Methylene Blue: Towards Self-Cleaning Construction Materials”, *Journal of Cleaner Production*, Vol. 288, No. 125120, 2021.
26. Liu, R. and C. Poon, “Utilization of Red Mud Derived from Bauxite in Self-Compacting Concrete”, *Journal of Cleaner Production*, Vol. 112, pp. 384–391, 2016.
27. Xie, W., F. Zhou, J. Liu, X. Bi, Z., Huang, Y. Li, D. Chen, H. Zou, and S. Sun, “Synergistic Reutilization of Red Mud and Spent Pot Lining for Recovering Valuable Components and Stabilizing Harmful Element”, *Journal of Cleaner Production*, Vol. 243, p. 118624, 2020.
28. Pontikes, Y. and G. N. Angelopoulos, “Bauxite Residue in Cement and Cementitious Applications: Current Status and a Possible Way Forward”, *Resources, Conservation and Recycling*, Vol. 73, pp. 53–63, 2013.
29. Wang, S., Y. Boyjoo, A. Choueib, and Z. H. Zhu, “Removal of Dyes from Aqueous Solution Using Fly Ash and Red Mud”, *Water Research*, Vol. 39, No. 1, pp. 129–138, 2005.
30. Zhang, L., H. Zhang, Y. Tian, Z. Chen, and L. Han, “Adsorption of Methylene Blue from Aqueous Solutions onto Sintering Process Red Mud”, *Desalination and Water Treatment*, Vol. 47, No. 1–3, pp. 31–41, 2012.
31. Coruh, S., F. Geyikci, and O. Nuri Ergun, “Adsorption of Basic Dye from Wastewater Using Raw and Activated Red Mud”, *Environmental Technology*, Vol. 32, No. 11, pp. 1183–1193, 2011.
32. Hu, Z. and Z. Gao, “High-Surface-Area Activated Red Mud for Efficient Removal of Methylene Blue from Wastewater”, *Adsorption Science & Technology*, Vol. 36, No. 1–2, pp. 62–79, 2018.
33. Thakare, S. R., J. Thakare, P. T. Kosankar, and M. R. Pal, “A Chief, Industrial Waste,

- Activated Red Mud for Subtraction of Methylene Blue Dye from Environment”, *Materials Today: Proceedings*, 2020.
34. Martins, Y. J. C., A. C. M. Almeida, B. M. Viegas, R. do Nascimento, and N. F. da P. Ribeiro, “Use of Red Mud from Amazon Region as an Adsorbent for the Removal of Methylene Blue: Process Optimization, Isotherm and Kinetic Studies”, *International Journal of Environmental Science and Technology*, Vol. 17, No. 10, 2020.
 35. Shi, W., H. Ren, X. Huang, M. Li, Y. Tang, and F. Guo, “Low Cost Red Mud Modified Graphitic Carbon Nitride for the Removal of Organic Pollutants in Wastewater by the Synergistic Effect of Adsorption and Photocatalysis”, *Separation and Purification Technology*, Vol. 237, 2020.
 36. Sahu, M. K. and R. K. Patel, “Novel Visible-Light-Driven Cobalt Loaded Neutralized Red Mud (Co/NRM) Composite With Photocatalytic Activity Toward Methylene Blue Dye Degradation”, *Journal of Industrial and Engineering Chemistry*, Vol. 40, pp. 72–82, 2016.
 37. Kumar, A. and S. Kumar, “Development of Paving Blocks from Synergistic Use of Red Mud and Fly Ash Using Geopolymerization”, *Construction and Building Materials*, Vol. 38, pp. 865–871, 2013.
 38. Kaya, K. and S. Soyer-Uzun, “Evolution of Structural Characteristics and Compressive Strength in Red Mud–Metakaolin Based Geopolymer Systems”, *Ceramics International*, Vol. 42, No. 6, pp. 7406–7413, 2016.
 39. Kaya, K., S. F. Kurtoglu, A. Uzun, and S. Soyer-Uzun, “Consequences of Simple Acid-Pretreatments on Geopolymerization and Thermal Stability of Red Mud-Based Geopolymers”, *Industrial and Engineering Chemistry Research*, Vol. 57, No. 21, pp. 7156–7168, 2018.
 40. Wang, K., N. Peng, J. Sun, G. Lu, M. Chen, F. Deng, R. Dou, L. Ne, and Y. Zhong,

- “Synthesis of Silica-Composited Biochars from Alkali-Fused Fly Ash and Agricultural Wastes for Enhanced Adsorption of Methylene Blue”, *Science of the Total Environment*, Vol. 729, 2020.
41. Taylor, P., D. A. Fungaro, M. Bruno, and L. C. Grosche, “Adsorption and Kinetic Studies of Methylene Blue on Zeolite Synthesized From Fly Ash”, *Desalination and Water Treatment*, pp. 37–41, 2012.
 42. Osmanlioglu, A. E., “Utilization of Coal Fly Ash in Solidification of Liquid Radioactive Waste from Research Reactor”, *Waste Management & Research*, 2014.
 43. Çelik, Ö., E. Damcı, and S. Pi, “Characterization of Fly Ash and Its Effects on the Compressive Strength Properties of Portland Cement”, *Indian Journal of Engineering & Materials Sciences*, Vol. 15, pp. 433–440, 2008.
 44. Ozden, B., E. Guler, T. Vaasma, M. Horvath, and M. Kiisk, “Enrichment of Naturally Occurring Radionuclides and Trace Elements in Yatagan and Yenikoy Coal- Fired Thermal Power Plants , Turkey”, *Journal of Environmental Radioactivity*, Vol. 188, pp. 100–107, 2018.
 45. Banerjee, S., G. C. Sharma, M. C. Chattopadhyaya, and Y. Chandra, “Kinetic and Equilibrium Modeling for the Adsorptive Removal of Methylene Blue from Aqueous Solutions on of Activated Fly Ash (AFSH)”, *Journal of Environmental Chemical Engineering*, Vol. 2, No. 3, 2014.
 46. Nuccetelli, C., Y. Pontikes, F. Leonardi, and R. Trevisi, “New Perspectives and Issues Arising from the Introduction of (NORM) Residues In Building Materials : A Critical Assessment on The Radiological Behaviour”, *Construction and Building Materials*, Vol. 82, pp. 323–331, 2015.
 47. Wang, K., M. Wei, T. Peng, H. Li, S. Chao, T. Hsu, H. Lee, and S. Chang, “Treatment and Toxicity Evaluation of Methylene Blue Using Electrochemical Oxidation, Fly Ash Adsorption and Combined Electrochemical Oxidation-Fly Ash Adsorption”,

- Journal of Environmental Management*, Vol. 91, No. 8, pp. 1778–1784, 2010.
48. Gupta, V. K., “Application of Low-Cost Adsorbents for Dye Removal – A Review”, *Journal of Environmental Management*, Vol. 90, No. 8, pp. 2313–2342, 2009.
 49. Augustus, E. N., I. A. Kesiye, A. Nimibofa, and W. Donbebe, “Modeling of Adsorption Isotherms for Methylene Blue Sorption onto Fly Ash Modified with Hydrochloric Acid”, *Journal of Chemical Science and Technology*, Vol. 6, pp. 1–9, 2017.
 50. Wang, S., Y. Boyjoo, and A. Choueib, “A Comparative Study of Dye Removal Using Fly Ash Treated by Different Methods”, *Chemosphere*, Vol. 60, pp. 1401–1407, 2005.
 51. Wang, S., Q. Ma, and Z. H. Zhu, “Characteristics of Coal Fly Ash and Adsorption Application”, *Fuel*, Vol. 87, pp. 3469–3473, 2008.
 52. Wang, S. and Z. H. Zhu, “Sonochemical Treatment of Fly Ash for Dye Removal from Wastewater”, *Journal of Hazardous Materials*, Vol. B126, pp. 91–95, 2005.
 53. Taylor, P., P. Saha, and S. Datta, “Assessment on Thermodynamics and Kinetics Parameters on Reduction of Methylene Blue Dye Using Flyash Assessment on Thermodynamics and Kinetics Parameters”, *Desalination and Water Treatment*, pp. 37–41, 2014.
 54. Li, H., M. Dai, S. Dai, X. Dong, and F. Li, “Methylene Blue Adsorption Properties of Mechanochemistry Modified Coal Fly Ash”, *Human and Ecological Risk Assessment : An International Journal*, Vol. 7039, 2018.
 55. Sun, Z., C. Li, and D. Wu, “Removal of Methylene Blue from Aqueous Solution by Adsorption onto Zeolite Synthesized from Coal Fly Ash and Its Thermal Regeneration”, *Journal of Chemical Technology and Biotechnology*, Vol. 85, No. 6, pp. 845–850, 2010.

56. Khan, T. A., I. Ali, V. V. Singh, and S. Sharma, "Utilization of Fly Ash as Low-Cost Adsorbent for the Removal of Methylene Blue, Malachite Green and Rhodamine B Dyes from Textile Wastewater", *Journal of Environmental Protection Science*, Vol. 3, pp. 11–22, 2009.
57. Sulistiyo, Y. A., N. Andriana, B. Piluharto, and Z. Zulfikar, "Silica Gels from Coal Fly Ash as Methylene Blue Adsorbent: Isotherm and Kinetic Studies", *Bulletin of Chemical Reaction Engineering & Catalysis*, Vol. 12, No. 2, pp. 263–272, 2017.
58. Jin, H., Y. Liu, C. Wang, X. Lei, and M. Guo, "Two-Step Modification Towards Enhancing the Adsorption Capacity of Fly Ash for Both Inorganic Cu (II) and Organic Methylene Blue from Aqueous Solution", *Environmental Science and Pollution Research*, Vol. 25, pp. 36449–36461, 2018.
59. Lin, J. X., S. L. Zhan, M. H. Fang, X. Q. Qian, and H. Yang, "Adsorption of Basic Dye From Aqueous Solution onto Fly Ash", *Journal of Environmental Management*, Vol. 87, pp. 193–200, 2008.
60. Kelesoglu, S., L. Sütçü, and H. Polat, "Adsorption of Methylene Blue from Aqueous Solution on High Lime Fly Ash: Kinetic, Equilibrium, and Thermodynamic Studies Adsorption of Methylene Blue From Aqueous Solution on High Lime Fly Ash: Kinetic, Equilibrium, and Thermodynamic Studies", *Journal of Dispersion Science and Technology*, pp. 37–41, 2013.
61. Fan, C., N. Dang, and H. Ma, "Adsorption of Methylene Blue from Aqueous Solutions onto Fly Ash", *2011 International Symposium on Water Resource and Environmental Protection*, Vol. 3, pp. 2217–2220, 2011.
62. Padmapriya, M., S. T. Ramesh, and V. M. Biju, "Synthesis of Seawater Based Geopolymer: Characterization and Adsorption Capacity of Methylene Blue From Wastewater", *Materials Today: Proceedings*, 2021.
63. Kaewmee, P., M. Song, M. Iwanami, H. Tsutsumi, and F. Takahashi, "Porous and

- Reusable Potassium-Activated Geopolymer Adsorbent with High Compressive Strength Fabricated from Coal Fly Ash Wastes”, *Journal of Cleaner Production*, Vol. 272, p. 122617, 2020.
64. El Alouani, M., S. Alehyen, M. El Achouri, and M. Taibi, “Comparative Study of the Adsorption of Micropollutant Contained in Aqueous Phase Using Coal Fly Ash and Activated Coal Fly Ash: Kinetic and Isotherm Studies”, *Chemical Data Collections*, Vol. 23, No. 100265, 2019.
65. El Alouani, M., S. Alehyen, M. El Achouri, and M. Taibi, “Removal of Cationic Dye – Methylene Blue – from Aqueous Solution by Adsorption on Fly Ash-Based Geopolymer”, *Journal of Materials and Environmental Sciences*, Vol. 9, No. 1, pp. 32–46, 2018.
66. Pardo, L. J. A. Cecilia, C. Lopez-Moreno, V. Hernandez, M. Pozo, M. Bentabol, and F. Franco, “Influence of the Structure and Experimental Surfaces Modifications of 2:1 Clay Minerals on the Adsorption Properties of Methylene Blue”, *Minerals*, Vol. 8, pp. 1–18, 2018.
67. Künceç, I. and S. Şener, “Adsorption of Methylene Blue onto Sonicated Sepiolite From Aqueous Solutions”, *Ultrasonics Sonochemistry*, Vol. 17, No. 1, pp. 250–257, 2010.
68. Largo, F. R. Haounati, S. Akhouairi, H. Ouachtak, R. El Haouti, A. El Guerdaoui, N. Hafid, D. M. F. Santos, F. Akbal, A. Kuleyin, A. Jada, and A. A. Addi, “Adsorptive Removal of both Cationic and Anionic Dyes by Using Sepiolite Clay Mineral as Adsorbent: Experimental and Molecular Dynamic Simulation Studies”, *Journal of Molecular Liquids*, Vol. 318, 2020.
69. Doğan, M., Y. Özdemir, and M. Alkan, “Adsorption Kinetics and Mechanism of Cationic Methyl Violet and Methylene Blue Dyes onto Sepiolite”, *Dyes and Pigments*, Vol. 75, No. 3, pp. 701–713, 2007.

70. Han, Z., Z. Zhu, D. Wu, J. Wu, Y. Liu, “Adsorption Kinetics and Thermodynamics of Acid Blue 25 and Methylene Blue Dye Solutions on Natural Sepiolite”, *Synthesis and Reactivity in Inorganic, Metal-Organic, and Nano-Metal Chemistry*, Vol. 44, No. 1, pp. 37–41, 2014.
71. Cheng, Z., R. Yang, and X. Zhu, “Adsorption Behaviors of the Methylene Blue Dye onto modified Sepiolite from Its Aqueous Solutions”, *Desalination and Water Treatment*, Vol. 135, pp. 394–404, 2016.
72. Marrakchi, F., W. A. Khanday, M. Asif, and B. H. Hameed, “Cross-Linked Chitosan/Sepiolite Composite for The Adsorption of Methylene Blue and Reactive Orange 16”, *International Journal of Biological Macromolecules*, Vol. 93, pp. 1231–1239, 2016.
73. Li, T., R. Li, Z. Ma, A. Yang, C. Jiao, and J. Wang, “Preparation of Cellulose / Sodium Alginate / Sepiolite Porous Microspheres and Their Adsorption Properties for Methylene Blue Preparation of Cellulose / Sodium Alginate / Sepiolite Porous Microspheres and Their Adsorption Properties for Methylene Blue”, *Journal of Physics: Conference Series Conference Series*, Vol. 1790, 2021.
74. Moreira, M. A., K. J. Ciuffi, V. Rives, M. A. Vicente, R. Trujillano, A. Gil, S. A. Korili, and E. H. de Faria, “Effect of Chemical Modification of Palygorskite and Sepiolite By 3-Aminopropyltriethoxysilane on Adsorption of Cationic and Anionic Dyes”, *Applied Clay Science*, Vol. 135, pp. 394 – 404, 2016.
75. Sabzi, M., “Assembly of Gelatin Biopolymer to Fibrous Sepiolite Clay for Efficient Dye Removal from Wastewater”, *Journal of Applied Polymer Science*, Vol. 136, pp. 1–10, 2019.
76. Rodriguez, A., “Removal of Dyes from Wastewaters by Adsorption on Sepiolite and Pansil”, *Industrial and Engineering Chemistry Research*, Vol. 49, pp. 3207–3216, 2010.

77. MacKenzie, K. J. D., S. Bradley, J. V. Hanna, and M. E. Smith, “Magnesium Analogues of Aluminosilicate Inorganic Polymers (Geopolymers) from Magnesium Minerals”, *Journal of Materials Science*, Vol. 48, No. 4, pp. 1787–1793, 2013.
78. Amran, M., S. Debbarma, and T. Ozbakkaloglu, “Fly Ash-Based Eco-Friendly Geopolymer Concrete: A Critical Review of the Long-Term Durability Properties”, *Construction and Building Materials*, Vol. 270, p. 121857, 2021.
79. Komnitsas, K. and D. Zaharaki, “Geopolymerisation: A Review and Prospects for the Minerals Industry”, *Minerals Engineering*, Vol. 20, No. 14, pp. 1261–1277, 2007.
80. Hertel, T., R. M. Novais, and R. Murillo, “Use of Modified Bauxite Residue-Based Porous Inorganic Polymer Monoliths as Adsorbents of Methylene Blue”, *Journal of Cleaner Production*, Vol. 227, pp. 877–889, 2019.
81. Tome, S., D. T. Hermann, V. O. Shikuku, and S. Otieno, “Synthesis, Characterization and Application of Acid and Alkaline Activated Volcanic Ash-Based Geopolymers for Adsorptive Removal of Cationic and Anionic Dyes from Water,” *Ceramics International*, 2021.
82. Zhang, Y. and L. Liu, “Fly Ash-Based Geopolymer as a Novel Photocatalyst for Degradation of Dye From Wastewater”, *Particuology*, Vol. 11, No. 3, pp. 353–358, 2013.
83. Zhang, Y. J., L. C. Liu, Y. Xu, Y. C. Wang, and D. L. Xu, “A New Alkali-Activated Steel Slag-Based Cementitious Material for Photocatalytic Degradation of Organic Pollutant from Waste Water”, *Journal of Hazardous Materials*, Vol. 209–210, pp. 146–150, 2012.
84. Banerjee, S., D. D. Dionysiou, and S. C. Pillai, “Self-Cleaning Applications of TiO₂ By Photo-Induced Hydrophilicity and Photocatalysis”, *Applied Catalysis B: Environmental*, Vol. 177, pp. 396–428, 2015.

85. Nakata, K. and A. Fujishima, "TiO₂ Photocatalysis: Design and Applications", *Journal of Photochemistry and Photobiology C: Photochemistry Reviews*, Vol. 13, No. 3, pp. 169–189, 2012.
86. Ramírez, A. M. and M. E. Rodríguez, "Ion-Exchanged Geopolymer for Photocatalytic Degradation of a Volatile Organic Compound", *Materials Letters*, Vol. 134, pp. 222–224, 2015.
87. Chowdhury, S. and R. Balasubramanian, "Graphene/Semiconductor Nanocomposites (GSNs) for Heterogeneous Photocatalytic Decolorization of Wastewaters Contaminated with Synthetic Dyes: A Review", *Applied Catalysis B: Environmental*, Vol. 160–161, pp. 307–324, 2014.
88. Zhang, Y. J., P. Y. He, M. Y. Yang, and L. Kang, "A New Graphene Bottom Ash Geopolymeric Composite for Photocatalytic H₂ Production and Degradation of Dyeing Wastewater", *International Journal of Hydrogen Energy*, Vol. 42, No. 32, pp. 20589–20598, 2017.
89. Chen, L., K. Zheng, and Y. Liu, "Geopolymer-Supported Photocatalytic TiO₂ Film: Preparation and Characterization," *Construction and Building Materials*, Vol. 151, pp. 63–70, 2017.
90. Aghighi, A. and F. Haghghat, "Evaluation of Nano-Titanium Dioxide (TiO₂) Catalysts for Ultraviolet Photocatalytic Oxidation Air Cleaning Devices", *Journal of Environmental Chemical Engineering*, Vol. 3, No. 3, pp. 1622–1629, 2015.
91. Zhang, Y. J., P. Y. He, Y. X. Zhang, and H. Chen, "A Novel Electroconductive Graphene Fly Ash-Based Geopolymer Composite and Its Photocatalytic Performance", *Chemical Engineering Journal*, Vol. 334, No. 13, pp. 2459–2466, 2018.
92. Vasanth Kumar, K. and S. Sivanesan, "Isotherms for Malachite Green onto Rubber Wood (*Hevea Brasiliensis*) Sawdust: Comparison of Linear and Non-Linear

- Methods”, *Dyes and Pigments*, Vol. 72, No. 1, pp. 124–129, 2007.
93. Ahmadijokani, F., R. Mohammadkhani, S. Ahmadipouya, A. Shokrgozar, M. Rezakazemi, H. Molavi, T. M. Aminabhavi, and M. Arjmand, “Superior Chemical Stability of UiO-66 Metal-Organic Frameworks (MOFs) For Selective Dye Adsorption”, *Chemical Engineering Journal*, Vol. 399, No. 125346, 2020.
 94. Febrianto, J., A. Natasia, J. Sunarso, Y. Ju, N. Indraswati, and S. Ismadji, “Equilibrium and Kinetic Studies in Adsorption of Heavy Metals Using Biosorbent: A Summary of Recent Studies”, *Journal of Hazardous Materials*, Vol. 162, pp. 616–645, 2009.
 95. Salehi, M., H. Hashemipour, and M. Mirzaee, “Experimental Study of Influencing Factors and Kinetics in Catalytic Removal of Methylene Blue With TiO₂ Nanopowder”, *American Journal of Environmental Engineering*, Vol. 2, No. 1, pp. 1–7, 2012.
 96. Liu, Y., W. Jin, Y. Zhao, G. Zhang, and W. Zhang, “Enhanced Catalytic Degradation of Methylene Blue by α -Fe₂O₃ Graphene Oxide via Heterogeneous Photo-Fenton Reactions Graphene Oxide via Heterogeneous Photo-Fenton Reactions,” *Applied Catalysis B: Environmental*, Vol. 206, pp. 642–652, 2017.
 97. Kaya-Özkiper, K., A. Uzun, and S. Soyer-Uzun, “A Novel Alkali Activated Magnesium Silicate as an Effective and Mechanically Strong Adsorbent for Methylene Blue Removal”, *Journal of Hazardous Materials*, Vol. 424, 2022.
 98. Nikbin, I. M., M. Aliaghazadeh, Sh Charkhtab, and A. Fathollahpour, “Environmental Impacts and Mechanical Properties of Lightweight Concrete Containing Bauxite Residue (Red Mud)”, *Journal of Cleaner Production*, Vol. 172, pp. 2683–2694, Jan. 2018.
 99. Kurtoglu, S. F. and A. Uzun, “Red Mud As An Efficient, Stable, and Cost-Free Catalyst for CO_x-Free Hydrogen Production from Ammonia”, *Scientific Reports*,

Vol. 6, No. 32279, 2016.

100. S. F. Kurtoğlu, S. Soyer-Uzun, and A. Uzun, “Utilizing Red Mud Modified by Simple Treatments as a Support to Disperse Ruthenium Provides a High and Stable Performance for CO_x-Free Hydrogen Production from Ammonia,” *Catalysis Today*, Vol. 357, 2019.
101. Hertel, T. and Y. Pontikes, “Geopolymers, Inorganic Polymers, Alkali-Activated Materials and Hybrid Binders from Bauxite Residue (Red Mud) – Putting Things in Perspective”, *Journal of Cleaner Production*, Vol. 258, No. 120610, 2020.
102. Pontikes, Y. and G. N. Angelopoulos, “Bauxite Residue in Cement and Cementitious Applications: Current Status and a Possible Way Forward”, *Resources, Conservation and Recycling*, Vol. 73, pp. 53–63, 2013.
103. Raj, R. R., M. Á. Strength, and Á. M. Á. Red, “Microstructure Evolution in Ordinary Portland Cement – Metakaolin – Red Mud-Based Ternary Blended Cement”, *Journal of The Institution of Engineers (India): Series A*, Vol. 100, No. 4, pp. 707–718, 2019.
104. Villa, C., E. T. Pecina, R. Torres, and L. Gómez, “Geopolymer Synthesis Using Alkaline Activation of Natural Zeolite,” *Construction and Building Materials*, Vol. 24, No. 11, pp. 2084–2090, 2010.
105. Wang, L., L. Chen, J. L. Provis, D. C. W. Tsang, and C. Sun, “Accelerated Carbonation of Reactive MgO and Portland Cement Blends Under Flowing CO₂ Gas”, *Cement and Concrete Composites*, Vol. 106, No. 103489, 2020.
106. Xi, F., S. J. Davis, P. Ciais, D. Crawford-Brown, D. Guan, C. Pade, T. Shi, M. Syddall, J. Lv, and L. Ji et al., “Substantial Global Carbon Uptake by Cement Carbonation”, *Nature Geoscience*, Vol. 9, No. 12, pp. 880–883, 2016.
107. Fallah, M., K. J. D. MacKenzie, J. V Hanna, and S. J. Page, “Novel Photoactive Inorganic Polymer Composites of Inorganic Polymers With Copper(I) Oxide

- Nanoparticles,” *Journal of Materials Science*, Vol. 50, No. 22, pp. 7374–7383, 2015.
108. Al-Harashseh, M. S., K. Al Zboon, L. Al-Makhadmeh, M. Hararah, and M. Mahasneh, “Fly Ash Based Geopolymer for Heavy Metal Removal: A Case Study on Copper Removal”, *Journal of Environmental Chemical Engineering*, Vol. 3, No. 3, pp. 1669–1677, 2015.
 109. Falah, M., K. J. D. MacKenzie, R. Knibbe, S. J. Page, and J. V. Hanna, “New Composites Of Nanoparticle Cu (I) Oxide And Titania in a Novel Inorganic Polymer (Geopolymer) Matrix for Destruction of Dyes and Hazardous Organic Pollutants”, *Journal of Hazardous Materials*, Vol. 318, pp. 772–782, 2016.
 110. Ozer, I. and S. Soyer-Uzun, “Relations Between the Structural Characteristics and Compressive Strength in Metakaolin Based Geopolymers with Different Molar Si/Al Ratios”, *Ceramics International*, Vol. 41, No. 8, pp. 10192–10198, 2015.
 111. Rowles, M. and B. O. Connor, “Chemical Optimisation of the Compressive Strength of Aluminosilicate Geopolymers Synthesised by Sodium Silicate Activation of Metakaolinite”, *Journal of Materials Chemistry*, Vol. 13, pp. 1161–1165, 2003.
 112. Ye, N. *et al.*, “Synthesis and Characterization of Geopolymer from Bayer Red Mud with Thermal Pretreatment,” *Journal of the American Ceramic Society*, Vol. 97, No. 5, pp. 1652–1660, 2014.
 113. Nath, S. K. and S. Kumar, “Influence of Iron Making Slags on Strength and Microstructure of Fly Ash Geopolymer,” *Construction and Building Materials*, Vol. 38, pp. 924–930, 2013.
 114. Dimas, D. D., I. P. Giannopoulou, and D. Papias, “Utilization of Alumina Red Mud for Synthesis of Inorganic Polymeric Materials”, *Mineral Processing and Extractive Metallurgy Review*, Vol. 30, No. 3, pp. 211–239, 2009.
 115. Wang, W., J. Chen, M. Gao, Y. Huang, X. Zhang, and H. Yu, “Photocatalytic

- Degradation Of Atrazine By Boron-Doped TiO₂ With A Tunable Rutile/Anatase Ratio”, *Applied Catalysis B, Environmental*, Vol. 195, 2016.
116. Mejía de Gutiérrez, R., M. A. Villaquirán-Caicedo, and L. A. Guzmán-Aponte, “Alkali-Activated Metakaolin Mortars Using Glass Waste as Fine Aggregate: Mechanical and Photocatalytic Properties,” *Construction and Building Materials*, Vol. 235, 2020.
 117. Essawy, A. A. and S. Abd, “Physico-Mechanical Properties, Potent Adsorptive and Photocatalytic Efficacies of Sulfate Resisting Cement Blends Containing Micro Silica and Nano-TiO₂”, *Construction and Building Materials*, Vol. 52, pp. 1–8, 2014.
 118. Simonsen, M. E., C. Sønderby, Z. Li, and E. G. Søgaard, “XPS and FT-IR Investigation of Silicate Polymers”, *Journal of Materials Science*, Vol. 44, No. 8, pp. 2079–2088, 2009.
 119. Xie, J., D. Jiang, M. Chen, D. Li, J. Zhu, X., Li, and C. Yan, “Preparation and Characterization of Monodisperse Ce-Doped TiO₂ Microspheres with Visible Light Photocatalytic Activity”, *Colloids and Surfaces A : Physicochemical and Engineering Aspects*, Vol. 372, pp. 107–114, 2010.
 120. Xu, Z., W. Li, Y. Zhang, Z. Xue, X. Guo, and G. Zhang, “Facile Synthesis of Mesoporous Reduced Graphene Oxide Microspheres with Well-Distributed Fe₂O₃ Nanoparticles for Photochemical Catalysis”, *Industrial and Engineering Chemistry Research*, Vol. 55, p. 10591–10599, 2016.
 121. Chen, Y., Y. Wang, W. Li, Q. Yang, Q. Hou, L. Wei, L. Liu, F. Huang, and M. Ju, “Enhancement of Photocatalytic Performance with the Use of Noble-Metal-Decorated TiO₂ Nanocrystals as Highly Active Catalysts for Aerobic Oxidation Under Visible-Light Irradiation”, *Applied Catalysis B, Environmental*, Vol. 210, pp. 352–367, 2017.
 122. Yalçın, Y., M. Kiliç, and Z. Çınar, “Fe⁺³-Doped TiO₂: A Combined Experimental

- And Computational Approach To The Evaluation Of Visible Light Activity”, *Applied Catalysis B: Environmental*, Vol. 99, No. 3–4, pp. 469–477, 2010.
123. Ho, Y. S. and M. G., “A Comparison of Chemisorption Kinetic Models Applied to Pollutant Removal on Various Sorbents”, *Process Safety and Environmental Protection*, Vol. 76, No. 4, 1998.
 124. Baraka, A., “Adsorptive Removal of Tartrazine and Methylene Blue from Wastewater Using Melamine-Formaldehyde-Tartaric Acid Resin (And a Discussion About Pseudo Second Order Model)”, *Desalination and Water Treatment*, Vol. 44, pp. 128–141, 2012.
 125. Duxson, P., J. L. Provis, G. C. Lukey, S. W. Mallicoat, W. M. Kriven, and J. S. J. Van Deventer, “Understanding the Relationship Between Geopolymer Composition, Microstructure and Mechanical Properties”, *Colloids and Surfaces A: Physicochemical and Engineering Aspects*, Vol. 269, pp. 47–58, 2005.
 126. Hui, S., M. Abbas, and A. Zaini, “Development of Activated Carbon Pellets Using a Facile Low-Cost Binder for Effective Malachite Green Dye Removal”, *Journal of Cleaner Production*, Vol. 253, p. 119970, 2020.
 127. Othman, N. W., H. Radde, P. Yang, P. Yee, S. Ling, and P. Yan, “Enhancing Photocatalytic Activity of Titanium Dioxide Through Incorporation of MIL-53 (Fe) Toward Degradation of Organic Dye,” *Journal of the Chinese Chemical Society*, Vol. 66, No. 1, pp. 81–88, 2018.
 128. Khataee, A. R., M. Fathinia, and S. Aber, “Kinetic Modeling of Liquid Phase Photocatalysis on Supported TiO₂ Nanoparticles in a Rectangular Flat-Plate Photoreactor”, *Industrial and Engineering Chemistry Research*, Vol. 49, No. 24, pp. 12358–12364, 2010.
 129. Houas, A., H. Lachheb, M. Ksibi, E. Elaloui, C. Guillard, and J. M. Herrmann, “Photocatalytic Degradation Pathway of Methylene Blue in Water”, *Applied*

Catalysis B: Environmental, Vol. 31, No. 2, pp. 145–157, 2001.

130. Moztahida, M. and D. S. Lee, “Photocatalytic Degradation of Methylene Blue with P25/Graphene/Polyacrylamide Hydrogels: Optimization Using Response Surface Methodology”, *Journal of Hazardous Materials*, Vol. 400, No. 123314, 2020.
131. Zhao, D., G. Sheng, C. Chen, and X. Wang, “Enhanced Photocatalytic Degradation of Methylene Blue Under Visible Irradiation on Graphene@TiO₂ Dyade Structure”, *Applied Catalysis B: Environmental*, Vol. 111–112, pp. 303–308, 2012.
132. Egerton, T. A. and I. R. Tooley, “Effect Of Changes in TiO₂ Dispersion on Its Measured Photocatalytic Activity”, *The Journal of Physical Chemistry B*, pp. 5066–5072, 2004.
133. Strini, A., G. Roviello, L. Ricciotti, C. Ferone, F. Messina, L. Schiavi, D. Corsaro, and R. Cioffi, “TiO₂-Based Photocatalytic Geopolymers for Nitric Oxide Degradation”, *Materials*, Vol. 9, No. 7, pp. 1–13, 2016.
134. Li, Z. H. Hanafy, L. Zhang, L. Sellaoui, M. S. Netto, M. L. S. Oliveira, M. K. Seliem, G. L. Dotto, A. Bonilla-Petriciolet, and Q. Li, “Adsorption of Congo Red and Methylene Blue Dyes on an Ashitaba Waste and a Walnut Shell-Based Activated Carbon from Aqueous Solutions: Experiments, Characterization and Physical Interpretations”, *Chemical Engineering Journal*, Vol. 388, No. 124263, 2020.
135. Li, Q., Y. Li, X. Ma, Q. Du, K. Sui, D. Wang, C. Wang, H. Li, and Y. Xia, “Filtration and Adsorption Properties of Porous Calcium Alginate Membrane for Methylene Blue Removal From Water”, *Chemical Engineering Journal*, Vol. 316, pp. 623–630, 2017.
136. Russo, V., D. Masiello, M. Trifuoggi, M. Di Serio, and R. Tesser, “Design of an Adsorption Column for Methylene Blue Abatement over Silica: From Batch To Continuous Modeling”, *Chemical Engineering Journal*, Vol. 302, pp. 287–295, 2016.

137. World Health Organization, 2019 *Drinking-Water*, <https://www.who.int/en/news-room/fact-sheets/detail/drinking-water> (accessed May 02, 2021).
138. Punzi, M. F. Nilsson, A. Anbalagan, B. M. Svensson, K. Jönsson, B. Mattiasson, and M. Jonstrup, “Combined Anaerobic-Ozonation Process for Treatment of Textile Wastewater: Removal of Acute Toxicity and Mutagenicity,” *Journal of Hazardous Materials*, Vol. 292, pp. 52–60, 2015.
139. Dotto, G. L. and G. McKay, “Current Scenario and Challenges in Adsorption for Water Treatment”, *Journal of Environmental Chemical Engineering*, Vol. 8, No. 103988, 2020.
140. Lyu, H., B. Gao, F. He, A. R. Zimmerman, C. Ding, J. Tang, and J. C. Crittenden, “Experimental And Modeling Investigations of Ball-Milled Biochar for the Removal of Aqueous Methylene Blue”, *Chemical Engineering Journal*, Vol. 335, pp. 110–119, 2018.
141. Tang, X., G. Ran, J. Li, Z. Zhang, and C. Xiang, “Extremely Efficient and Rapidly Adsorb Methylene Blue Using Porous Adsorbent Prepared from Waste Paper: Kinetics And Equilibrium Studies”, *Journal of Hazardous Materials*, Vol. 402, No. 123579, 2021.
142. Ouyang, J., L. Zhou, Z. Liu, J. Y. Y. Heng, and W. Chen, “Biomass-Derived Activated Carbons for The Removal of Pharmaceutical Mircopollutants from Wastewater: A Review,” *Separation and Purification Technology*, Vol. 253, No. 117536, 2020.
143. Fan, S., Y. Wang, Z. Wang, J. Tang, J. Tang, and X. Li, “Removal of Methylene Blue from Aqueous Solution by Sewage Sludge-Derived Biochar: Adsorption Kinetics, Equilibrium, Thermodynamics and Mechanism”, *Journal of Environmental Chemical Engineering*, Vol. 5, No. 1, pp. 601–611, 2017.
144. Mouni, L. L. Belkhiri, J. C. Bollinger, A. Bouzaza, A. Assadi, A. Tiri, F. Dahmoune,

- K. Madani, and H. Remini, "Removal of Methylene Blue from Aqueous Solutions by Adsorption on Kaolin: Kinetic and Equilibrium Studies", *Applied Clay Science*, Vol. 153, pp. 38–45, 2018.
145. Yoo, D. K., B. N. Bhadra, and S. H. Jung, "Adsorptive Removal of Hazardous Organics from Water and Fuel with Functionalized Metal-Organic Frameworks: Contribution of Functional Groups", *Journal of Hazardous Materials*, Vol. 403, No. 123655, 2021.
146. Shao, N., S. Tang, S. Li, H. Chen, and Z. Zhang, "Defective Analcime / Geopolymer Composite Membrane Derived from Fly Ash for Ultrafast and Highly Efficient Filtration of Organic Pollutants", *Journal of Hazardous Materials*, Vol. 388, No. 121736, 2020.
147. Yousef, R. I., B. El-Eswed, M. Alshaaer, F. Khalili, and H. Khoury, "The Influence of Using Jordanian Natural Zeolite on the Adsorption, Physical, and Mechanical Properties of Geopolymers Products", *Journal of Hazardous Materials*, Vol. 165, No. 1–3, pp. 379–387, 2009.
148. Hua, P., L. Sellaoui, D. S. Franco, M. S. Netto, G. Dotto, A. Bajahzar, H. Belmabrouk, A.B. Petriciolet, and Z. Li "Adsorption of Acid Green and Procion Red on a Magnetic Geopolymer Based Adsorbent: Experiments, Characterization and Theoretical Treatment", *Chemical Engineering Journal*, Vol. 383, No. 123113, 2020.
149. Giustetto, R., O. Wahyudi, I. Corazzari, and F. Turci, "Chemical Stability and Dehydration Behavior of a Sepiolite/Indigo Maya Blue Pigment", *Applied Clay Science*, Vol. 52, No. 1–2, pp. 41–50, 2011.
150. Kuang, W., G. A. Facey, and C. Detellier, "Dehydration and Rehydration of Palygorskite and the Influence of Water on the Nanopores", *Clays and Clay Minerals*, Vol. 52, No. 5, pp. 635–642, 2004.
151. Sarikaya, Y., M. Önal, and A. D. Pekdemir, "Thermal Degradation Kinetics of

- Sepiolite”, *Clay Minerals*, Vol. 55, No. 1, pp. 96–100, 2020.
152. Galan, E., “The Minerology, Geology, And Main Occurences Of Sepiolite And Palygorskite Clays”, in *Natural Mineral Nanotubes: Properties and Applications*, 1st ed., P. Pasbakhsh, Ed. Apple Academic Press and CRC Press, 2015.
 153. Esteban-Cubillo, A., R. Pina-Zapardiel, J. S. Moya, M. F. Barba, and C. Pecharromán, “The Role of Magnesium on the Stability of Crystalline Sepiolite Structure”, *Journal of the European Ceramic Society*, Vol. 28, No. 9, pp. 1763–1768, 2008.
 154. Kurtoğlu, S. F., S. Sarp, C. Yılmaz, M.B. Yağcı, A. Motallebzadeh, S. Soyer-Uzun, A. Uzun, “CO_x-Free Hydrogen Production from Ammonia Decomposition over Sepiolite-Supported Nickel Catalysts”, *International Journal of Hydrogen Energy*, Vol. 43, No. 21, pp. 9954–9968, 2018.
 155. Pu, S., P. Duan, C. Yan, and D. Ren, “Influence of Sepiolite Addition on Mechanical Strength and Microstructure of Fly Ash-Metakaolin Geopolymer Paste”, *Advanced Powder Technology*, Vol. 27, No. 6, pp. 2470–2477, 2016.
 156. Kavas, T., E. Sabah, and M. S. Çelik, “Structural Properties of Sepiolite-Reinforced Cement Composite”, *Cement and Concrete Research*, Vol. 34, No. 11, pp. 2135–2139, 2004.
 157. Alkan, M., S. Çelikçapa, Ö. Demirbaş, and M. Dogan, “Removal of Reactive Blue 221 And Acid Blue 62 Anionic Dyes from Aqueous Solutions by Sepiolite”, *Dyes and Pigments*, Vol. 65, No. 3, pp. 251–259, 2005.
 158. Barroso-Solares, S., B. Merillas, P. Cimavilla-Román, M. A. Rodriguez-Perez, and J. Pinto, “Enhanced Nitrates-Polluted Water Remediation by Polyurethane/Sepiolite Cellular Nanocomposites”, *Journal of Cleaner Production*, Vol. 254, No. 120038, 2020.
 159. Frost, R. L. and Z. Ding, “Controlled Rate Thermal Analysis and Differential

- Scanning Calorimetry of Sepiolites and Palygorskites”, *Thermochimica Acta*, Vol. 397, No. 1–2, pp. 119–128, 2003.
160. Walczyk, A. A. Michalik, B. d. Napruszewska, J. K. Czerwenka, R. Karcz, D. Duraczynska, R. P. Socha, Z. Olejniczak, A. Gawel, A. Klimek, and et al., “New Insight into the Phase Transformation of Sepiolite upon Alkali Activation: Impact on Composition, Structure, Texture, and Catalytic/Sorptive Properties”, *Applied Clay Science*, Vol. 195, 2020.
161. Kamyab, S. M., S. Modabberi, C. D. Williams, and A. Badiei, “Synthesis of Sodalite from Sepiolite by Alkali Fusion Method and Its Application to Remove Fe^{3+} , Cr^{3+} , and Cd^{2+} From Aqueous Solutions”, *Environmental Engineering Science*, Vol. 37, No. 10, pp. 689–701, 2020.
162. David, E., “Mechanical Strength and Reliability of The Porous Materials Used as Adsorbents/ Catalysts and the New Development Trends”, *Archives of Materials Science and Engineering*, Vol. 73, No. 1, pp. 5–17, 2015.
163. Ghosal, P. S. and A. K. Gupta, “Determination of Thermodynamic Parameters from Langmuir Isotherm Constant-Revisited”, *Journal of Molecular Liquids*, Vol. 225, pp. 137–146, 2017.
164. Tahmasebi Yamchelou, M., D. Law, R. Brkljača, C. Gunasekara, J. Li, and I. Patnaikuni, “Geopolymer Synthesis Using Low-Grade Clays”, *Construction and Building Materials*, Vol. 268, 2021.
165. Suárez, M. and E. García-Romero, “Variability of the Surface Properties of Sepiolite”, *Applied Clay Science*, Vol. 67–68, pp. 72–82, 2012.
166. Önal, Y., M; Yilmaz, H; Sarikaya, “Some Physicochemical Properties of the White Sepiolite Known as Pipestone from Eskişehir, Turkey”, *Clays and Clay Minerals*, Vol. 56, No. 5, pp. 511–519, 2008.
167. Simão, L., A. De-Rossi, D. Hotza, M. J. Ribeiro, R. M. Novais, O. R. K. Montedo,

- and F. R. Pereira, “Zeolites-Containing Geopolymers Obtained from Biomass Fly Ash: Influence of Temperature, Composition, And Porosity”, *Journal of the American Ceramic Society*, Vol. 104, No. 2, pp. 803–815, 2021.
168. Van Jaarsveld, J. G. S., J. S. J. Van Deventer, and G. C. Lukey, “The Effect Of Composition and Temperature on the Properties of Fly Ash- and Kaolinite-Based Geopolymers”, *Chemical Engineering Journal*, Vol. 89, pp. 63–73, 2002.
169. Razak, S., F. F. Zainal, and S. R. Shamsudin, “Effect of Porosity and Water Absorption on Compressive Strength of Fly Ash Based Geopolymer and OPC Paste”, *IOP Conference Series: Materials Science and Engineering*, Vol. 957, No. 1, 2020.
170. Glukhovskiy, V., “Soil Silicates”, Gosstroyizdat, Kiev, 1959.
171. Provis, J. L., P. Duxson, J. S. J. van Deventer, and G. C. Lukey, “The Role of Mathematical Modelling and Gel Chemistry in Advancing Geopolymer Technology”, *Chemical Engineering Research and Design*, Vol. 83, No. 7 A, pp. 853–860, 2005.
172. Temuujin, J. and A. van Riessen, “Effect of Fly Ash Preliminary Calcination on the Properties of Geopolymer”, *Journal of Hazardous Materials*, Vol. 164, No. 2–3, pp. 634–639, 2009.
173. Perraki, T. and A. Orfanoudaki, “Study of Raw And Thermally Treated Sepiolite From the Mantoudi Area, Euboea, Greece: X-Ray Diffraction, TG/DTG/DTA and FTIR Investigations”, *Journal of Thermal Analysis and Calorimetry*, Vol. 91, No. 2, pp. 589–593, 2008.
174. Casal, B., J. Merino, J. M. Serratosa, and E. Ruiz-Hitzky, “Sepiolite-Based Materials for the Photo- and Thermal-Stabilization of Pesticides”, *Applied Clay Science*, Vol. 18, No. 5–6, pp. 245–254, 2001.
175. Olszówka, J. E. *et al.*, “New Insight into the Preferred Valency of Interlayer Anions in Hydrotalcite-Like Compounds: The Effect Of Mg/Al Ratio”, *Applied Clay Science*,

Vol. 155, pp. 84–94, 2018.

176. Bukas, V. J., M. Tsampodimou, V. Gionis, and G. D. Chryssikos, “Synchronous ATR Infrared and NIR-Spectroscopy Investigation of Sepiolite Upon Drying”, *Vibrational Spectroscopy*, Vol. 68, pp. 51–60, 2013.
177. Vicente-Rodríguez, M. A., M. Suarez, M. A. Bañares-Muñoz, and J. D. D. Lopez-Gonzalez, “Comparative FT-IR Study of the Removal of Octahedral Cations and Structural Modifications During Acid Treatment of Several Silicates,” *Spectrochimica Acta - Part A Molecular Spectroscopy*, Vol. 52, No. 13, pp. 1685–1694, 1996.
178. Rees, C. A., J. L. Provis, G. C. Lukey, and J. S. J. Van Deventer, “In Situ ATR-FTIR Study of the Early Stages of Fly Ash Geopolymer Gel Formation”, *Langmuir*, Vol. 23, No. 17, pp. 9076–9082, 2007.
179. Fernández-Jiménez, A., A. Palomo, I. Sobrados, and J. Sanz, “The Role Played by the Reactive Alumina Content in the Alkaline Activation of Fly Ashes”, *Microporous and Mesoporous Materials*, Vol. 91, No. 1–3, pp. 111–119, 2006.
180. Çetintaş, R. and S. Soyer-Uzun, “Relations Between Structural Characteristics and Compressive Strength in Volcanic Ash Based One-Part Geopolymer Systems”, *Journal of Building Engineering*, Vol. 20, pp. 130–136, 2018.
181. Provis, J. L. and S. A. Bernal, “Geopolymers and Related Alkali-Activated Materials”, *Annual Review of Materials Research*, Vol. 44, pp. 299–327, 2014.
182. Temuujin, J. A. Minjigmaa, B. Davaabal, U. Bayarzul, A. Ariunbold, T. Jadambaa, and K. J. D. Mackenzie, “Utilization of Radioactive High-Calcium Mongolian Flyash for the Preparation of Alkali-Activated Geopolymers for Safe Use as Construction Materials”, *Ceramics International*, Vol. 40, pp. 16475–16483, 2014.
183. Sarı Yılmaz, M., Y. Kalpaklı, and S. Pişkin, “Thermal Behavior and Dehydroxylation

- Kinetics of Naturally Occurring Sepiolite and Bentonite”, *Journal of Thermal Analysis and Calorimetry*, Vol. 114, No. 3, pp. 1191–1199, 2013.
184. Yang, T., Q. Wu, H. Zhu, and Z. Zhang, “Geopolymer with Improved Thermal Stability by Incorporating High-Magnesium Nickel Slag”, *Construction and Building Materials*, Vol. 155, pp. 475–484, 2017.
185. Zhou, F., C. Yan, Q. Sun, and S. Komarneni, “TiO₂/Sepiolite Nanocomposites Doped with Rare Earth Ions: Preparation, Characterization and Visible Light Photocatalytic Activity”, *Microporous and Mesoporous Materials*, Vol. 274, pp. 25–32, 2019.
186. Zhuang, G., Z. Zhang, and H. Chen, “Influence of the Interaction Between Surfactants and Sepiolite on the Rheological Properties and Thermal Stability of Organo-Sepiolite in Oil-Based Drilling Fluids,” *Microporous and Mesoporous Materials*, Vol. 272, pp. 143–154, 2018.
187. Vengatesan, M. R., S. Singh, S. Stephen, K. Prasanna, C. W. Lee, and V. Mittal, “Facile Synthesis of Thermally Reduced Graphene Oxide-Sepiolite Nanohybrid Via Intercalation and Thermal Reduction Method”, *Applied Clay Science*, Vol. 135, pp. 510–515, 2017.
188. Detweiler, Z. M., S. M. Wulfsberg, M. G. Frith, A. B. Bocarsly, and S. L. Bernasek, “The Oxidation and Surface Speciation of Indium and Indium Oxides Exposed to Atmospheric Oxidants”, *Surface Science*, Vol. 648, pp. 188–195, 2016.
189. Khalifa, A. Z. Ö. Cizer, Y. Pontikes, A. Heath, P. Patureau, S. A. Bernal, and A. T. M. Marsh, “Advances in Alkali-Activation of Clay Minerals”, *Cement and Concrete Research*, Vol. 132, No. 106050, 2020.
190. Chen Qingze, L. S., Zhu Runliang, “Self-Templating Synthesis of Silicon Nanorods from Nature Sepiolite for High-Performance Lithium-Ion Battery Anodes”, *Journal of Materials Chemistry A*, No. 15, 2018.
191. Mittal, V. K., S. Bera, R. Nithya, M. P. Srinivasan, S. Velmurugan, and S. V.

- Narasimhan, "Solid State Synthesis of Mg-Ni Ferrite and Characterization by XRD and XPS", *Journal of Nuclear Materials*, Vol. 335, No. 3, pp. 302–310, 2004.
192. Luukkonen, T., A. Heponiemi, H. Runtti, J. Pesonen, J. Yliniemi, and U. Lassi, "Application of Alkali-Activated Materials for Water and Wastewater Treatment: A Review", *Reviews in Environmental Science and Biotechnology*, Vol. 18, No. 2, pp. 271–297, 2019.
193. Ngulube, T., J. R. Gumbo, V. Masindi, and A. Maity, "An Update on Synthetic Dyes Adsorption onto Clay Based Minerals: A State-Of-Art Review", *Journal of Environmental Management*, Vol. 191, pp. 35–57, 2017.
194. Kashani, A., J. L. Provis, G. G. Qiao, and J. S. J. Van Deventer, "The Interrelationship Between Surface Chemistry and Rheology in Alkali Activated Slag Paste", *Construction and Building Materials*, Vol. 65, pp. 583–591, 2014.
195. Malik, R., D. S. Ramteke, and S. R. Wate, "Adsorption of Malachite Green on Groundnut Shell Waste Based Powdered Activated Carbon", *Waste Management*, Vol. 27, No. 9, pp. 1129–1138, 2007.
196. Liu, Y., C. Yan, Z. Zhang, Y. Gong, H. Wang, and X. Qiu, "A Facile Method for Preparation of Floatable and Permeable Fly Ash-Based Geopolymer Block", *Materials Letters*, Vol. 185, pp. 370–373, 2016.
197. Hameed, B. H., A. A. Ahmad, and N. Aziz, "Isotherms, Kinetics and Thermodynamics of Acid Dye Adsorption on Activated Palm Ash", *Chemical Engineering Journal*, Vol. 133, No. 1–3, pp. 195–203, 2007.
198. Kuang, Y., X. Zhang, and S. Zhou, "Adsorption of Methylene Blue in Water onto Activated Carbon by Surfactant Modification", *Water (Switzerland)*, Vol. 12, No. 2, pp. 1–19, 2020.
199. Toor, M. and B. Jin, "Adsorption Characteristics, Isotherm, Kinetics, and Diffusion

- of Modified Natural Bentonite for Removing Diazo Dye”, *Chemical Engineering Journal*, Vol. 187, pp. 79–88, 2012.
200. Siyal, A. A., M. R. Shamsuddin, N. E. Rabat, M. Zulfiqar, Z. Man, and A. Low, “Fly Ash Based Geopolymer for the Adsorption of Anionic Surfactant from Aqueous Solution”, *Journal of Cleaner Production*, Vol. 229, pp. 232–243, 2019.
201. Rasaki, S. A., Z. Bingxue, R. Guarecuco, T. Thomas, and Y. Minghui, “Geopolymer for Use in Heavy Metals Adsorption, and Advanced Oxidative Processes: A Critical Review”, *Journal of Cleaner Production*, Vol. 213, pp. 42–58, 2019.
202. Salimi, A. and A. Roosta, “Experimental Solubility and Thermodynamic Aspects of Methylene Blue in Different Solvents”, *Thermochimica Acta*, Vol. 675, pp. 134–139, 2019.
203. Al Ghouti, M. A. and R. S. Al Absi, “Mechanistic Understanding of the Adsorption and Thermodynamic Aspects of Cationic Methylene Blue Dye onto Cellulosic Olive Stones Biomass from Wastewater”, *Scientific Reports*, Vol. 10, No. 15928, 2020.
204. Jaimes, J. E., A. M. Montao, and C. P. González, “Geopolymer Derived from Bentonite: Structural Characterization and Evaluation as a Potential Sorbent of Ammonium in Waters”, *Journal of Physics: Conference Series*, Vol. 1587, No. 1, 2020.
205. Dai, Y., N. Zhang, C. Xing, Q. Cui, and Q. Sun, “The Adsorption , Regeneration and Engineering Applications of Biochar for Removal Organic Pollutants : A Review”, *Chemosphere*, Vol. 223, pp. 12–27, 2019.
206. Peng, X., Z. Luan, and H. Zhang, “Montmorillonite – Cu (II)/ Fe (III) Oxides Magnetic Material as Adsorbent for Removal of Humic Acid and Its Thermal Regeneration”, *Chemosphere*, Vol. 63, pp. 300–306, 2006.
207. El Mouzdahir, Y., A. Elmchaouri, R. Mahboub, A. Gil, and S. A. Korili, “Equilibrium

- Modeling for the Adsorption of Methylene Blue From Aqueous Solutions on Activated Clay Minerals”, *Desalination*, Vol. 250, No. 1, pp. 335–338, 2010.
208. Anfar, Z., R. El Haouti, S. Lhanafi, M. Benafqir, Y. Azougarh, and N. El Alem, “Treated Digested Residue During Anaerobic Co-Digestion of Agri-Food Organic Waste: Methylene Blue Adsorption, Mechanism and CCD-RSM Design”, *Journal of Environmental Chemical Engineering*, Vol. 5, No. 6, pp. 5857–5867, 2017.
209. Huang, W., Y. Hu, Y. Li, Y. Zhou, D. Niu, Z. Lei, and Z. Zhang, “Citric Acid-Crosslinked β -Cyclodextrin for Simultaneous Removal of Bisphenol A, Methylene Blue And Copper: The Roles of Cavity and Surface Functional Groups”, *Journal of the Taiwan Institute of Chemical Engineers*, Vol. 82, pp. 189–197, 2018.
210. Xu, B., C. Zheng, H. Zheng, Y. Wang, C. Zhao, C. Zhao, and Z. Zhang, “Polymer-Grafted Magnetic Microspheres for Enhanced Removal of Methylene Blue from Aqueous Solutions”, *RSC Advances*, Vol. 7, No. 74, pp. 47029–47037, 2017.
211. Donat, R., A. Akdogan, E. Erdem, and H. Cetisli, “Thermodynamics Of Pb^{2+} and Ni^{2+} Adsorption onto Natural Bentonite from Aqueous Solutions”, *Journal of Colloid and Interface Science*, Vol. 286, No. 1, pp. 43–52, 2005.
212. Thomas, J. M., “The Existence of Endothermic Adsorption”, *Journal of Chemical Education*, Vol. 38, No. 3, p. 138, 1961.
213. Lertcumfu, N. P. Jaita, S. Thammarong, S. Lamkhao, S. Tandorn, C. Randorn, T. Tunkasiri, and G. Rujjanagul, “Influence of Graphene Oxide Additive on Physical, Microstructure, Adsorption, and Photocatalytic Properties of Calcined Kaolinite-Based Geopolymer Ceramic Composites”, *Colloids and Surfaces A: Physicochemical and Engineering Aspects*, Vol. 602, No. 125080, 2020.
214. Papa, E., M. Mor, A. Natali Murri, E. Landi, and V. Medri, “Ice-Templated Geopolymer Beads for Dye Removal”, *Journal of Colloid and Interface Science*, Vol. 572, pp. 364–373, 2020.

215. Piallat, T., O. Grauby, D. Ferry, and A. Poulesquen, “Functionalized Geopolymer Foams for Cesium Removal from Liquid Nuclear Waste”, Vol. 269, 2020.
216. Vaou, V. and D. Papias, “Thermal Insulating Foamy Geopolymers from Perlite,” *Minerals Engineering*, Vol. 23, No. 14, pp. 1146–1151, 2010.
217. Kamseu, E., B. Nait-Ali, M. C. Bignozzi, C. Leonelli, S. Rossignol, and D. S. Smith, “Bulk Composition and Microstructure Dependence of Effective Thermal Conductivity of Porous Inorganic Polymer Cements”, *Journal of the European Ceramic Society*, Vol. 32, No. 8, pp. 1593–1603, 2012.
218. Petlitckaia, S. and A. Poulesquen, “Design Of Lightweight Metakaolin Based Geopolymer Foamed with Hydrogen Peroxide,” *Ceramics International*, Vol. 45, No. 1, pp. 1322–1330, 2019.
219. Novais, R. M., L. H. Buruberry, M. P. Seabra, and J. A. Labrincha, “Novel Porous Fly-Ash Containing Geopolymer Monoliths for Lead Adsorption from Wastewaters”, *Journal of Hazardous Materials*, Vol. 318, pp. 631–640, 2016.
220. Luukkonen, T., M. Sarkkinen, K. Kemppainen, J. Rämö, and U. Lassi, “Metakaolin Geopolymer Characterization and Application for Ammonium Removal from Model Solutions and Landfill Leachate”, *Applied Clay Science*, Vol. 119, pp. 266–276, 2016.
221. Novais, R. M., L. H. Buruberry, M. P. Seabra, D. Bajare, and J. A. Labrincha, “Novel Porous Fly Ash-Containing Geopolymers for pH Buffering Applications”, *Journal of Cleaner Production*, Vol. 124, pp. 395–404, 2016.
222. Ghanbari, M., A. M. Hadian, A. A. Nourbakhsh, and K. J. D. MacKenzie, “Modeling and Optimization of Compressive Strength and Bulk Density of Metakaolin-Based Geopolymer Using Central Composite Design: A Numerical and Experimental Study”, *Ceramics International*, Vol. 43, No. 1, pp. 324–335, 2017.
223. Abbasi, M., A. Ullah, B. Ismail, and M. Bilal, “Simultaneous Physisorption and Chemisorption of Reactive Orange 16 onto Hemp Stalks Activated Carbon: Proof

- from Isotherm Modeling”, *Biointerface Research in Applied Chemistry*, Vol. 7, No. 2, pp. 2021–2029, 2017.
224. Mojoudi, N., N. Mirghaffari, M. Soleimani, H. Shariatmadari, C. Belver, and J. Bedia, “Phenol Adsorption on High Microporous Activated Carbons Prepared from Oily Sludge: Equilibrium, Kinetic And Thermodynamic Studies”, *Scientific Reports*, Vol. 9, No. 1, pp. 1–12, 2019.
225. Cheung, W. H., Y. S. Szeto, and G. McKay, “Intraparticle Diffusion Processes During Acid Dye Adsorption onto Chitosan”, *Bioresource Technology*, Vol. 98, No. 15, pp. 2897–2904, 2007.
226. Milenković, D. D., P. V. Dašić, and V. B. Veljković, “Ultrasound-Assisted Adsorption of Copper(II) Ions on Hazelnut Shell Activated Carbon”, *Ultrasonics Sonochemistry*, Vol. 16, No. 4, pp. 557–563, 2009.
227. Román, S., B. Ledesma, J. F. González, A. Al-Kassir, G. Engo, and A. Álvarez-Murillo, “Two Stage Thermal Regeneration of Exhausted Activated Carbons. Steam Gasification of Effluents”, *Journal of Analytical and Applied Pyrolysis*, Vol. 103, pp. 201–206, 2013.
228. Benhalima, T. and H. Ferfera-harrar, “Eco-Friendly Porous Carboxymethyl Cellulose /Dextran Sulfate Composite Beads as Reusable and Efficient Adsorbents of Cationic Dye Methylene Blue”, *International Journal of Biological Macromolecules*, Vol. 132, pp. 126–141, 2019.
229. Mohan, S. V., N. C. Rao, and J. Karthikeyan, “Adsorptive Removal of Direct Azo Dye From Aqueous Phase onto Coal Based Sorbents: A Kinetic and Mechanistic Study”, *Journal of Hazardous Materials*, Vol. 90, pp. 189–204, 2002.
230. Jia, P., H. Tan, K. Liu, and W. Gao, “Removal Of Methylene Blue from Aqueous Solution by Bone Char”, *Applied Sciences*, Vol. 8, No. 10, p. 1903, 2018.

231. Fronczak, M., “Adsorption Performance of Graphitic Carbon Nitride-Based Materials: Current State of the Art”, *Journal of Environmental Chemical Engineering*, Vol. 8, No. 5, p. 104411, 2020.
232. Ren, B., Y. Xu, L. Zhang, and Z. Liu, “Carbon-Doped Graphitic Carbon Nitride as Environment-Benign Adsorbent for Methylene Blue Adsorption: Kinetics, Isotherm and Thermodynamics Study”, *Journal of the Taiwan Institute of Chemical Engineers*, Vol. 88, pp. 114–120, 2018.
233. Dong, G., Y. Zhang, Q. Pan, and J. Qiu, “A Fantastic Graphitic Carbon Nitride (g-C₃N₄) Material: Electronic Structure, Photocatalytic and Photoelectronic Properties”, *Journal of Photochemistry and Photobiology C: Photochemistry Reviews*, Vol. 20, No. 1, pp. 33–50, 2014.
234. Bian, J., Q. Li, C. Huang, J. Li, and Y. Guo, “Thermal Vapor Condensation of Uniform Graphitic Carbon Nitride Films with Remarkable Photocurrent Density for Photoelectrochemical Applications”, *Nano E*, pp. 353–361, 2015.
235. Liu, J., T. Zhang, Z. Wang, G. Dawson, and W. Chen, “Simple Pyrolysis of Urea into Graphitic Carbon Nitride with Recyclable Adsorption and Photocatalytic Activity” *Journal of Materials and Environmental Sciences*, Vol. 21, pp. 14398–14401, 2011.
236. Zhang, H., L. Guo, L. Zhao, B. Wan, and Y. Yang, “Switching Oxygen Reduction Pathway by Exfoliating Graphitic Carbon Nitride for Enhanced Photocatalytic Phenol Degradation”, *The Journal of Physical Chemistry Letters*, Vol. 6, No. 6, pp. 958-963, 2015.
237. Lee, I.H., J. Cho, K. H. Chae, M. K. Cho, J. Jung, J. Cho, H. J. Lee, H.C. Ham, and J. Y. Kim, “Polymeric Graphitic Carbon Nitride Nanosheet-Coated Amorphous Carbon Supports for Enhanced Fuel Cell Electrode Performance and Stability”, *Applied Catalysis B: Environmental*, Vol. 237, pp. 318–326, 2018.
238. Hui, J. *et al.*, “Graphitic-C₃N₄ Coated Floating Glass Beads for Photocatalytic Destruction of Synthetic and Natural Organic Compounds in Water Under UV Light”,

- Journal of Photochemistry & Photobiology, A: Chemistry*, Vol. 405, No. 112935, 2021.
239. Luo, Y., X. Wei, B. Gao, W. Zou, Y. Zheng, and Y. Yang, “Synergistic Adsorption-Photocatalysis Processes of Graphitic Carbon Nitrate (g-C₃N₄) for Contaminant Removal: Kinetics, Models, and Mechanisms”, *Chemical Engineering Journal*, Vol. 375, 2019.
240. Gaddam, S. K., R. Pothu, and R. Boddula, “Graphitic Carbon Nitride (g-C₃N₄) Reinforced Polymer Nanocomposite Systems—A Review”, *Polymer Composites*, Vol. 41, No. 2, pp. 430–442, 2020.
241. Choudhury, B. and P. K. Giri, “Isotype Heterostructure of Bulk and Nanosheets of Graphitic Carbon Nitride for Efficient Visible Light Photodegradation of Methylene Blue”, *RSC Advances*, Vol. 6, No. 30, pp. 24976–24984, 2016.
242. Wang, Y., X. Wang, and M. Antonietti, “Polymeric Graphitic Carbon Nitride as a Heterogeneous Organocatalyst: From Photochemistry to Multipurpose Catalysis to Sustainable Chemistry”, *Angewandte Chemie - International Edition*, Vol. 51, No. 1, pp. 68–89, 2012.
243. Wan, X. M. A. Khan, F. Wang, M. Xia, W. Lei, S. Zhu, C. Fu and Y. Ding, “Facile Synthesis of Protonated g-C₃N₄ and Acid-Activated Montmorillonite Composite with Efficient Adsorption Capacity for PO₄³⁻ and Pb(II),” *Chemical Engineering Research and Design*, Vol. 152, pp. 95–105, 2019.
244. Fronczak, M., K. Demby, P. Strachowski, M. Strawski, and M. Bystrzejewski, “Graphitic Carbon Nitride Doped With The S-Block Metals: Adsorbent for the Removal of Methyl Blue and Copper(II) Ions”, *Langmuir*, Vol. 34, No. 25, pp. 7272–7283, 2018.
245. Zhang, J. H., M. J. Wei, Z. W. Wei, M. Pan, and C. Y. Su, “Ultrathin Graphitic Carbon Nitride Nanosheets For Photocatalytic Hydrogen Evolution”, *ACS Applied Nano*

Materials, Vol. 3, No. 2, pp. 1010–1018, 2020.

246. Zhu, B., P. Xia, W. Ho, and J. Yu, “Isoelectric Point and Adsorption Activity of Porous g-C₃N₄”, *Applied Surface Science*, Vol. 344, pp. 188–195, 2015.
247. Yao S., S. Xue, S. Peng, M. Jing, X. Qian, X. Shen, and T. Li, “Synthesis of Graphitic Carbon Nitride at Different Thermal-Pyrolysis Temperature of Urea and Its Application in Lithium–Sulfur Batteries”, *Journal of Materials Science: Materials in Electronics*, Vol. 29, No. 20, pp. 17921–17930, 2018.
248. Sun, Z., C. Li, X. Du, S. Zheng, and G. Wang, “Facile Synthesis of Two Clay Minerals Supported Graphitic Carbon Nitride Composites as Highly Efficient Visible-Light-Driven Photocatalysts”, *Journal of Colloid and Interface Science*, Vol. 511, pp. 268–276, 2018.
249. Panneri, S., P. Ganguly, M. Mohan, and B. N. Nair, “Photoregenerable, Bifunctional Granules of Carbon-Doped g-C₃N₄ as Adsorptive Photocatalyst for the Efficient Removal of Tetracycline Antibiotic”, *ACS Sustainable Chemistry & Engineering*, 2017.
250. Hatamie, A., F. Marahel, and A. Sharifat, “Green Synthesis of Graphitic Carbon Nitride Nanosheet (g-C₃N₄) and Using It as a Label-Free Fluorosensor for Detection of Metronidazole via Quenching of the Fluorescence”, *Talanta*, Vol. 176, pp. 518–525, 2018.
251. Rees, C. A., J. L. Provis, G. C. Lukey, and J. S. J. Van Deventer, “Attenuated Total Reflectance Fourier Transform Infrared Analysis of Fly Ash Geopolymer Gel Aging”, *Langmuir*, Vol. 23, pp. 8170–8179, 2007.
252. Li, S., L. Huang, H. Zhang, Z. Huang, Q. Jia, and S. Zhang, “Adsorption Mechanism of Methylene Blue on Oxygen-Containing Functional Groups Modified Graphitic Carbon Spheres: Experiment and DFT Study”, *Applied Surface Science*, Vol. 540, No. 148386, 2021.

253. Wang, X., Z. Zhao, Z. Shu, Y. Chen, J. Zhou, L. T. Tian, W. Wang, Y. Tan, and N. Sun, "One-Pot Synthesis of Metakaolin/ g-C₃N₄ Composite for Improved Visible-Light Photocatalytic H₂ Evolution", *Applied Clay Science*, Vol. 166, pp. 80–87, 2018.
254. Li, H. J., B. W. Sun, L. Sui, D. J. Qian, and M. Chen, "Preparation of Water-Dispersible Porous g-C₃N₄ with Improved Photocatalytic Activity by Chemical Oxidation", *Physical Chemistry Chemical Physics*, Vol. 17, No. 5, pp. 3309–3315, 2015.
255. Zhang, L., J. Zhang, Y. Xia, M. Xun, H. Chen, and X. Liu, "Metal-Free Carbon Quantum Dots Implant Graphitic Carbon Nitride: Enhanced Photocatalytic Dye Wastewater Purification with Simultaneous Hydrogen Production", *Molecular Sciences*, 2020.
256. López, F. J., S. Sugita, M. Tagaya, and T. Kobayashi, "Metakaolin-Based Geopolymers for Targeted Adsorbents to Heavy Metal Ion Separation", *Journal of Materials Science and Chemical Engineering*, Vol. 2, pp. 16–27, 2014.
257. Maleki, A., M. Mohammad, Z. Emdadi, N. Asim, M. Azizi, and J. Safaei, "Adsorbent Materials Based on a Geopolymer Paste for Dye Removal From Aqueous Solutions", *Arabian Journal of Chemistry*, Vol. 13, No. 1, pp. 3017–3025, 2020.
258. Labbez, C., B. Jönsson, I. Pochard, A. Nonat, and B. Cabane, "Surface Charge Density and Electrokinetic Potential of Highly Charged Minerals: Experiments and Monte Carlo Simulations on Calcium Silicate Hydrate," *Journal of Physical Chemistry B*, Vol. 110, No. 18, pp. 9219–9230, 2006.
259. Deng, Y., C. Feng, L. Tang, G. Zeng, Z. Chen, and M. Zhang, "Nanohybrid Photocatalysts for Heavy Metal Pollutant Control", in *Nanohybrid and Nanoporous Materials for Aquatic Pollution Control*, Vol. 2, Elsevier Inc., 2018, pp. 125–153.
260. Pathania, D., S. Sharma, and P. Singh, "Removal of Methylene Blue by Adsorption onto Activated Carbon Developed from Ficus Carica Bast," *Arabian Journal of*

Chemistry, Vol. 10, pp. 1445–1451, 2017.

261. Aljeboree, A. M., A. N. Alshirifi, and A. F. Alkaim, “Kinetics and Equilibrium Study for the Adsorption of Textile Dyes on Coconut Shell Activated Carbon”, *Arabian Journal of Chemistry*, Vol. 10, pp. 3381–3393, 2017.
262. Shah, L. A., M. Khan, R. Javed, M. Sayed, M. S. Khan, A. Khan, and M. Ullah, “Superabsorbent Polymer Hydrogels With Good Thermal and Mechanical Properties for Removal of Selected Heavy Metal Ions”, *Journal of Cleaner Production*, Vol. 201, pp. 78–87, 2018.
263. Xiao, G., Y. Wang, S. Xu, P. Li, C. Yang, Y. Jin, Q. Sun, and H. Su, “Superior Adsorption Performance of Graphitic Carbon Nitride Nanosheets for Both Cationic and Anionic Heavy Metals From Wastewater”, *Chinese Journal of Chemical Engineering*, Vol. 27, No. 2, pp. 305–313, 2019.
264. Paul, D. R., R. Sharma, S. P. Nehra, and A. Sharma, “Effect of Calcination, Temperature, pH and Catalyst Loading on Photodegradation Efficiency of Urea Derived Graphitic Carbon Nitride Towards Methylene Blue Dye Solution”, *RSC Advances*, Vol. 9, pp. 15381–15391, 2019.
265. Li, X., “Preparation and Adsorption Properties of Biochar/g-C₃N₄ Composites for Methylene Blue in Aqueous Solution,” *Journal of Nanomaterials*, Vol. 2019, 2019.
266. Hu, R., X. Wang, S. Dai, D. Shao, T. Hayat, and A. Alsaedi, “Application of Graphitic Carbon Nitride for the Removal Of Pb(II) and Aniline From Aqueous Solutions”, *Chemical Engineering Journal*, Vol. 260, pp. 469–477, 2015.
267. Wang, L. and A. Wang, “Adsorption Properties of Congo Red from Aqueous Solution onto Surfactant-Modified Montmorillonite”, *Journal of Hazardous Materials*, Vol. 160, pp. 173–180, 2008.
268. Shen, C., C. Chen, T. Wen, Z. Zhao, X. Wang, and A. Xu, “Superior Adsorption

- Capacity of g-C₃N₄ for Heavy Metal Ions From Aqueous Solutions”, *Journal of Colloid and Interface Science Superior*, Vol. 456, pp. 7–14, 2015.
269. Park, J. E., G. B. Lee, B. U. Hong, and S. Y. Hwang, “Regeneration of Activated Carbons Spent by Waste Water Treatment Using KOH Chemical Activation”, *Applied Sciences (Switzerland)*, Vol. 9, No. 23, 2019.
270. Fronczak, M., M. Krajewska, K. Demby, and M. Bystrzejewski, “Extraordinary Adsorption of Methyl Blue onto Sodium-Doped Graphitic Carbon Nitride”, *Journal of Physical Chemistry C*, Vol. 121, No. 29, pp. 15756–15766, 2017.
271. Tian, L., J. Li, F. Liang, J. Wang, S. Li, H. Zhang, and S. Zhang, “Molten Salt Synthesis of Tetragonal Carbon Nitride Hollow Tubes and Their Application for Removal of Pollutants from Wastewater,” *Applied Catalysis B: Environmental*, Vol. 225, pp. 307–313, 2018.
272. Zhang Y., Z. Zhou, Y. Zhen, Q. Zhou, J. Wang, A.Liu, S. Liu, and Y. Zhang, “Reversible Assembly of Graphitic Carbon Nitride 3D Network for Highly Selective Dyes Absorption and Regeneration”, *ACS Nano*, Vol. 10, No. 9, pp. 9036–9043, 2016.
273. Chegeni, M. and N. Dehghan, “Preparation of Phosphorus Doped Graphitic Carbon Nitride Using a Simple Method and Its Application for Removing Methylene Blue”, *Physical Chemistry Research*, Vol. 8, No. 1, pp. 31–44, 2020.

APPENDIX A: SUPPLEMENTARY INFORMATION 1

Table A.1. Chemical compositions (wt%) of MK, raw RM, and calcined RM used in Chapter 2.

Material	SiO ₂	Al ₂ O ₃	TiO ₂	Fe ₂ O ₃	K ₂ O	CaO	MgO	Na ₂ O
MK	56.21	41.04	1.15	0.36	0.46	0.09	0.07	-
RM	11.67	14.02	5.78	37.1	0.31	1.1	0.23	9.39
Calcined RM	12.59	16.85	5.94	37.45	0.31	1.44	0.2	10.55

Table A.2. The amounts of raw materials (in g) used in geopolymer synthesis, corresponding molar Si/Al and Al/Na ratios, and synthesis conditions used in RMGP synthesis in Chapter 2.

Sample	Anatase (g)	RM (g)	MK (g)	Na ₂ Si ₃ O ₇ solution (g)	NaOH (g)	Molar Si/Al	Molar Al/Na	Activating solution	Thermal treatment
0%A-RMGP	0	2	8	14.01	1.69	2	0.83	NaOH & Na ₂ Si ₃ O ₇	1 day 60 °C + 1 week 25 °C
0.4%A-RMGP	0.1	2	8	14.01	1.69	2	0.83	NaOH & Na ₂ Si ₃ O ₇	1 day 60 °C + 1 week 25 °C
1.2%A-RMGP	0.3	2	8	14.01	1.69	2	0.83	NaOH & Na ₂ Si ₃ O ₇	1 day 60 °C + 1 week 25 °C
1.9%A-RMGP	0.5	2	8	14.01	1.69	2	0.83	NaOH & Na ₂ Si ₃ O ₇	1 day 60 °C + 1 week 25 °C
3.7%A-RMGP	1	2	8	14.01	1.69	2	0.83	NaOH & Na ₂ Si ₃ O ₇	1 day 60 °C + 1 week 25 °C

Table A.3. BET surface area, average pore size, pore volume, and density of RMGP samples.

Sample	BET surface area (m ² /g)	Average pore size (Å)	Pore volume (cm ³ /g)	Density (g/cm ³)
0%A-RMGP	15.9	409.2	0.1	2.10 ± 0.01
0.4%A-RMGP	12.9	535.3	0.1	2.13 ± 0.03
1.2%A-RMGP	17.2	472.6	0.2	2.10 ± 0.01
1.9%A-RMGP	11.5	446.7	0.1	2.11 ± 0.01
3.7%A-RMGP	14.0	443.2	0.1	2.11 ± 0.03

Figure A.1 shows the XRD patterns of the raw materials used as aluminosilicate sources for the geopolymer synthesis. XRD pattern of MK shows an amorphous feature located at approximately 23° together with quartz as an impurity. Calcined RM, on the other hand, has mainly an iron oxide phase, hematite. FTIR spectra of raw materials MK and RM are given in Figure A.2. FTIR band observed at 1080 cm⁻¹ in MK corresponds to the presence of Si–O bonds that is present in amorphous SiO₂ and peak at 811 cm⁻¹ refers to the AlO₄ tetrahedra in MK [1]. The feature at a lower frequency of 445 cm⁻¹ is related with the presence of Al–O–Si bridge aluminosilicates [2, 3]. A small contribution observed at a higher frequency of 1436 cm⁻¹ in RM is attributed to the presence of carbonate bonds [4], whereas band observed at 980 cm⁻¹ refers to the asymmetric stretching vibrations of Si–O–Si and Al–O–Si bonds. Features detected table at 550 and 440 cm⁻¹ are most possibly associated with stretching vibrations of Fe–O bonds sourcing from the iron content of RM [5]. The band located at 680 cm⁻¹ is assigned to the symmetric stretching vibrations of Si–O–Si and Al–O–Si bonds [6].

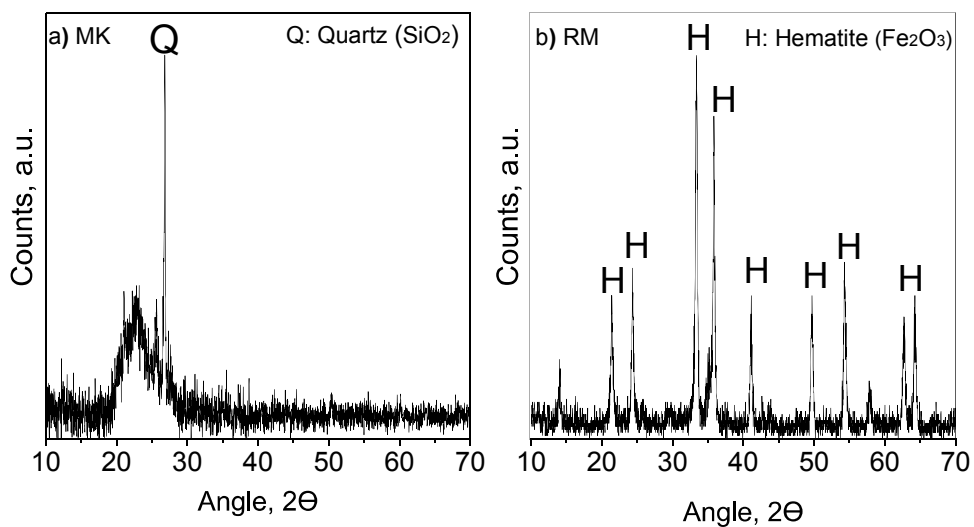


Figure A.1. XRD patterns of the aluminosilicate sources used for geopolymer synthesis: a) MK b) Calcined RM.

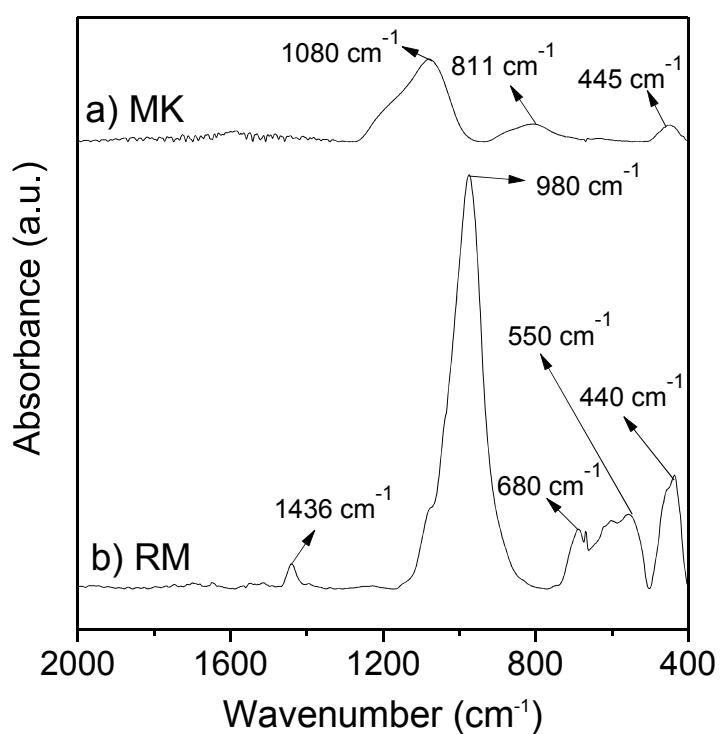


Figure A.2. FTIR spectra of raw materials a) MK and b) RM.

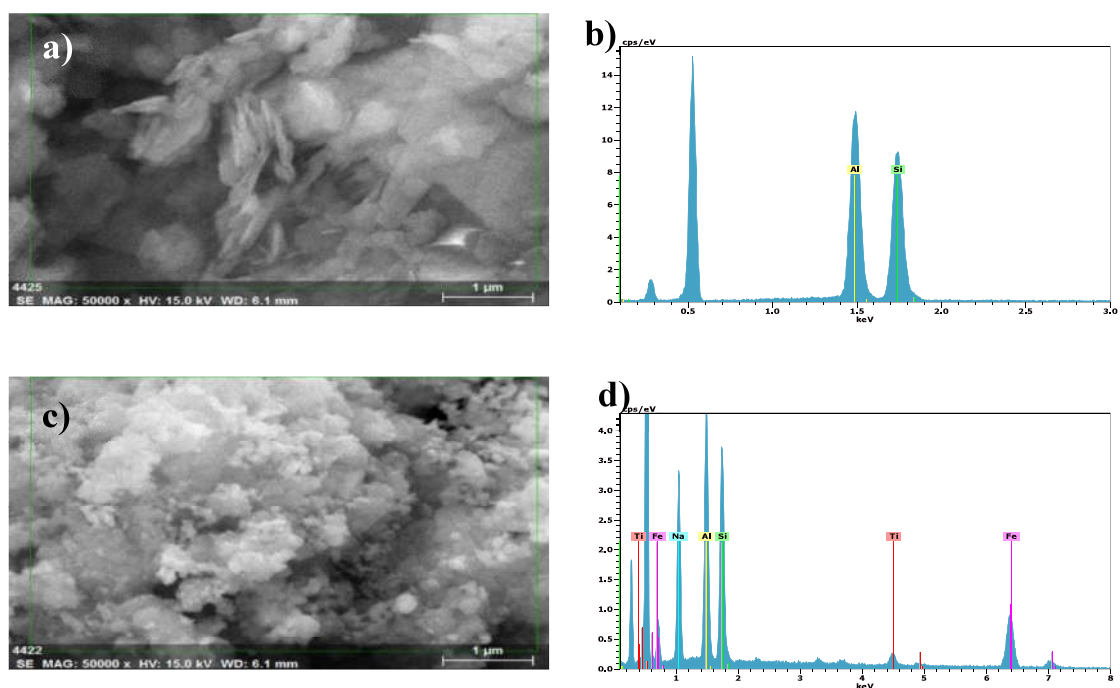


Figure A.3. SEM images and corresponding EDS spectrum of a) MK, b) EDS spectrum of MK, c) calcined RM, d) EDS spectrum of calcined RM.

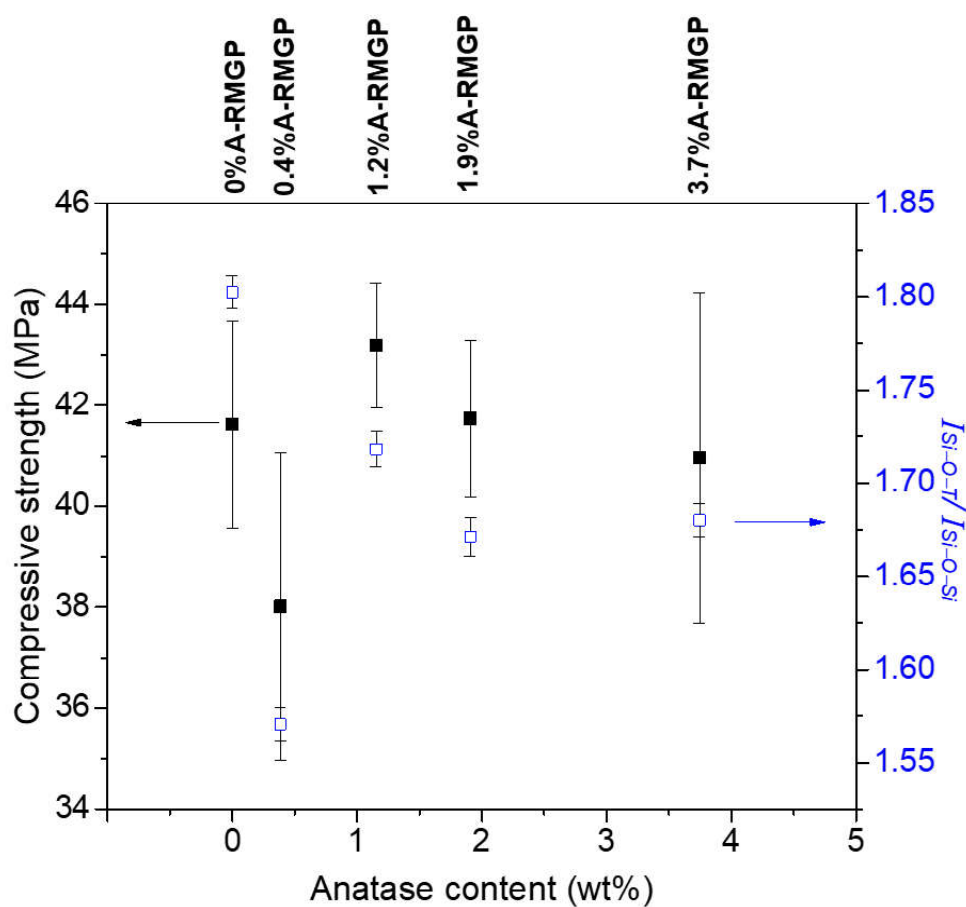


Figure A.4. Evolution of the ratios of the intensities of the bands corresponding to Si–O–T and Si–O–Si vibrations ($I_{Si-O-T}/I_{Si-O-Si}$ ratio) and compressive strength of geopolymers as a function of anatase content (wt%) in the geopolymer pastes. Error bars represent the standard errors.

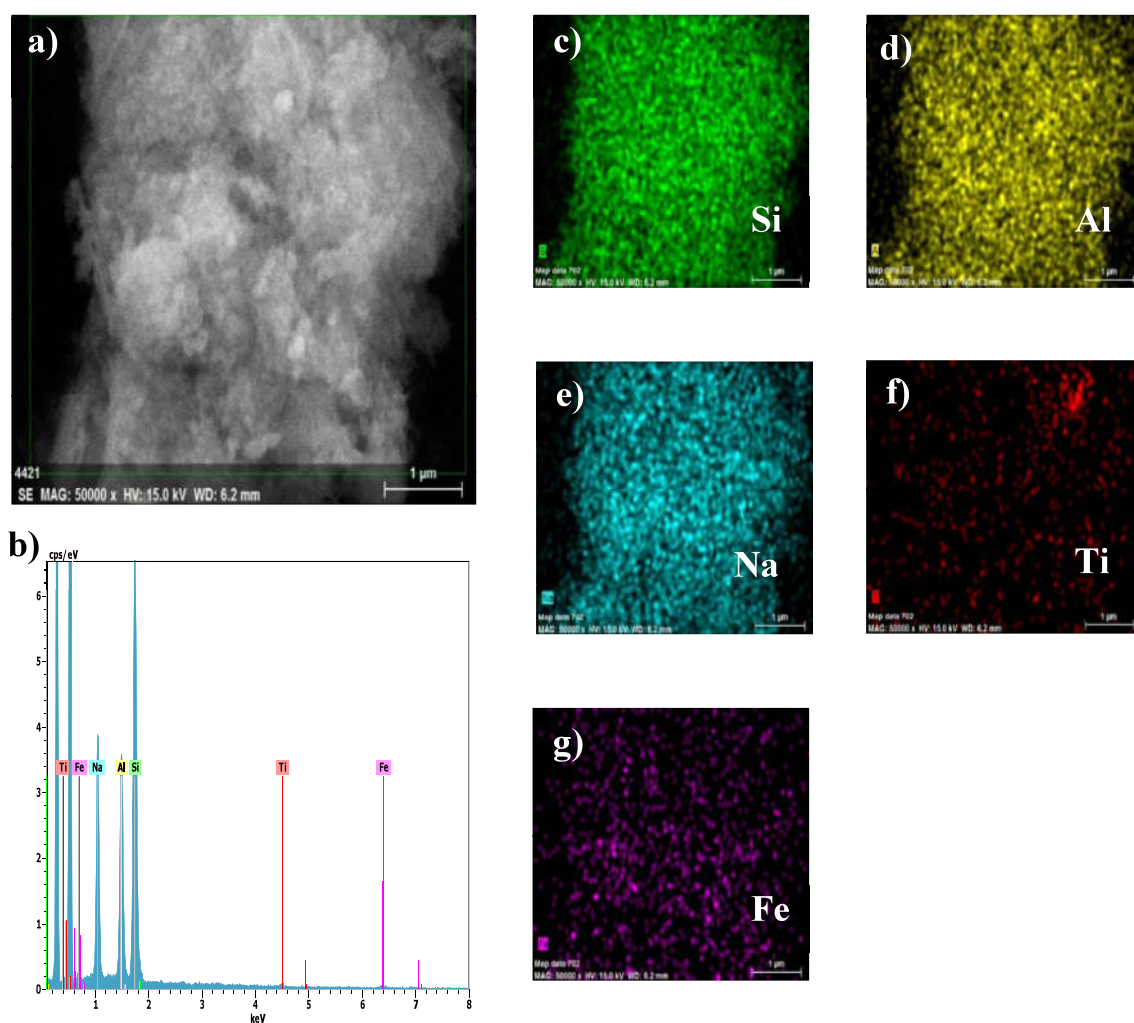


Figure A.5. SEM image, corresponding elemental analysis and EDS mapping of 0%A-RMGP: a) SEM image b) Elemental analysis and EDS mapping, including elemental analysis, c) Si, d) Al, e) Na, f) Ti, and g) Fe.

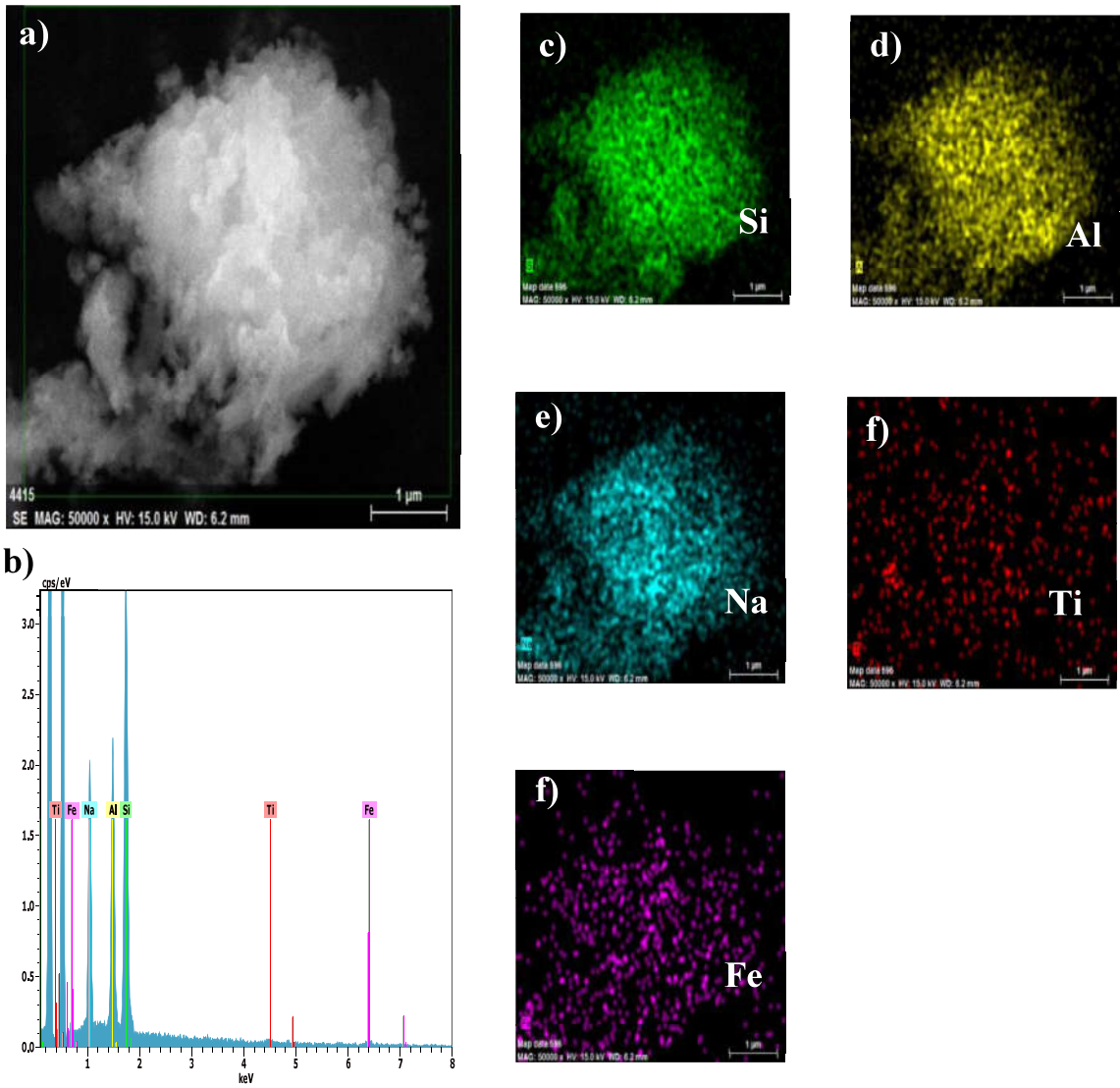


Figure A.6. SEM image, corresponding elemental analysis and EDS mapping of 0.4%A-RMGP: a) SEM image b) Elemental analysis and EDS mapping, including elemental analysis, c) Si, d) Al, e) Na, f) Ti, and g) Fe.

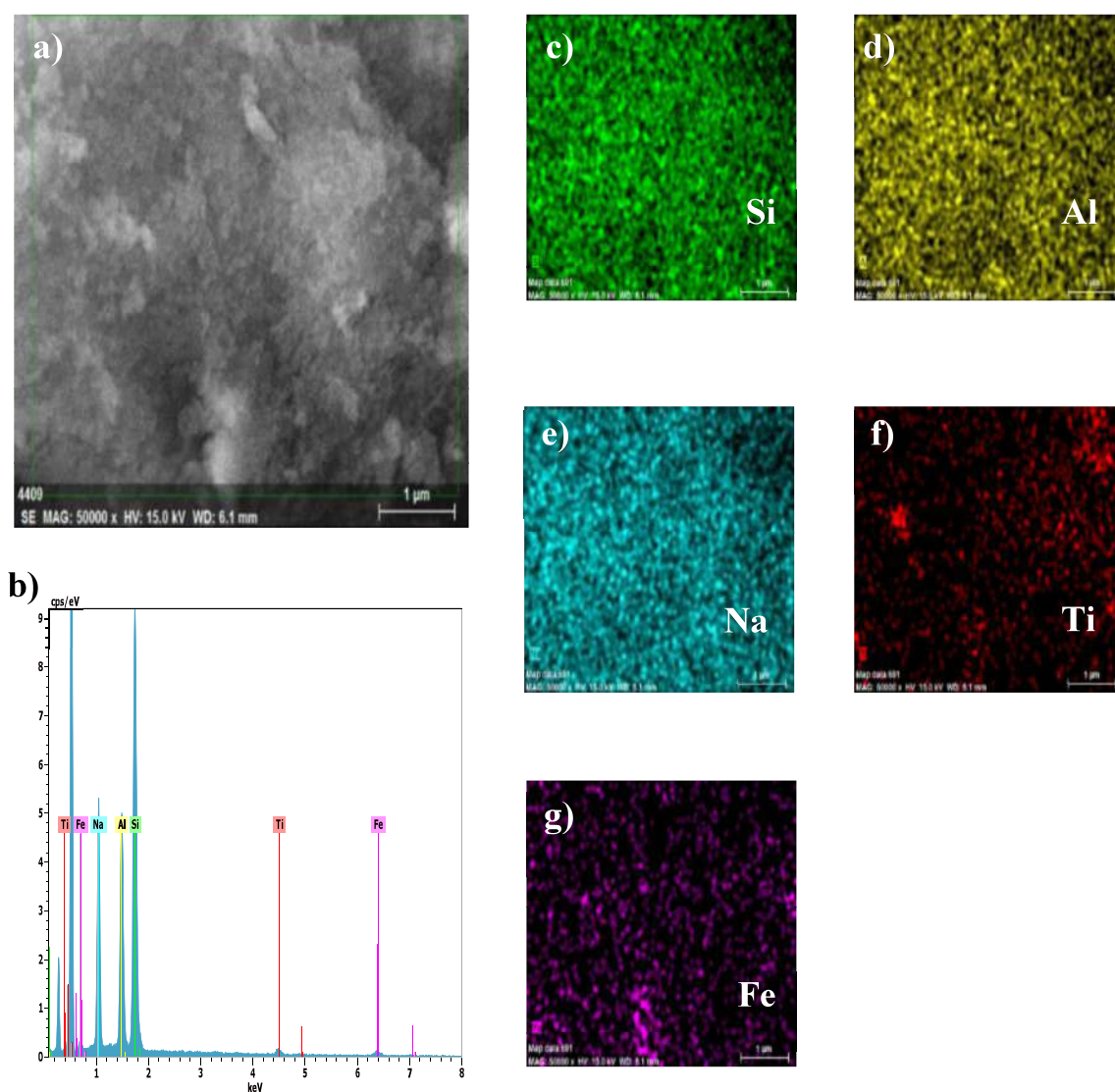


Figure A.7. SEM image, corresponding elemental analysis and EDS mapping of 1.2%A-RMGP: a) SEM image b) Elemental analysis and EDS mapping, including elemental analysis, c) Si, d) Al, e) Na, f) Ti, and g) Fe.

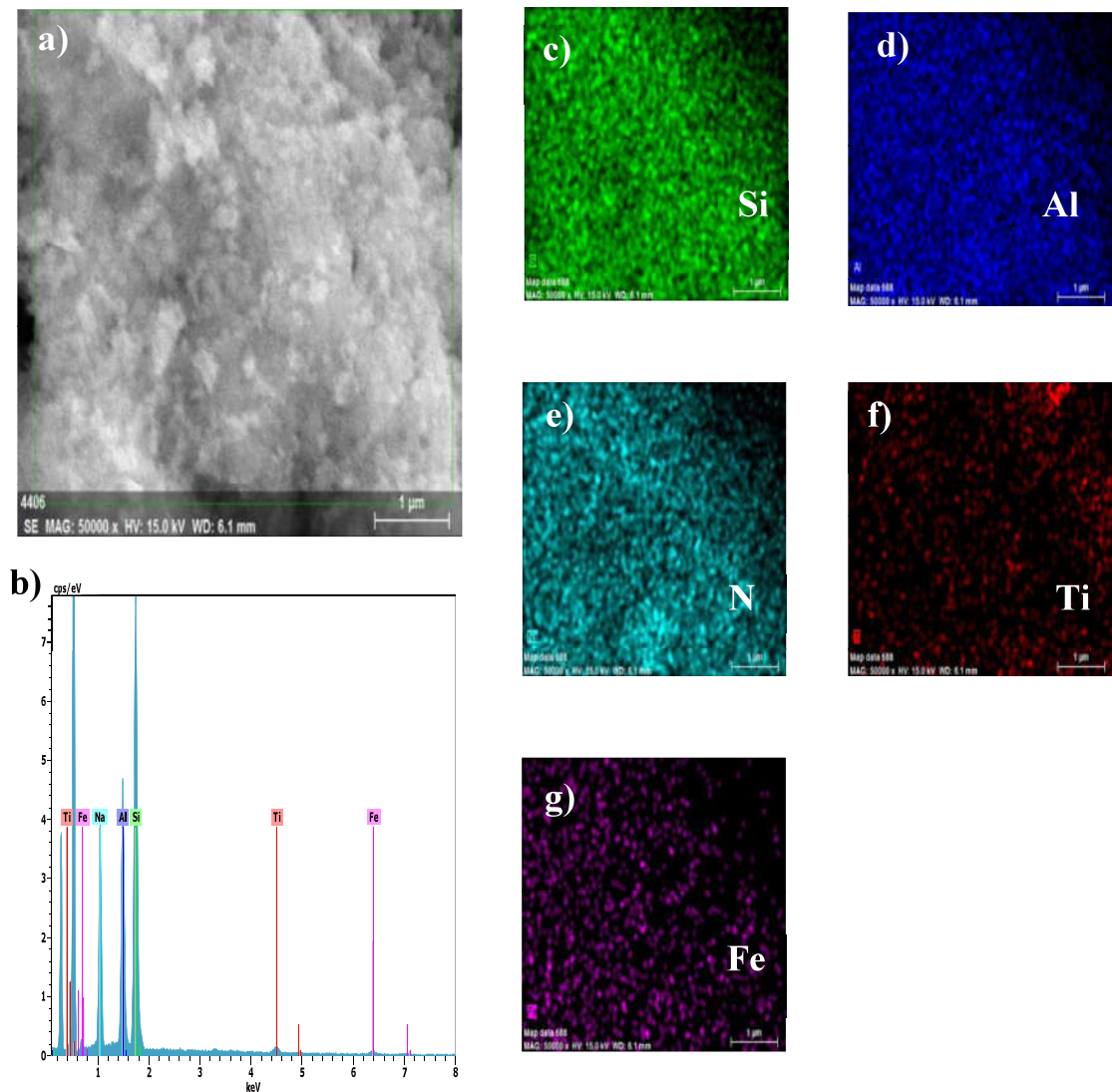


Figure A.8. SEM image, corresponding elemental analysis and EDS mapping of 1.9%A-RMGP: a) SEM image b) Elemental analysis and EDS mapping, including elemental analysis, c) Si, d) Al, e) Na, f) Ti, and g) Fe.

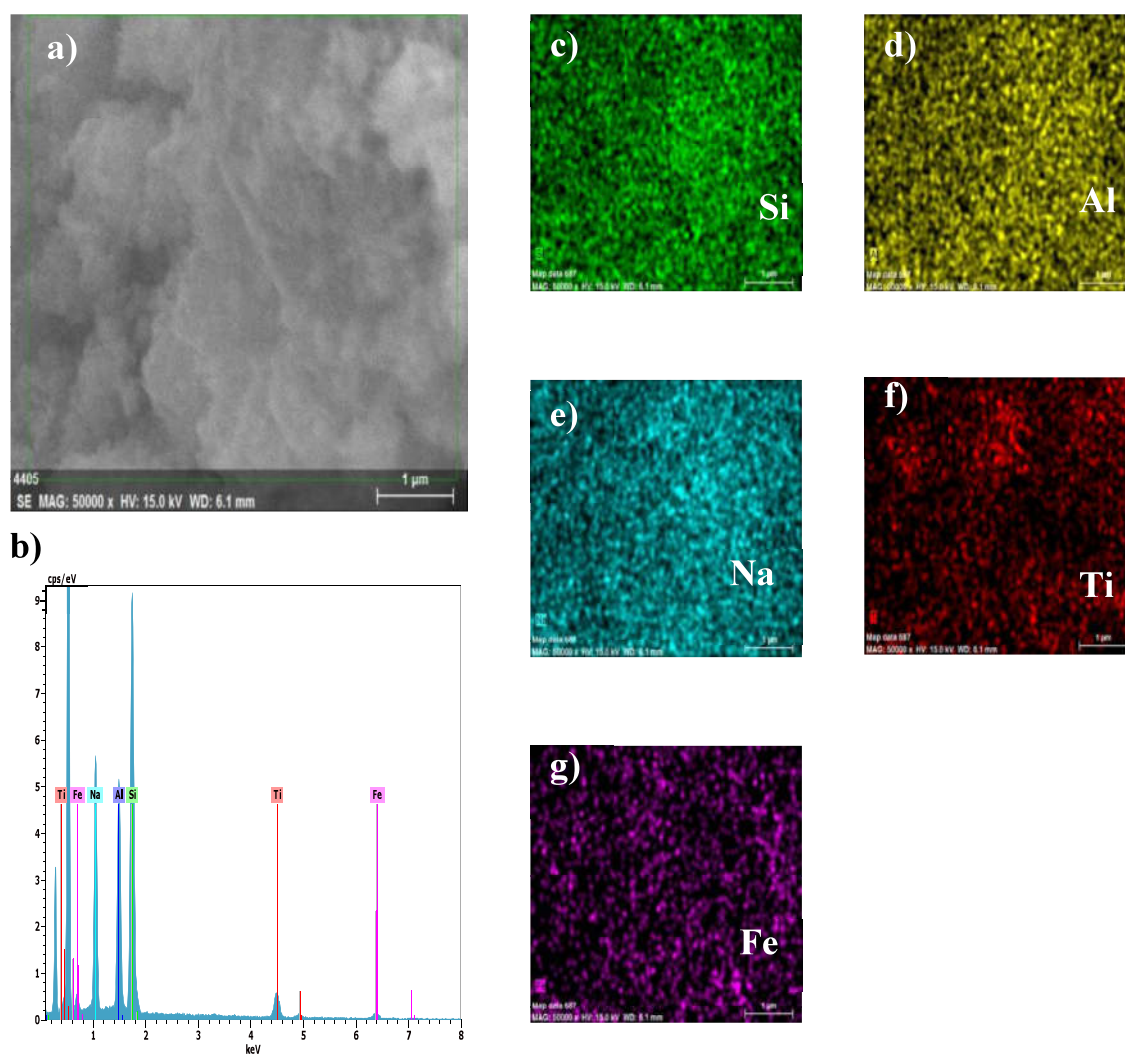


Figure A.9. SEM image, corresponding elemental analysis and EDS mapping of 3.7%A-RMGP: a) SEM image b) Elemental analysis and EDS mapping, including elemental analysis, c) Si, d) Al, e) Na, f) Ti, and g) Fe.

Table A.4. Atomic % of Si, Al, Na, Fe, and Ti in geopolymers which are calculated by taking the average of values from EDS spectra recorded from 3 spots.

Sample	Atomic %				
	Si	Al	Na	Fe	Ti
0%A-RMGP	48	21.9	26.3	3.56	0.74
0.4%A-RMGP	46.2	20.5	28.3	3.18	1.79
1.2%A-RMGP	46.2	20.5	26.1	3.54	2.18
1.9%A-RMGP	43.2	21.8	24.9	2.48	3.08
3.7%A-RMGP	42.4	18.8	23.9	3.19	6.99

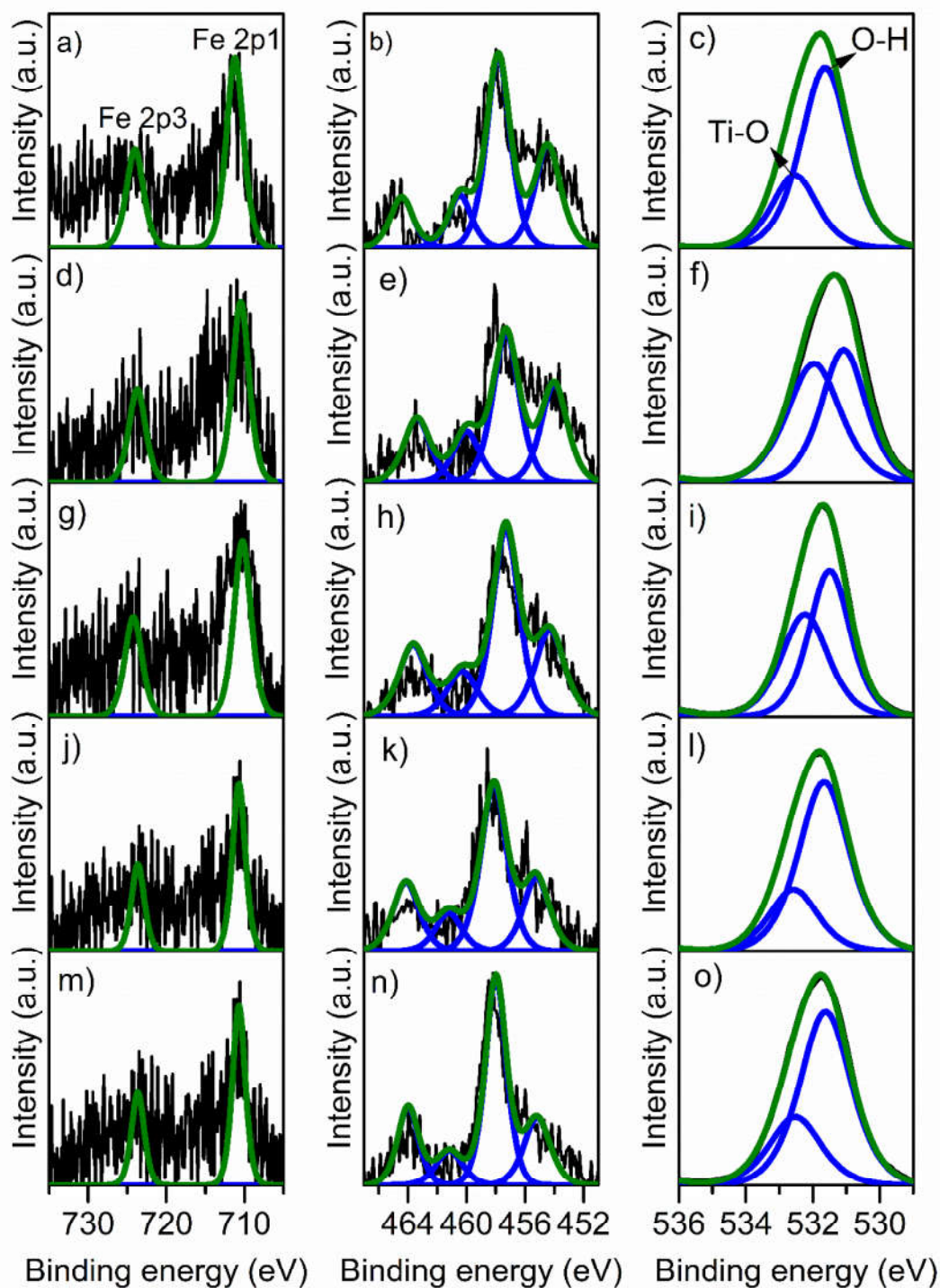


Fig A.10. XPS patterns of a) Fe 2p, b) Ti 2p, and c) O 1s spectrum of 0%A-RMGP, d) Fe 2p, e) Ti 2p and f) O 1s spectrum of 0.4%A-RMGP, g) Fe 2p, h) Ti 2p, and i) O 1s spectrum of 1.2%A-RMGP, j) Fe 2p, k) Ti 2p and l) O 1s spectrum of 1.9%A-RMGP, m) Fe 2p, n) Ti 2p, and o) O 1s spectrum of 3.7%A-RMGP (Blue lines: fitted individual peaks, green lines: envelope of all fitted peaks).

Table A.5. Binding energy values of geopolymers derived from XPS analysis.

Sample	O 1s position (eV)		Ti 2p positions (eV)				Fe 2p positions (eV)	
	~531 Ti-O	~532 Ti-OH	~454 Ti 2p _{3/2}	~457 Ti 2p _{3/2}	~460 Ti 2p _{1/2}	~464 Ti 2p _{1/2}	~711 Fe 2p _{3/2}	~723 Fe 2p _{1/2}
0%A-RMGP	531.63	532.54	454.45	457.82	460.45	464.42	711.21	724.01
0.4%A-RMGP	530.98	531.87	454.01	457.29	460.01	463.38	710.48	723.72
1.2%A-RMGP	530.86	531.7	454.31	457.31	460.31	463.64	710.07	723.57
1.9%A-RMGP	531.66	532.57	455.22	458.12	461.22	464.12	710.71	723.64
3.7%A-RMGP	531.62	532.52	455.17	457.99	461.17	463.99	710.55	723.35

Table A.6. Atomic % of Ti and Fe obtained from fitted peak information of Ti 2p and Fe 2p XP spectra.

Sample	Ti (at%)	Fe (at%)
0%A-RMGP	0.3	0.22
0.4%A-RMGP	0.33	0.18
1.2%A-RMGP	0.36	0.19
1.9%A-RMGP	0.42	0.17
3.7%A-RMGP	0.46	0.19

Table A.7. Band gap and maximum absorption wavelength values.

Sample	Band gap, E _g (eV)	Maximum absorption wavelength, λ _{max} (nm)
MK	3.6	390
RM	2.2	590
0%A-RMGP	2.9	600
0.4%A-RMGP	2.9	600
1.2%A-RMGP	2.9	600
1.9%A-RMGP	3.2	604
3.7%A-RMGP	3.2	604

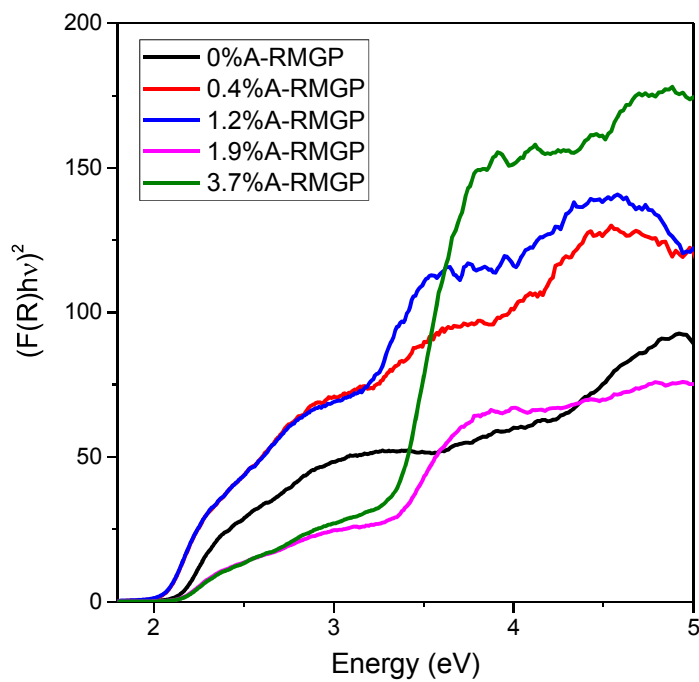


Fig A.11. Band gap values of geopolymers calculated by Kubelka Munk function.

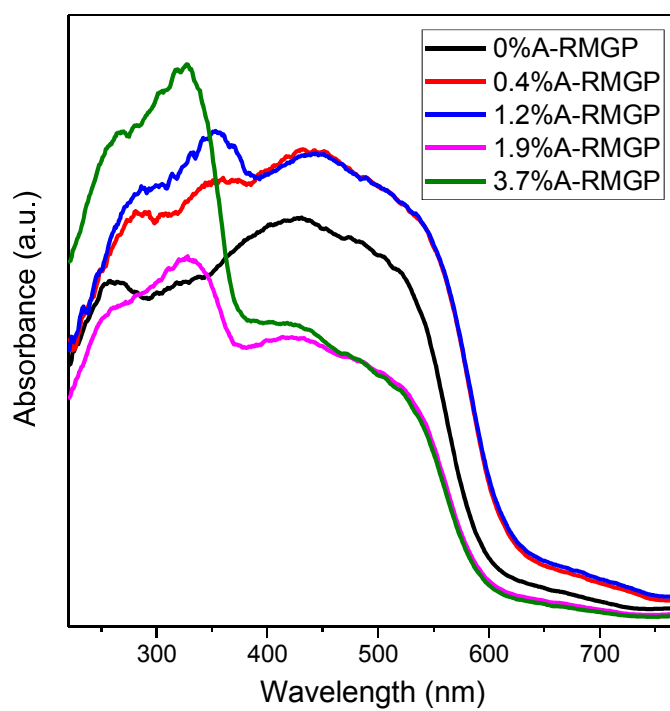


Fig A.12. Absorbance vs wavelength values of the geopolymers.

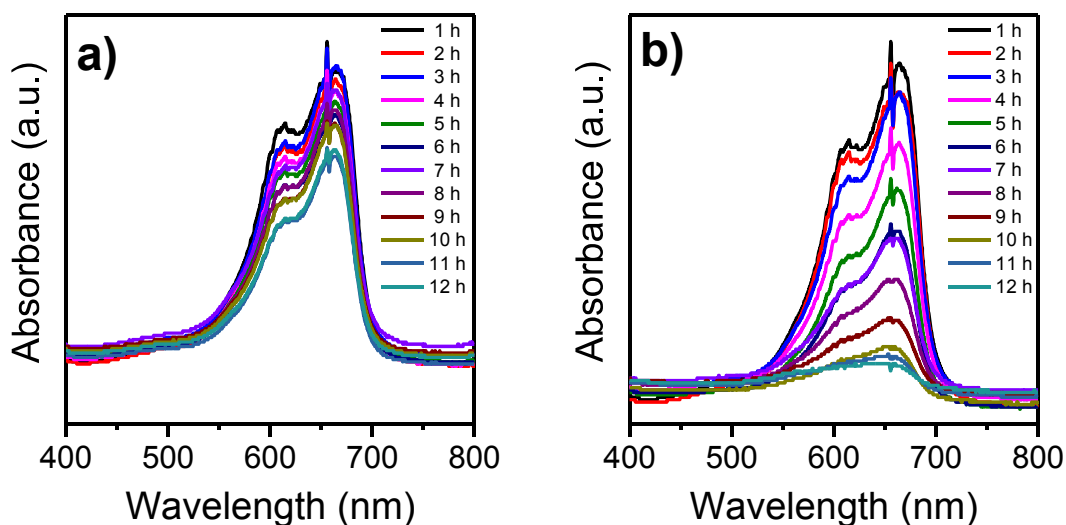


Figure A.13. UV-Vis spectrum of a) 0%A-RMGP and b) 10%A-RMGP.

- A1. Ozer, I. and S. Soyer-Uzun, “Relations Between the Structural Characteristics and Compressive Strength in Metakaolin Based Geopolymers with Different Molar Si/Al Ratios”, *Ceramics International*, Vol. 41, No. 8, pp. 10192–10198, 2015.
- A2. Kaya, K. and S. Soyer-Uzun, “Evolution of Structural Characteristics and Compressive Strength in Red Mud–Metakaolin Based Geopolymer Systems”, *Ceramics International*, Vol. 42, No. 6, pp. 7406–7413, 2016.
- A3. Kim, W., D. Choi, and S. Kim, “Sonochemical Synthesis of Zeolite A From Metakaolinite in NaOH Solution”, *Materials Transactions*, Vol. 51, No. 9, pp. 1694–1698, 2010.
- A4. Nath, S. K. and S. Kumar, “Influence of Iron Making Slags on Strength And Microstructure of Fly Ash Geopolymer”, *Construction and Building Materials*, Vol. 38, pp. 924–930, 2013.
- A5. Rendon, J. L. and C. J. Serna, “IR Spectra of Powder Hematite: Effects of Particle Size and Shape”, *Clay Minerals*, Vol. 16, No. 4, pp. 375–382, 1981.

- A6. Ye, N., J. Yang, X. Ke, J. Zhu, Y. Li, C. Xiang, H. Wang, and B. Xiao, "Synthesis and Characterization of Geopolymer from Bayer Red Mud with Thermal Pretreatment", *Journal of the American Ceramic Society*, Vol. 97, No. 5, pp. 1652–1660, 2014.

APPENDIX B: SUPPLEMENTARY INFORMATION 2

Table B.1. Chemical compositions (wt%) of Sep and 1 h 750 °C calcined Sep used in this study, as determined by XRF spectroscopy.

Material	SiO ₂	MgO	CaO	Al ₂ O ₃	TiO ₂	Fe ₂ O ₃	K ₂ O	SO ₃
Sep	42.8	24.8	11	1.20	0.10	0.50	0.20	0.10
Calcined Sep	52.7	31.0	13.61	1.51	0.07	0.59	0.25	0.09

Table B.2. The amounts of raw materials (in g) used in the synthesis of Sep based AAM, corresponding molar Si/Mg and Na/Mg ratios, and synthesis conditions used in Sep-AAM synthesis in this study.

Sample	Calcined Sep (g)	Na ₂ Si ₃ O ₇ solution (g)	Molar Si/Mg	Molar Na/Mg	Activating solution	Thermal treatment
Sep-AAM	6	19.08	3	1	Na ₂ Si ₃ O ₇	1 day 40 °C + 1 week 25 °C

Table B.3. Mix quantities per unit volume (kg m⁻³) calculated based on densities of the raw materials and assuming that the volumes of the components are additive. Corresponding wt% are given in parenthesis for the Sep-AAM paste.

Sample	Calcined Sep	Na ₂ Si ₃ O ₇ solution	Total
Sep-AAM	368.2 (23.9)	1171.2 (76.1)	1539.4 (100)

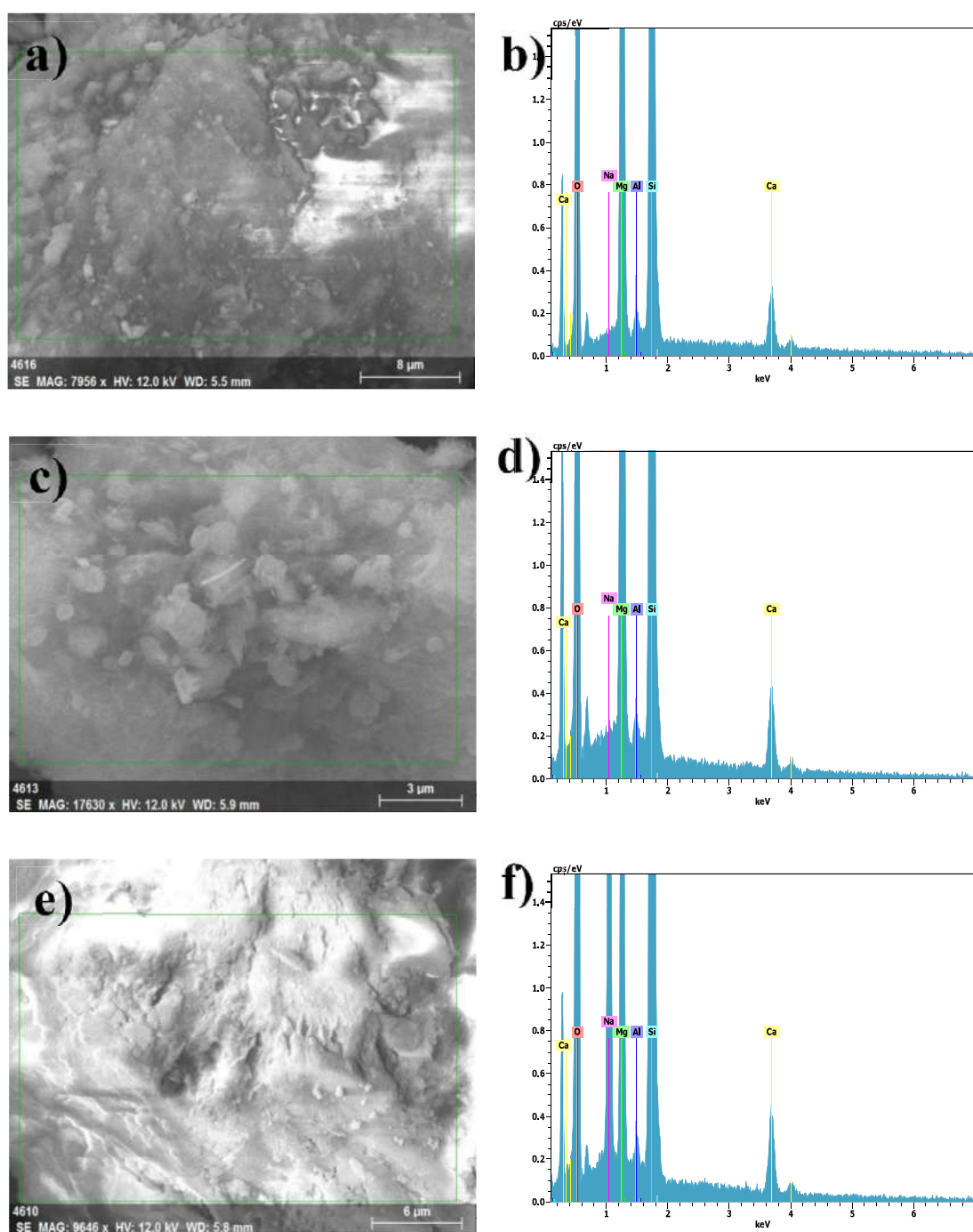


Figure B.1. SEM images and corresponding EDX spectra of materials: a) As-received Sep (at a magnification of 7956 \times), b) EDX spectrum of green \square in a), c) Calcined Sep (at a magnification of 17630 \times), d) EDX spectrum of green \square in c), e) Sep-AAM (at a magnification of 9646 \times), f) EDX spectrum of green \square in e).

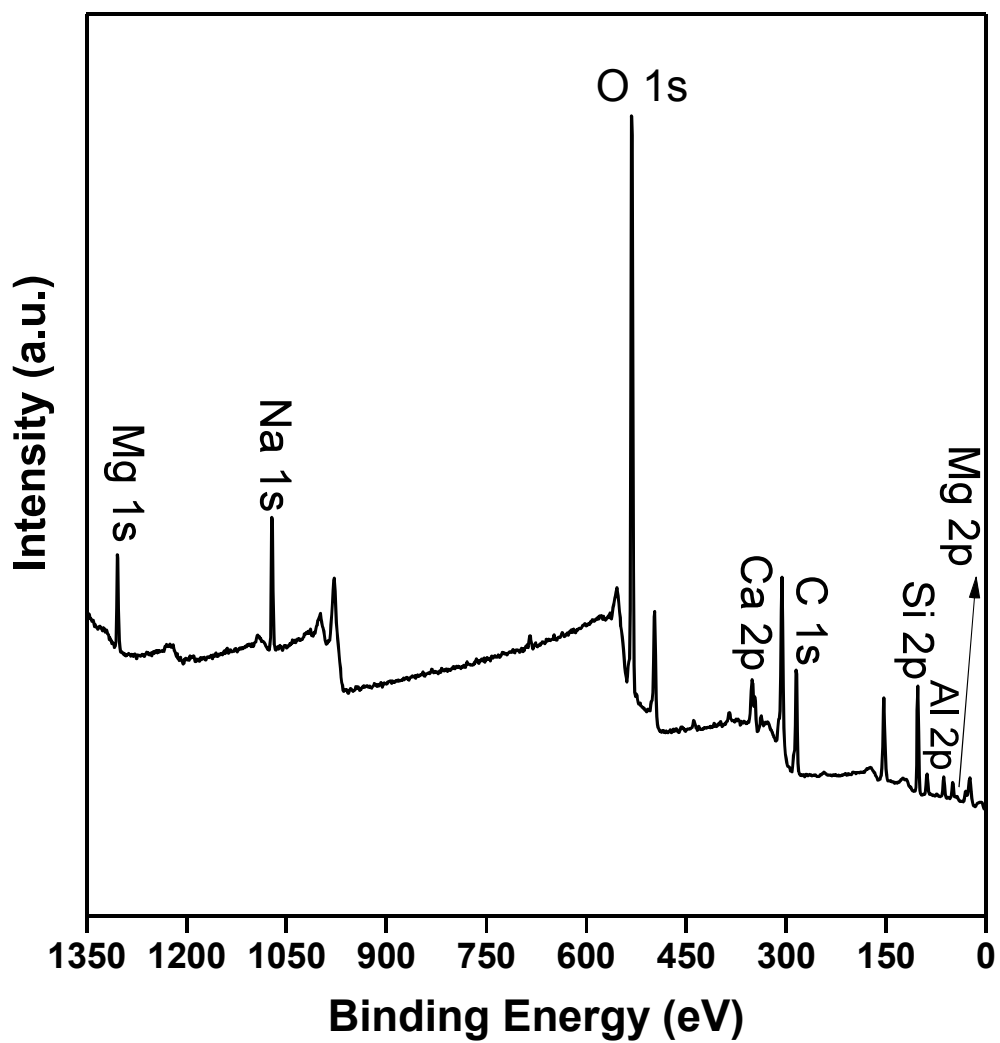


Figure B.2. XPS pattern of survey spectrum for Sep-AAM.

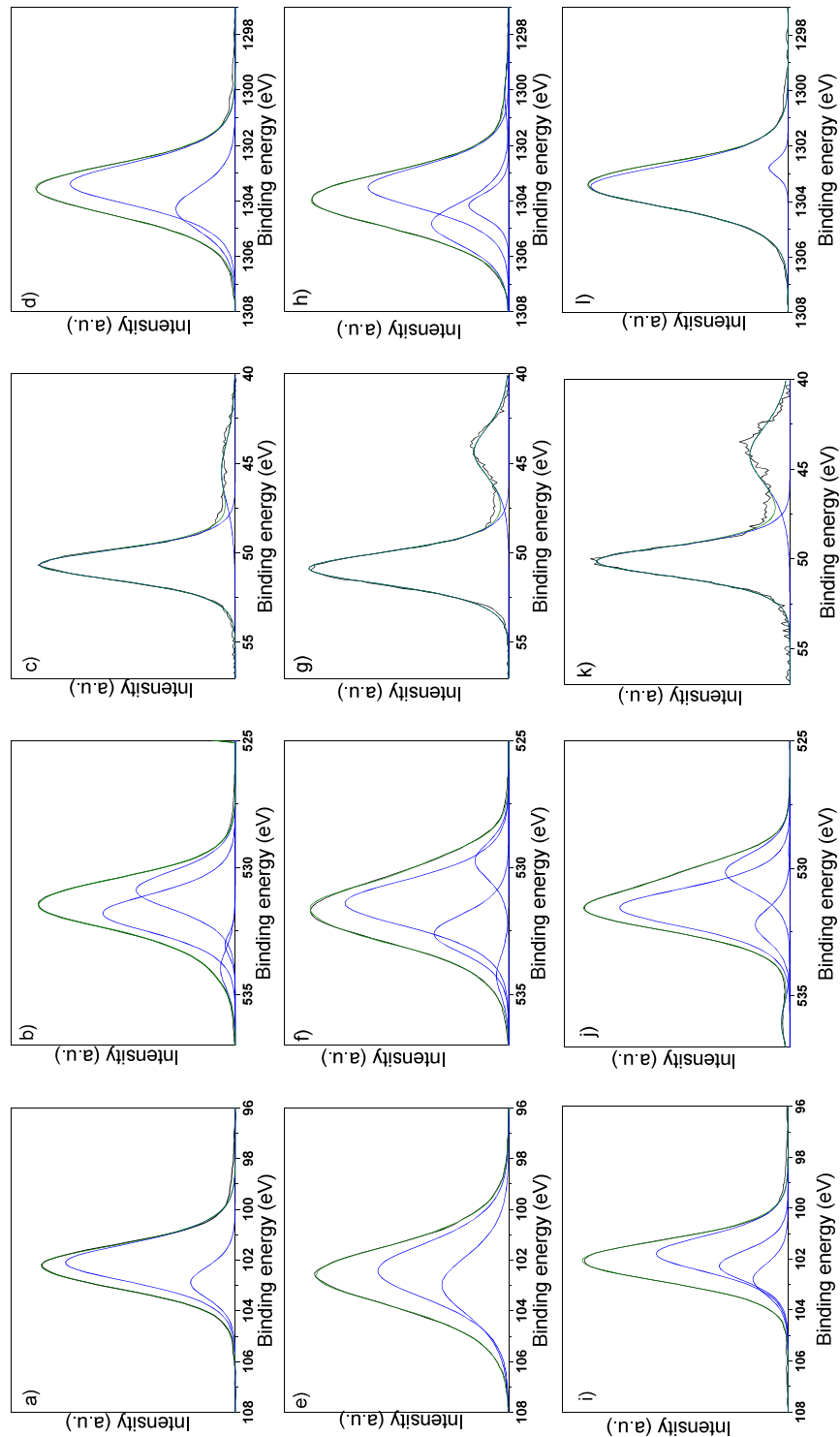


Figure B.3. XPS patterns of a) Si 2p, b) O 1s, c) Mg 2p, and d) Mg 1s spectrum of as-received Sep, e) Si 2p, f) O 1s, g) Mg 2p and h) Mg 1s spectrum of calcined Sep, i) Si 2p, j) O 1s, k) Mg 2p, and l) Mg 1s spectrum of Sep-AAM (Blue lines: fitted individual peaks, green lines: envelope of all fitted peaks)

Table B.4. Binding energy values of samples derived from XPS analysis for O 1s spectrum.

Sample	O 1s position (eV)						
	~529	~530	~531	~532	~533	~534	~536
Sep	-	-	530.9	531.8	533.04	533.98	-
Calcined Sep	-	529.54	531.2	532.4	-	534.06	-
Sep-AAM	529.29	530.15	531.54	532.22	-	-	536.07

Table B.5. Binding energy values of samples derived from XPS analysis for Si 2p spectrum.

Sample	Si 2p position (eV)		
	~102	~103	
Sep	102.09	102.88	
Calcined Sep	102.42	102.98	
Sep-AAM	101.79	102.26	102.79

Table B.6. Binding energy values of samples derived from XPS analysis for Mg 1s and Mg 2p spectrum.

Sample	Mg 1s and Mg 2p position (eV)				
	~1303	~1304	~1305	~45	~50
Sep	1303.39	1304.3	-	45.48	50.66
Calcined Sep	1303.52	1304.17	1304.83	44.36	50.87
Sep-AAM	1302.79	1303.45	-	44.22	50.13

Table B.7. Atomic % of Si, O, Mg, Ca, Al and Na obtained from fitted peak information of these elements' XP spectra.

Sample	Si (at%)	O (at%)	Mg (at%)	Ca (at%)	Al (at%)	Na (at%)
Sep	32.97	48.39	11.61	4.84	2.2	-
Calcined Sep	38.55	44.05	9.22	6.44	1.74	-
Sep-AAM	30.51	52.56	5.19	3.92	1.35	6.46

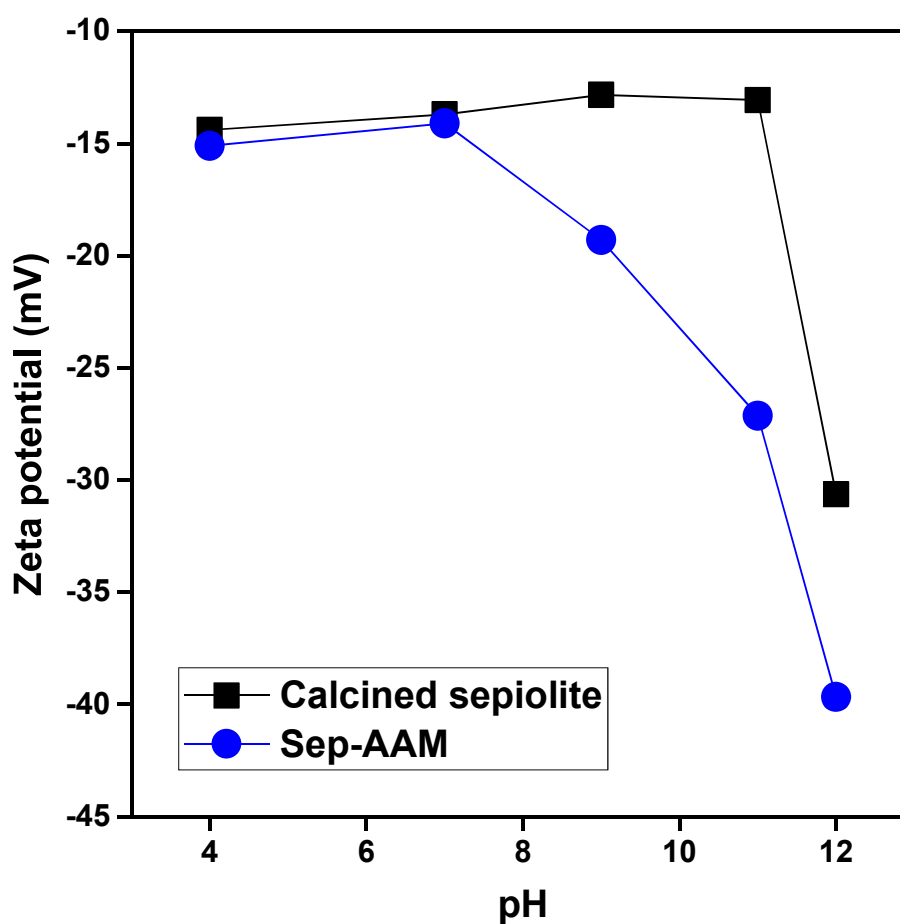


Figure B.4. The change of zeta potential with pH for calcined Sep and Sep-AAM.

Table B.8. The effect of temperature and adsorbent amount on the apparent pseudo-second-order adsorption kinetic rate constant and adsorption parameters for calcined Sep, and Sep-AAM (*Contact time* = 3.5 h, $C_0 = 20 \text{ mg L}^{-1}$).

Sample	Temperature (°C)	Adsorbent amount (g)	$k_{2,ads,app}$ ($\text{g mg}^{-1} \text{ min}^{-1}$)	$q_{e,exp}$ (mg g^{-1})	Removal (%)	R^2
Calcined Sep	31	0.006	3.8×10^{-3}	39.37	23.17	0.99
		0.008	5.3×10^{-3}	39.37	30.89	0.98
		0.01	2.7×10^{-2}	47.25	44.8	0.99
		0.012	3.2×10^{-2}	35.43	41.71	0.99
	40	0.006	2.8×10^{-2}	23.62	13.9	0.94
		0.008	4.6×10^{-2}	29.53	23.17	0.97
		0.01	3.2×10^{-1}	49.02	42.85	0.99
		0.012	3.8×10^{-1}	40.68	47.89	0.98
	50	0.006	9.2×10^{-4}	68.24	40.8	0.98
		0.008	1.1×10^{-3}	64.96	51.8	0.98
		0.01	1.5×10^{-2}	63	54	0.98
		0.012	1.8×10^{-2}	45.1	53	0.98
Sep-AAM	31	0.006	4.4×10^{-4}	73.49	40.10	0.96
		0.008	5.3×10^{-4}	74.80	54.49	0.91
		0.01	6.5×10^{-4}	74.64	72.11	0.98
		0.012	7.8×10^{-4}	71.12	73.5	0.99
	40	0.006	6.0×10^{-4}	89.24	47.4	0.98
		0.008	7.7×10^{-4}	78.74	54.0	0.98
		0.01	9.4×10^{-4}	79.06	75.2	0.98
		0.012	1.0×10^{-4}	74.80	79.48	0.98

Table B.8. The effect of temperature and adsorbent amount on the apparent pseudo-second-order adsorption kinetic rate constant and adsorption parameters for calcined Sep, and Sep-AAM (*Contact time* = 3.5 h, $C_0 = 20 \text{ mg L}^{-1}$). (cont.)

Sep-AAM	50	0.006	6.1×10^{-4}	94.49	49.49	0.98
		0.008	8.9×10^{-4}	75.50	55.8	0.98
		0.01	9.8×10^{-4}	93.70	81.25	0.99
		0.012	1.1×10^{-3}	80.87	84.72	0.99

Table B.9. Uptake performance and removal efficiency (%) for adsorption of MB onto as-received Sep at different temperatures (*Contact time* = 3.5h, $C_0 = 20 \text{ mg L}^{-1}$, and $m = 10 \text{ mg}$).

Adsorbent	$q_{e,exp} \text{ (mg g}^{-1}\text{)}$	Removal (%)
As-received Sep, 31 °C	31.5	30.9
As-received Sep, 40 °C	26.8	26.3
As-received Sep, 50 °C	26.8	26.3

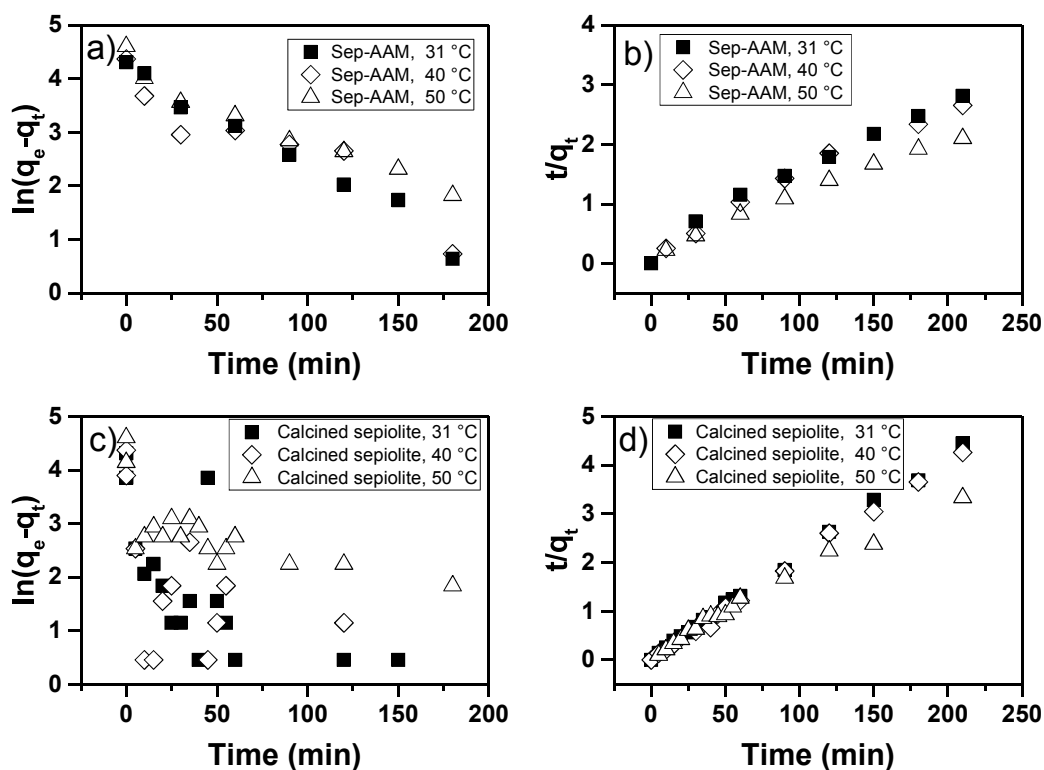


Figure B.5. Pseudo-first and pseudo-second-order kinetic models for the adsorption of MB onto a-b) Sep-AAM, and c-d) Calcined Sep, at different temperatures.

Table B.10. Pseudo-first and pseudo-second-order kinetic model parameters and removal efficiency (%) for adsorption of MB onto calcined Sep at different temperatures (*Contact time* = 3.5 h, $C_0 = 20 \text{ mg L}^{-1}$ and $m = 10 \text{ mg}$).

Adsorbent	$q_{e,exp}$ (mg g^{-1})	Pseudo-first-order adsorption kinetics ($C_0 = 20 \text{ mg L}^{-1}$)			Pseudo-second-order adsorption kinetics ($C_0 = 20 \text{ mg L}^{-1}$)			Removal (%)
		$k_{1,ads,app}$ (min^{-1})	$q_{e,cal}$ (mg g^{-1})	R^2	$k_{2,ads,app}$ ($\text{g mg}^{-1} \text{ min}^{-1}$)	$q_{e,cal}$ (mg g^{-1})	R^2	
		Calcined Sep, 31 °C	47.25	1.48×10^{-2}	7.0	0.50	2.67×10^{-2}	
Calcined Sep, 40 °C	49.28	9.7×10^{-3}	7.15	0.09	3.20×10^{-1}	49.01	0.99	42.85
Calcined Sep, 50 °C	63	7.8×10^{-3}	22.02	0.50	1.53×10^{-1}	63.29	0.98	54.0

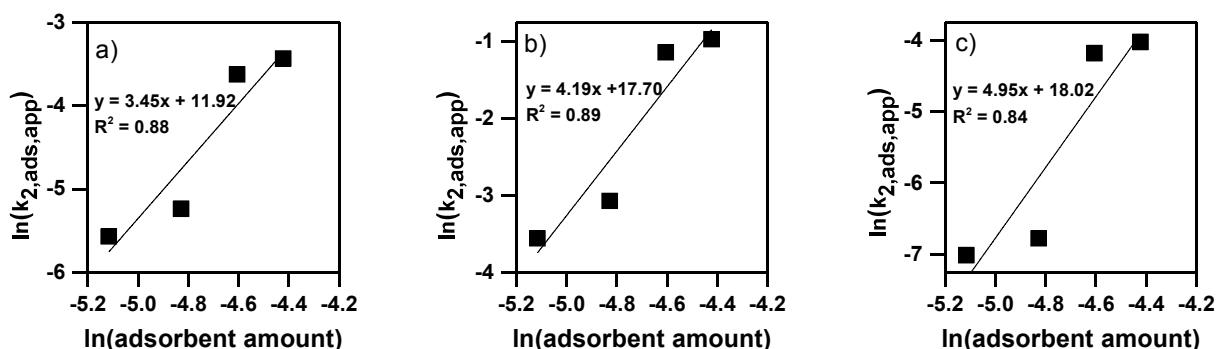


Figure B.6. Experimental data fit to pseudo-second-order adsorption kinetics for calcined Sep at a) 31 °C, b) 40 °C, and c) 50 °C.

Table B.11. Actual second-order adsorption rate constants ($k_{2,ads}$) of calcined Sep at different temperatures.

Temperature (°C)	$k_{2,ads} ((\text{g adsorbent})^{-3.2} (\text{mg MB})^{-1} \text{min}^{-1}) \times 10^{-5}$
31	1.5
40	484.5
50	667.2

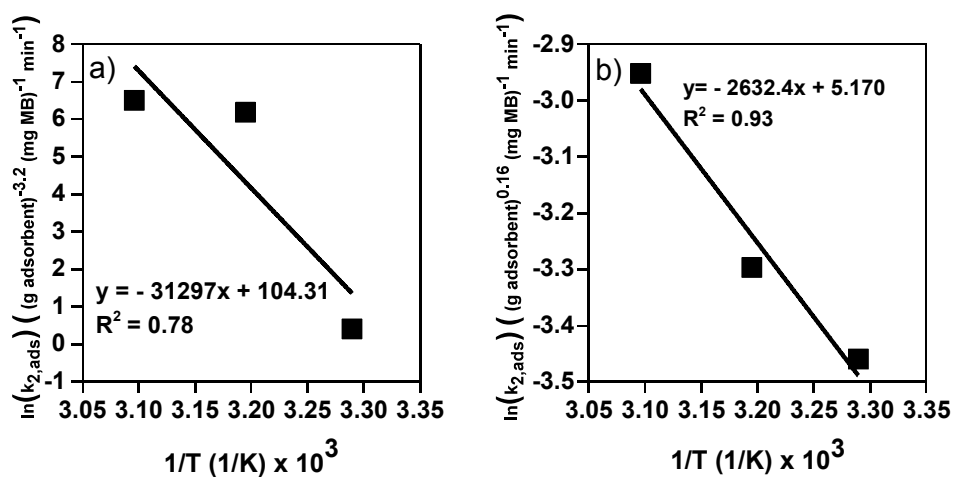


Figure B.7. The plot of $\ln(k_{2,ads})$ vs $1/T$ for a) calcined Sep and b) Sep-AAM.

According to the plot of $\ln(k_{2,ads})$ vs $1/T$, pre-exponential factor A of Arrhenius equation is $175.94 ((\text{g adsorbent})^{0.16} (\text{mg MB}^{-1}) (\text{min}^{-1}))$ and $2 \times 10^{45} ((\text{g adsorbent})^{-3.2} (\text{mg}$

MB⁻¹) (min⁻¹), for Sep-AAM and calcined Sep, respectively. $k_{2,ads}$ is the actual second-order adsorption rate constant.

The adsorption rate can be controlled by different processes involving external mass transfer or boundary layer diffusion that is followed by intraparticle diffusion, where adsorbate molecules diffuse from the surface to the internal sites. Therefore, this model gives information about the diffusion mechanism of adsorption process that can be dominated by film or pore diffusion [1]. The intraparticle diffusion model applied on Sep-AAM shown in Figure B.8 shows multilinearity that includes two steps pointing out the existence of boundary layer diffusion and intraparticle diffusion in the adsorption process of MB dyes onto Sep-AAM particles. The second line which represents the intraparticle diffusion range, not passing through the origin implies that intraparticle diffusion is not the only rate controlling step for this adsorption process [2–4]. In our system, boundary layer diffusion has the main effect on the adsorption process at initial time periods and at the later stages of adsorption, intraparticle diffusion controls the adsorption. However, for calcined Sep no such trend was observed and experimental data were found to be poorly fitted to this model. Table B.12 summarizes these findings for Sep-AAM samples operated at different temperatures. The first sharper region in Figure B.8 detected at the initial time values of adsorption process is related with the diffusion of MB dye molecules through the solution to the external surface of Sep-AAM and the boundary layer diffusion of MB molecules. The slope of the first region being high shows that there is a rapid adsorption within first 30 minutes. The intercept obtained from the second linear region is proportional to the boundary layer thickness and shows the presence of viscous drag between the adsorbate and the adsorbent [1]. This second step also defines the adsorption step, where the MB molecules are transported via intraparticle diffusion. For our system, as it can be seen from Table B.12, for the second step, the value of C increases with temperature revealing the higher uptake values detected at higher temperatures. As it can be seen from Figure B.8, this second stage, that covers the time region after first 30 minutes, is rather slow showing that intraparticle diffusion of MB molecules into Sep-AAM pores was rate limiting after first 30 minutes of the adsorption process [5]. Similar results were also reported by Küncek et. al. who also studied the intraparticle diffusion mechanism on the sonicated Sep [6]. For calcined Sep in this study, the correlation coefficient obtained from fitting experimental data to intraparticle diffusion model was low ($R^2 = 0.63$).

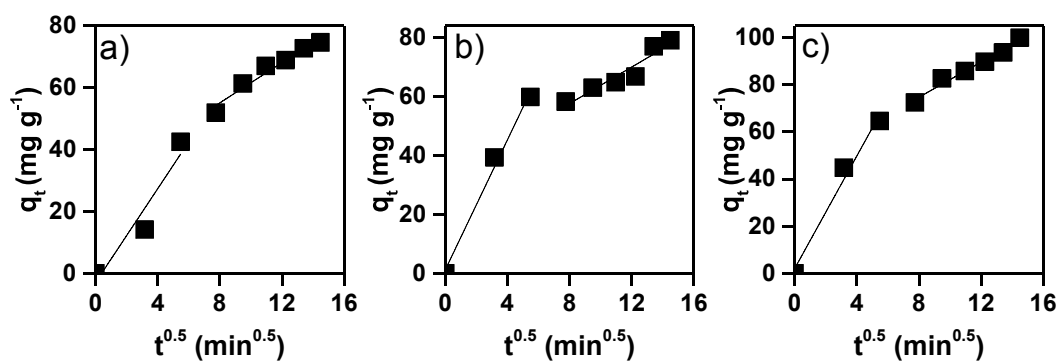


Figure B.8. Intraparticle diffusion model for the adsorption of MB onto Sep-AAM at a) 31 °C, b) 40 °C, and c) at 50 °C.

Table B.12. Parameters of intraparticle diffusion model for Sep-AAM at different temperatures.

Temperature (°C)	$k_{p,1}$ ($\text{mg g}^{-1} \text{min}^{-0.5}$)	C_1 (mg g^{-1})	R^2	$k_{p,2}$ ($\text{mg g}^{-1} \text{min}^{-0.5}$)	C_2 (mg g^{-1})	R^2
31	7.56	-2.90	0.92	3.24	1.34	0.99
40	11.01	1.34	0.99	3.09	32.85	0.91
50	11.93	2.12	0.98	3.73	44.85	0.97

Table B.13. Concentration (ppm) of leached elements from adsorbent to MB solution measured by ICP-MS.

Element concentration (ppm)	Calcined Sep	Sep-AAM
Al	0.048	0.026
Mg	4.073	2.098
Fe	0.186	0

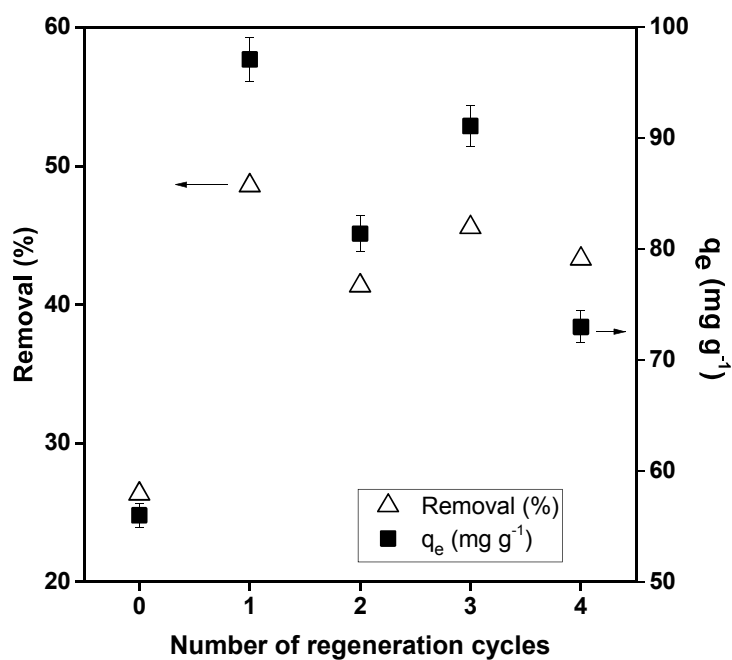


Figure B.9. MB removal (%) and uptake values for calcined Sep after regeneration cycles.

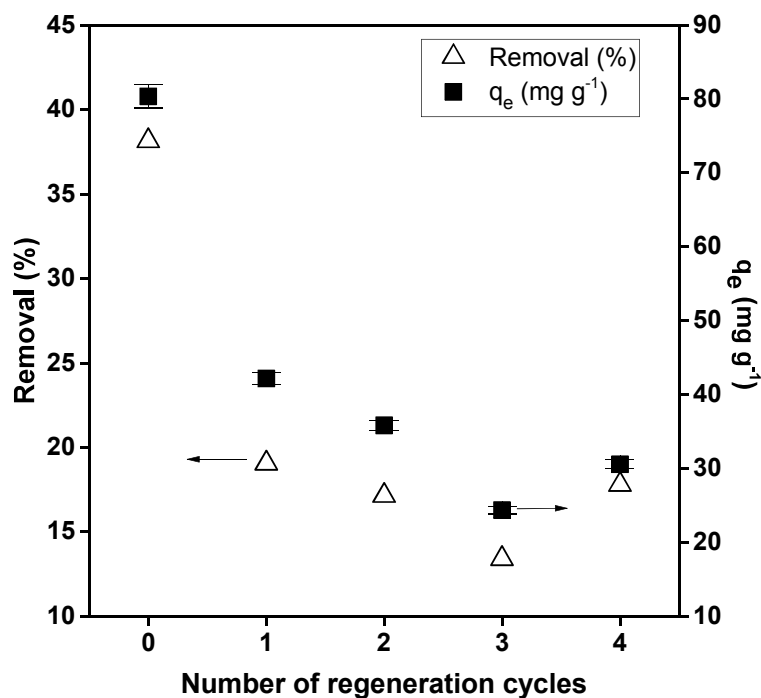


Figure B.10. MB removal (%) and uptake values for Sep-AAM after regeneration cycles.

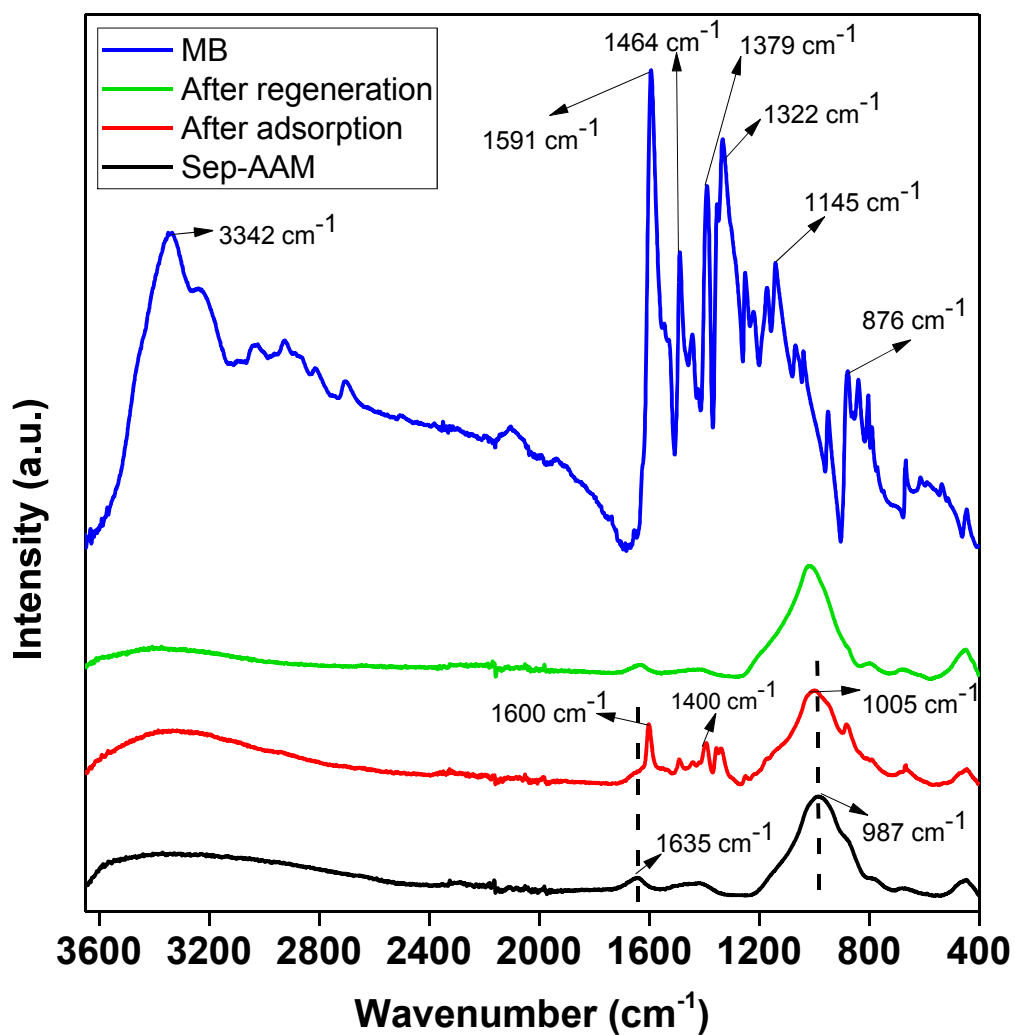


Figure B.11. FTIR spectra of MB and Sep-AAM sample before and after adsorption, and after 4 cycles of regeneration (*Contact time = 3.5 h*).

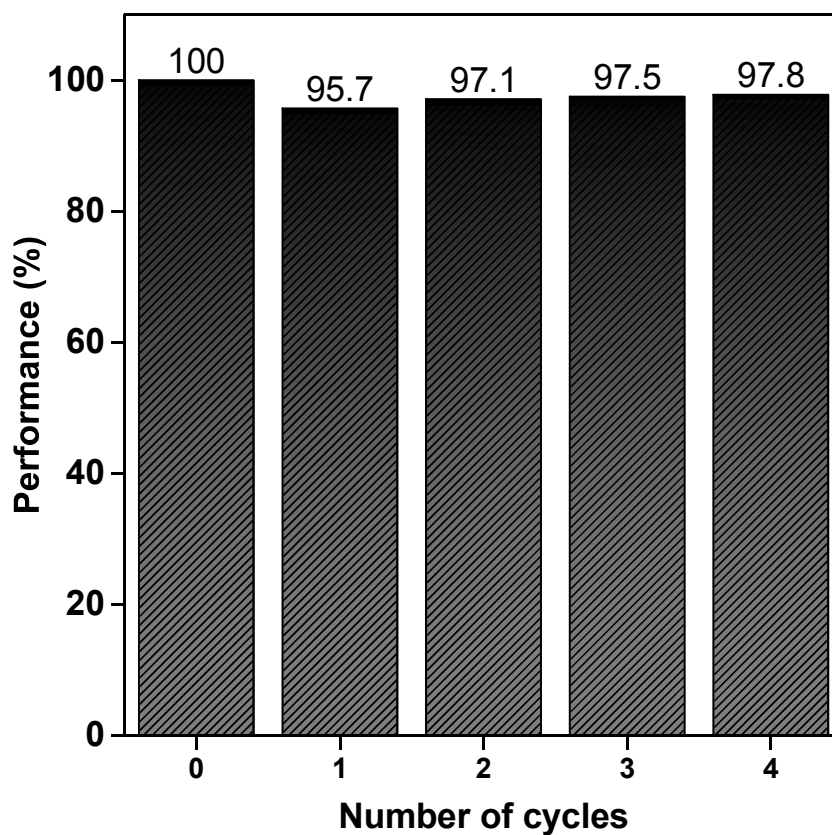


Figure B.12. The change in the performance (%) of Sep-AAM monoliths during regeneration experiments.

Table B.14. Langmuir and Freundlich isotherm constants for MB adsorption on calcined Sep at different temperatures.

Adsorbents	Langmuir Model			Freundlich Model		
	K_L (L mg ⁻¹)	q_{max} (mg g ⁻¹)	R^2	K_F (mg g ⁻¹)	n (g L ⁻¹)	R^2
Calcined Sep, 31 °C	1.25	56.18	0.99	34.17	6.58	0.89
Calcined Sep, 40 °C	1.29	54.35	0.99	30.26	5.30	0.68
Calcined Sep, 50 °C	1.48	75.19	0.98	42.19	4.89	0.78

Table B.15. Langmuir separation factor R_L for calcined Sep and Sep-AAM at different temperatures, at all the initial MB concentrations used.

Sample	Initial MB concentration (mg L ⁻¹)	R_L		
		31 °C	40 °C	50 °C
Calcined Sep	5	0.138	0.154	0.120
	7	0.102	0.110	0.089
	10	0.074	0.077	0.064
	15	0.050	0.051	0.044
	20	0.038	0.038	0.033
	30	0.026	0.026	0.022
	35	0.022	0.022	0.019
	40	0.019	0.019	0.017
Sep-AAM	5	0.095	0.079	0.061
	7	0.070	0.058	0.044
	10	0.050	0.041	0.032
	15	0.034	0.027	0.021
	20	0.026	0.021	0.016
	30	0.017	0.014	0.011
	35	0.015	0.012	0.009
	40	0.013	0.011	0.008

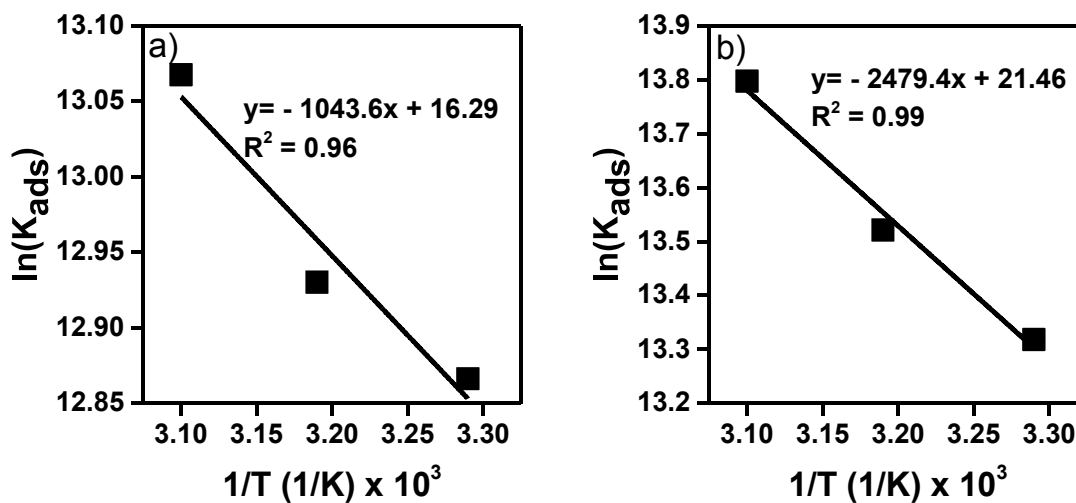


Figure B.13. $\ln(K_{ads})$ vs $1/T$ plot for MB adsorption onto a) Calcined Sep, and b) Sep-AAM.

Table B.16. Thermodynamic parameters for adsorption of MB onto calcined Sep for 31, 40, and 50 °C.

Sample	T (°C)	Thermodynamic parameters				
		K_L (L/mg)	K_{ads} (L/mol) $\times 10^4$	ΔG° (kJ/mol)	ΔH° (kJ/mol)	ΔS° (J/mol.K)
Calcined Sep	31	1.25	38.70	-41.08	8.68	135.41
	40	1.29	41.26	-42.30		
	50	1.48	47.34	-43.65		

- B1. Toor, M. and B. Jin, "Adsorption Characteristics, Isotherm, Kinetics, and Diffusion of Modified Natural Bentonite for Removing Diazo Dye", *Chemical Engineering Journal*, Vol. 187, pp. 79–88, 2012.
- B2. Cheung, W. H., Y. S. Szeto, and G. McKay, "Intraparticle Diffusion Processes During Acid Dye Adsorption onto Chitosan", *Bioresource Technology*, Vol. 98, No. 15, pp. 2897–2904, 2007.

- B3. Nandi, B. K., A. Goswami, and M. K. Purkait, "Removal of Cationic Dyes From Aqueous Solutions by Kaolin: Kinetic and Equilibrium Studies", *Applied Clay Science*, Vol. 42, No. 3–4, pp. 583–590, 2009.
- B4. Li, Q., Y. Li, X. Ma, Q., Du, K. Sui, D. Wang, C. Wang, H. Li, and Y. Xia, "Filtration and Adsorption Properties of Porous Calcium Alginate Membrane for Methylene Blue Removal from Water", *Chemical Engineering Journal*, Vol. 316, pp. 623–630, 2017.
- B5. Milenković, D. D., P. V. Dašić, and V. B. Veljković, "Ultrasound-Assisted Adsorption of Copper(II) Ions on Hazelnut Shell Activated Carbon", *Ultrasonics Sonochemistry*, Vol. 16, No. 4, pp. 557–563, 2009.
- B6. KünceK, I. and S. Şener, "Adsorption of Methylene Blue onto Sonicated Sepiolite from Aqueous Solutions", *Ultrasonics Sonochemistry*, Vol. 17, No. 1, pp. 250–257, 2010.

APPENDIX C: SUPPLEMENTARY INFORMATION 3

Table C.1. Chemical compositions (wt%) of 1 h 750 °C calcined Sep and MK used in this study, as determined by XRF spectroscopy.

Material	SiO ₂	MgO	CaO	Al ₂ O ₃	TiO ₂	Fe ₂ O ₃	K ₂ O
Calcined Sep	52.7	31.0	13.61	1.51	0.07	0.59	0.25
MK	56.2	0.07	0.09	41.0	1.15	0.36	0.46

Table C.2. The amounts of raw materials (in g) used in the synthesis of Sep-AAMs with distinct H₂O₂ contents, corresponding molar Si/Mg and Na/Mg, and synthesis conditions.

Sample	Calcined Sep	H ₂ O ₂	Na ₂ Si ₃ O ₇ solution	NaOH	Si/Mg	Na/Mg	Thermal treatment
Sep-AAM	12	0	38.17	0.5	3	1.2	1 day 40 °C +1 week 25°C
0.5%H ₂ O ₂ -Sep-AAM	12	0.25	38.17	0.5	3	1.2	1 day 40 °C +1 week 25°C
1%H ₂ O ₂ -Sep-AAM	12	0.51	38.17	0.5	3	1.2	1 day 40 °C +1 week 25°C
2%H ₂ O ₂ -Sep-AAM	12	1.01	38.17	0.5	3	1.2	1 day 40 °C +1 week 25°C
3%H ₂ O ₂ -Sep-AAM	12	1.52	38.17	0.5	3	1.2	1 day 40 °C +1 week 25°C
6%H ₂ O ₂ -Sep-AAM	12	3.04	38.17	0.5	3	1.2	1 day 40 °C +1 week 25°C
8%H ₂ O ₂ -Sep-AAM	12	4.05	38.17	0.5	3	1.2	1 day 40 °C + 1 week 25 °C

Table C.3. The amounts of raw materials (in g) used in the synthesis of MKGPs with distinct H₂O₂ contents, corresponding molar Si/Al and Na/Al ratios, and synthesis conditions.

Sample	MK	H ₂ O ₂	Na ₂ Si ₃ O ₇ solution	NaOH	Si/Al	Na/Al	Thermal treatment
MKGP	12	0	18.0	2.8	2	1.2	1 day 60 °C + 1 week 25 °C
0.5%H ₂ O ₂ -MKGP	12	0.16	18.0	2.8	2	1.2	1 day 60 °C + 1 week 25 °C
1%H ₂ O ₂ -MKGP	12	0.33	18.0	2.8	2	1.2	1 day 60 °C + 1 week 25 °C

Table C.4. BET surface area, average pore size, and pore volume of raw materials.

Sample	Surface area (m ² /g)	Pore volume (cm ³ /g)	Pore size (Å)
Calcined Sep	101.8	0.5	273.8
MK	14.4	0.09	312.5

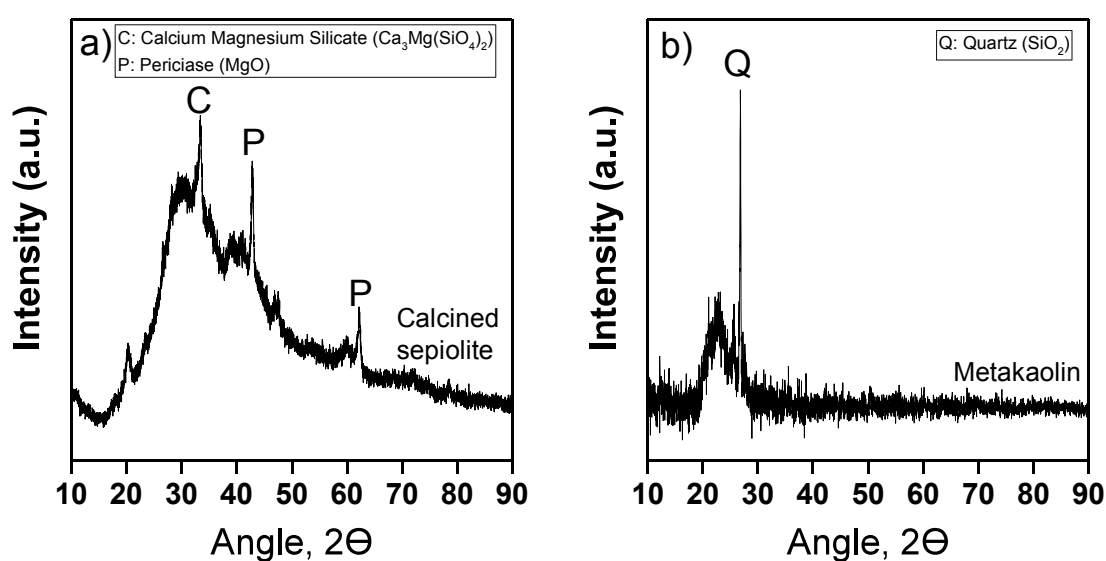


Figure C.1. XRD patterns of a) Calcined Sep and b) MK.

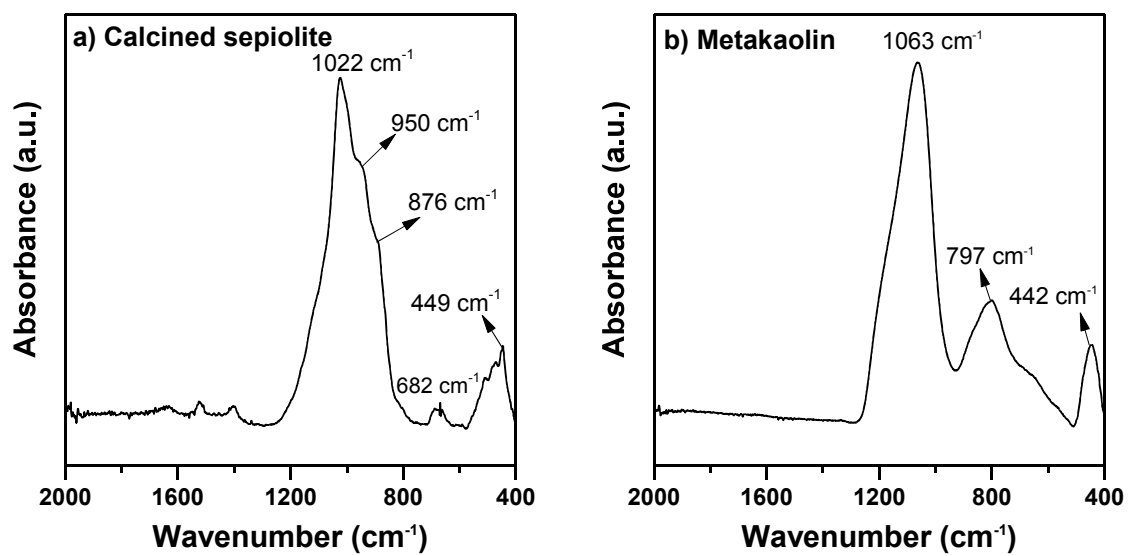


Figure C.2. FTIR patterns of a) Calcined Sep and b) MK.

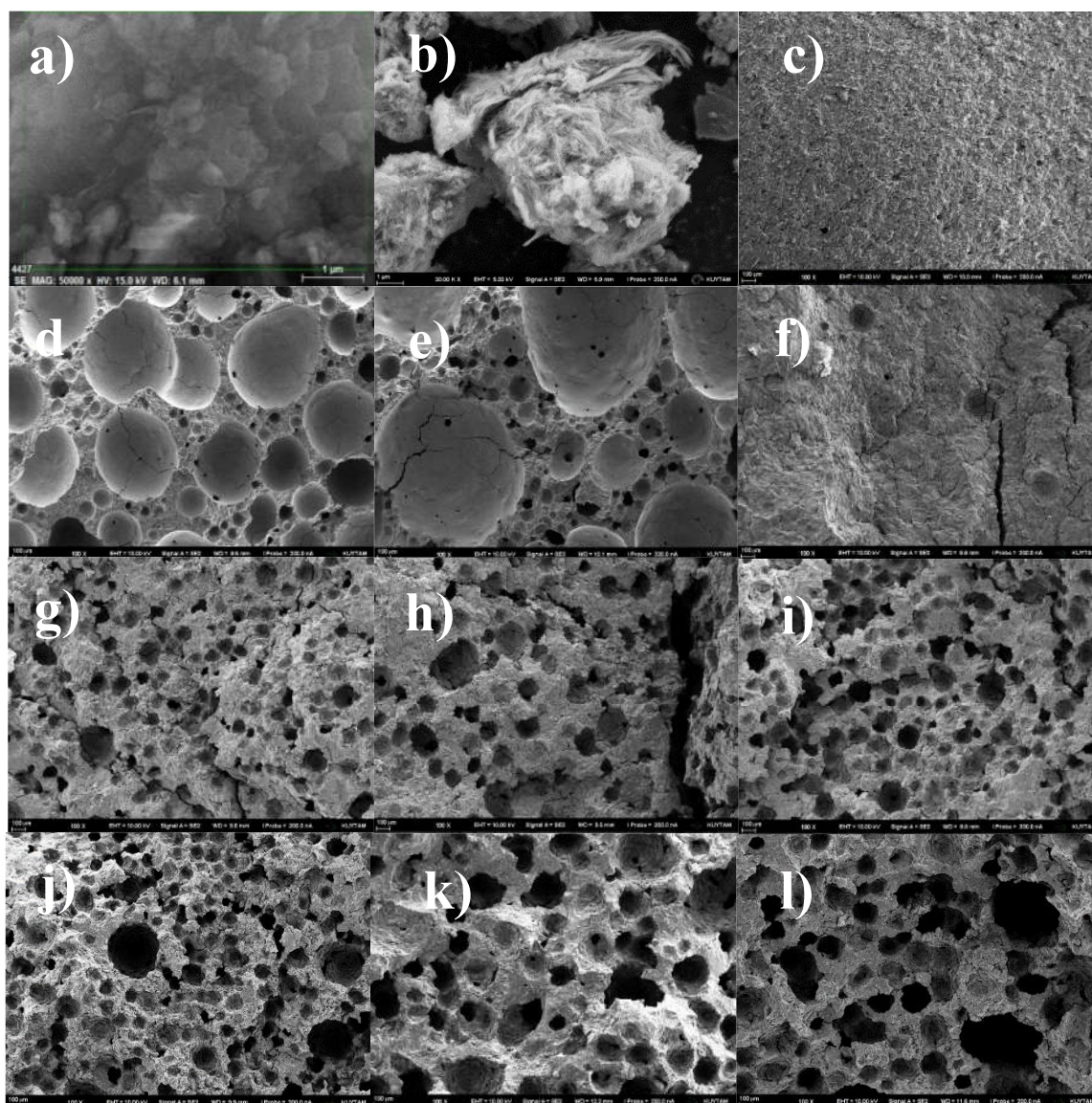


Figure C.3. SEM images of materials: a) MK- at a magnification of 50 k \times , b) Calcined Sep- at a magnification of 20 k \times , synthesized materials at a magnification of 100 \times : c) MKGP, d) 0.5% H_2O_2 -MKGP, e) 1% H_2O_2 -MKGP, f) Sep-AAM, g) 0.5% H_2O_2 -Sep-AAM, h) 1% H_2O_2 -Sep-AAM, i) 2% H_2O_2 -Sep-AAM, j) 3% H_2O_2 -Sep-AAM, k) 6% H_2O_2 -Sep-AAM, and l) 8% H_2O_2 -Sep-AAM.

Table C.5. Compressive strength values of the synthesized samples.

Sample	Compressive strength (MPa)
Sep-AAM	37
0.5% H_2O_2 -Sep-AAM	15.8
1% H_2O_2 -Sep-AAM	16.3
2% H_2O_2 -Sep-AAM	11.7
3% H_2O_2 -Sep-AAM	9.2
6% H_2O_2 -Sep-AAM	6.9
8% H_2O_2 -Sep-AAM	6.5
MKGP	28
0.5% H_2O_2 -MKGP	4.2
1% H_2O_2 -MKGP	2.1

For 8% H_2O_2 -Sep-AAM, zeta potential had decreased from -6.2 to -26.4eV when pH is increased from 2 to 12. In a similar manner, zeta potential of 1% H_2O_2 -MKGP was -54.9 eV when pH is equal to 12. Even though zeta potential measurements imply a more negatively charged surface for 8% H_2O_2 -Sep-AAM than it is for 1% H_2O_2 -MKGP, 8% H_2O_2 -Sep-AAM displayed comparatively higher adsorption capacity towards cationic MB dye. Due to heterogeneous nature of clay minerals, electrostatic interactions and adsorptive properties of these minerals is a complex phenomenon [1]. Cation exchange capacity (CEC) is a measure demonstrating the ability of clay minerals ability for adsorbing cations from the solution medium [2]. For layered minerals (i.e. MK and Sep) that are swelled in the water, the amount of adsorbed adsorbate may be greater than corresponding clay mineral's cation exchange capacity [1]. When this occurs, the value and even the sign of the zeta potential of the clay mineral may alter owing to the formation of micelles [1, 3]. CEC of kaolinite mineral was reported to be mostly in the region between 0.028 - 0.058 mol/kg [4]. Sep mineral's CEC, on the other hand was reported to be in the range of 0.1 to 0.15 mol/kg [5]. Therefore,

higher CEC of Sep-based AAM possessed higher adsorption performance towards cationic MB dye.

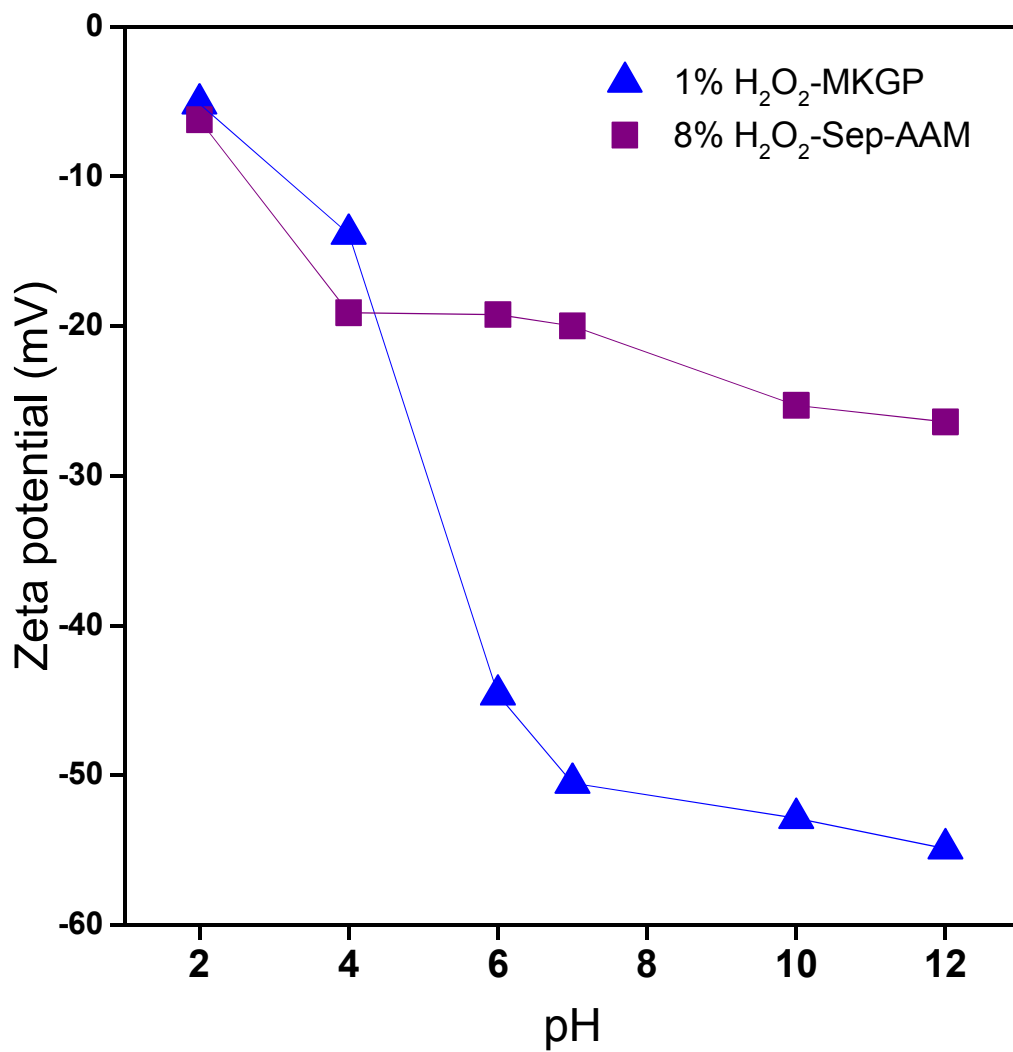


Figure C.4. The change of zeta potential with pH for 1%H₂O₂-MKGP and 8%H₂O₂-Sep-AAM.

Table C.6. The effect of initial MB concentration on uptake and removal efficiency for synthesized AAMs..

Adsorbent	C_0 (mg L ⁻¹)	$q_{e,exp}$ (mg g ⁻¹)	Removal efficiency (%)
Sep-AAM	30	2.35	96.35
	40	3.48	94.10
	50	3.93	90.32
	60	4.44	88.92
	70	4.59	79.8
	90	6.37	75.70
	110	6.64	66.87
0.5% H_2O_2 -Sep-AAM	30	3.50	96.07
	40	3.85	86.23
	50	4.68	84.29
	60	5.47	85.28
	70	5.70	76.98
	90	6.60	76.22
	110	6.54	64.65
1% H_2O_2 -Sep-AAM	30	2.62	81.71
	40	4.30	87.55
	50	4.55	83.43
	60	5.29	84.74
	70	4.77	65.74
	90	6.33	63.42
	110	7.08	61.98
2% H_2O_2 -Sep-AAM	30	3.53	96.35
	40	4.71	93.44
	50	5.83	90.39
	60	6.36	84.52
	70	7.26	82.75

Table C.6. The effect of initial MB concentration on uptake performances and removal efficiency for synthesized AAMs. (cont.)

Adsorbent	C_0 (mg L ⁻¹)	$q_{e,exp}$ (mg g ⁻¹)	Removal efficiency (%)
2% H_2O_2 -Sep-AAM	90	9.08	72.12
	110	10.15	69.98
3% H_2O_2 -Sep-AAM	30	3.89	91.16
	40	4.89	85.93
	50	6.06	83.22
	60	7.06	82.56
	70	7.41	73.67
	90	8.88	66.49
	110	9.36	61.98
6% H_2O_2 -Sep-AAM	30	4.45	95.46
	40	6.27	85.43
	50	6.95	84.82
	60	7.80	84.61
	70	8.28	77.45
	90	8.83	63.43
	110	9.79	56.42
8% H_2O_2 -Sep-AAM	30	4.38	93.78
	40	7.27	97.13
	50	8.08	89.15
	60	9.99	82.54
	70	9.02	72.26
	90	11.30	70.59
	110	10.26	58.42
MKGP	30	1.34	73.0
	40	2.17	72.93

Table C.6. The effect of initial MB concentration on uptake performances and removal efficiency for synthesized AAMs. (cont.)

Adsorbent	C_0 (mg L ⁻¹)	$q_{e,exp}$ (mg g ⁻¹)	Removal efficiency (%)
MKGP	50	2.47	69.99
	60	2.73	66.03
	70	2.78	57.62
	90	3.53	53.71
	110	4.35	58.87
0.5% H_2O_2 -MKGP	30	2.54	62.98
	40	4.73	74.41
	50	4.56	62.93
	60	4.98	59.43
	70	5.69	58.56
	90	6.09	45.52
	110	7.19	46.42
1% H_2O_2 -MKGP	30	5.00	92.66
	40	6.30	73.67
	50	5.97	60.36
	60	7.85	67.13
	70	7.95	59.51
	90	8.06	42.97
	110	7.81	37.08

Table C.7. Pseudo-first and pseudo-second-order kinetic model parameters and removal efficiency (%) for adsorption of MB onto synthesized AAMs for different initial MB concentrations (*Contact time* = 24 h).

Adsorbent	$q_{e,exp}$ (mg g ⁻¹)	C_0 (mg L ⁻¹)	Pseudo-first-order adsorption kinetics			Pseudo-second-order adsorption kinetics			Removal (%)
			$k_{1,ads,app}$ (min ⁻¹)	$q_{e,cal}$ (mg g ⁻¹)	R^2	$k_{2,ads,app}$ (g mg ⁻¹ min ⁻¹)	$q_{e,cal}$ (mg g ⁻¹)	R^2	
Sep-AAM	2.35	30	6×10^{-4}	2.44	0.89	3.5×10^{-3}	2.51	0.99	96.35
	3.48	40	3.8×10^{-3}	3.36	0.97	1.9×10^{-3}	3.77	0.99	94.10
	3.93	50	3.1×10^{-3}	4.22	0.96	8.7×10^{-4}	4.47	0.95	90.32
	4.44	60	1×10^{-3}	3.06	0.79	7.7×10^{-4}	5.15	0.95	88.92
	4.59	70	2.5×10^{-3}	4.44	0.93	6.8×10^{-4}	5.22	0.93	79.8
	6.37	90	1.3×10^{-3}	6.06	0.96	1.6×10^{-4}	9.22	0.78	75.70
	6.64	110	2.1×10^{-3}	6.93	0.95	2.2×10^{-4}	8.64	0.79	66.87
0.5% H ₂ O ₂ - Sep-AAM	3.50	30	2.9×10^{-3}	3.204	0.97	1.2×10^{-3}	3.93	0.98	96.07
	3.85	40	3.1×10^{-3}	4.40	0.98	7.3×10^{-4}	4.57	0.96	86.23
	4.68	50	2.7×10^{-3}	4.71	0.97	4.1×10^{-4}	6.07	0.99	84.29
	5.47	60	2.1×10^{-3}	5.06	0.96	5.2×10^{-4}	6.54	0.95	85.28
	5.70	70	1.7×10^{-3}	4.86	0.87	4.3×10^{-4}	6.90	0.93	76.98
	6.60	90	2.3×10^{-3}	6.51	0.96	8.2×10^{-5}	11.24	0.60	76.22
	6.54	110	2.5×10^{-3}	8.43	0.95	9.7×10^{-5}	10.29	0.58	64.65
1% H ₂ O ₂ -Sep- AAM	2.62	30	3×10^{-3}	2.70	0.99	9.4×10^{-4}	3.22	0.93	81.71
	4.30	40	4.2×10^{-3}	4.62	0.97	9.1×10^{-4}	5.13	0.97	87.55
	4.55	50	3.2×10^{-3}	5.86	0.96	3.5×10^{-4}	5.93	0.89	83.43
	5.29	60	1.7×10^{-3}	4.80	0.93	3.9×10^{-4}	6.64	0.92	84.74
	4.77	70	2.8×10^{-3}	5.24	0.96	5.6×10^{-4}	5.67	0.93	65.74
	6.33	90	2.4×10^{-3}	6.00	0.95	3.7×10^{-4}	7.97	0.94	63.42
	7.08	110	2.2×10^{-3}	7.20	0.94	3.4×10^{-4}	8.27	0.90	61.98
2% H ₂ O ₂ -Sep- AAM	3.53	30	5.7×10^{-3}	3.73	0.82	2.2×10^{-3}	3.85	0.97	96.35
	4.71	40	2.8×10^{-3}	3.66	0.98	1.3×10^{-3}	5.13	0.99	93.44
	5.83	50	2.5×10^{-3}	3.73	0.83	1.3×10^{-3}	6.21	0.99	90.39
	6.36	60	2.7×10^{-3}	5.16	0.74	7.8×10^{-4}	7.03	0.97	84.52
	7.26	70	1.7×10^{-3}	5.98	0.87	4.2×10^{-4}	8.31	0.93	82.75

Table C.7. Pseudo-first and pseudo-second-order kinetic model parameters and removal efficiency (%) for adsorption of MB onto synthesized AAMs for different initial MB concentrations (*Contact time* = 24 h). (cont.)

Adsorbent	$q_{e,exp}$ (mg g ⁻¹)	C_0 (mg L ⁻¹)	Pseudo-first-order adsorption kinetics			Pseudo-second-order adsorption kinetics			Removal (%)
			$k_{1,ads,app}$ (min ⁻¹)	$q_{e,cal}$ (mg g ⁻¹)	R^2	$k_{2,ads,app}$ (g mg ⁻¹ min ⁻¹)	$q_{e,cal}$ (mg g ⁻¹)	R^2	
2% H_2O_2 -Sep-AAM	9.08	90	3.3×10^{-3}	14.11	0.95	1.2×10^{-5}	28.90	0.15	72.12
	10.15	110	1.8×10^{-3}	9.51	0.96	1.9×10^{-4}	12.64	0.89	69.98
3% H_2O_2 -Sep-AAM	3.89	30	4.3×10^{-3}	4.37	0.97	1.5×10^{-3}	4.28	0.99	91.16
	4.89	40	3.1×10^{-3}	5.93	0.99	3.9×10^{-4}	6.15	0.93	85.93
	6.06	50	2.2×10^{-3}	5.75	0.98	3.8×10^{-4}	7.45	0.95	83.22
	7.06	60	2.2×10^{-3}	6.49	0.98	4.8×10^{-4}	7.90	0.93	82.56
	7.41	70	1.9×10^{-3}	8.85	0.98	2.7×10^{-4}	9.49	0.92	73.67
	8.88	90	2.6×10^{-3}	8.50	0.99	3.4×10^{-4}	10.47	0.96	66.49
	9.36	110	2.5×10^{-3}	8.12	0.93	3.3×10^{-4}	11.56	0.95	61.98
6% H_2O_2 -Sep-AAM	4.45	30	2.6×10^{-3}	3.70	0.99	1×10^{-3}	4.99	0.98	95.46
	6.27	40	2.8×10^{-3}	4.99	0.92	9.6×10^{-4}	6.78	0.99	85.43
	6.95	50	2.7×10^{-3}	6.80	0.99	4.6×10^{-4}	8.04	0.97	84.82
	7.80	60	3×10^{-3}	7.35	0.99	5.7×10^{-4}	8.77	0.98	84.61
	8.28	70	2.3×10^{-3}	6.24	0.96	7×10^{-4}	9.06	0.99	77.45
	8.83	90	2.6×10^{-3}	8.83	0.86	4.1×10^{-4}	11.01	0.95	63.43
	9.79	110	1.3×10^{-3}	11.39	0.80	1.5×10^{-4}	15.03	0.81	56.42
8% H_2O_2 -Sep-AAM	4.38	30	2.9×10^{-3}	5.420	0.99	3.6×10^{-4}	5.70	0.89	93.78
	7.27	40	3.3×10^{-3}	7.91	0.99	4.5×10^{-4}	8.47	0.97	97.13

Table C.7. Pseudo-first and pseudo-second-order kinetic model parameters and removal efficiency (%) for adsorption of MB onto synthesized AAMs for different initial MB concentrations (*Contact time* = 24 h). (cont.)

Adsorbent	$q_{e,exp}$ (mg g ⁻¹)	C_0 (mg L ⁻¹)	Pseudo-first-order adsorption kinetics			Pseudo-second-order adsorption kinetics			Removal (%)
			$k_{1,ads,app}$ (min ⁻¹)	$q_{e,cal}$ (mg g ⁻¹)	R^2	$k_{2,ads,app}$ (g mg ⁻¹ min ⁻¹)	$q_{e,cal}$ (mg g ⁻¹)	R^2	
8% H_2O_2 -Sep- AAM	8.08	50	3.2×10^{-3}	9.46	0.97	2.5×10^{-4}	10.15	0.91	89.15
	9.99	60	2.4×10^{-3}	9.57	0.99	2.1×10^{-4}	11.36	0.92	82.54
	9.02	70	3.3×10^{-3}	11.94	0.95	2.2×10^{-4}	11.17	0.88	72.26
	11.30	90	2.6×10^{-3}	10.25	0.98	3.4×10^{-4}	12.97	0.97	70.59
	10.26	110	2.6×10^{-3}	9.25	0.99	4.3×10^{-4}	11.37	0.97	58.42
MKGP	1.34	30	2.5×10^{-3}	1.24	0.96	1.4×10^{-3}	1.67	0.92	73.0
	2.17	40	3.3×10^{-3}	2.53	0.97	1.5×10^{-3}	2.48	0.95	72.93
	2.47	50	3.2×10^{-3}	3.12	0.96	8.2×10^{-4}	3.06	0.93	69.99
	2.73	60	2.2×10^{-3}	2.538	0.93	6.8×10^{-4}	3.47	0.89	66.03
	2.78	70	1.6×10^{-3}	2.49	0.91	6.2×10^{-4}	3.64	0.88	57.62
	3.53	90	2.2×10^{-3}	4.63	0.95	1.2×10^{-4}	6.12	0.22	53.71
	4.35	110	9×10^{-4}	4.14	0.95	1.8×10^{-4}	6.55	0.61	58.87
0.5% H_2O_2 - MKGP	2.54	30	1.1×10^{-3}	2.37	0.95	4.2×10^{-4}	3.53	0.71	62.98
	4.73	40	1.9×10^{-3}	4.86	0.99	3.4×10^{-4}	5.87	0.85	74.41
	4.56	50	1.1×10^{-3}	4.16	0.92	2.4×10^{-4}	6.44	0.75	62.93
	4.98	60	1.5×10^{-3}	4.65	0.96	2.9×10^{-4}	6.77	0.86	59.43
	5.69	70	1.8×10^{-3}	5.56	0.99	3.4×10^{-4}	6.82	0.89	58.56

Table C.7. Pseudo-first and pseudo-second-order kinetic model parameters and removal efficiency (%) for adsorption of MB onto synthesized AAMs for different initial MB concentrations (*Contact time = 24 h*). (cont.)

Adsorbent	$q_{e,exp}$ (mg g ⁻¹)	C_0 (mg L ⁻¹)	Pseudo-first-order adsorption kinetics			Pseudo-second-order adsorption kinetics			Removal (%)
0.5% H ₂ O ₂ - MKGP	6.09	90	2.1×10 ⁻³	7.12	0.95	3.9×10 ⁻⁴	7.07	0.85	45.52
	7.19	110	2×10 ⁻²	7.90	0.73	6.5×10 ⁻⁵	13.11	0.56	46.42
1% H ₂ O ₂ - MKGP	5.00	30	2.7×10 ⁻³	8.12	0.90	1.8×10 ⁻⁵	15.58	0.09	92.66
	6.30	40	2×10 ⁻³	7.47	0.96	1.3×10 ⁻⁴	9.66	0.65	73.67
	5.97	50	2.3×10 ⁻³	8.40	0.93	2.7×10 ⁻⁵	14.56	0.13	60.36
	7.85	60	3×10 ⁻³	11.95	0.92	5.2×10 ⁻⁵	14.51	0.51	67.13
	7.95	70	3×10 ⁻³	11.52	0.92	1×10 ⁻⁴	11.52	0.63	59.51
	8.06	90	2.1×10 ⁻³	5.92	0.94	6.4×10 ⁻⁴	8.73	0.97	42.97
	7.81	110	3.3×10 ⁻³	6.71	0.91	6.2×10 ⁻⁴	9.25	0.97	37.08

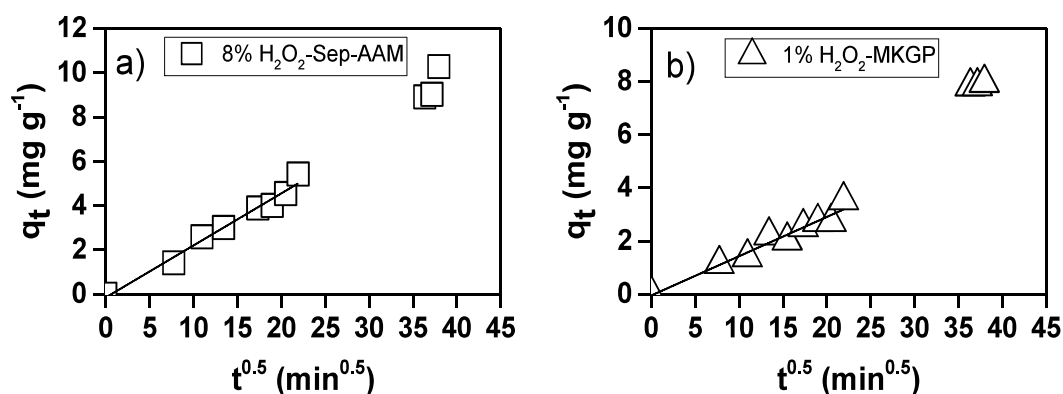


Figure C.5. Intraparticle diffusion model for the adsorption of MB onto a) 8% H₂O₂-Sep-AAM and b) 1% H₂O₂-MKGP (*Contact time = 24h*, $C_0 = 70$ mg L⁻¹).

Table C.8. Parameters of intraparticle diffusion model for the synthesized AAMs (*Contact time = 24h, C₀ = 70 mg L⁻¹*).

Sample	k_p ($\text{mg g}^{-1} \text{min}^{-0.5}$)	C (mg g^{-1})	R^2
Sep-AAM	0.13	-0.01	0.99
0.5% H ₂ O ₂ -Sep-AAM	0.16	0.045	0.99
1% H ₂ O ₂ -Sep-AAM	0.13	0.05	0.99
2% H ₂ O ₂ -Sep-AAM	0.19	0.35	0.97
3% H ₂ O ₂ -Sep-AAM	0.21	0.06	0.99
6% H ₂ O ₂ -Sep-AAM	0.30	0.10	0.97
8% H ₂ O ₂ -Sep-AAM	0.24	-0.14	0.98
MKGP	0.07	-0.03	0.97
0.5% H ₂ O ₂ -MKGP	0.13	-0.04	0.97
1% H ₂ O ₂ -MKGP	0.15	-0.05	0.96

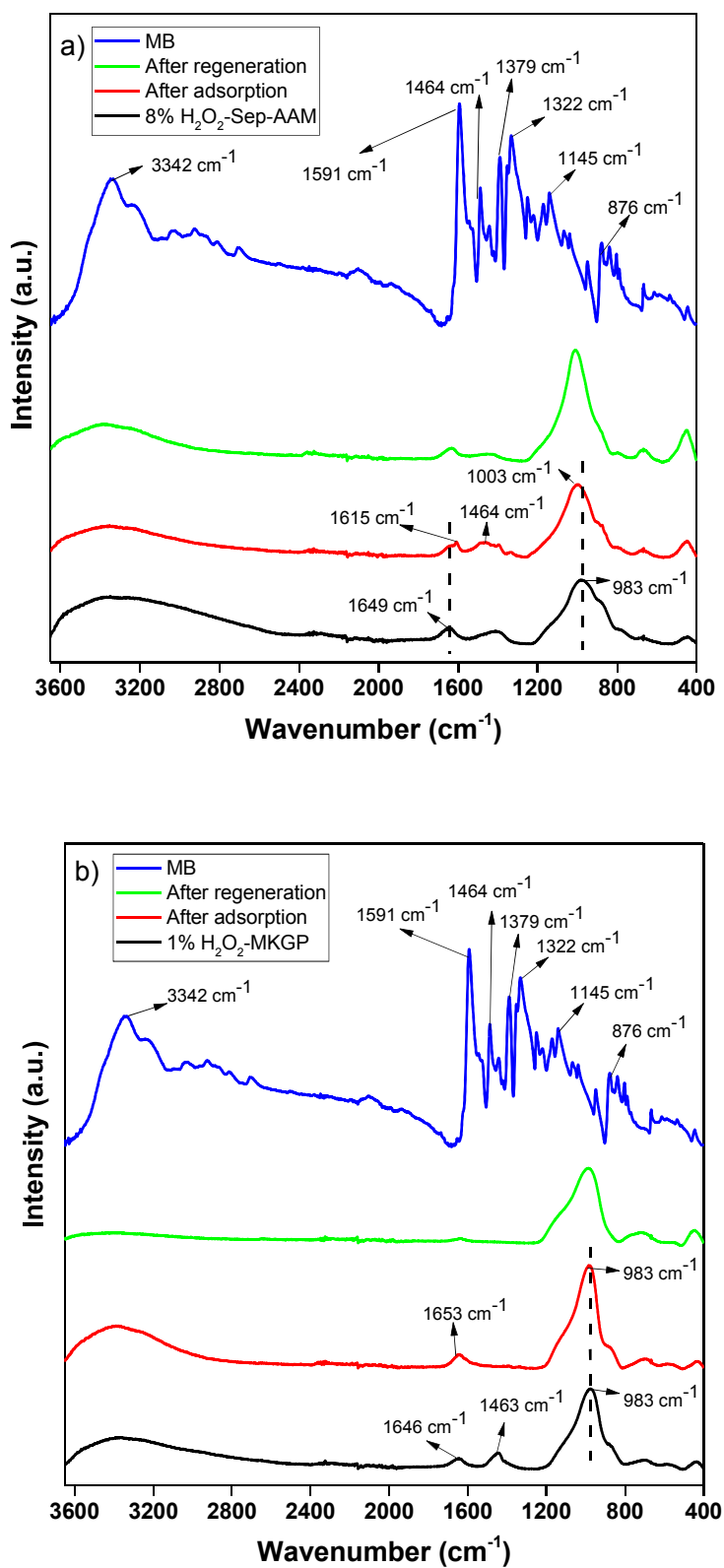


Figure C.6. FTIR spectra of MB and a) 8% H_2O_2 -Sep-AAM and b) 1% H_2O_2 -MKGP sample before and after adsorption, and after 4 cycles of regeneration (*Contact time* = 24 h).

Table C.9. Langmuir separation factor R_L for synthesized AAMs at different temperatures, at all the initial MB concentrations used.

Adsorbent	C_0 (mg L⁻¹)	R_L
Sep-AAM	30	0.034
	40	0.026
	50	0.021
	60	0.017
	70	0.015
	90	0.012
	110	0.009
0.5% H_2O_2 -Sep-AAM	30	0.089
	40	0.068
	50	0.055
	60	0.047
	70	0.040
	90	0.031
	110	0.026
1% H_2O_2 -Sep-AAM	30	0.185
	40	0.145
	50	0.120
	60	0.102
	70	0.089
	90	0.070
	110	0.058
2% H_2O_2 -Sep-AAM	30	0.120

Table C.9. Langmuir separation factor R_L for synthesized AAMs at different temperatures, at all the initial MB concentrations used. (cont.)

Adsorbent	C_0 (mg L⁻¹)	R_L
2%H ₂ O ₂ -Sep-AAM	40	0.093
	50	0.076
	60	0.064
	70	0.055
	90	0.044
	110	0.036
3%H ₂ O ₂ -Sep-AAM	30	0.160
	40	0.125
	50	0.102
	60	0.087
	70	0.075
	90	0.059
	110	0.049
6%H ₂ O ₂ -Sep-AAM	30	0.098
	40	0.075
	50	0.061
	60	0.051
	70	0.044
	90	0.035
	110	0.029
8%H ₂ O ₂ -Sep-AAM	30	0.029
	40	0.035

Table C.9. Langmuir separation factor R_L for synthesized AAMs at different temperatures, at all the initial MB concentrations used. (cont.)

Adsorbent	C_0 (mg L ⁻¹)	R_L
8% H_2O_2 -Sep-AAM	50	0.029
	60	0.024
	70	0.021
	90	0.016
	110	0.013
MKGP	30	0.421
	40	0.353
	50	0.304
	60	0.267
	70	0.238
	90	0.195
	110	0.166
0.5% H_2O_2 -MKGP	30	0.366
	40	0.302
	50	0.257
	60	0.224
	70	0.198
	90	0.161
	110	0.136
1% H_2O_2 -MKGP	30	0.082
	40	0.063
	50	0.051

Table C.9. Langmuir separation factor R_L for synthesized AAMs at different temperatures, at all the initial MB concentrations used. (cont.)

Adsorbent	C_0 (mg L ⁻¹)	R_L
1%H ₂ O ₂ -MKGP	60	0.043
	70	0.037
	90	0.029
	110	0.024

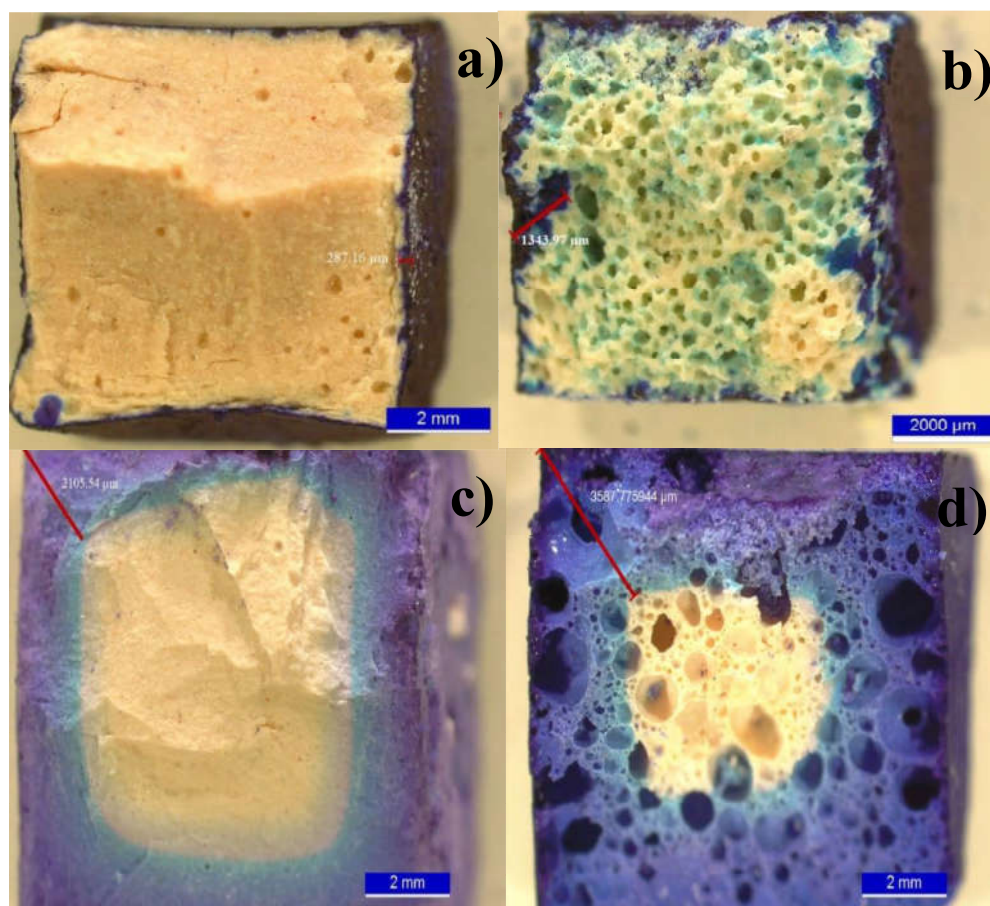


Figure C.7. Stereo microscopy micrographs of the distinct MB diffusion throughout a) Sep-AAM, b) 8%H₂O₂-Sep-AAM, c) MKGP, and d) 1%H₂O₂-MKGP, after adsorption (*Contact time* = 24 h, C_0 = 110 mg L⁻¹).

- C1. Hrenovic, J., M. Rozic, T. Ivankovic, and A. Farkas., “Biosorption of Phosphate from Synthetic Wastewater by Biosolids”, *Central European Journal of Biology*, Vol. 4, No. 3, 2009.
- C2. Ugochukwu, U. C., “Chapter 9. Characteristics of Clay Minerals Relevant to Bioremediation of Environmental Contaminated Systems”, in *Modified Clay and Zeolite Nanocomposite Materials*, Elsevier Inc., 2019, pp. 219–242.
- C3. Zadaka, D., A. Radian, and Y. G. Mishael., “Applying Zeta Potential Measurements to Characterize the Adsorption on Montmorillonite of Organic Cations as Monomers, Micelles, or Polymers”, *Journal of Colloid and Interface Science*, Vol. 352, pp. 171–177, 2010.
- C4. Ma, C. and R. Eggleton., “Cation Exchange Capacity of Kaolinite”, *Clays and Clay Minerals*, Vol. 47, No. 2, pp. 174–180, 1999.
- C5. Rytwo G., S. Nir, L. Margulies, B. Casal, J. Merino, E. Ruiz-Hitzky, and J. M. Serratos, “Adsorption of Monovalent Organic Cations on Sepiolite: Experimental Results and Model Calculations”, *Clays and Clay Minerals*, Vol. 46, No. 3, pp. 340–348, 1998.

APPENDIX D: SUPPLEMENTARY INFORMATION 4

Table D.1. Chemical compositions (wt%) of MK, raw RM, and calcined RM used in this study.

Material	SiO ₂	Al ₂ O ₃	TiO ₂	Fe ₂ O ₃	K ₂ O	CaO	MgO	Na ₂ O
MK	56.21	41.04	1.15	0.36	0.46	0.09	0.07	-
RM	11.67	14.02	5.78	37.1	0.31	1.1	0.23	9.39
Calcined RM	12.59	16.85	5.94	37.45	0.31	1.44	0.2	10.55

Table D.2. The amounts of raw materials (in g) used in geopolymer synthesis, corresponding molar Si/Al and Al/Na ratios, and synthesis conditions used in RMGP synthesis in this study.

Sample	RM	MK	Na ₂ Si ₃ O ₇ solution	NaOH	Si/Al	Al/Na	Thermal treatment
RMGP	2	8	14.01	1.69	2	0.83	1 day 60 °C + 4 weeks 25 °C

Table D.3. BET surface area, average pore size, and pore volume of RMGP and calcined RMGP.

Sample	Surface area (m ² /g)	Pore volume (cm ³ /g)	Pore size (Å)
RMGP	27.14	0.159	324.13
Calcined RMGP	21.14	0.135	404.25

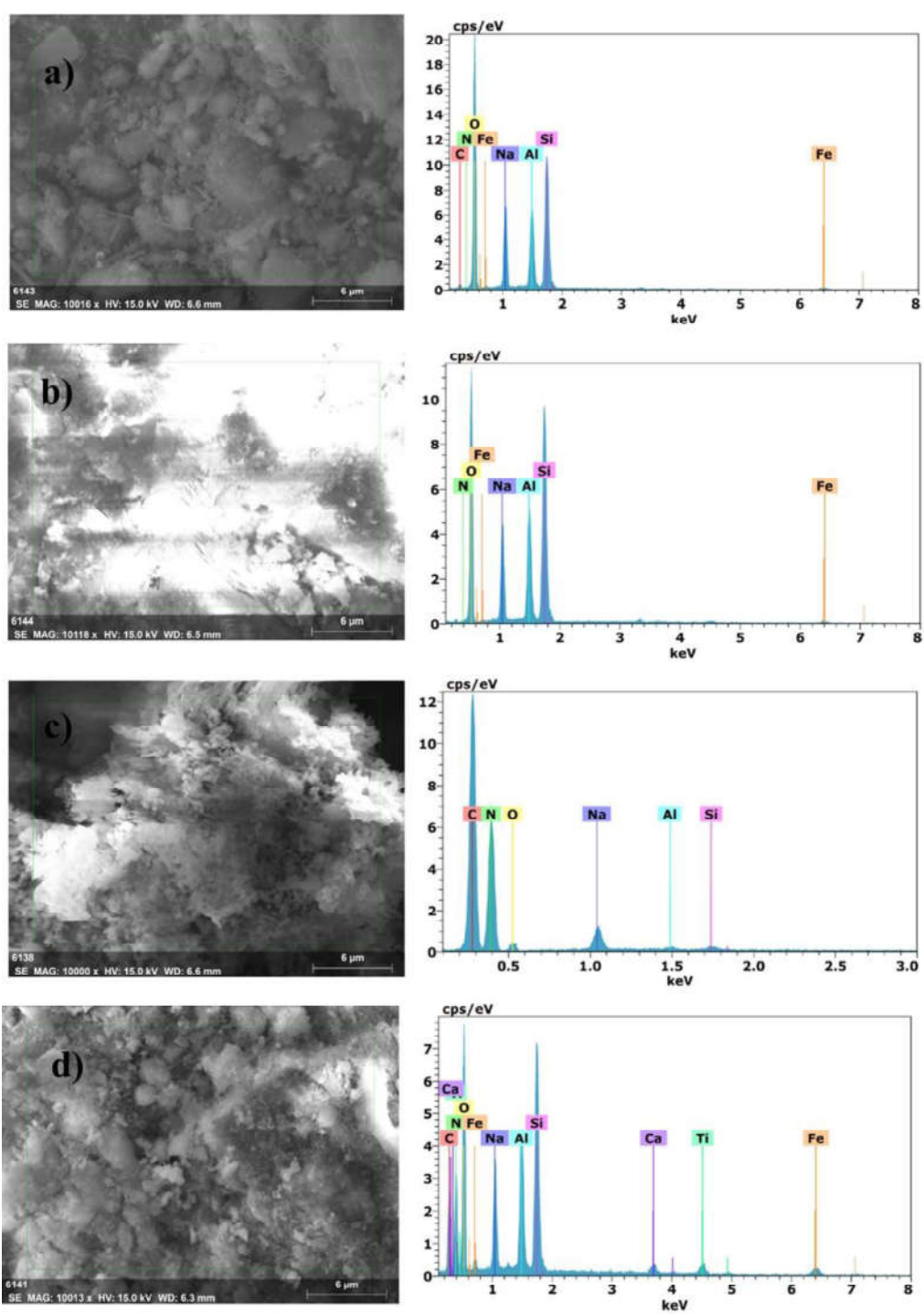


Figure D.1. SEM image, corresponding elemental analysis of a) RMGP, b) Calcined RMGP, c) g-C₃N₄, and d) g-C₃N₄/RMGP.

Table D.4. Atomic % of C, N, O, Si, Al, Na, and Fe in samples which are calculated from EDS spectra.

Sample	Atomic %						
	C	N	O	Si	Al	Na	Fe
RMGP	6.5	0.4	62.3	13.9	6.3	8.6	1.1
Calcined RMGP	-	1.2	59.8	20.6	8.2	9.6	0.6
g-C ₃ N ₄	36.9	57.9	3.9	0.1	0.1	1.1	-
g-C ₃ N ₄ /RMGP	20.2	24.1	38.9	6.9	3.7	3.6	1.2

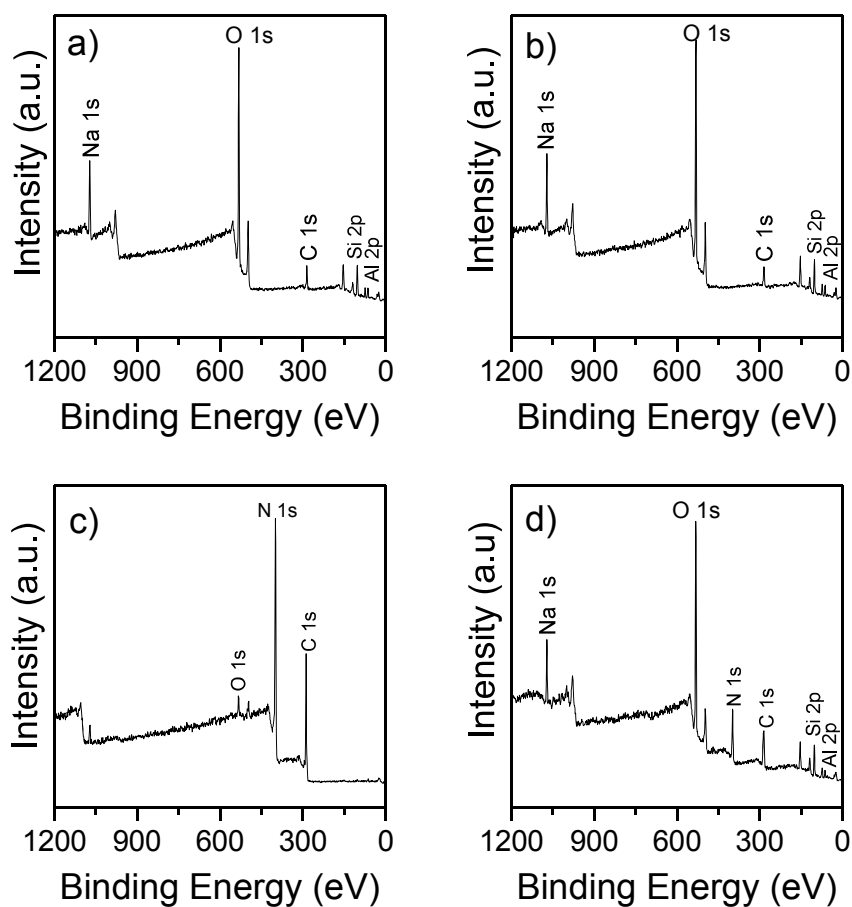


Figure D.2. XP survey spectrum of a) RMGP, b) Calcined RMGP, c) g-C₃N₄, and d) g-C₃N₄/RMGP.

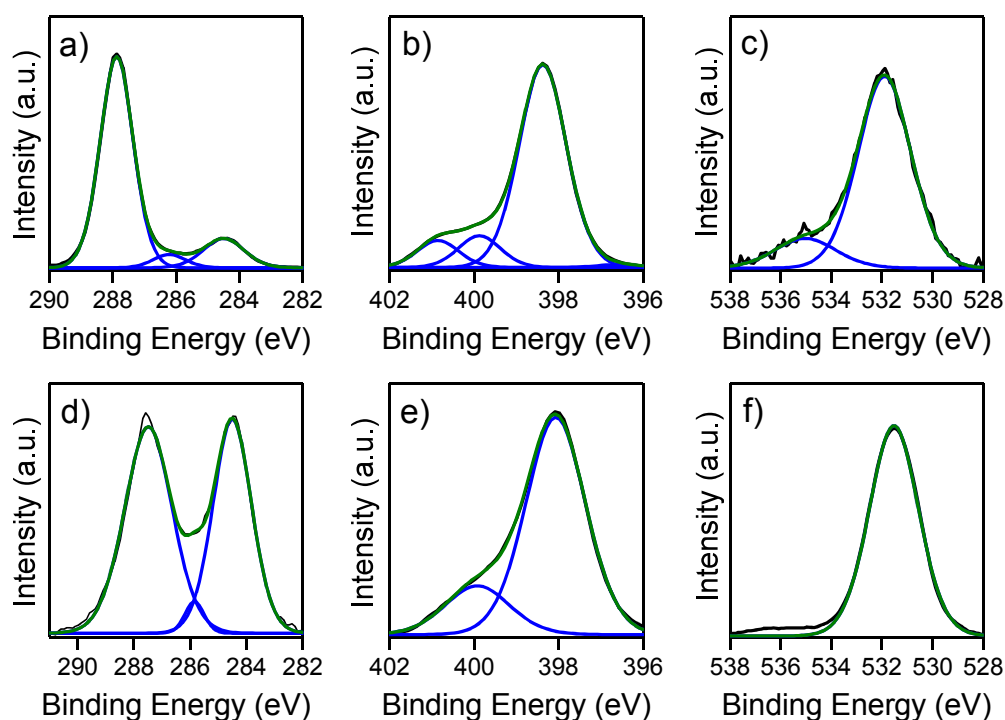


Figure D.3. XPS patterns of a) C 1s, b) N 1s, c) O 1s of g-C₃N₄, d) C 1s, e) N 1s, and f) O 1s of g-C₃N₄/RMGP (Blue lines: fitted individual peaks, green lines: envelope of all fitted peaks).

Table D.5. Atomic % of different elements obtained from fitted peak information of C 1s, O 1s, N 1s, Si 2p, Al 2p, Fe 2p, and Na 1s XP spectra.

Sample	C (at%)	N (at%)	O (at%)	Si (at%)	Al (at%)	Na (at%)	Fe (at%)
RMGP	-	-	60.9	19.6	8.5	10.8	0.2
Calcined RMGP	-	-	59.4	19.6	9.0	11.7	0.2
g-C ₃ N ₄	43.2	53.4	3.4	-	-	-	-
g-C ₃ N ₄ /RMGP	22.3	15.2	38.6	12.2	5.5	5.6	0.6

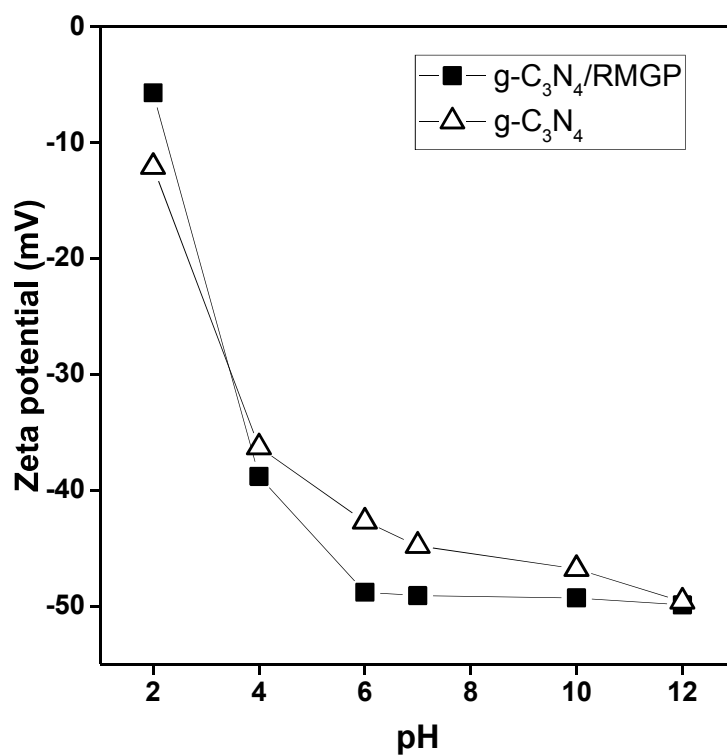


Figure D.4. The change of zeta potential with pH for g-C₃N₄ and g-C₃N₄/RMGP.

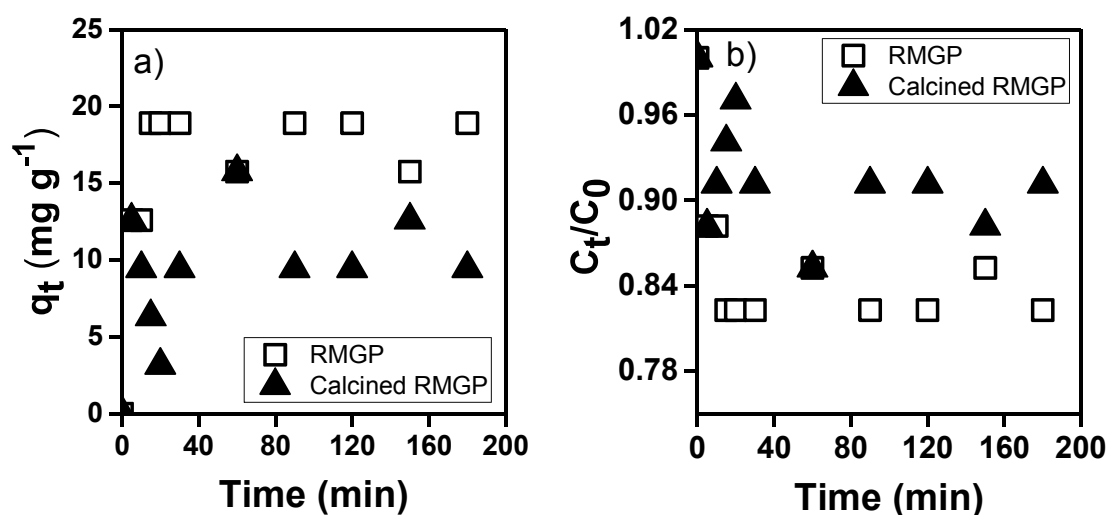


Figure D.5. The influence of contact time on a) Uptake and b) C_t/C_0 of RMGP and Calcined RMGP.

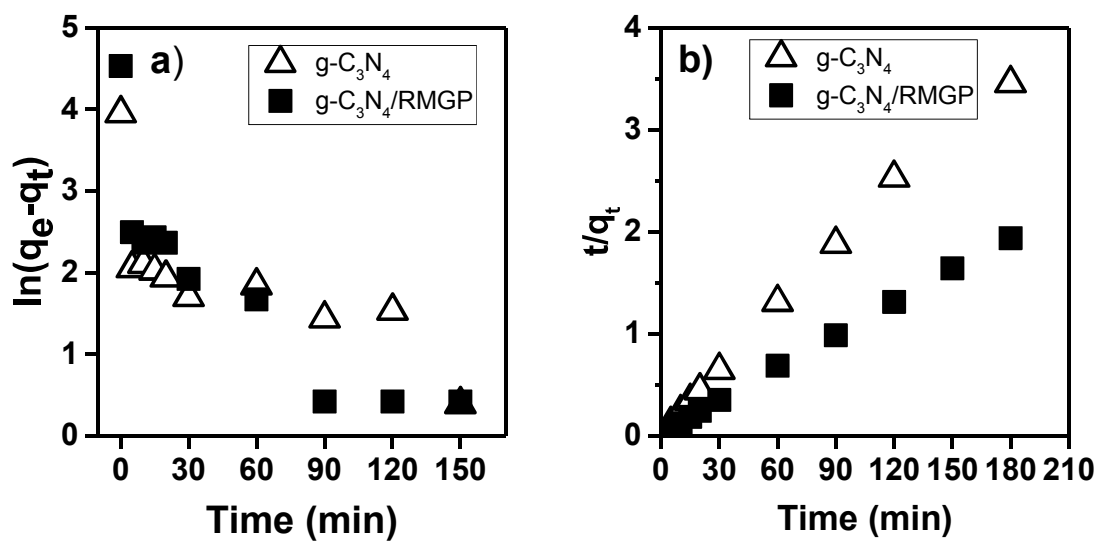


Figure D.6. Pseudo-first and pseudo-second-order kinetic models for the adsorption of MB onto a) $g-C_3N_4$ and b) $g-C_3N_4/RMGP$.

Table D.6. Pseudo-first and pseudo-second-order kinetic model parameters and removal efficiency (%) for adsorption of MB onto RMGP and calcined RMGP.

Adsorbent	$q_{e,exp}$ ($mg\ g^{-1}$)	Pseudo-first-order adsorption kinetics			Pseudo-second-order adsorption kinetics			Removal (%)
		$k_{1,ads,app}$ (min^{-1})	$q_{e,cal}$ ($mg\ g^{-1}$)	R^2	$k_{2,ads,app}$ ($g\ mg^{-1}\ min^{-1}$)	$q_{e,cal}$ ($mg\ g^{-1}$)	R^2	
RMGP	18.89	8.2×10^{-3}	8.61	0.51	5×10^{-2}	17.9	0.98	17.72
Calcined RMGP	12.60	6.1×10^{-3}	6.53	0.37	3×10^{-2}	10.9	0.95	11.81

Table D.7. The influence of adsorbent amount on the apparent pseudo-second-order adsorption kinetic rate constant and adsorption parameters for g-C₃N₄ and g-C₃N₄/RMGP.

Sample	Adsorbent amount (g)	$k_{2,ads,app}$ (g mg ⁻¹ min ⁻¹)	$q_{e,exp}$ (mg g ⁻¹)	Removal (%)	R^2
g-C ₃ N ₄	0.006	5.4×10^{-3}	70.8	42.5	1
	0.008	7.08×10^{-3}	60.2	48.1	0.99
	0.01	1.10×10^{-2}	52.07	48.82	0.99
	0.012	3.0×10^{-2}	46.41	55.7	1
g-C ₃ N ₄ /RMGP	0.006	1.65×10^{-3}	143.6	80.8	1
	0.008	2.30×10^{-3}	115.2	86.4	1
	0.01	5.0×10^{-3}	92.9	87.1	1
	0.012	6.38×10^{-3}	72.7	81.8	1

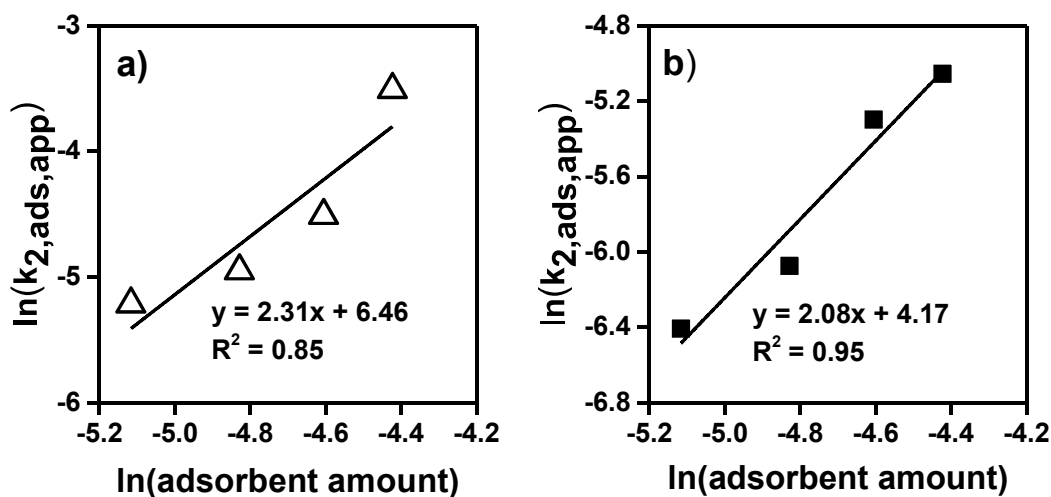


Figure D.7. Influence of adsorbent amount on the apparent pseudo-second-order adsorption rate constant for a) g-C₃N₄ and b) g-C₃N₄/RMGP.

To identify the diffusion mechanism, intraparticle diffusion model should be applied to the experimental data, as corresponding diffusion-related mechanisms cannot be understood from pseudo-first- and pseudo-second-order adsorption kinetic models. The

intraparticle diffusion model was applied on g-C₃N₄ and g-C₃N₄/RMGP samples and shown in Figure D.7. This figure displays that there are two main different characteristics of the diffusion process within this time period (3 h). For both of these two different adsorbents, first steep portion of the figure implies the presence of boundary layer diffusion. Second portion provides information on the intraparticle diffusion and as it is seen from this figure, this portion does not pass through the origin. This situation shows that for the adsorption of MB molecules on both g-C₃N₄ and g-C₃N₄/RMGP, intraparticle diffusion is not the only rate controlling step [1, 2]. As it is deduced from Figure D.7, very rapid adsorption takes place initially within the first 5 minutes, and at the later stages intraparticle diffusion becomes determinant in the whole adsorption process. Results extracted from fitting the experimental data to intraparticle diffusion model is summarized in Table D.8. As stated previously, first sharper portion of Figure D.7 within the first 5 minutes of adsorption signifies that MB dye molecules are diffused through the solution to reach the external surface of the adsorbents. Results presented in Table D.8, implies that the value of $k_{p,1}$ is higher for g-C₃N₄/RMGP than it is for g-C₃N₄, showing that a more rapid adsorption occurs. The intercept of the second portion provides information on the boundary layer thickness and the existence of viscous drag between MB molecules and corresponding adsorbent. In this regard, C_2 value being greater for g-C₃N₄/RMGP (Table D.8) shows that adsorption intensity is higher for g-C₃N₄/RMGP than it is for g-C₃N₄. Second step also denotes to the step where intraparticle diffusion occurs and MB molecules being transported via intraparticle diffusion. Consequently, after the first 5 minutes of adsorption, intraparticle diffusion is the rate determining step. Similar trends in adsorption behaviour were also observed by Li et al. for biochar/g-C₃N₄ composites for MB adsorption where results pointed out that adsorption was affected by both external and internal diffusion mechanisms [3].

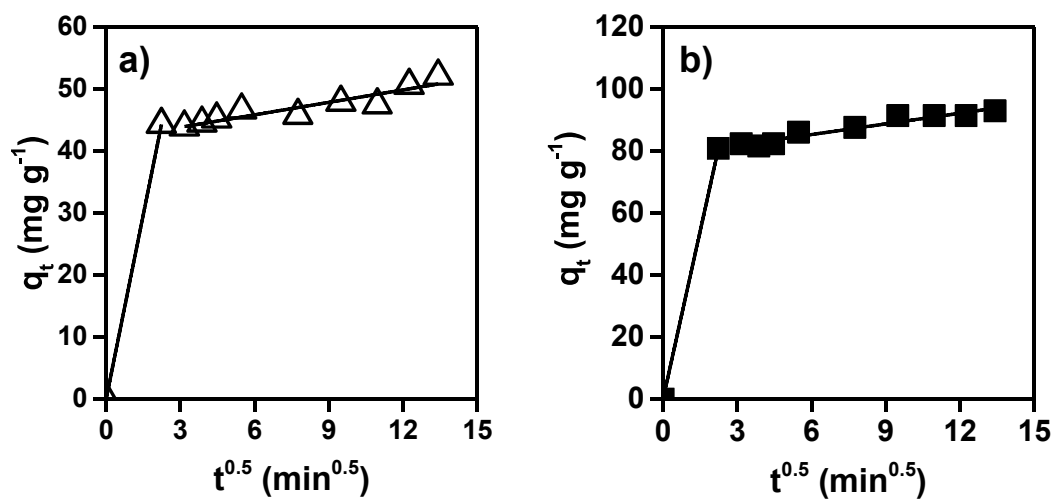


Figure D.8. Intraparticle diffusion model for the adsorption of MB onto a) g-C₃N₄ and b) g-C₃N₄/RMGP.

Table D.8. Parameters of intraparticle diffusion model for g-C₃N₄ and g-C₃N₄/RMGP.

Sample	$k_{p,1}$ (mg g ⁻¹ min ^{-0.5})	C_1 (mg g ⁻¹)	R^2	$k_{p,2}$ (mg g ⁻¹ min ^{-0.5})	C_2 (mg g ⁻¹)	R^2
g-C ₃ N ₄	19.81	0	1	0.67	41.83	0.85
g-C ₃ N ₄ /RMGP	36.15	0	1	1.15	78.46	0.92

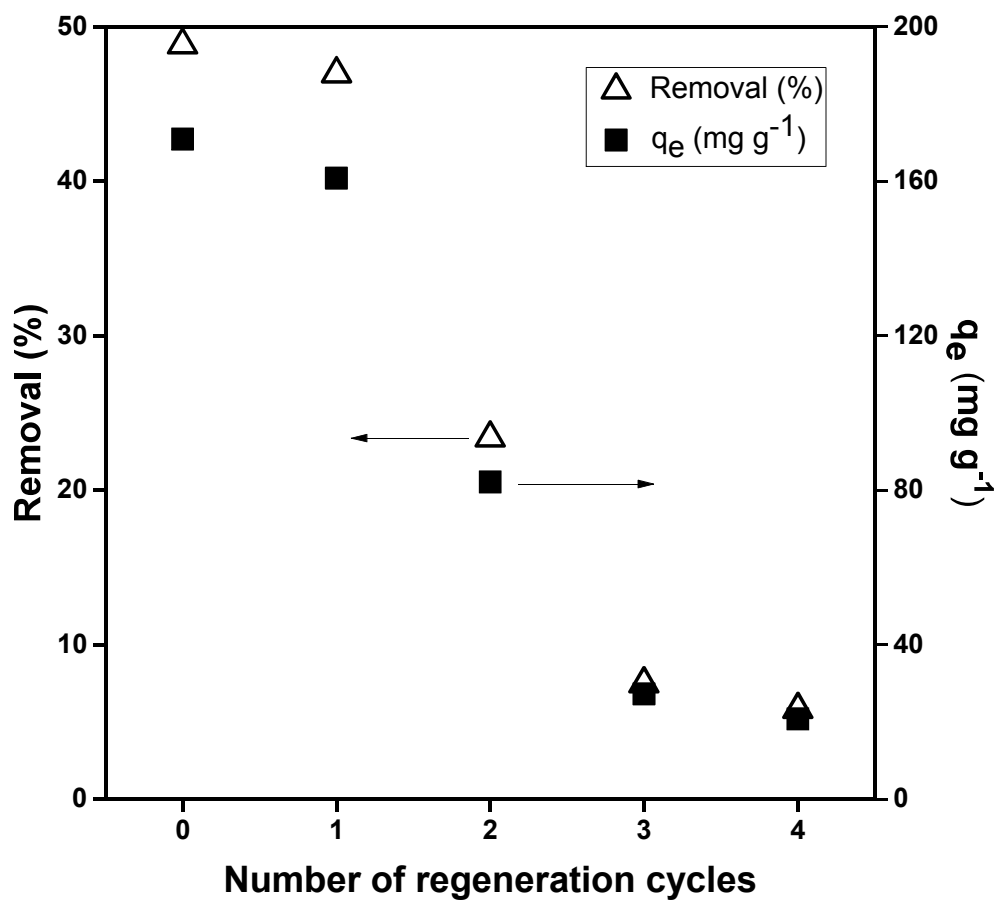


Figure D.9. MB removal (%) and uptake values for g-C₃N₄/RMGP after regeneration cycles.

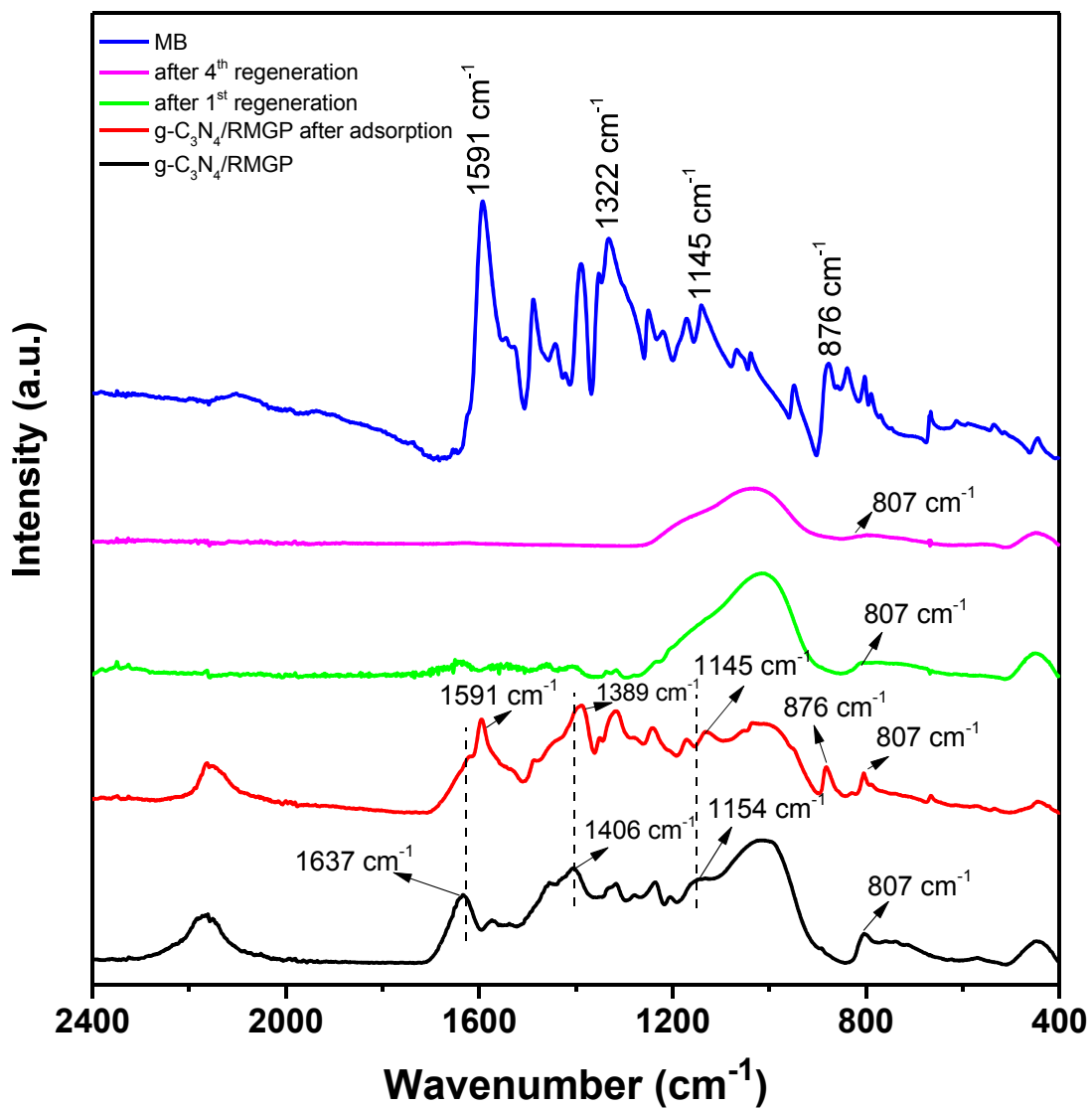


Figure D.10. FTIR spectra of MB and g-C₃N₄/RMGP sample before and after adsorption, and after 4 cycles of regeneration (*Contact time* = 3 h).

Table D.9. Langmuir separation factor R_L for g-C₃N₄ and g-C₃N₄/RMGP for all the initial MB concentrations used.

Sample	Initial MB concentration (mg L ⁻¹)	R_L
g-C ₃ N ₄	10	0.044
	20	0.022
	30	0.015
	40	0.011
	50	0.009
	60	0.007
	70	0.006
g-C ₃ N ₄ /RMGP	10	0.218
	20	0.122
	30	0.085
	40	0.065
	50	0.053
	60	0.044
	70	0.038

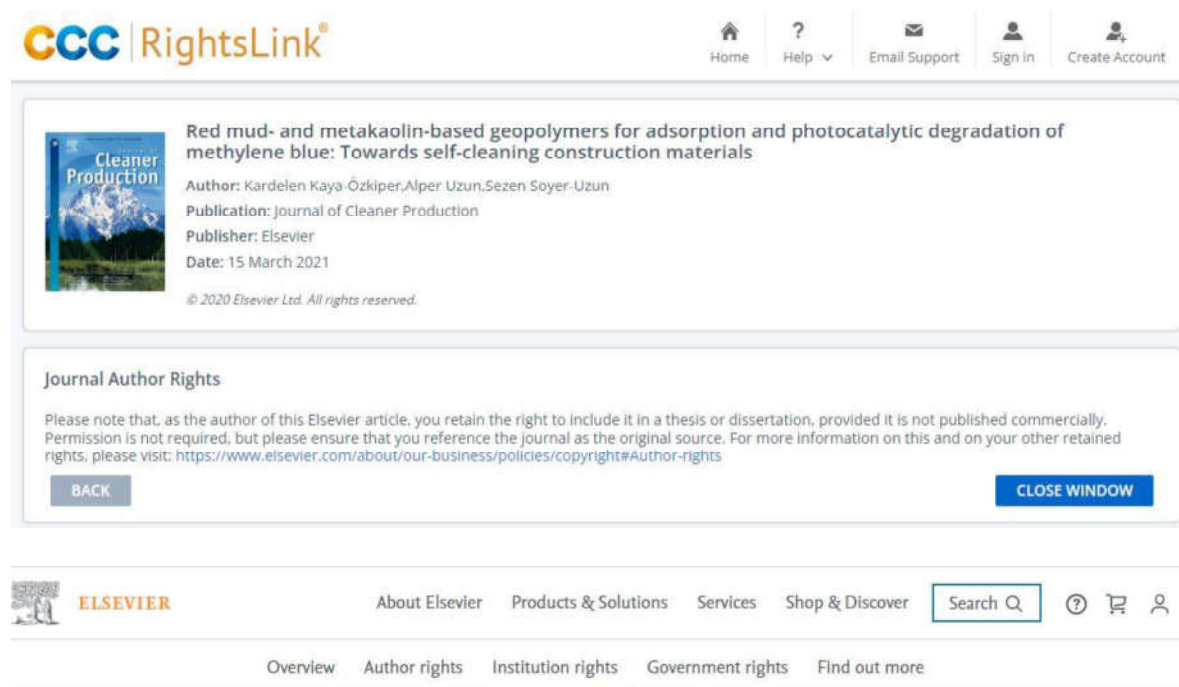
- D1. Nandi, B. K., A. Goswami, and M. K. Purkait, "Removal of Cationic Dyes from aqueous Solutions by Kaolin: Kinetic and Equilibrium Studies", *Applied Clay Science*, Vol. 42, No. 3–4, pp. 583–590, 2009.
- D2. Cheung, W. H., Y. S. Szeto, and G. McKay, "Intraparticle Diffusion Processes During Acid Dye Adsorption onto Chitosan", *Bioresource Technology*, Vol. 98, No. 15, pp. 2897–2904, 2007.

- D3. Li, X. "Preparation and Adsorption Properties of Biochar/g-C₃N₄ Composites for Methylene Blue in Aqueous Solution", *Journal of Nanomaterials*, Vol. 2019, 2019.

PERMISSIONS

Permission for Figures and Tables of Chapter 2, which were originally published in:

Kaya-Özkipir, K., A. Uzun, and S. Soyer-Uzun, “Red Mud- And Metakaolin-Based Geopolymers For Adsorption And Photocatalytic Degradation Of Methylene Blue: Towards Self-Cleaning Construction Materials”, *Journal of Cleaner Production*, Vol. 288, p. 125120, 2021. DOI: <https://doi.org/10.1016/j.jclepro.2020.125120>



The screenshot shows the CCC RightsLink interface. At the top, there are navigation icons for Home, Help, Email Support, Sign in, and Create Account. The main content area displays the article title: "Red mud- and metakaolin-based geopolymers for adsorption and photocatalytic degradation of methylene blue: Towards self-cleaning construction materials". Below the title, it lists the author (Kardelen Kaya-Özkipir, Alper Uzun, Sezen Soyer-Uzun), publication (Journal of Cleaner Production), publisher (Elsevier), and date (15 March 2021). A "Journal Author Rights" section follows, containing a disclaimer and a "CLOSE WINDOW" button. The bottom part of the screenshot shows the Elsevier website header with navigation links and a search bar.

not just by the author:

Institution rights in Elsevier's proprietary journals (providing full acknowledgement of the original article is given)	All articles
Copies can be distributed electronically as well as in physical form for classroom teaching and internal training purposes	√
Material can be included in coursework and courseware programs for use within the institution (but not in Massive Open Online Courses)	√
Articles can be included in applications for grant funding	√
Theses and dissertations which contain embedded final published articles as part of the formal submission can be posted publicly by the awarding Institution with DOI links back to the formal publication on ScienceDirect	√

Permission for Figures and Tables of Chapter 3, which were originally published in:

Kaya-Özkipir, K., A. Uzun, and S. Soyer-Uzun, “A Novel Alkali Activated Magnesium Silicate As An Effective And Mechanically Strong Adsorbent For Methylene Blue Removal”, *Journal of Hazardous Materials*, Vol. 424, 2022. DOI: <https://doi.org/10.1016/j.jhazmat.2021.127256>

CCC RightsLink® Home Help Email Support Sign in Create Account



A novel alkali activated magnesium silicate as an effective and mechanically strong adsorbent for methylene blue removal

Author: Kardelen Kaya-Özkipir, Alper Uzun, Sezen Soyer-Uzun
 Publication: Journal of Hazardous Materials
 Publisher: Elsevier
 Date: 15 February 2022
 © 2021 Elsevier B.V. All rights reserved.

Journal Author Rights

Please note that, as the author of this Elsevier article, you retain the right to include it in a thesis or dissertation, provided it is not published commercially. Permission is not required, but please ensure that you reference the journal as the original source. For more information on this and on your other retained rights, please visit: <https://www.elsevier.com/about/our-business/policies/copyright#Author-rights>

BACK
CLOSE WINDOW

ELSEVIER About Elsevier Products & Solutions Services Shop & Discover Search ?

[Overview](#)
[Author rights](#)
[Institution rights](#)
[Government rights](#)
[Find out more](#)

not just by the author:

Institution rights in Elsevier's proprietary journals (providing full acknowledgement of the original article is given)	All articles
Copies can be distributed electronically as well as in physical form for classroom teaching and internal training purposes	✓
Material can be included in coursework and courseware programs for use within the institution (but not in Massive Open Online Courses)	✓
Articles can be included in applications for grant funding	✓
Theses and dissertations which contain embedded final published articles as part of the formal submission can be posted publicly by the awarding institution with DOI links back to the formal publication on ScienceDirect	✓